

# Development of diamond-like carbon-based nanocomposite as protective coatings

Bui, Xuan Lam

2005

Bui, X. L. (2005). Development of diamond-like carbon-based nanocomposite as protective coatings. Doctoral thesis, Nanyang Technological University, Singapore.

<https://hdl.handle.net/10356/6118>

<https://doi.org/10.32657/10356/6118>

---

Nanyang Technological University

*Downloaded on 13 Mar 2024 15:43:17 SGT*

# **Development of Diamond-like Carbon-based Nanocomposite as Protective Coatings**

**Bui Xuan Lam**

**School of Mechanical & Aerospace Engineering**

A thesis submitted to the Nanyang Technological University in  
fulfilment of the requirement for the degree of  
Doctor of Philosophy

**2005**

## **ABSTRACT**

Diamond-like carbon (DLC) is well known as a preferred material for tribological applications since it exhibits high hardness, good wear resistance and very low friction when sliding against most engineering materials. Apart from these desirable properties, DLC has drawbacks such as very high internal stress, low toughness, bad thermal stability and poor oxidation resistance. These drawbacks strongly limit the coating thickness, load-bearing capability, working temperature and working environment of DLC.

Piston rings play an important role in internal combustion engines and contribute a large part to the total friction losses. Therefore, huge benefits in reduction of friction losses (thus fuel consumption) and increase of working life and reliability of the engines can be achieved if DLC is utilized as the protective coating for piston rings. However, due to the above mentioned drawbacks, pure DLC is not suitable for this application.

In this study, a DLC-based nanocomposite with TiC crystallites embedded in an amorphous matrix of Al-doped DLC has been developed. This novel coating has low residual stress, very high toughness, good thermal stability and excellent oxidation resistance while the hardness is maintained at an adequate level. This nanocomposite coating exhibits low friction (less than 0.25) under dry and extremely low friction (less than 0.05) under boundary lubrication with engine oil.

DLC-based nanocomposite is a new generation of materials as protective coatings for piston rings. The initial engine tests indicate that DLC-based nanocomposite is superior

compared to TiN, one of the best materials for protective coatings of piston rings, in both wear resistance and fuel consumption.



## **ACKNOWLEDGEMENTS**

I would like to express my deep gratitude to my supervisor, Associate Professor Sam Zhang Shanyong for his effective academic advisory, his encouragement and care in my study and my living.

I would like to thank Nanyang Technological University and School of Mechanical and Production Engineering for granting me the research scholarship and providing me an opportunity to work on this project.

I would like to thank Dr. Fu Yongqing and Dr. Cheng Kui for their discussions, suggestions and assistance.

I would like to thank the technicians in Materials Laboratory A and B for their helpful support in experimental part. The warm friendship and kind assistance of my friends in the research group are also acknowledged.

I would like to thank my parents and my younger sister for their support and encouragement.

Last but not least, I sincere dedicate this thesis to my wife, Xuan Vinh, and my daughter, Quynh Lam, thanks for their love and support.

## PUBLICATIONS

### Book chapter

Sam Zhang and Xuan Lam Bui, Adhesion improvement of magnetron sputtered amorphous carbon on cemented carbide, in *Adhesion Aspects of Thin Films*, Vol. 2, Edited by K. L. Mittal and Published by VSP, Utrecht, The Netherlands, 2005 (ISBN 90 6764 421 8)

### Journal papers

1. Sam Zhang, Xuan Lam Bui et al. Magnetron sputtered hard a-C coatings of very high toughness, *Surface and Coatings Technology* 167 (2003)137-142
2. Sam Zhang, Xuan Lam Bui et al. Magnetron-sputtered nc-TiC/a-C(Al) tough nanocomposite coatings, *Thin Solid Films* 467(2004)261-266
3. Sam Zhang, Xuan Lam Bui et al. Bias-graded deposition of diamond-like carbon for tribological applications, *Diamond and Related Materials* 13(2004)867-871
4. Sam Zhang, Xuan Lam Bui et al. Development of carbon-based coating of extremely high toughness with good hardness, *International Journal of Nanoscience* 3(4-5) (2004)571-578
5. Sam Zhang, Yongqing Fu, Xuan Lam Bui et al. XPS study of diamond-like carbon-based nanocomposite films, *International Journal of Nanoscience* 3 (6) (2004) 1-6
6. Sam Zhang, Xuan Lam Bui et al. Towards high adherent and tough a-C coatings, *Thin Solid Films* 482 (2005) 138-144
7. Sam Zhang, Xuan Lam Bui et al. Microstructure and tribological properties of magnetron sputtered nc-TiC/a-C nanocomposite, *Surface and Coatings Technology* 198 (2005) 206-211

### Conferences

1. Sam Zhang and Xuan Lam Bui, Magnetron sputtered carbon and carbon-based nanocomposite coatings of high hardness and low residual stress, *The 4th International*

*Ceramics Conference (Austceram 2004), Melbourne, Victoria, Australia, 29 November-1 December, 2004 (Invited paper)*

2. Sam Zhang and Xuan Lam Bui, Tribological behaviors of diamond-like carbon and carbon-based protective coatings in dry and fluid-lubricated conditions, *The First International Conference on Flow Dynamics*, Sendai, Japan, 11-12 November, 2004 (Invited paper)

3. Sam Zhang and Xuan Lam Bui, Microstructure and tribological properties of magnetron sputtered nc-TiC/a-C nanocomposite, *The 2nd International Conference on Advances of Thin Films and Coatings Technology Singapore*, 13-17 July, 2004

4. Sam Zhang, Xuan Lam Bui et al. Superhard and tough nanocomposite thin films for engineering application, *Functional Hard Coatings: Aseva Summer School for Vacuum and Applications 2004*, Avila, Spain, 4-8 July, 2004 (Invited keynote)

5. Sam Zhang, Xuan Lam Bui et al. Adhesion and tribological properties of amorphous carbon and carbon-based nanocomposite coatings, *European Materials Research Society, Spring Meeting, Symposium J: "Synthesis, Characterisation and Advanced Applications of Amorphous Carbon Films"*, Strasbourg, France, 24-28 May, 2004 (Invited paper)

6. Sam Zhang, Xuan Lam Bui et al. Magnetron sputtered DLC and nanocomposite with DLC matrix coatings of high hardness and toughness for tribological applications, *International Conference on Materials for Advanced Technology (ICMAT 2003)*, Singapore, 29 June - 4 July, 2003

7. Sam Zhang and Xuan Lam Bui, Adhesion improvement of magnetron sputtered amorphous carbon on cemented carbide, *Adhesion Aspects of Thin Films (Including Adhesion Measurement and Metallized Plastics)*, Grosvenor Resort Hotel, Orlando, FL, USA, 15-17 December, 2003

8. Sam Zhang, Xuan Lam Bui et al. Magnetron sputtered nanocomposite thin films: The quest for hardness together with toughness, *The 2nd International Conference on Materials Processing for Properties and Performance (MP3)*, Yokohama, Japan, 8 -13 October, 2003 (Invited keynote)

9. Sam Zhang, Xuan Lam Bui et al. Bias-graded deposition of diamond-like carbon for tribological applications, *The 14th European Conference on Diamond, Diamond-Like Materials, Carbon Nanotubes, Nitrides and Silicon Carbide, Salzburg, Austria, 7-13 September, 2003*
10. Sam Zhang, Xuan Lam Bui et al. XPS study of diamond-like carbon based nanocomposite films, *International Conference on Materials for Advanced Technology (ICMAT 2003), Singapore, 7 - 12 December, 2003*
11. Sam Zhang, Xuan Lam Bui et al. Magnetron sputtered hard a-C coatings of very high toughness, *1st International Conference on Materials Processing for Properties and Performance (MP3), Singapore, 1-3 August, 2002*

## TABLE OF CONTENTS

|   |     |
|---|-----|
| <b>ABSTRACT</b>   | I   |
| <b>ACKNOWLEDGEMENTS</b>   | III |
| <b>PUBLICATIONS</b>   | IV  |
| <b>TABLE OF CONTENTS</b>  | VII |
| <b>LIST OF FIGURES</b>  | XI  |
| <b>TABLE OF ABBREVIATIONS</b>   | XIX |
| <b>Chapter 1. INTRODUCTION</b>  | 1   |
| 1.1. Background and objectives of the project                                 | 1   |
| 1.2. Scope of the project   | 3   |
| 1.3. Organization of this thesis  | 3   |
| <b>Chapter 2. LITERATURE REVIEW</b>   | 6   |
| 2.1. Carbon and diamond-like carbon   | 6   |
| 2.1.1. Carbon   | 6   |
| 2.1.1.1. Diamond  | 7   |
| 2.1.1.2. Graphite   | 11  |
| 2.1.2. Diamond-like carbon  | 14  |
| 2.1.2.1. Preparation techniques for DLC                                       | 15  |
| 2.1.2.1.1. Physical Vapor Deposition  | 16  |
| 2.1.2.1.2. Chemical Vapor Deposition  | 18  |
| 2.1.2.2. Applications of diamond -like carbon                                 | 21  |
| 2.2. Mechanical and tribological properties of diamond-like carbon            | 22  |
| 2.2.1. Hardness and Young's modulus   | 22  |
| 2.2.2. Tribological behavior of DLC   | 25  |
| 2.2.2.1. Influence of environment on friction of DLC coatings                 | 26  |
| 2.2.2.2. Friction and wear of hydrogenated DLC and hydrogen-free DLC coatings | 31  |
| 2.2.3. Residual stress of DLC coatings  | 34  |
| 2.2.4. High temperature behavior and oxidation                                | 38  |

|   |    |
|---|----|
| 2.2.5. Summary  | 39 |
| 2.3. Nanocomposite and DLC-based nanocomposite coatings                   | 40 |
| 2.3.1. Nanocrystalline materials  | 40 |
| 2.3.2. DLC-based nanocomposite coatings                                   | 41 |
| 2.3.2.1. Doped DLC coatings   | 41 |
| 2.3.2.2. DLC nanocomposite coatings                                       | 43 |
| 2.3.2.2.1. Concept  | 43 |
| 2.3.2.2.2. Magnetron sputtering of nanocomposite coatings                 | 48 |
| 2.3.3. Summary  | 51 |
| 2.4. Piston rings and protective coatings for piston rings                | 52 |
| 2.4.1. Piston rings   | 52 |
| 2.4.2. Friction and wear of piston rings                                  | 54 |
| 2.4.2.1. Lubrication of piston rings                                      | 54 |
| 2.4.2.2. Friction of piston rings   | 57 |
| 2.4.2.2.1. Friction losses  | 57 |
| 2.4.2.2.2. Reduction of friction losses of piston rings - cylinder system | 57 |
| 2.4.2.3. Wear of piston rings   | 59 |
| 2.4.3. Coatings for piston rings  | 62 |
| 2.4.3.1. Running-in coatings  | 62 |
| 2.4.3.2. Wear resistance coatings   | 63 |
| 2.4.3.2.1. Chromium, Molybdenum   | 63 |
| 2.4.3.2.2. Nitride coatings   | 64 |
| 2.4.3.2.3. Composite  | 65 |
| 2.4.3.2.4. K-ramic  | 66 |
| 2.4.3.3. Evaluation of recent protective coatings for piston rings        | 66 |
| 2.4.4. Summary  | 67 |
| <b>CHAPTER 3. EXPERIMENTAL METHODS</b>                                    | 69 |
| 3.1. Coating deposition   | 69 |
| 3.2. Characterization   | 72 |
| 3.2.1. Image characterization   | 72 |
| 3.2.2. Structure of coatings  | 73 |

|   |     |
|---|-----|
| 3.2.3. Coating chemistry  | 73  |
| 3.2.4. Mechanical and tribological evaluation of the coatings                   | 74  |
| 3.2.4.1. Residual stress  | 74  |
| 3.2.4.2. Hardness and Young's modulus   | 75  |
| 3.2.4.3. Adhesion strength  | 76  |
| 3.2.4.4. Tribotests   | 77  |
| <b>CHAPTER 4. MAGNETRON SPUTTERED HYDROGEN-FREE DLC (a-C)</b>                   |     |
| <b>COATINGS</b>   | 79  |
| 4.1. Effect of plasma cleaning on the adhesion of DLC coatings to the substrate | 79  |
| 4.2. Process pressure   | 83  |
| 4.3. Power density  | 87  |
| 4.4. Substrate bias   | 89  |
| 4.5. Characterization of magnetron sputtered DLC coatings                       | 92  |
| 4.5.1. Surface morphology   | 92  |
| 4.5.2. Structure of DLC coatings  | 98  |
| 4.5.3. Hardness and residual stress of DLC coatings                             | 102 |
| 4.5.3.1. Hardness   | 102 |
| 4.5.3.2. Residual stress  | 105 |
| 4.5.4. Adhesion strength  | 113 |
| 4.6. Tribological properties of magnetron sputtered DLC coatings                | 117 |
| 4.7. Enhancement of performance of magnetron sputtered DLC coatings             | 134 |
| 4.8. Thermal stability and oxidation resistance of magnetron sputtered DLC      | 139 |
| 4.9. Summary  | 142 |
| <b>CHAPTER 5. MAGNETRON SPUTTERED DLC NANOCOMPOSITE</b>                         |     |
| <b>COATINGS</b>   | 145 |
| 5.1. Effect of Al-incorporation on the properties of DLC                        | 146 |
| 5.1.1. Composition and coating structure  | 146 |
| 5.1.2. Hardness, residual stress and adhesion strength of Al-doped DLC coatings | 153 |
| 5.2. Effect of Ti-incorporation on the properties of DLC                        | 157 |
| 5.2.1. Composition and coating structure  | 157 |
| 5.2.2. Hardness and residual stress   | 171 |

|   |     |
|---|-----|
| 5.2.3. Surface roughness and coefficient of friction in dry conditions  | 175 |
| 5.3. nc-TiC/a-C(Al) nanocomposite coatings  | 177 |
| 5.3.1. Deposition and structure of the nc-TiC/a-C(Al) coatings  | 178 |
| 5.3.2. Mechanical properties of nc-TiC/a-C(Al) nanocomposite coatings   | 184 |
| 5.4. Thermal stability of nc-TiC/a-C(Al) coatings   | 190 |
| 5.5. Tribology of nc-TiC/a-C(Al) coatings   | 197 |
| 5.5.1. Dry (non-lubricated) condition   | 197 |
| 5.5.2. Oil-lubricated condition   | 202 |
| 5.6. Summary  | 206 |
| <b>CHAPTER 6. PRELIMINARY CASE STUDY: APPLICATION OF nc-TiC/a-C(Al) NANOCOMPOSITE AS PROTECTIVE COATING FOR PISTON RING IN INTERNAL COMBUSTION ENGINE</b> | 208 |
| 6.1. The engine   | 209 |
| 6.2. Piston ring  | 211 |
| 6.3. Testing procedure  | 212 |
| 6.4. Results  | 212 |
| 6.5. Summary  | 216 |
| <b>CHAPTER 7. CONCLUSIONS AND FUTURE WORK</b>   | 218 |
| 7.1. Conclusions  | 218 |
| 7.2. Future work  | 220 |
| <b>REFERENCES</b>   | 222 |



## LIST OF FIGURES

|  |    |
|--|----|
| <i>Figure 2.1.</i> Cubic diamond structure   | 9  |
| <i>Figure 2.2.</i> $sp^3$ hybrid orbitals  | 10 |
| <i>Figure 2.3.</i> Hexagonal diamond structure   | 11 |
| <i>Figure 2.4.</i> $sp^2$ hybrid orbitals  | 12 |
| <i>Figure 2.5.</i> Hexagonal graphite structure  | 13 |
| <i>Figure 2.6.</i> Carbon motion in the (a) $E_{2g}$ G mode and (b) $A_{1g}$ D mode  | 15 |
| <i>Figure 2.7.</i> Deposition techniques using solid carbon  | 17 |
| <i>Figure 2.8.</i> Hot filament CVD system   | 19 |
| <i>Figure 2.9.</i> Microwave- PECVD system   | 19 |
| <i>Figure 2.10.</i> DC jet PECVD system  | 20 |
| <i>Figure 2.11.</i> Relationship between coefficient of friction of hydrogenated DLC (sliding against steel counterpart) and relative humidity | 27 |
| <i>Figure 2.12.</i> Influence of humidity on coefficient of friction (with steel as the counterpart)   | 30 |
| <i>Figure 2.13.</i> Influence of humidity on coefficient of friction (with sapphire as the counterpart)  | 30 |
| <i>Figure 2.14.</i> Magnetron configuration and effect of magnetic field   | 50 |
| <i>Figure 2.15.</i> Piston rings and related details   | 53 |
| <i>Figure 2.16.</i> Distribution of gas pressure on the working surface of piston rings  | 54 |
| <i>Figure 2.17.</i> Stribeck diagram and probable lubrication regimes of typical friction couples in internal combustion engine                | 56 |
| <i>Figure 2.18.</i> Representation of piston ring-cylinder wall system approach to tribology   | 58 |
| <i>Figure 2.19.</i> Adhesive wear  | 59 |
| <i>Figure 2.20.</i> Abrasive wear  | 60 |
| <i>Figure 3.1.</i> The picture (a) and schematic diagram (b) of E303A magnetron sputtering system  | 71 |
| <i>Figure 3.2.</i> Berkovich indenter of XP nanoindentation hardness tester  | 75 |
| <i>Figure 3.3.</i> Load and unload curve obtained from nanoindentation hardness tester.  |    |

|   |    |
|---|----|
| The plasticity of coating is estimated by dividing the displacement after complete unloading by the maximum displacement  | 76 |
| <i>Figure 3.4.</i> Schematic diagram of scratch test  | 77 |
| <i>Figure 3.5.</i> Schematic diagram of tribotest   | 77 |
| <i>Figure 4.1.</i> The relationship between RF bias voltage and surface roughness of the steel substrate after plasma cleaning. The surface roughness considerably increases at bias voltages higher than 200 V                         | 80 |
| <i>Figure 4.2.</i> Effect of plasma cleaning on the surface of steel substrate (a) The surface without plasma cleaning (b) Plasma cleaned at RF voltage of 200 V (c) Plasma cleaned at RF voltage of 500 V                              | 81 |
| <i>Figure 4.3.</i> Influence of plasma cleaning voltage on the adhesion strength of DLC coatings deposited under (a) - 60 V and (b) -140 V bias. Plasma cleaning at 300 V for 30 min gives the best adhesion strength for both coatings | 83 |
| <i>Figure 4.4.</i> The influence of process pressure on the deposition rate of DLC coatings. At the same process pressure, the deposition rate is considerably higher as the substrate is located nearer to the target                  | 85 |
| <i>Figure 4.5.</i> The deposition rate as a function of power density, it increases as increasing the power density   | 89 |
| <i>Figure 4.6.</i> DLC coating deposited at power density of 4.5 W/cm <sup>2</sup> and DC bias voltage of -20 V   | 91 |
| <i>Figure 4.7.</i> Deposition rate as a function of negative bias voltage   | 92 |
| <i>Figure 4.8.</i> Effect of ion energy on the surface roughness. Higher ion energy results in smoother surface   | 94 |
| <i>Figure 4.9.</i> AFM images of DLC coatings (about 1.2 μm thickness) deposited on [100] Si wafers (2nm R <sub>a</sub> ) under different bias voltages: (a) -20 V, (b) -60 V, (c) -100 V, and (d) -140 V                               | 95 |
| <i>Figure 4.10.</i> Figure 4.10. The influence of bias voltage on the surface roughness of DLC coating: coating deposited under higher bias voltage has smoother surface (lower R <sub>a</sub> )  | 96 |
| <i>Figure 4.11.</i> Surface morphology of DLC coating deposited at power density of 10.5 W/cm <sup>2</sup> , bias voltage of -100 V and different process pressures: (a) 0.6 Pa and   |    |

|   |     |
|---|-----|
| (b) 1.2 Pa. Rougher surface with larger graphite clusters was seen with coating deposited under higher process pressures  | 97  |
| <i>Figure 4.12.</i> TEM image of DLC coating showing the amorphous nature with a broad halo observed from diffraction pattern   | 98  |
| <i>Figure 4.13.</i> Raman spectrum with deconvoluted peaks of DLC coating deposited at power density of 10.5 W/cm <sup>2</sup> and bias voltage of (a) - 60 V and (b) -150 V  | 99  |
| <i>Figure 4.14.</i> I <sub>G</sub> /I <sub>G</sub> ratios obtained from Raman spectra as a function of negative bias voltage: higher bias voltage results in lower I <sub>D</sub> /I <sub>G</sub> ratio   | 100 |
| <i>Figure 4.15.</i> sp <sup>3</sup> fraction as a function of energy of carbon deposited at room temperature as reported by several authors (The data was collected and drawn by Lifshitz [13])   | 101 |
| <i>Figure 4.16.</i> Hardness and Young's modulus of DLC coating as a function of negative bias voltage. As bias voltage increases, hardness and Young's modulus increase as a result of increase in sp <sup>3</sup> fraction  | 102 |
| <i>Figure 4.17.</i> Ar content in the DLC coating as a function of process pressure. The Ar content increases linearly as process pressure increases  | 104 |
| <i>Figure 4.18.</i> Hardness and Young's modulus of DLC coatings as a function of process pressure. The hardness and Young's modulus decreases as process pressure increases  | 105 |
| <i>Figure 4.19.</i> Surface of 1.2 μm DLC coating (14 days after deposition), no sign of damage was observed (a). The self-destruction of a 1.5 μm DLC coating deposited on a Si wafer due to high residual stress: (b) just after unloading from the chamber (c) after 15 minutes (d) after 30 minutes and (e) after 120 minutes | 108 |
| <i>Figure 4.20.</i> Illustration of stress relaxation style   | 110 |
| <i>Figure 4.21.</i> Compressive residual stress in DLC coatings as a function of negative bias voltage  | 112 |
| <i>Figure 4.22.</i> Influence of negative bias voltage on the critical load from scratch tests. The critical load decreases and the stress increases as bias voltage increases  | 114 |
| <i>Figure 4.23.</i> Scratches on 1.2 μm DLC coatings deposited at a power density of 10.5 W/cm <sup>2</sup> , process pressure of 0.4 Pa under different bias voltages: (a) -20 V, (b) - 60 V, (c) -100 V, and (d) -140 V. The tiny cracks are seen before the damage on  |     |

|  |     |
|--|-----|
| coatings deposited under low bias voltages (-20 V and -60 V)   | 116 |
| <i>Figure 4.24.</i> Coefficient of friction as a function of sliding distance with DLC coatings deposited under different bias voltages (counterpart is alumina)   | 119 |
| <i>Figure 4.25.</i> Coefficient of friction as a function of sliding distance of DLC coating deposited under – 140 V bias (with rotation radius of 16 mm and 8 mm)   | 120 |
| <i>Figure 4.26.</i> Coefficient of friction as a function of sliding distance of DLC coating deposited under – 140 V bias (with applied loads of 5 and 10 N)   | 121 |
| <i>Figure 4.27.</i> Wear scar with debris accumulated on the alumina ball and wear track on the DLC coating after a 2.5 Km tribotest   | 122 |
| <i>Figure 4.28.</i> Comparison of Raman spectra of as deposited DLC coating, wear track, and wear debris   | 123 |
| <i>Figure 4.29.</i> Schematic explanation of the formation of the graphite-like structure and the transfer layer accumulation observed after the wear test   | 124 |
| <i>Figure 4.30.</i> Coefficient of friction as a function of sliding distance of DLC coatings deposited under different bias voltages (counterpart is 100Cr6 steel)  | 125 |
| <i>Figure 4.31.</i> The wear scar (on the alumina ball) and wear track (on the coating) after tribotests (1 Km sliding, 16 mm rotation radius, sliding speed of 20 cm/s) for DLC coatings deposited at (a) -140 V (b) -100 V (c) - 60 V and (d) -20 V bias   | 128 |
| <i>Figure 4.32.</i> The wear scar (on the steel ball) and wear track (on the coating) after tribotests (1 Km sliding, 16 mm rotation radius, sliding speed of 20 cm/s) for DLC coatings deposited under (a) -140 V (b) -100 V (c) -60 V and (d) -20 V bias   | 130 |
| <i>Figure 4.33.</i> Wear rate of the alumina and 100Cr6 steel counterparts when sliding against DLC coatings deposited under different bias voltage (note: UD means undetectable)  | 131 |
| <i>Figure 4.34.</i> Wear track profile of DLC coatings deposited under different bias voltage after 1 Km sliding against an alumina counterpart in ambient air (22 °C, 75 % humidity) with applied load of 5 N. Coatings deposited under higher bias voltage exhibit better wear resistance (low wear) | 132 |
| <i>Figure 4.35.</i> Wear track on the DLC coatings deposited under -20 V and -60 V bias after 1 Km sliding against a steel counterpart in ambient air (22 °C, 75 % humidity) with applied load of 5 N  | 133 |

|  |     |
|--|-----|
| <i>Figure 4.36.</i> Schematic diagram of bias-graded deposition of DLC coatings: the bias voltage is gradually increased from a minimum to a maximum value as the deposition is progressing and coating thickness is increasing                      | 135 |
| <i>Figure 4.37.</i> Relationship between the coating thickness and the rate of increasing bias voltage in bias-graded deposition   | 136 |
| <i>Figure 4.38.</i> Load and unload curve from nanoindentation of coatings deposited at (a) constant bias of -140 V and (b) bias-grading over the range of -20 to -150 V with a rate of 2 V/min  | 137 |
| <i>Figure 4.39.</i> Optical image of scratch on bias-graded DLC coating after scratch test   | 138 |
| <i>Figure 4.40.</i> Raman spectra of DLC coatings annealed at different temperature for 60 minutes   | 140 |
| <i>Figure 4.41.</i> The relationship between annealing temperature, $I_D/I_G$ ratio and G-peak position  | 141 |
| <i>Figure 4.42.</i> Correlation between hardness and annealing temperature of DLC coating  | 141 |
| <i>Figure 4.43.</i> The change of the coating thickness after 60 minutes annealing in air at different temperatures  | 142 |
| <i>Figure 5.1.</i> XPS spectrum of Al-doped DLC coating  | 147 |
| <i>Figure 5.2.</i> XPS spectra of the Al 2p for Al-“doped” DLC deposited under -150 V bias at different power densities on the Al target (power density of graphite: 10.5 W/cm <sup>2</sup> )  | 148 |
| <i>Figure 5.3.</i> XPS spectra of Al 2p for Al-“doped” DLC before and after etching for 15 minutes   | 149 |
| <i>Figure 5.4.</i> XPS spectrum of C 1s for Al-“doped” DLC after etching for 15 minutes  | 149 |
| <i>Figure 5.5.</i> Relationship between bias voltage and Al concentration in Al-“doped” DLC coatings deposited under different power densities on the Al target. The Al concentration does not considerably change as applied bias voltage is varied | 151 |
| <i>Figure 5.6.</i> XRD spectra of Al-“doped” DLC coating (19 at.% Al) and a [100] Si substrate. No noticeable peak is seen except the one of [100] Si wafer at 69° 2 $\theta$  | 151 |
| <i>Figure 5.7.</i> TEM micrograph with diffraction pattern of Al-“doped” DLC coating (19 at.% Al). The coating is amorphous: a broad halo is seen from the diffraction   |     |

|  |     |
|--|-----|
| pattern  | 152 |
| <i>Figure 5.8.</i> Raman spectra of Al-“doped” DLC coatings with different Al concentrations   | 153 |
| <i>Figure 5.9.</i> The hardness of DLC coating as a function of Al concentration   | 154 |
| <i>Figure 5.10.</i> Residual stress as a function of Al content in Al-“doped” DLC coatings   | 155 |
| <i>Figure 5.11.</i> Optical micrographs of scratches on the coatings after scratch tests of Al-“doped” DLC coatings: (a) 5 at.% Al and (b) 19 at.% Al  | 156 |
| <i>Figure 5.12.</i> XPS spectra of C 1s of Ti-“doped” DLC coatings deposited under -150 V bias with different Ti contents  | 159 |
| <i>Figure 5.13.</i> XPS spectra of Ti 2p in Ti-“doped” DLC coatings deposited under -150 V bias with different Ti contents   | 159 |
| <i>Figure 5.14.</i> The content of a-C, TiC and metallic Ti as a function of Ti addition (calculated from the XPS data presented in Figures 5.12 and 5.13)   | 161 |
| <i>Figure 5.15.</i> XRD spectra of Ti-“doped” DLC coatings deposited under -150 V bias with different Ti concentrations  | 162 |
| <i>Figure 5.16.</i> Grain size of TiC as a function of Ti concentration (calculated from XRD results in figure 5.15)   | 163 |
| <i>Figure 5.17.</i> TEM micrographs of coatings with different Ti contents. At 3at.%Ti, the coating is amorphous. The TiC nanograins are observed from 8 at.%Ti onwards. The size and fraction of crystallites increase with increasing Ti content. At 45 at.%Ti, the coating contains almost TiC grains (bright field (BF TEM) is added for an easier recognition of grains ) | 168 |
| <i>Figure 5.18.</i> Diffraction pattern of nc-TiC/a-C coatings indicating the random orientation of the TiC crystallites   | 169 |
| <i>Figure 5.19.</i> Grain size of TiC determined from TEM and XRD. The grain size increases as Ti content increases  | 169 |
| <i>Figure 5.20.</i> Raman spectra of nc-TiC/a-C nanocomposite coatings for compositions of Ti of 0, 16, 30, 36, and 45 at.%  | 171 |
| <i>Figure 5.21.</i> Coating hardness and Young’s modulus of nc-TiC/a-C as a function of Ti concentration   | 172 |

|  |     |
|--|-----|
| <i>Figure 5.22.</i> Residual stress of nc-TiC/a-C coatings as a function of Ti concentration   | 174 |
| <i>Figure 5.23.</i> Surface roughness ( $R_a$ ) as a function of Ti concentration  | 176 |
| <i>Figure 5.24.</i> Coefficient of friction of nc-TiC/a-C coatings with different Ti contents (the values in the diagram were steady after 1 Km sliding). The coefficient of friction increases as more Ti is added to the a-C                       | 177 |
| <i>Figure 5.25.</i> C 1s, Ti 2p and Al 2p XPS spectra of $C_{56}Ti_{31}Al_{13}$ coating (power density of graphite: $10.5 \text{ W/cm}^2$ , Ti: $2.7 \text{ W/cm}^2$ and Al: $1.8 \text{ W/cm}^2$ ) (15 minutes etching was applied before analysis) | 180 |
| <i>Figure 5.26.</i> XRD spectra of nc-TiC/a-C(Al) coatings   | 181 |
| <i>Figure 5.27.</i> BF TEM (with diffraction pattern) and HR TEM of a nc-TiC/a-C(Al) ( $C_{56}Ti_{31}Al_{13}$ ) nanocomposite coating. In BF TEM, the dark spots are TiC nanograins  | 182 |
| <i>Figure 5.28.</i> AFM images of $C_{62}Ti_{35}Al_3$ and $C_{56}Ti_{31}Al_{13}$ nanocomposite coatings  | 183 |
| <i>Figure 5.29.</i> Load and unload curves from the nanoindentation of a nc-TiC/a-C(Al) coating. The plasticity of the coating was 58 %  | 185 |
| <i>Figure 5.30.</i> Lower critical load obtained from scratch tests of DLC (-140 V bias), DLC (bias-graded), nc-TiC/a-C, and nc-TiC/a-C(Al) coatings   | 187 |
| <i>Figure 5.31.</i> Optical micrographs of scratch tracks on the coating of (a) DLC deposited under constant bias of -140 V, (b) bias-graded DLC, (c) nc-TiC/a-C and (d) nc-TiC/a-C(Al)  | 189 |
| <i>Figure 5.32.</i> Raman spectra of nc-TiC/a-C(Al) nanocomposite annealed at different temperatures for 60 minutes in an Ar environment   | 191 |
| <i>Figure 5.33.</i> Hardness of nc-TiC/a-C(Al) nanocomposite as a function of annealing temperature  | 191 |
| <i>Figure 5.34.</i> XRD spectrum of nc-TiC/a-C(Al) coating before and after 60 minutes annealing in an Ar environment at $600^\circ\text{C}$   | 192 |
| <i>Figure 5.35.</i> XPS spectra (Al 2p) of nc-TiC/a-C(Al) nanocomposite coating at different annealing temperatures in air for 60 minutes  | 193 |
| <i>Figure 5.36.</i> XPS spectra (Ti 2p) of nc-TiC/a-C(Al) nanocomposite coating at different annealing temperatures in air for 60 minutes  | 194 |

|  |     |
|--|-----|
| <i>Figure 5.37.</i> The coating thickness of nc-TiC/a-(Al) nanocomposite coating before and after annealing in air at 600 °C obtained from profilometer  | 195 |
| <i>Figure 5.38.</i> XPS depth profile of nc-TiC/a-C(Al) nanocomposite coating (a) without annealing (b) after annealing at 300 °C for 60 min and (c) after annealing at 600 °C for 60 minutes in air                   | 196 |
| <i>Figure 5.39.</i> Coefficient of friction vs. sliding distance of nc-TiC/a-C(Al) (C <sub>56</sub> Ti <sub>31</sub> Al <sub>13</sub> ) and nc-TiC/a-C (C <sub>64</sub> Ti <sub>36</sub> )                             | 198 |
| <i>Figure 5.40.</i> Wear track profiles on the coatings and wear scars on steel balls after 1Km ball-on-disc tribotests in ambient air (22 °C, 75 % humidity)  | 201 |
| <i>Figure 5.41.</i> Coefficient of friction of nc-TiC/a-C(Al), DLC and nc-TiC/a-C as a function of sliding distance in the oil-lubricated condition  | 204 |
| <i>Figure 5.42.</i> Wear scars on steel counterparts after 1 Km sliding against (a) DLC, (b) nc-TiC/a-C and (c) nc-TiC/a-C(Al) sliding under oil lubricated condition  | 205 |
| <i>Figure 6.1.</i> The engine (a) without propeller (b) installed with propeller for testing   | 210 |
| <i>Figure 6.2.</i> Piston ring and the ring gap area   | 211 |
| <i>Figure 6.3.</i> SEM cross-section images of (a) TiN and (b) nc-TiC/a-C(Al) coatings deposited on piston ring. The thickness was estimated to be 23.2 ±0.3 and 21.3 ±0.3 µm for TiN and nc-TiC/a-C(Al), respectively | 213 |
| <i>Figure 6.4.</i> SEM images of TiN (a) and nc-TiC/a-C(Al) after 30 hours engine test. The thickness remaining was estimated to be 19.9 ±0.8 and 18.4 ±0.5 µm for TiN and nc-TiC/a-C(Al), respectively                | 214 |
| <i>Figure 6.5.</i> Remaining coating after engine test for 610 hours. The TiN wore out (a) and for the nc-TiC/a-C(Al) a 2.1±0.2 µm thickness remained (b)  | 215 |



## TABLE OF ABBREVIATIONS

a-C: hydrogen-free amorphous carbon

a-C:H: hydrogenated amorphous carbon

AFM: atomic force microscope

BDC: bottom dead center

CVD: chemical vapor deposition

DC: direct current

DLC: Diamond-like carbon

E: Young's modulus

H: hardness

HP: horse power

PECVD: plasma enhanced chemical vapor deposition

PVD: physical vapor deposition

R<sub>a</sub>: average surface roughness

RF: radio frequency

RPM: round per minute

SEM: scanning electron microscope

TEM: transmission electron microscope

TDC: top dead center

UHV: ultra high vacuum

XRD: X-ray diffraction

XPS: X-ray photoelectron spectroscopy

# **CHAPTER ONE**

## **INTRODUCTION**

### **1.1. Background and objectives of the project**

Diamond-like carbon (DLC) is well known as a preferred material for wear protective coatings since it exhibits high hardness, high wear resistance and very low friction when sliding against most engineering materials as compared to conventional hard ceramics such as TiN, TiAlN, CrN, etc. However, the following drawbacks limit its applications in engineering fields.

Firstly, high residual stress limits the coating thickness to less than 2  $\mu\text{m}$  since residual stress weakens the adhesion strength of DLC coatings on almost substrates [1]. Such a thickness is not suitable for most engineering applications since it cannot ensure a long working life. Secondly, DLC exhibits brittle behavior at applied high load [2]. Therefore the load-bearing capability of DLC is limited. Thirdly, the thermal stability and oxidation resistance of DLC is very poor. They do not allow this material to work at temperatures higher than 400  $^{\circ}\text{C}$  [3]. Thus, modification of the DLC structure to overcome these drawbacks becomes imperative for effective utilization of DLC in engineering applications.

Piston rings play an important role in the internal combustion engine. They prevent gas leakage from the combustion chamber to the crankcase and the invasion of lubricating oil from the crankcase to the combustion chamber. The correct amount of oil to lubricate the

upper cylinder is also distributed by piston rings. The piston ring set also contributes a large part to the total friction losses of the engine. The friction losses in the piston system are about 22 % to 33 % for gasoline engines and about 20% to 30% for diesel engines [4]. Therefore, the working circumstance of piston rings strongly influences the working quality of the engine such as output, oil and fuel consumption, noise, emission, working life, etc. Working life, reliability and friction of piston rings are critical topics identified by tribologists and engine producers around the world. Surface treatment is one of the most effective solutions. On the one hand, protective coatings should have good wear resistance, low friction during sliding against the cylinder liner and on the other hand the deposition process should be "clean", i.e. it does not cause adverse effects to the environment. With environmental considerations, conventional electroplating is no longer employed. Chromium, Molybdenum, K-ramic, nitrides, and some composites have been developed as materials for protective coating of piston rings. So far, nitride coatings (such as TiN, CrN) show the best wear resistance and friction behavior.

With these considerations, DLC is a potential candidate for protective coatings of piston rings if the drawbacks of residual stress, toughness, thermal stability and oxidation resistance are overcome. The good wear resistance and low friction of DLC bring great benefits such as fuel saving, long working life and reliability of the engine.

*This project concentrates on the design, deposition and characterization of DLC-based coatings with low residual stress, high hardness and toughness, good thermal stability and oxidation resistance, good wear resistance and low friction.*

## **1.2. Scope of the project**

To achieve the objectives of this project, the work to be undertaken includes:

- Investigation of the influence of DLC structure (which strongly depends on the deposition conditions) on coating hardness, residual stress, toughness, thermal stability, and tribological properties. The mechanisms that drive these properties will be studied in detail.
- Deposition and characterization of bias-graded DLC coatings. For pure DLC, bias-graded deposition is the most effective method to reduce the residual stress, enhance the toughness and adhesion strength while maintaining the hardness of the coating at a high level.
- Investigation of the effects of incorporation of Al and Ti on the microstructure, mechanical and tribological properties of DLC and development of DLC-based nanocomposite coatings (nc-TiC/a-C(Al)).
- Characterization and undertaking the mechanical and tribological tests as well as the tests on thermal stability and oxidation resistance to assess the working ability of the nanocomposite coating in different environments.
- Deposition of nc-TiC/a-C(Al) coating on piston rings; undertaking initial engine tests to evaluate the feasibility of application of nanocomposite as protective coating for piston rings. In the engine tests TiN coating is chosen as the control group.

## **1.3. Organization of this thesis**

Chapter 1 introduces the background, the objectives and scope of the project.

Chapter 2 briefly introduces carbon, diamond, graphite and diamond-like carbon as well as the deposition methods for diamond-like carbon coatings. Reviews of mechanical and tribological properties of DLC, properties of nanocrystalline phase, designs and properties of nanocomposite coatings, piston rings and protective coatings for piston rings are also included in this chapter.

Chapter 3 describes the experimental method and equipment used in this project.

Chapter 4 presents investigations on the magnetron sputtered pure DLC coatings. The influences of deposition parameters on the coating structure and deposition rate are analyzed. The mechanical properties, tribological behaviors, thermal stability and oxidation resistance of the coatings are studied in detail. Design and characterization of bias-graded DLC coatings are included in this chapter.

Chapter 5 investigates the effects of doping Al and Ti on the microstructure, mechanical and tribological properties of DLC. Design of DLC-based nanocomposite coatings with high hardness, toughness, low residual stress, good thermal stability and oxidation resistance is also developed. The microstructure of the nanocomposite coatings is studied in detail. The deposition parameters are optimized for the best performance of the coatings.

Chapter 6 considers a case study of the application of nc-TiC/a-C(Al) as protective coating for piston rings. The results from engine tests of nc-TiC/a-C(Al) coating are analyzed in comparison with TiN coating.

The conclusions and recommendations on future work are presented in chapter 7.

## CHAPTER TWO

### LITERATURE REVIEW

#### 2.1. Carbon and diamond-like carbon

##### 2.1.1. Carbon

Carbon is one of the most common elements in the Universe. Many compounds contain carbon as a principal element. This is because carbon has the ability to form various types of covalent bonds. Commonly, carbon forms bonds with hydrogen, oxygen, sulfur and nitrogen. The flexibility in structure is responsible for the wide varieties of complex molecules, which are necessary for living organisms.

Carbon is the sixth element in the Mendeleyev periodic table of elements. It is in the 4A group which consists of 5 elements: Carbon (C), Silicon (Si), Germanium (Ge), Tin (Sn), and Lead (Pb). Carbon is the lightest element of the 4A group. These elements lack four electrons to satisfy their outer atomic shell electronic configuration. The electronic configuration for carbon is  $1s^2 2s^2 2p^2$ . Carbon is a non-metallic element. Depending on its allotropic form and the impurities, carbon can be an insulator, conductor, or semiconductor.

There are three isotopes of carbon in nature. These isotopes have atomic masses of 12, 13, and 14. The isotopes of  $C_{12}$  and  $C_{13}$  are stable and comprise 98.89% and 1.11% of the carbon on earth respectively [5].  $C_{14}$  is radioactive and spontaneously decays into

nitrogen. The half-life of  $C_{14}$  is 5730 years.  $C_{14}$  is used to date materials less than 30,000 years old [6].

In nature carbon is found as diamond, graphite and amorphous carbon.

#### **2.1.1.1. Diamond**

Diamond possesses a large number of excellent qualities, which have placed it in demand over centuries. Diamond has the highest value of atomic number density, hardness, thermal conductivity at 298 °K, and elastic modulus of any known material. Diamond also has a high refractive index and optical dispersion. If nitrogen is absent, diamond is extremely transparent from 230 nm to at least 40  $\mu\text{m}$  in the infrared (apart from a few intrinsic absorption bands from 2.5 to 6.0  $\mu\text{m}$ ). Diamond with a band gap of 5.45 eV is considered among the best electrical insulators. Through doping, diamond can be made into an excellent p-type semiconductor.

The surface of diamond repels water making it feel greasy. This improves the quality of thin biological samples cut by diamond knives. Diamond is simple to clean using acetone. The atomic structure and strong covalent bonding of carbon are responsible for the wide variety of characteristics exhibited by diamond.

The following table summarizes some typically physical parameters of natural diamond (type IIA) [7]:



Table 2.1. Physical parameters of natural diamond

| Properties (Unit)                              | Value               |
|--|---------------------|
| Band gap (eV)                                  | 5.45                |
| Breakdown field (V/cm)                         | $10^7$              |
| Electron mobility ( $\text{cm}^2/\text{V.s}$ ) | 1900                |
| Hole mobility ( $\text{cm}^2/\text{V.s}$ )     | 1600                |
| Dielectric constant                            | 5.5                 |
| Melting point ( $^{\circ}\text{C}$ )           | 3800                |
| Hardness (GPa)                                 | 100                 |
| Mass density ( $\text{g}/\text{cm}^3$ )        | 3.515               |
| Molar density( $\text{g-atom}/\text{cm}^3$ )   | 0.293               |
| Thermal conductivity (W/cmK)                   | 20                  |
| Thermal expansion coefficient                  | $0.8 \cdot 10^{-6}$ |
| Refractive index at 589.19 nm                  | 2.4                 |

Diamond has a cubic crystal lattice. The spatial lattice of diamond is defined as face-center cubic (fcc) [7]. Cubic diamond has a lattice constant of  $3.567 \text{ \AA}$ . The structure of cubic diamond is shown in Figure 2.1.

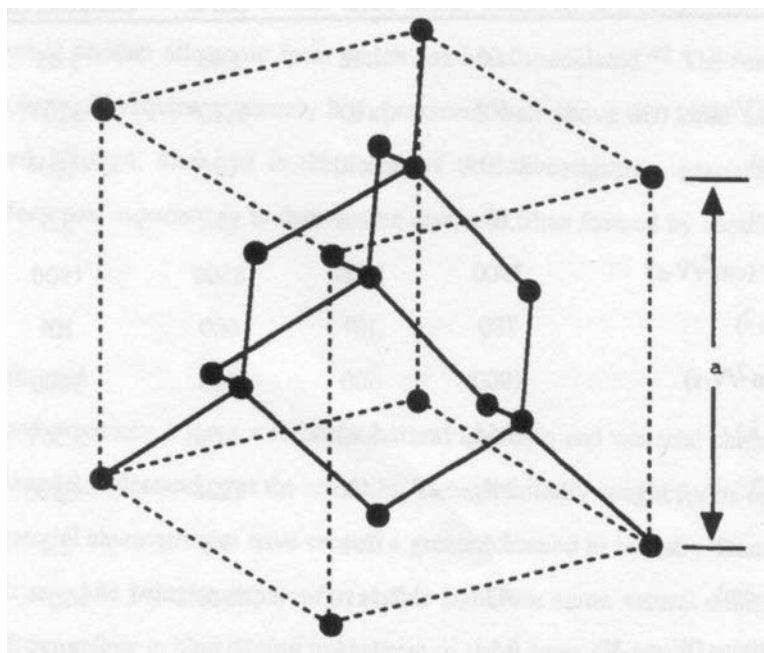


Figure 2.1 Cubic diamond structure [7]

Each carbon atom is surrounded by four other carbon atoms arranged at the corner of a tetrahedron. Bonds between carbon atoms are described as using  $sp^3$  hybrid orbitals in forming a sigma bond between each atom.  $sp^3$  orbitals are necessary to form a tetrahedral system of covalent bonds. To achieve this, the carbon atom must change its electronic configuration to  $1s^2 2s^1 2p^3$ . This transition requires 96 Kcal/mol to excite an electron from the 2s orbital to a 2p orbital. This allows the recombination of one 2s orbital and three 2p orbitals into four  $sp^3$  orbital (c.f., Figure 2.2).  $sp^3$  orbitals are oriented at  $109.5^\circ$  with respect to each other. These form C-C bonds with a separation of 1.53 Å. The stability of the diamond lattice is attributed to the three dimensional array of these strong C-C bonds.

There is another structure of diamond: the hexagonal structure known as longsdaleite. This structure is shown in Figure 2.3. Still other forms or “polytypes” of diamond are thought to exist- particularly in very small particles [8].

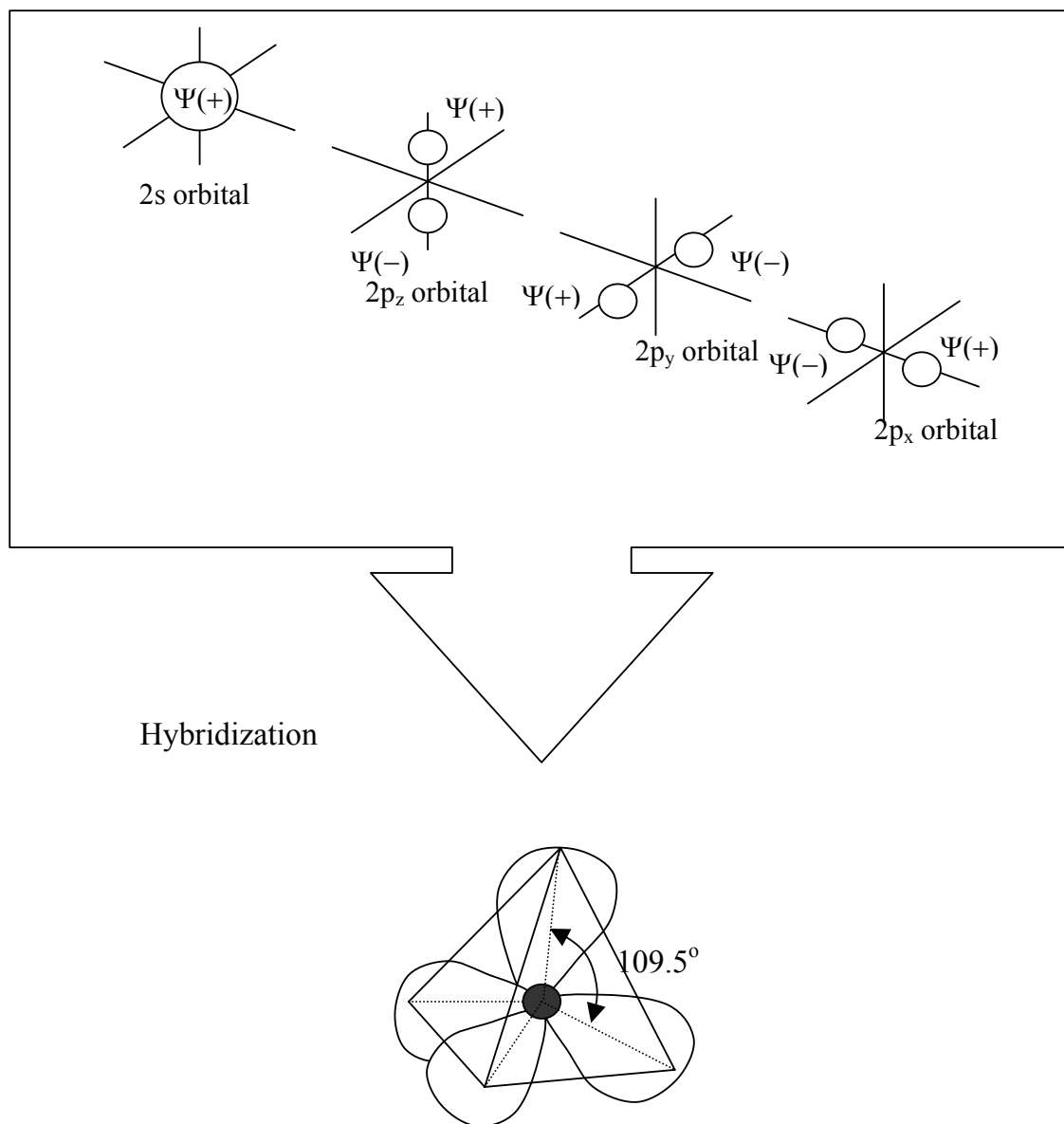


Figure 2.2.  $sp^3$  hybrid orbitals

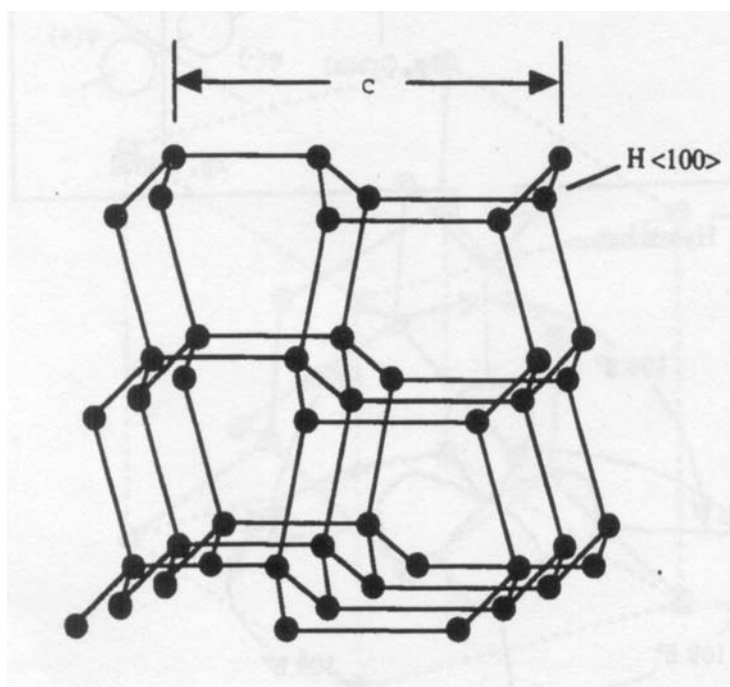


Figure 2.3 Hexagonal diamond structure [7]

#### 2.1.1.2. Graphite

The most abundant allotropic form of carbon is graphite. In the natural state, graphite appears as grey, shiny plates that mass together in easily separated sheets. Graphite is constructed of layers of carbon atoms [9]. In each layer a carbon atom is surrounded by three other carbon atoms in a trigonal planar geometry with a separation distance of 1.42 Å. These C-C bonds are created from the overlap of two  $sp^2$  orbitals. Most carbon atoms in graphite consist of three  $sp^2$  hybrid orbitals in a planar arrangement separated from each other by  $120^\circ$  as seen in Figure 2.4. This creates a layer of hexagonal rings in a planar geometry. The two unused 2p<sub>z</sub> orbitals for each carbon atom combine forming a concentrated electron density above and below the plane of carbon atoms. This sideways overlap of the p orbitals is called a  $\pi$  bond. The layers are then stacked one upon another

with a distance of 3.35 Å. The distance between two successive layers is referred to as the c-axis. This leads to graphite being a conductor along the planes separated by  $\pi$  bonds. There is very little electron interaction between the planes making graphite an insulator in the c-axis. The weak  $\pi$  bonds allow the separate planes of graphite to slide apart with little effort thus making graphite a good solid lubricant.

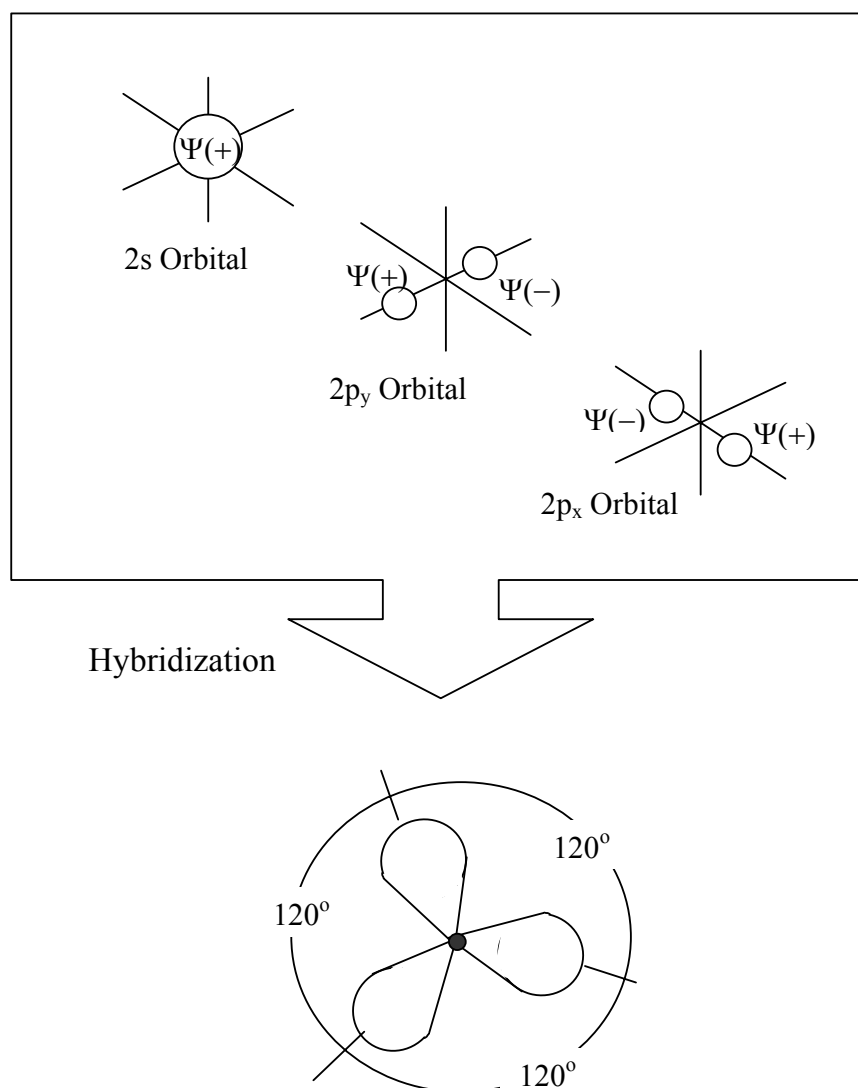


Figure 2.4.  $sp^2$  hybrid orbitals

Figure 2.5 shows the hexagonal lattice structure of graphite, one of the two kinds of lattice structure of graphite ever observed (the other one being rhombohedral). Graphite normally contains both types of lattice structures. The relative amounts of hexagonal versus rhombohedral stacking may be altered through mechanical and chemical means. The effective technique used to identify the existence of diamond ( $sp^3$ ) and graphite ( $sp^2$ ) is the Raman spectroscopy [10, 11]. The Raman peaks of natural diamond and graphite are at wave numbers of  $1332$  and  $1581\text{ cm}^{-1}$ , respectively.

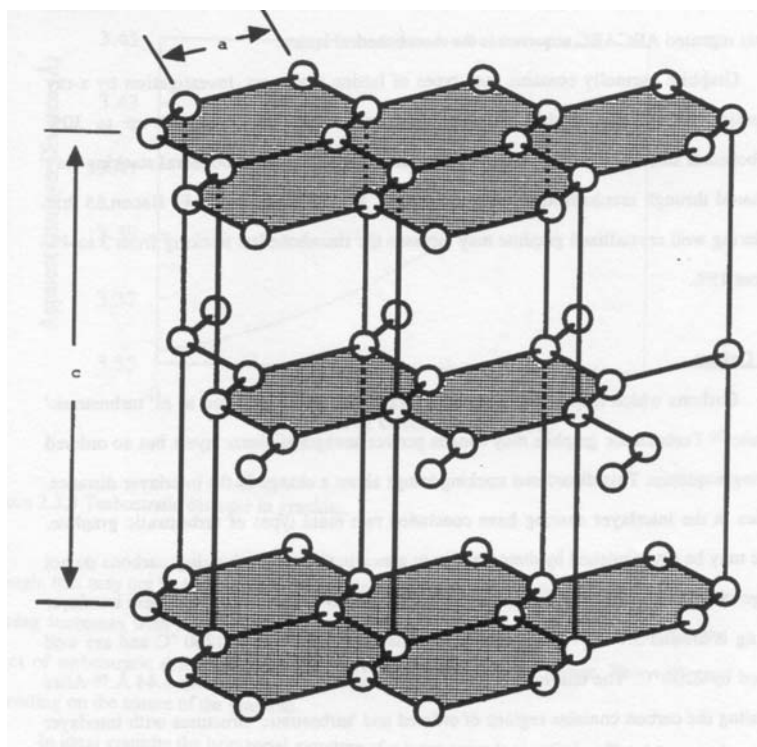


Figure 2.5. Hexagonal graphite structure [7].

### 2.1.2. Diamond-like carbon

The name diamond-like carbon was first coined by Sol Aisenberg in 1971 to describe the hard carbon coatings that he prepared by direct deposition from low energy carbon ion beams [12]. Now, diamond-like carbon (DLC) is the name commonly accepted for hard carbon coatings, which have similar mechanical, optical, electrical and chemical properties to natural diamond but do not have a dominant crystalline lattice structure. They are amorphous and consist of a mixture of  $sp^3$  and  $sp^2$  structures with  $sp^2$  bonded graphite clusters embedded in an amorphous  $sp^3$  bonded carbon matrix. So, the term “diamond-like” emphasizes a set of properties akin to diamond and, at the same time implies the absence of crystalline diamond order. By this definition, all diamond-like carbons are amorphous but not all amorphous carbons are “diamond-like”.

Diamond-like carbons are divided into two broad categories: hydrogenated (a-C:H) and non-hydrogenated (a-C). The latter is sometimes called hydrogen-free diamond-like carbon. In hydrogen-free diamond-like carbon, the hydrogen content is lower than one atomic percent whereas in hydrogenated diamond-like carbon the atomic percent of hydrogen may reach to 65 % [9]. The name “tetrahedral hydrogen free diamond-like carbon (ta-C)” is used for DLC coatings with high content of  $sp^3$  ( $sp^3 > 70\%$ ) [13].

In Raman spectra, DLC coatings are characterized by a broad single peak centered at around  $1530\text{ cm}^{-1}$  (G-band or graphite band) with a shoulder at around  $1350\text{ cm}^{-1}$  (D-band or disorder band). The shoulder is the signature of DLC (otherwise a sharp peak at around  $1580\text{ cm}^{-1}$  would be that of graphite). The G mode of graphite has  $E_{2g}$  symmetry. Its eigenvectors are shown in Figure 2.6 (a) involving the in-plane bond-stretching motion of

pairs of C  $sp^2$  atoms. This mode does not require the present of sixfold rings, and so it occurs at all  $sp^2$  sites, not only those in rings. The D peak is a breathing mode of  $A_{1g}$  symmetry involving phonons near the K zone boundary (Figure 2.6 (b)). This mode is forbidden in perfect graphite and only becomes active in the presence of disorder. The D mode is dispersive; it varies with photon excitation energy. The composition of  $sp^3$  in amorphous DLC is inversely proportional to  $I_D/I_G$  ratio [14]. Where  $I_D$  is the intensity of D band and  $I_G$  is the intensity of G band.

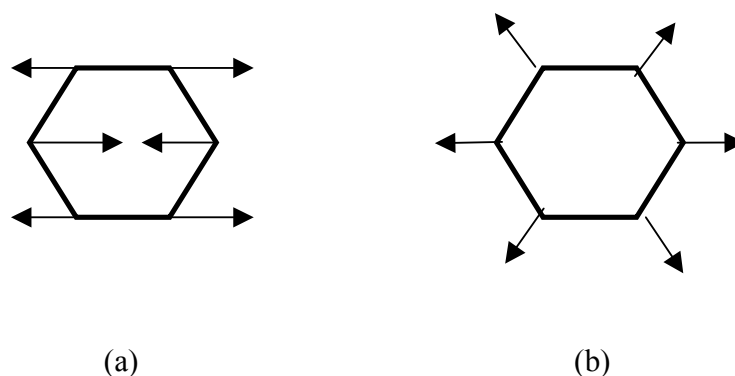


Figure 2.6. Carbon motion in the (a)  $E_{2g}$  G mode and (b)  $A_{1g}$  D mode [15].

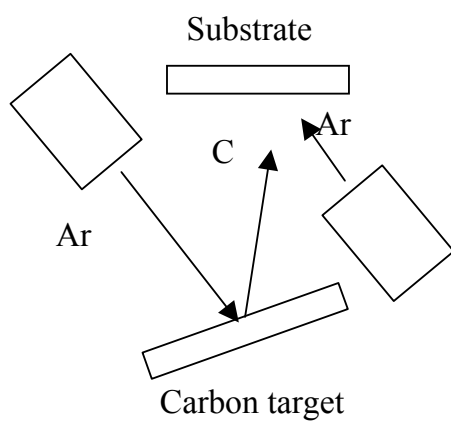
#### 2.1.2.1. Preparation techniques for DLC

The techniques to produce DLC coatings can be divided into two categories depending on their starting materials. In the first category, carbon comes from a solid source. Most of these processes are versions of Physical Vapor Deposition (PVD). The second category uses carbons and hydrocarbon radicals from hydrocarbon gases. These processes are mostly Chemical Vapor Deposition (CVD).



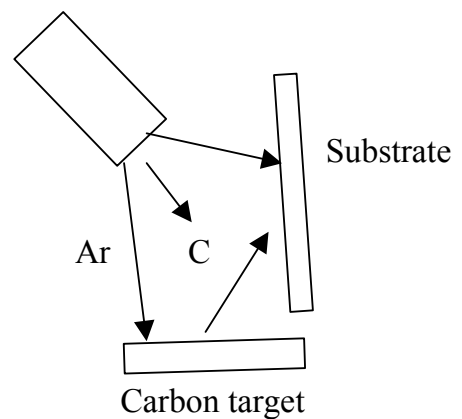
### 2.1.2.1.1. Physical Vapor Deposition

The PVD techniques often use a carbon source in a solid form. With PVD techniques, non-hydrogenated or hydrogenated DLC coatings can be produced, depending on application. This is a big advantage compared to the CVD techniques, which can only produce hydrogenated DLC. Typical PVD deposition techniques are shown in Figure 2.7.



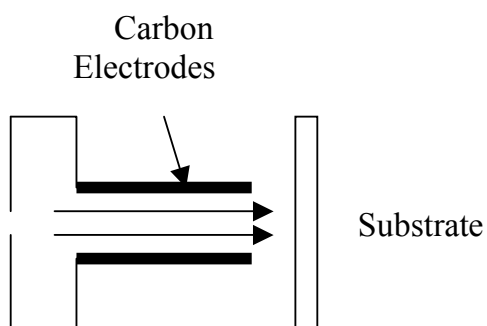
Dual beam sputtering

(a)



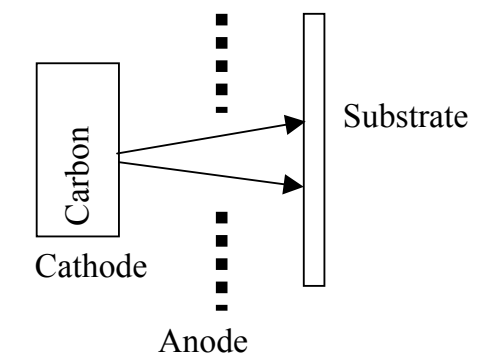
Single beam sputtering

(b)



Arc discharge with electrode erosion

(c)



Carbon ion beam source with cathode erosion

(d)

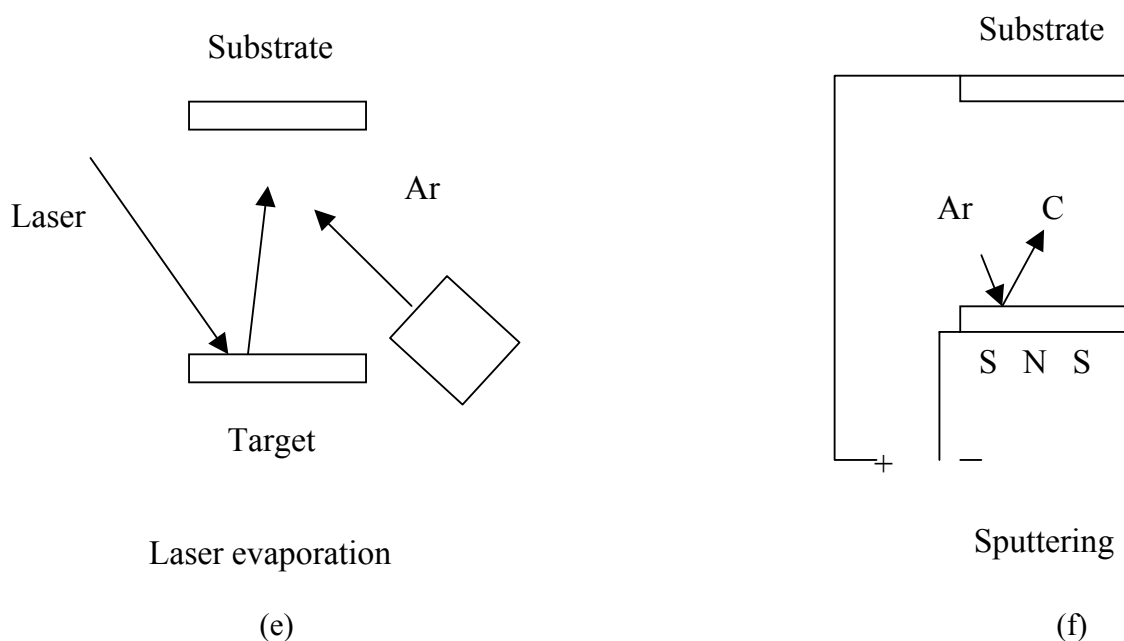


Figure 2.7. Deposition techniques using solid carbon [16].

In Figure 2.7 (a), a primary argon ion beam impinges at about 0.5 to 1 KeV onto pyrolytic graphite target and sputters carbon onto the substrate where a second Ar ion beam impinges at about 0.1 to 0.3 KeV. The second ion beam is used to increase the resistivity and the optical transmittance of the coatings. Figure 2.7 (b) shows the simpler type of ion beam sputtering technique. Only one beam source is used instead of two. This beam source is used both to sputter the target and to bombard the substrate. In Figure 2.7 (c) and 2.7 (d) an argon arc is used to erode the carbon electrodes which are sources of the carbon atoms. These carbon atoms are ionized in the plasma and extracted through a differentially pumped aperture along an axial magnetic field. In Figure 2.7 (e) the laser is a heat source to vaporize the graphite, the auxiliary ion beam is employed to increase the quality of the coatings. Figure 2.7 (f) shows a sputtering discharge using carbon cathode and argon plasma. Argon atoms are ionized and bombard the carbon cathode.

Consequently, carbon atoms are sputtered onto the substrate. In order to increase the effect, magnetron systems have been used. The hybrid sputtering systems are sometimes used. These use both solid carbon and hydrocarbon gas as sources of carbon [17, 18].

#### **2.1.2.1.2. Chemical Vapor Deposition**

Chemical vapor deposition uses hydrocarbon gases as the source of carbon. DLC coatings that are produced by CVD are hydrogenated DLC. Many techniques of CVD have been applied for deposition of DLC coatings, they can be categorized as thermal CVD, plasma enhanced CVD (PECVD) and some other methods such as laser conversion of carbon [16, 19]. Thermal CVD techniques are considered as: thermal decomposition, halogen assisted, hot filament and oxy-acetylene torch. PECVD can be divided into three subgroups: DC-PECVD, RF-PECVD, and Microwave-PECVD. The hybrid of two of the above techniques has been employed such as hot filament + DC discharge, hot filament + microwave, etc [19].

Figure 2.8 shows a typical hot filament system. The filament should have a high melting point (W or Mo) as it is heated up to 2800 °K. The gases used in this system are hydrogen and methane, the latter demonstrates the role of a carbon source. The filament produces radicals and atomic hydrogen, which support the nucleation process of DLC. The substrate is biased negatively. Figure 2.9 shows a Microwave-PECVD system. The substrate temperatures depend on the power density and the location of plasma. Figure 2.10 shows a DC jet PECVD system. The plasma jet is produced from a plasma gun. The gases used are hydrogen, methane, oxygen and argon. A DC voltage is applied to the plasma gun during operation.

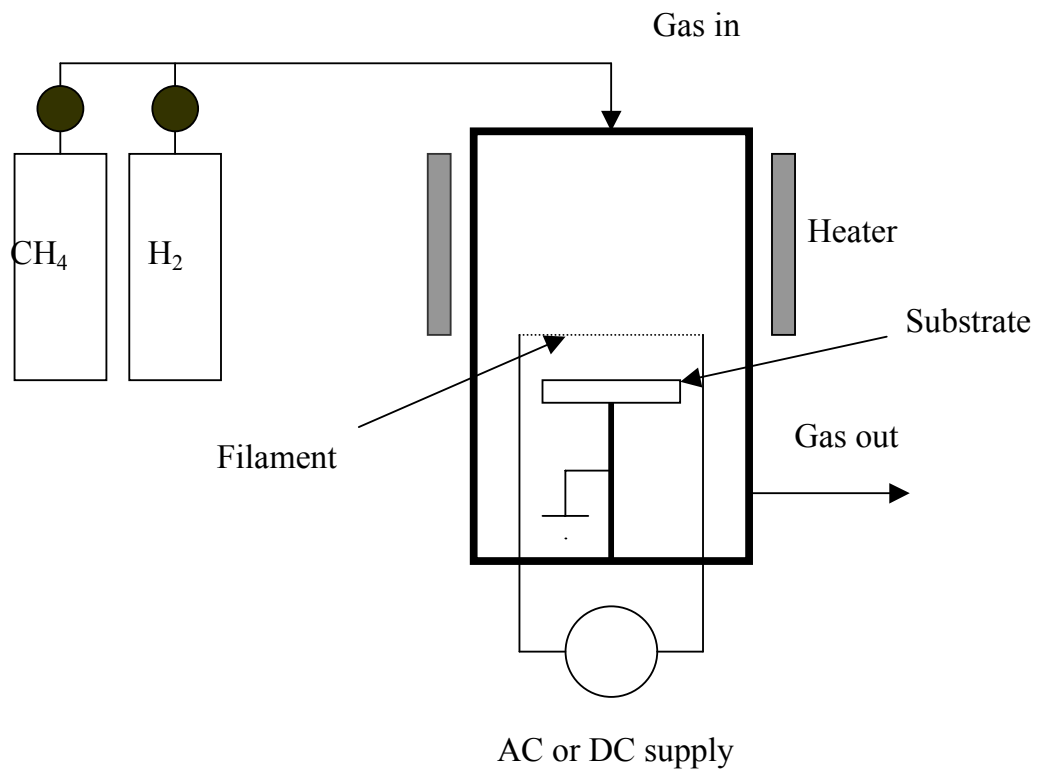


Figure 2.8. Hot filament CVD system

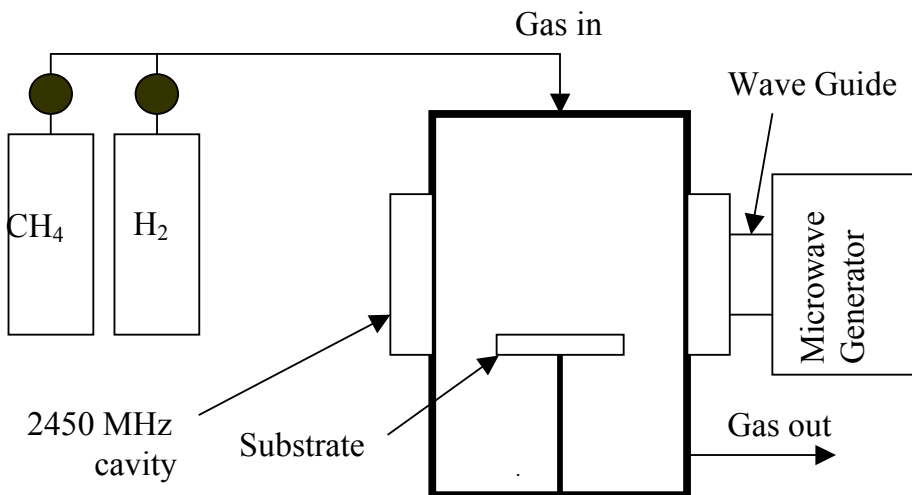


Figure 2.9. Microwave- PECVD system

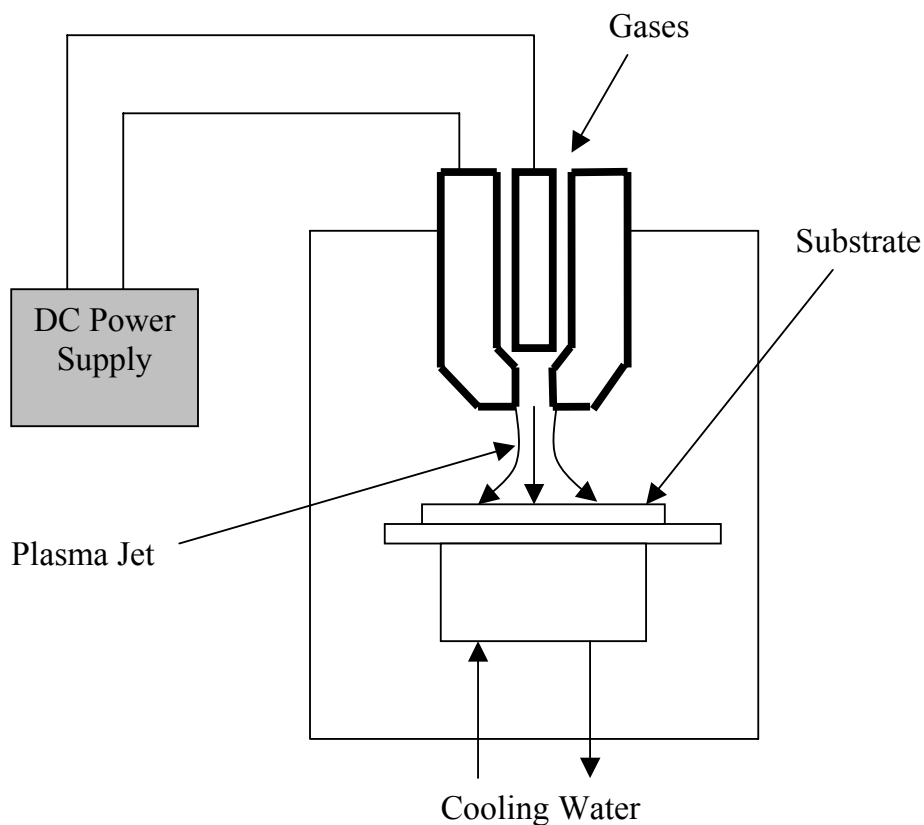
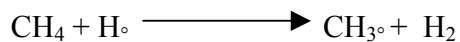
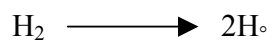


Figure 2.10. DC jet PECVD system

In the CVD process the gaseous reactants, methane and hydrogen for example, are fed into the reactor and reactions are initiated by a hot filament or plasma [20].



...

The small open circle “°” in the chemical notations identifies an unpaired electron.

On the substrate, adsorption, diffusion, reaction and desorption of various species occurs resulting in the nucleation of diamond structure ( $sp^3$ ) and graphite structure ( $sp^2$ ). The coatings contain a certain amount of hydrogen, so the coatings produced by CVD are called hydrogenated DLCs.

Substrate heating plays an important role for the nucleation and growth of the coatings in CVD process [16, 21]. High substrate temperatures limit the application for substrates that are temperature sensitive. Furthermore, annealed substrates may possess some unexpected characteristics.

#### **2.1.2.2. Applications of diamond -like carbon**

Applications of DLC stem from the following set of properties:

- High hardness and elastic modulus, low friction coefficient and low wear rate when contacting with various materials
- Chemical inertness and biocompatibility.
- High electrical resistance and dielectric strength.
- Large band gap.
- High room temperature thermal conductivity.

The applications of DLC can be seen in many fields such as [2, 22, 23]:

- Cutting tools for non-ferrous metals like aluminum and titanium alloys, brass, graphite, wood, plastics, etc. DLC coatings cannot be used with ferrous metals due to the high chemical affinity of carbon to iron.

- Tribology: DLC exhibits excellent tribological properties that will be discussed extensively in the following section.
- Biocompatible coatings for biomedical implants.
- Heat sinks for integrated circuits.
- Semi-conducting devices.
- High quality acoustical parts (microphones, speakers).

## **2.2. Mechanical and tribological properties of diamond-like carbon**

### **2.2.1. Hardness and Young's modulus**

Hardness (H) is the ability of a material to resist permanent indentation. Less commonly, hardness may also be defined as resistance to scratching or to wear. Hardness is measured by indentation and is defined by the pressure over the indented area at a given applied load. Elastic modulus (E) is a measure of the stiffness. It is determined as a ratio of applied stress to the respective elastic strain. For coatings, to prevent the influence of the substrate, the indentation depth is normally set not to exceed 10 % of the coating thickness. Since the thickness of hard coatings is normally about 2-3  $\mu\text{m}$ , the indentation depth, therefore is less than 0.2  $\mu\text{m}$  or 200 nm. At that scale, the indented area cannot be measured directly using optical techniques. The hardness, in this case, is measured by nanoindentation, where the depth of penetration beneath the specimen surface is measured as the load is applied to the indenter. The known geometry of the indenter allows the size of the area of contact to be determined. The procedure also allows for the modulus of the coating to be obtained from a measurement of the stiffness of the contact that is the rate of change of load and depth.

The elastic modulus of diamond and many other materials can be calculated by the following formula [24]:

$$E = \frac{N_c}{4} (1971 - 220\lambda) a_0^{-3.5} \quad [\text{GPa}] \quad (2.1)$$

where:

$N_c$  - coordination number

$a_0$  - bond distance (Å)

$\lambda$  - polarity of the bond

The hardness of diamond can be explained from the formula above due to its fourfold covalent bond and small atomic size (atom radius: 0.071 nm), which result in a strong, short non-polar bond. It should be noted that in most engineering materials, the microstructure plays a vital role in hardness. More details will be discussed in section 2.3.

In DLC coatings, the hardness stems from its strong, directional  $sp^3$  bonds, which form a three-dimensional network. Therefore, hardness strongly depends on the  $sp^3$  fraction in the coating and thus, the method and parameters of the deposition process. Table 2.2 summarizes the hardness and density of hydrogen-free DLC coatings deposited using PVD techniques such as cathodic vacuum arc, magnetron sputtering, pulsed laser deposition, and mass-selected ion beam deposition.



Table 2.2. Some properties of natural diamond and selected DLC coatings

| Material | Preparation Technique  | Density<br>(g/cm <sup>3</sup> ) | % sp <sup>3</sup> | Hardness<br>(GPa) | Reference |
|----------|------------------------|---------------------------------|-------------------|-------------------|-----------|
| Diamond  | Natural                | 3.52                            | 100               | 100               | [25]      |
| a-C      | Vacuum Arc             | 2.8-3.4                         | 85-95             | 40-80             | [26-28]   |
| a-C      | Sputtering             | 1.9-2.6                         | <60               | 20-30             | [29-31]   |
| a-C      | Pulse Laser Deposition | 2.4-3.0                         | 70-90             | 30-60             | [32-35]   |
| a-C      | Ion beam               | 1.8-3.4                         | -                 | 32-75             | [36-39]   |

The existence of hydrogen causes a decrease in the hardness and Young's modulus of DLC because of the addition of C-H bonds in the structure [13]. Raveh et al [40] investigated the influence of hydrogen content on the hardness of a-C:H coatings deposited by various types of CVD and reported that hardness typically decreased from 40 GPa to 18 GPa as the content of hydrogen increased from 20% to 40%. The hardness reached very low values of less than 5 GPa as the hydrogen content exceeds 55 %. Holmberg and Matthew [9] classified hydrogenated DLCs as:

- Hard a-C:H: Hydrogen content in the range of 10 to 40 %.
- Soft a-C:H: Hydrogen content in the range of 40 to 65 %.

### 2.2.2. Tribological behavior of DLC

The tribological behavior of a coating is evaluated by friction, wear, and stability in various conditions. The friction property is evaluated through the coefficient of friction,  $\mu$ , the ratio of the frictional force  $F$  to the normal load  $W$  on the contact:  $\mu = \frac{F}{W}$ . Wear is defined as the removal of material from solid surfaces during relative motion between two surfaces.

Friction and wear are simultaneous results of the same tribological contact process that takes place between two moving surfaces. Wear is often thought of as a harmful phenomenon. This is true in many cases since wear may result in reduced efficiency, increased power losses and an increased rate of component replacement.

Worn volume is inversely proportional to the surface hardness and proportional to the applied load and the moving distance [9]:

$$V = K' \frac{WS}{H} \quad (2.2)$$

where:

V- worn volume

W- applied load

S- moving distance

H- hardness

K'- constant

Wear rate is determined by the ratio of  $K'$  to  $H$ :

$$K = \frac{K'}{H} = \frac{V}{WS} \quad (2.3)$$

DLC coatings exhibit a very low coefficient of friction and provide wear protection when sliding against metallic or ceramic counterparts. The friction and wear resistance of the coatings is strongly dependent on the deposition method, the deposition parameters, counterpart materials, the testing environments and regimes. Typically, the range of coefficient of frictions observed in the literature is from 0.05 to 0.2 [41]. These values are considerably lower than that of other hard coatings such as TiN, TiC, BN for which the values of coefficient of friction are typically higher than 0.4 [42-44].

#### **2.2.2.1. Influence of environment on friction of DLC coatings**

In an inert controlled environment, DLC coatings display a tribological behavior similar to that of bulk diamond. However, in humid air or with water vapor influence, the coatings behave much like bulk graphite. Note that graphite has good tribological properties in the presence of moisture or other vapor. Hydrogen has been investigated to have the same effect on graphite. Atomic hydrogen forms dangling bonds at the edge of the graphite crystallites, leaving only the possibility of weak interactions with the  $\pi$  bonds, thus resulting in reduced friction. The coefficient of friction of hydrogenated DLC is extremely low in inert controlled environments such as dry nitrogen, argon or ultra high vacuum [45] and, generally, increases with humidity. Frank et al. [46] carried out experiments with a steel counterpart sliding on hydrogenated DLC as the humidity was increased gradually. A very low coefficient of friction (often below 0.05) was observed in

dry air but it reached a value of about 0.3 as the humidity reached 100 % (c.f., Figure 2.11).

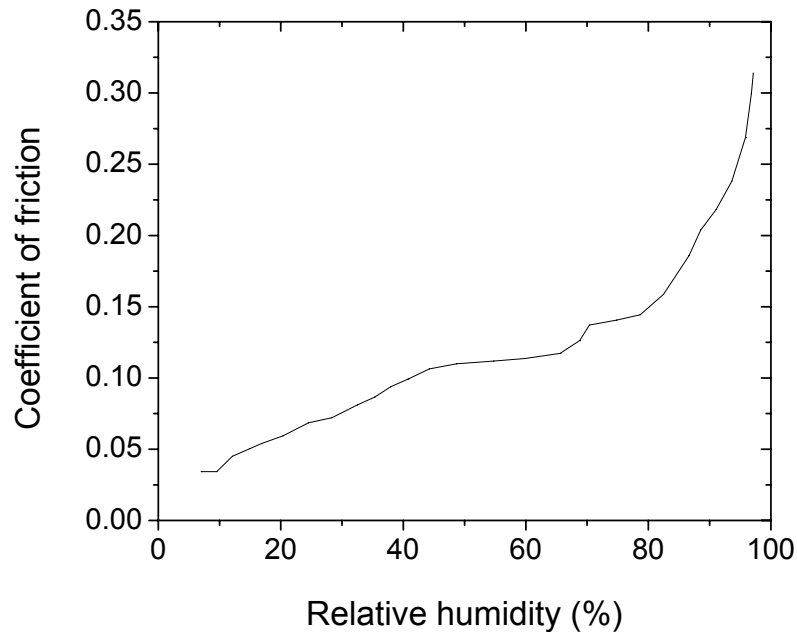


Figure 2.11. Relationship between coefficient of friction of hydrogenated DLC (sliding against steel counterpart) and relative humidity [46]

Miyosi [47] studied the behavior of hydrogenated DLC deposited by PACVD in sliding wear against spherical silicon nitride counterparts, the coefficient of friction was found to be 0.1 in dry nitrogen and 0.18 in laboratory air condition. For coatings deposited at high power density (results in high coating density), after about 1000 passes, the coefficient of friction reached a value of 0.01 in dry nitrogen. The author explained that the decrease of the coefficient of friction was due to the formation of a hydrocarbon rich layer. Memming et al. [48] deposited a-C:H and measured the friction between coating and the steel

counterpart. A very low coefficient of friction was obtained ( $<0.02$ ) in ultrahigh vacuum. The coefficient of friction remained low in dry nitrogen (0.02) but drastically increased (up to 0.6) when nitrogen was substituted by oxygen. In humid nitrogen and humid oxygen, the coefficient of friction was the same. Material transfer was detected. The material transfer changed the chemical composition of the interface layer and influenced the coefficient of friction under various conditions. It was also found that loss of hydrogen after annealing the DLC coatings above 550 °C caused large changes in the coefficient of friction, which reached 0.68 in vacuum or dry nitrogen. This proved that hydrogen in the coatings was responsible for the low coefficient of friction in the inert environments. However, in humid atmospheres, the coefficient of friction did not change. In studies of the influence of reactive gases on tribological behavior of DLC, Paumier et al. [49] deposited a-C:H coatings by hot filament CVD and carried out the tribotests with steel counterparts. The coefficient of friction was studied in vacuum, oxygen, hydrogen and inert gases. In vacuum ( $P=10^{-5}$  Pa) the coefficient of friction was about 0.08. This value was maintained with the introduction of argon or helium. With the introduction of molecular oxygen, the coefficient of friction increased to 0.1, and with atomic oxygen, it reached 0.21. The effect of hydrogen was opposite to that of oxygen. The introduction of molecular hydrogen did not significantly change the coefficient of friction. However, introduction of atomic hydrogen led to a decrease in the coefficient of friction. The adsorption of atomic hydrogen on the coating surface was considered one of the factors that reduced the coefficient of friction. The presence of moisture, as reported by the authors, caused the same effect as oxygen: increasing the coefficient of friction.

Voevodin et al. [32] studied the tribological behaviors of hydrogen-free DLC and hydrogenated DLC deposited by pulsed laser deposition and arrived at opposite conclusions. The results (after 1000 passes) are shown in table 2.3.

Table 2.3. Coefficient of friction of DLC sliding against sapphire and steel counterpart in various environments [32]

| Friction test environment                  | a-C:H      | a-C:H  | a-C        | a-C    |
|--|------------|--------|------------|--------|
|  | non biased | biased | non-biased | biased |
| <i>In sliding against 440C steel ball:</i> |            |        |            |        |
| Air, 50% RH                                | 0.19       | 0.17   | 0.12       | 0.08   |
| Nitrogen, <2 % RH                          | 0.20       | 0.16   | 0.10       | 0.04   |
| Vacuum, 10 Pa                              | 0.26       | 0.13   | 0.11       | 0.10   |
| <i>In sliding against sapphire ball:</i>   |            |        |            |        |
| Air, 50% RH                                | 0.07       | 0.05   | 0.08       | 0.06   |
| Nitrogen, <2 % RH                          | 0.1        | 0.06   | 0.07       | 0.03   |
| Vacuum, 10 Pa                              | 0.12       | 0.09   | 0.08       | 0.06   |

The influence of humidity on the coefficient of friction is described in Figures 2.12 and 2.13.

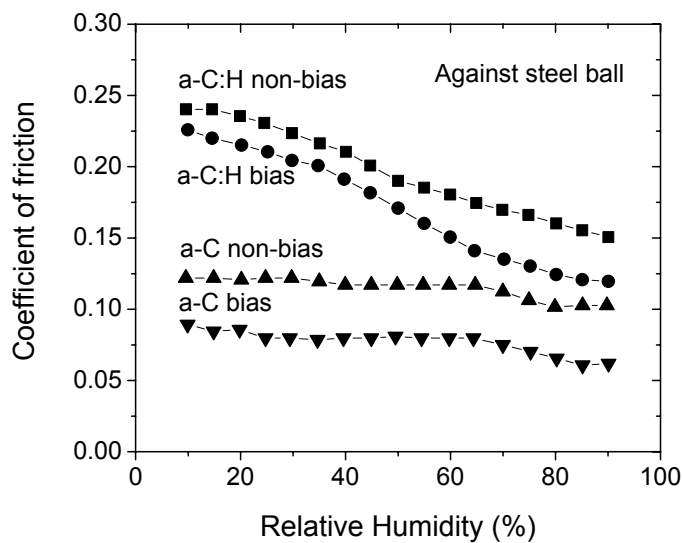


Figure 2.12. Influence of humidity on coefficient of friction (with steel as the counterpart)

[32]

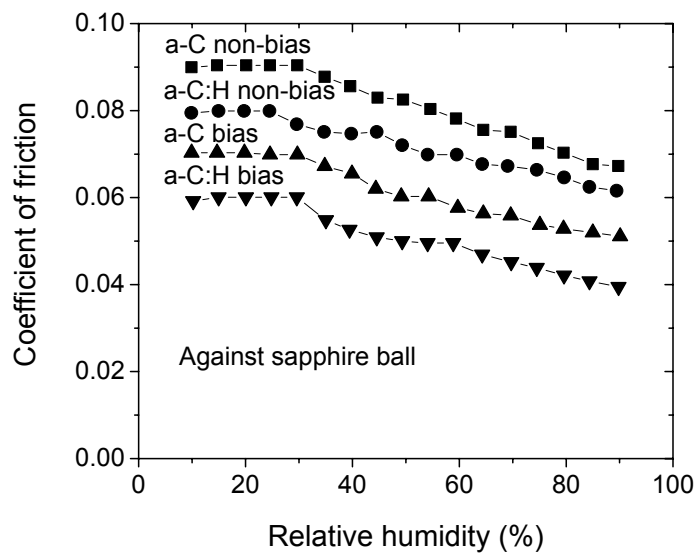


Figure 2.13. Influence of humidity on coefficient of friction (with sapphire as the counterpart) [32]

It is clear that these results were opposite to what had been observed. More detailed research was undertaken in [50] showing that there was a surface tribochemical reaction after a large number of cycles. Raman spectra showed that a  $sp^3$  to  $sp^2$  phase transition occurred. The  $sp^3$  to  $sp^2$  phase transformation was induced by the stresses produced by friction contacts. The graphite layer had lubricious properties in humidity that lead to low coefficient of friction. Miyosi also reported the decrease of coefficient of friction after a large number of sliding cycle [47].

Liu et al. [51] gave an account of the mechanism and conditions of enhanced graphitization. They believed that graphitization was related to the frictional energy and proceeded as a precursor hydrogen atom release. A shear deformation was required to convert the [111] planes of DLC into [0002] planes of graphite. They concluded that: (1) The graphitization rate was mainly a function of velocity and applied load. (2) High temperature at asperities facilitating hydrogen release from the DLC structure (hydrogen began to evolve from DLC at about 300 °C and significant hydrogen release occurred at about 450 °C), which was the first step of the wear-induced graphitization process. (3) A presence of humidity slowed the formation of a graphite tribolayer.

#### **2.2.2.2. Friction and wear of hydrogenated DLC and hydrogen-free DLC coatings**

To investigate the influence of hydrogen content on tribological properties of DLC, Ronkainen et al. [41, 52, 53] deposited a-C and a-C:H coatings by pulsed vacuum arc and coupled RF plasma, respectively. The test environments were dry air, humid air, water lubrication, and oil lubrication. The counterparts were alumina and steel. In the tests with water lubrication, only alumina counterparts were employed in order to avoid the



corrosive effect of the water on steel. For oil-lubricated tests, steel counterparts were chosen because in practice most of oil-lubricated surfaces in tribology are steel. The results indicated that the a-C coating was harder (56 GPa compared to 22 GPa of a-C:H coating [41]), denser and more stable. Therefore it exhibited a better wear resistance as compared to the a-C:H under both non-lubricated and lubricated conditions.

Under non-lubricated conditions [52], the wear rate of a-C was much lower than that of a-C:H. It was about  $0.05 \cdot 10^{-6} \text{ mm}^3/\text{Nm}$  whereas that of a-C:H was about  $0.11 \times 10^{-6} \text{ mm}^3/\text{Nm}$  (with the steel counterpart). However, the wear rate of respective counterparts was higher. The coefficient of friction was stable over a large range of sliding velocities and normal load in humid air. The values were in the range of 0.14 - 0.19 (with steel) and 0.1 - 0.12 (with alumina). In contrast, the coefficient of friction of the a-C:H coating was unstable and dependent on the normal load and sliding velocity. With high sliding velocities and high normal loads, the coefficient of friction decreased considerably, especially with the alumina counterpart (about 0.05). This was explained by the graphitization process, which formed a tribologically beneficial layer of graphite. The restricted formation of graphite due to the strong structure and low shear deformation resulted in higher coefficient of friction observed in a-C coating.

Under water-lubricated conditions, the ball on disc tests were done [41, 53] and the same conclusions were drawn. The a-C coatings showed an excellent wear resistance and very low coefficients of friction. Almost no wear of the coatings could be observed even after 21 hours of testing. The values of coefficients of friction were 0.03 [41] and 0.04 - 0.05 [53]. However, it was different with a-C:H coatings since they could not withstand the

process and were removed after a short duration of testing. The same phenomenon was observed by Drees et al [54]. Those observations on the a-C:H coatings lead to two conclusions for the hydrogenated DLC: low adhesion to the substrate and a rapid increase of wear process in water-lubricated condition. The properties of a-C:H can be improved with doping by some alloying agents.

In oil-lubricated tests (the oil was added with EP additives), almost no wear of the a-C coatings was seen and a small wear rate of about  $0.07 \times 10^{-6} \text{ mm}^3/\text{Nm}$  was detected with a-C:H coatings. With oil lubrication, the coefficient of friction could be decreased by 10 % to 40 % in boundary lubrication regimes. The a-C coating exhibited lowest coefficient of friction, about 0.08.

The tribologically beneficial tribolayer formed under dry sliding conditions, which reduced the counterparts (the balls) wear. The mechanism of tribology is different in the aqueous and oil conditions. The tribologically beneficial tribolayer had no opportunity to form in the aqueous and oil conditions therefore higher wear rates were observed on the counterparts.

Research by Voevodin et al. [32, 50] also showed a better tribological behavior of a-C in comparison with a-C:H coatings. Coefficients of friction of a-C coatings were in the range of 0.03-0.12 and that of a-C:H was in the range of 0.05-0.26 (c.f., table 2.3) depending on the test environment and the counterparts (steel or sapphire). The difference of friction between steel and sapphire balls when sliding against a-C was much less than that against a-C:H, indicating that the tribological behavior of a-C coatings was less sensitive to the

counterpart material. The coefficient of friction between DLC and sapphire was lower compared to that between DLC and steel. This was true for both a-C:H and a-C. The main reason was the applied load for sapphire is higher (0.8 GPa compared to 0.6 GPa) resulting in a higher rate of graphitization. The wear rate of the coatings was measured when sliding against sapphire ball. The results were the same as previous reports. a-C coatings exhibited a very low wear rate ( $10^{-9}$  mm<sup>3</sup>/Nm) compared to that of a-C:H ( $10^{-6}$  mm<sup>3</sup>/Nm). However the wear rate of counterpart was higher when sliding against a-C ( $10^{-10}$  mm<sup>3</sup>/Nm) compared to that against a-C:H ( $10^{-12}$  mm<sup>3</sup>/Nm).

### 2.2.3. Residual stress of DLC coatings

The internal residual stress plays a major role in the adhesion strength and wear resistance of the coatings. The residual stress consists of three parts: the thermal stress, the growth-induced stress, and the post-deposition stress [55]. The thermal stress comes from the difference in thermal expansion between the substrate and the coating. The thermal expansion of DLC is low compared to that of ceramics and very low compared to that of metals, thus the thermal stress exists as a result of deposition temperature. The growth-induced stress (some researchers call it intrinsic stress) comes from changes in the coating density as the coating growth under particle (ion or atom) bombardment. A higher energy of particles results in a higher growth-induced stress if no stress relaxation takes place during deposition (sometime the stress is relaxed in the coating at high energies of ion bombardment due to the change in the structure of the coating as a consequence of increased temperature, e.g. graphitization leading to the formation of more graphite clusters). Post-deposition stress (some researchers call it extrinsic stress) is induced by external factors after deposition of the coatings. A post-deposition stress may result from

interactions between the coating's materials and environment, e.g. adsorption of moisture or other contaminants. This stress is found in chemical reactive or porous coatings but not in DLC or ceramic coatings.

Normally, for DLC coatings deposited by PVD, low substrate temperature ( $<150\text{ }^{\circ}\text{C}$ ) during deposition does not cause high thermal stress. The main contribution to the residual stress is the intrinsic stress, which is introduced and built up in the DLC coatings during deposition at moderate temperature. The ion peening model proposed by d'Heurle [56] is appropriate in describing the phenomena leading to the intrinsic stress in coatings deposited by techniques involving "energetic" particle bombardment of the surface of growing coatings. According to this model, a tensile intrinsic stress is induced during deposition of a coating from "non-energetic" species condensed on the substrate surface, i.e. from species having kinetic energy corresponding to the deposition temperature ( $E=(3/2)kT$ ). Normally it is as low as 0.04 - 0.25 eV. A compressive intrinsic stress is found in coating deposited from the condensation of "energetic" species or grows under "energetic" particle bombardment. The kinetic energy of such species (ionized or neutral) is of order of several tens or hundreds eV. DLC coatings deposited from PVD exhibited compressive stress since they grow under high energetic particle bombardment.

Zhang et al. [57], investigated the influence of deposition parameters on the residual stress of DLC deposited by magnetron sputtering. High sputtering power and/or high substrate bias power lead to high energies of ion bombardments and thus high residual stresses. Damage due to the removal of highly biased a-C coating (deposited by pulsed laser deposition) after a few test cycles were observed by Voevodin et al. [32]. In contrast, non-

biased coating, which was produced by the same method, with the same parameters on the same substrate material (steel) exhibited good adhesion and tribological properties. The damage of the biased a-C coating was attributed to the high residual stress in the coating. The authors also declared that increasing the relative nitrogen flow reduced the compressive stress of the hydrogenated DLC coatings. That effect was due to the reduction of the average coordination number and the over-constraint in the coatings as a result of the replacement of C-H with N-H bonds. Mounier et al. [31, 58] investigated the effects of deposition parameters on the tribological behavior of sputtered a-C and gave some results. Using a conventional magnetron mode and grounded substrate, as the sputtering gas pressure increased from 0.1 to 2 Pa, the mass density decreased from 2.2 to 1.6 g/cm<sup>3</sup> and the compressive residual stress decreased from 0.6 to 0.2 GPa. Also, at a high process pressure of 2 Pa, the stress was almost independent of the bias voltage with low values of 0.2 - 0.3 GPa. That was explained to be due to the collisions of energetic carbon atoms with argon atoms. At low pressure, carbon atoms (and ions) can diffuse through the gas phase with few collisions so they have high energy when reaching the substrate surface. A high energy ensures carbon atoms (and ions) can diffuse into the surface and more to sites corresponding to the minimum surface energy. That results in higher mass density and higher residual stress. At high process pressure, considerably more collisions between carbon atoms and gas ions occur leading to a drop in the energy of carbon atoms (and ions) although high bias voltage is applied. Consequently, coatings exhibit low residual stress. With the unbalanced magnetron mode, much higher residual stress, which is responsible for the surface damage during friction performance, was observed. At process pressure of 0.25 Pa, the residual stress reached 3 GPa at -50 V bias

whereas that of the coating deposited using a conventional magnetron mode was about 1.5 GPa.

According to McKenzie et al. [59], a high residual stress of about 8 - 12 GPa can be seen in DLC and this value reduces with decrease in  $sp^3$  fraction. Sheeja et al. [60] also made the same conclusion after investigation of the residual stress of a-C coatings deposited by filtered cathodic vacuum arc. The coating with high hardness (52 GPa) had a compressive stress up to 10 GPa (corresponding to a substrate bias voltage of 85 V). As bias voltage was increased to 3000 V, the compressive stress decreased to about 1.7 GPa. At higher applied bias voltage, the excessive energy converted the  $sp^3$  to  $sp^2$  bonds (graphitization took place). This observation indicated that the formation of graphite-like structure in DLC strongly relaxes the coating stress even at high carbon atom energies. Ham and Lou [1] measured the compressive residual stress of a-C:H coatings deposited by RF CVD. From their measurements, the stress increased by increasing the coating thickness. The stress in a 0.53  $\mu\text{m}$  coating was 1.2 GPa. They concluded that in practice a coating of more than 2  $\mu\text{m}$  was too stressed to adhere well to most substrates. Also from Ham and Lou, the most suitable substrate for DLC coatings is silicon. Cu, Au, W, Co, or stainless steel containing Cu appear to have bad adhesion with DLC coatings.

Different methods have been utilized to enhance the adhesion of DLC coatings to the substrate. So far, the most commonly used methods are: (1) mechanical pretreatment (such as water peening [61] or plasma cleaning [62]) (2) using interface layers (such as TiC, TiN, TiCN etc. [63]) (3) doping other elements into the DLC matrix (such as Si, metals,

etc. [54, 64-67]) and (4) annealing [68]. The last two methods directly relate to enhancement of adhesion strength by relaxing the residual stress in the DLC coating.

#### 2.2.4. High temperature behavior and oxidation

The diamond-like carbon structure is metastable and it can only exist up to a certain temperature. Tay et al. [3] observed the phase change via Raman spectroscopy with annealed ta-C coatings deposited by filtered cathodic vacuum arc. They reported that the  $I_D/I_G$  ratio increased with increasing annealing time. If the temperature was below 500 °C, it increased gradually during the first two hours, after that, it was stable at a certain value. At temperatures higher than 500 °C, a sharp increase in  $I_D/I_G$  was observed at the third hour of annealing. Evidence of oxidation was observed (loss of coating thickness). An increase of  $I_D/I_G$  ratio reflected the  $sp^3$  to  $sp^2$  bond transformation. The rate of oxidation increased dramatically when the temperature reached 550 °C and a complete loss of coating thickness (200 nm) happened after 30 minutes. The authors concluded that ta-C coatings remained stable up to 300 °C for 4 hours. Graphitization began at 400 °C and at 550 °C intense oxidation happened causing the loss of coating within a short time. However, annealing leads to a decrease in residual stress. The temperature of 150 °C was found to be optimum because at that temperature only a minor increase in  $sp^2$  fraction was observed. However, work done by Ferrari et al. [68] indicated that the graphitization of ta-C only occurred at a temperature of about 600 °C and this also was a suitable temperature for post-deposition annealing for stress relaxation.

The thermal stability of hydrogenated DLC is worse than that of hydrogen free DLC. Tallant et al. [69] deposited a-C:H coatings by RF PECVD, annealed them, and revealed

that a-C:H started to graphitize at about 260 °C and lost hydrogen at an increasing rate above this temperature. Conversion of the  $sp^3$  structure to graphite was complete as the temperature reached 450 °C. Wang et al. [70] revealed that a-C:H started degrading at about 200 °C and that oxidation occurred at about 350 °C. The hardness decreased by 55 % as the annealing temperature reached 400 °C.

At high temperatures, the tribological properties of DLC coatings are considerably changed due to graphitization. Experiments carried out by Liu et al. [71] reinforced that conclusion. DLC coatings were deposited by RF plasma assisted CVD. The ball (alumina) on disc tests showed that an increase of the temperature resulted in a decrease in the coefficient of friction and an increase of wear rate. This was explained from the graphitization, which resulted in more graphite (more solid lubricant) but a decrease in hardness (loss of wear resistance). Above 300 °C, DLC coatings peeled off quickly due to shortened wear life. Below 200 °C the dominant damage mode was plastic deformation, but it changed to fracture and delamination when the temperature reached the critical value of 300 °C.

### 2.2.5. Summary

The mechanical and tribological properties of DLC coatings can be summarized as follows:

- The hardness of DLC coatings varies from a few GPa to about 80 GPa depending on deposition method and parameters. a-C:H has low hardness (< 20 GPa) due to the weak C-H bonds in the structure. Therefore, for wear resistance, it is worse than a-C.



- The coefficient of friction of DLC coatings is low but varies in a large range depending on test environments, counterpart materials, testing parameters, and of course, the types of DLC coatings. Therefore, literature values for coefficients of friction for DLC should be treated with much caution.
- High residual stress is a big drawback, which limits the deposition thickness and the adhesion strength of DLC coatings. The problem seems serious since the intrinsic stress is directly related to  $sp^3$  fraction, which, on the other hand, dictates the hardness and wear resistance.
- The operation temperature of DLC is limited to below 400 °C in atmosphere for a-C. For a-C:H, it is even lower. Graphitization and oxidation are the main reasons causing degradation of DLC coating at high temperatures.

### **2.3. Nanocomposite and DLC-based nanocomposite coatings**

#### **2.3.1. Nanocrystalline materials**

Nanocrystalline materials are solid state systems with the crystal sizes less than 100 nm in at least one dimension. Nanocrystalline materials can be metals, ceramics, and composites containing nanocrystalline and/or amorphous phase.

Nanophase materials possess many special properties that cannot be achieved in conventional materials. These include superplasticity (the capability of materials to undergo extensive tensile deformation without fracture), improved strength and hardness, higher electrical resistivity and lower thermal conductivity [72]. Unlike conventional solid materials, nanophase materials have an appreciable fraction of their atoms residing in defect environments (grain boundary). A nanophase material with a readily achievable

average grain size of 5 nm has about 50% of its atoms within the first two nearest-neighbor planes of a grain boundary [73]. It is well known that in conventional crystalline materials, dislocation motion is responsible for nearly all aspects of the plastic deformation. In the nanophase, the dislocation motion seems to be suppressed. Furthermore, very few dislocations are observed within the grain and they are normally in locked configurations. Grain boundary sliding is an important mechanism of plasticity and deformation since the number of mobile dislocations is not sufficient to cause plastic deformation.

Atomic diffusion at grain boundaries of nanophase materials, which can considerably affect the mechanical properties such as creep and superplasticity of nanophase materials, has been found to be more rapid than that in the conventional materials. The grain boundary energies are also reported higher in nanophase materials [74].

### **2.3.2. DLC-based nanocomposite coatings**

#### **2.3.2.1. “Doped” DLC coatings**

Recently, there have been attempts to improve the tribological behavior of DLC by addition of elements, such as silicon, nitrogen, fluorine, metals, etc.

Silicon-containing DLC coatings have been reported with low surface energy and residual stress in comparison with conventional DLC. Dorfman [65] “doped” DLC with silicon and declared that the structure of Si-“doped” DLC consists of a mixture of DLC and quartz-like (a-Si) atomic scale random network. Although these coatings had lower hardness than that of DLC they combined low stress, relatively high hardness with

elasticity and low friction. Very low coefficients of friction (less than 0.15) of Si-“doped” DLC coatings were also reported by Hioki et al. [75, 76] and Oguri et al. [77, 78].

Like silicon, fluorine incorporation in the DLC structure affects the surface properties. The reduction in stress is in the same range as that of Si-“doped” DLC, but the reduction in surface energy is higher. However, a high content of fluorine (>40%) causes a decrease of wear resistance of the coatings [79].

Wan et al. [80] attempted to produce the  $\beta$ -CN<sub>x</sub> crystalline phase, for which the bulk modulus reaches that of diamond. However, in general, most of carbon nitride coatings are amorphous. In fact, the amorphous CN<sub>x</sub> coating is already very hard and it is a good candidate for rigid magnetic disks [81]. Existence of nitrogen results in a decrease of residual stress but the hardness and tribological behavior require more systematic investigations.

Metal containing DLC is an important class of “doped” DLC coatings. Many metals such as Ti, Al, Ni, Co, Mo, Cr, W, Cu, Ag, Au, Ta, Ru [82-85] have been employed to “dope” into DLC for various reasons. Metals exist in the DLC matrix as crystallites of pure metals or amorphous or metal carbides depending on the nature and concentration of the metals. In general, Ti, Cr, W exist in the matrix of amorphous carbon in the form of carbides or carbon-nitrides if nitrogen is added during deposition whereas others exist in the form of pure elemental metals. The incorporation of metals strongly reduces the compressive stress of the coatings. Monteiro et al. [85] showed that the  $sp^3 \rightarrow sp^2$  transformation was the cause of stress relaxation when metal was added into DLC. With

10 at.% of W added to a-C (70 GPa hardness, 80 % sp<sup>3</sup>), the residual stress reduced from 11 GPa to about 2 GPa and the hardness of the coating was still at high level of 40 GPa (37 % sp<sup>3</sup>). The formation of nanograins of WC helped to maintain the hardness at such a high level even at a low sp<sup>3</sup> fraction of less than 40%. Grischke [86] and Fryda [87] proposed that crystallites of metal carbide were surrounded by a thin (about 1nm) sp<sup>2</sup>-rich carbon phase. They concluded that the metal changed the structure of the matrix and acted as a catalyst for more sp<sup>2</sup> fraction in the coating. Tay et al. [83] indicated that among the metals, Al showed the best effect in reduction of residual stress since more sp<sup>2</sup> was seen in the DLC when Al was added. Furthermore, Al exists as nanoclusters of elemental Al therefore more stress can be relaxed since Al is a soft material. Reactive sputtering is a favorable technique for this type of coating because *“this technique has a great potential for further scale up and also for the realization of in-line deposition processes”* [84]. The tribological behaviors of metal containing DLC have been recognized as a combination of ceramic-like (high hardness) and polymer-like properties (high elasticity and low surface energy). In general, metal-“doped” DLC exhibits a higher coefficient of friction compared to that of pure DLC.

### **2.3.2.2. DLC nanocomposite coatings**

#### **2.3.2.2.1. Concept**

Nanocomposite is one of the two kinds of hard and superhard coatings: super lattice coatings and nanocomposite coatings. The hardness of superlattice coatings is strongly dependent on the superlattice period ( $\lambda$ ). This is a big drawback for this type of hard coating because the same thickness of superlattice layers on the whole surface of substrate cannot be assured [88].

In nanocomposite coatings all of the unique properties of nanophase materials are utilized to enhance the strength. Recently, many hard nanocomposite coatings have been developed with nanocrystallites such as nc-MeN, nc-MeC, nc-MeB, nc-MeO embedded in an amorphous or crystalline matrix [88-94]. The matrix can be DLC, amorphous or crystalline nitrides (e.g. a-Si<sub>3</sub>N<sub>4</sub>, nc-BN, etc.), and metals (Cu, Ni, Y, etc.).

The hardness, thus the wear resistance is mainly dependent on the microstructure of the materials. Hardness increases by the suppression of plastic deformation caused by dislocation movement, grain boundary diffusion, and grain boundary sliding. Veprek et al. [89-92] first developed a concept for superhard nanocomposite coatings based on the so-called “reverse Hall-Petch effect”. The Hall-Petch relationship, which expresses the grain size dependence of the flow stress at any plastic strain out to ductile fracture, is given by the following formula [95]:

$$\sigma_0 = \sigma_i + \frac{k'}{\sqrt{D}} \quad (2.4)$$

where:

$\sigma_0$  – yield stress

$\sigma_i$  – friction stress opposing motion of dislocation

$k'$  - “Unpinning constant” measuring the extent to which dislocations are piled up at barriers

and  $D$  - grain diameter

With the absence of dislocation activities, the Griffith's equation for crack opening is the description of composite strength [95]:

$$\sigma_c = \sqrt{\frac{4E\gamma_s}{\pi a}} \quad (2.5)$$

where:

E - elastic modulus (Young's Modulus).

$\gamma_s$  - surface energy of the grain/matrix interface.

a - initial crack size. The maximum crack size is proportional to the grain size.

From equations 2.4 and 2.5, it is clear that the strength and hardness of coatings increases with decrease in grain size.

Veprek et al. suggested the reverse Hall-Petch effect, which causes the decrease of coatings hardness when the grain size decreases below 10-20 nm called "nanosoftening". This should be the consequence of the nanophase effect as mentioned previously: grain boundary sliding. That effect can operate without the existence of thermal effects in the nanocrystalline system. If grain boundary sliding is suppressed, the reverse Hall-Petch will be avoided. The "trick" is to combine a hard nanocrystalline with an amorphous matrix to form a strong interface. The principles are given as follows [89-91]: (1) Decrease the grain size of the nanocrystalline components to the stability limit of the crystalline phase. With that consideration, the activity of dislocations is locked. (2) The

amorphous matrix should be thin in order to reduce crack formation and propagation. (3) In order to ensure the formation of small nanocrystals close to the lower limit of their stability (2-3) nm and to avoid interdiffusion to get sharp interfaces, the preparation temperature should not be too high. Based on those principles, Veprék suggested a model of nanocomposite (nanograins/amorphous) coatings with the size of nanograins of 3 nm to 10 nm and separated by 1 nm to 3 nm within an amorphous  $\text{Si}_3\text{N}_4$  matrix. The superhard nanocomposite coatings with a hardness above 40 GPa ( $\text{TiN/a-Si}_3\text{N}_4$ ,  $\text{W}_2\text{N/a-Si}_3\text{N}_4$ ,  $\text{VN/a-Si}_3\text{N}_4$ ,  $\text{TiN/BN}$ ) have been successfully deposited by plasma CVD deposition. The substrate temperatures during deposition were 500 °C to 600 °C.

*“Diamond is not the hardest material anymore”* is the conclusion of Niederhofer et al. when they declared that nanocomposite  $\text{TiN/TiSi}_x$  deposited by CVD based on the above principles had a hardness of more than 100 GPa [96]. In order to increase the thermal stability of superhard nanocomposite with the matrix of amorphous  $\text{Si}_3\text{N}_4$ , Holubar et al. [97] developed a  $(\text{Ti}_{1-x}\text{Al}_x)\text{N/a-Si}_3\text{N}_4$  nanocomposite by vacuum arc cathodic evaporation. The hardness of this coating reached 40 GPa and thermal stability was maintained up to 800 °C. Coatings with a high content of Ti had higher hardness whereas the ones with a high content of aluminum exhibited higher thermal stability. So far, the applications of that kind of coatings are limited. It is clear that with this concept, the plasticity of the coatings is suppressed. They lack toughness and are very brittle. Therefore, at highly applied loads, these coatings will be the victims of brittle fracture.

DLC nanocomposites are a new class of material. They have been researched since 1980s. Dorfman [65] first grew this material by plasma polymerization of silicon organic

precursors of carbon and silicon. The hardness of these coatings was 10 - 22 GPa and their structure consisted of atomic scale composites of two interpenetrating diamond-like (a-C:H) and quartz-like (a-Si:O) random networks. The diamond-like network is stabilized by the hydrogen and the quartz-like network is stabilized by oxygen resulting in a purely amorphous structure. Such self-stabilized C-Si amorphous structures form an ideal matrix for the introduction of metal (W, Ti, etc.). These metals (with a low percentage of about 3 at.%) are distributed as separated atoms or separated networks, and all these networks (the carbon matrix, a-Si and MeO) are bonded to one another by weak chemical forces.

nc-TiC and nc-WC nanocrystallites are most widely used to embed into DLC to form a DLC nanocomposite. Meng et al. [98, 99] deposited DLC nanocomposites with TiC nanograins embedded in the a-C:H matrix by magnetron sputtering of a Ti target in a plasma of Ar/C<sub>2</sub>H<sub>2</sub>. The H content in the DLC matrix was about 40 at.%. This DLC nanocomposite showed a maximum hardness of 19 GPa as 43 at.% Ti was added. A hardness of about 16-17 GPa was reported by Wanstrand et al. [100] for a DLC nanocomposite with nc-WC embedded in the a-C:H matrix. Recently, Voevodin and co-workers [93, 94] pointed out that a-C:H had low hardness and was not suitable for producing hard DLC nanocomposite coatings. They also demonstrated the importance of grain boundary sliding in strain relaxation in a nanocomposite system under highly applied stresses. The equiaxial grain shapes, high angle grain boundaries, low surface energy and the presence of an amorphous boundary phase facilitate grain boundary sliding. It was believed that randomly oriented nanograins with sizes of 10 - 20 nm embedded in a DLC matrix with the matrix separation from 2-10 nm gave the best effect in enhancement of coating toughness. Meanwhile the hardness is maintained at relatively



high level. The nc-TiC/DLC and nc-WC/DLC coatings were deposited based on the above design by magnetron assisted pulse laser deposition technique. The hardness of nc-TiC/DLC and nc-WC/DLC was about 27 GPa and 32 GPa, respectively. In tribotests, graphitization was observed. The transfer film analysis indicated the conversion of DLC into graphite, similar to  $sp^3 \rightarrow sp^2$  interatomic bonding relaxation in single phase DLC [101]. As a consequence of graphitization, which results in a lubrication graphite-rich layer, low coefficients of friction of about 0.15 - 0.25 (sliding against a steel counterpart) were seen with DLC nanocomposites. The toughness of those coatings was considered high. They were hard and non-plastic at contact loads below the elastic limit but changed their behavior to the “plastic mode” if the load exceeded the limit. Then the brittle fracture can be avoided. Voevodin called these coatings “supertough chameleon coatings”.

It can be seen that both types of nanocomposite coatings designed by Veprek [89-91] and Voevodin [93, 94] are composed of nanograins embedded in an amorphous matrix. However they exhibit completely different physical properties due to different structures of the supertough and superhard nanocomposite coatings. In practice, coating with adequate hardness combined with high toughness finds more applications than superhard but brittle one.

#### **2.3.2.2.2. Magnetron sputtering of nanocomposite coatings**

As early as 1877, sputtering deposition was used to deposit thin films to coat mirrors [102]. The simplest configuration for sputtering deposition is DC plasma excitation with two configurations: diode and triode. The latter has an addition of an electron source (thermionically heated filament). In order to produce a dense plasma near the surface of

the cathode, a magnetic field, which is configured to be parallel to the cathode surface, is employed to trap electrons close to the cathode surface (c.f., Figure 2.14). This configuration is called magnetically enhanced plasma sputtering or magnetron sputtering. A magnetron can be designed as an “unbalanced” type when the strength of the inner magnet and outer one is not equal. Window and Savvides first developed this concept in 1980s [103]. If the outer magnet is stronger than the inner (center) magnet, some electrons in the plasma are no longer confined to the target region, but are able to follow the magnetic field lines and flow out towards the substrate. As a result, ion bombardment at the substrate was increased. Magnetron sputtering can operate with DC or RF excitation depending on the material to be deposited. If the depositing material is not electrically conductive, RF excitation should be employed to prevent electrode charge. Generally, RF magnetrons are less efficient than DC magnetrons by a factor of 2 [102].

Magnetron sputtering is a powerful process, which is widely used in industry for the production of coatings. Comparing to other PVD techniques, sputtering shows great advantages such as: (1) It is very simple and reliable; (2) the deposition rate of coatings is sufficient to meet economic and functional requirements in industrial production; (3) this technique has a great potential for further scaling up and also for the realization of in-line deposition processes; (4) the sputtering deposition process operates under different physical conditions compared to the evaporation, which makes it possible to form coatings with functional properties; (5) the alloy or composite coatings, which are extremely complicated to deposit by evaporation, are more simply deposited by magnetron sputtering; (6) this technique is considered “clean” compared to electroplating, which causes serious problems to the environment.

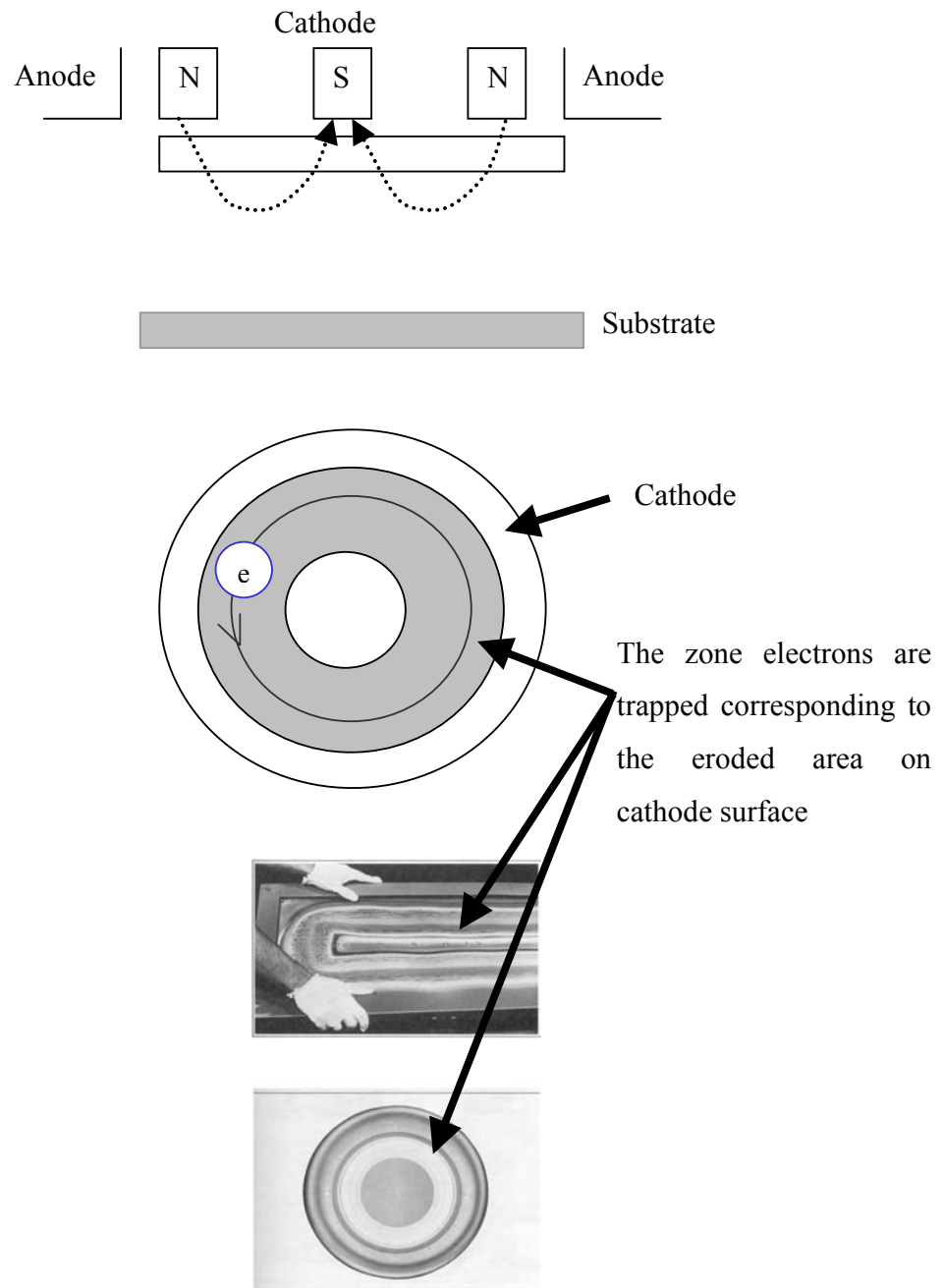


Figure 2.14. Magnetron configuration and effect of magnetic field

Musil et al. [88, 104] suggested that magnetron sputtering is a very promising technique for depositing nanocomposite coatings in industry. He and co-workers successfully

deposited ZnCu-N, NiCr-N, TiNiN, etc. nanocomposites by magnetron sputtering with the gas fed was a mixture of Ar and N<sub>2</sub>. Musil et al. also gave a very interesting conclusion that high-temperature phases in alloy coatings can be produced at low temperatures using magnetron sputtering. They explained that it is the consequence of rapid cooling (the cooling rate is about 10<sup>14</sup> K/s), which accompanies the highly non-equilibrium sputter deposition process occurring at an atomic level.

Magnetron sputtering has been widely used to deposit DLC nanocomposites. Mostly, metallic targets were sputtered in a plasma of Ar/Hydrocarbon gas [98-100].

### 2.3.3. Summary

The review of nanocomposite and DLC-based nanocomposite coatings can be summarized in the following few key points:

- The nanocomposite is a new generation of materials for engineering applications. Depending on the design, high toughness or high hardness can be obtained. However, it should be noted that superhard coatings are brittle therefore their application is limited.
- “Doping” with other elements is a good way to modify the structure of DLC for desirable properties.
- In DLC nanocomposites, the a-C matrix has a big advantage compared to a-C:H since a-C exhibits higher hardness, lower friction and better thermal stability.
- When Ti or W is added to DLC, the crystalline phase of carbide will form. This strong phase greatly contributes to the hardness of composite coatings.
- The graphitization of the DLC matrix during tribotests was seen in DLC nanocomposites. This helps to maintain the low friction in non-lubricated conditions. The

tribological behavior of DLC nanocomposites in lubricated conditions has not been well investigated, yet.

- Magnetron sputtering is a suitable technique for producing DLC nanocomposite coatings. Co-sputtering of graphite and metallic targets can be applied to deposit hydrogen-free DLC nanocomposite coatings. Since the deposition of DLC nanocomposites via magnetron sputtering can be carried out at low temperature, the thermal stress can be avoided and various materials can be employed as substrates.

## **2.4. Piston rings and protective coatings for piston rings**

### **2.4.1. Piston rings**

Piston rings are one of the most important details of internal combustion engines. They are divided into two categories: compression rings and oil control rings.

- The compression rings play a role as a seal preventing gas leakage from the combustion chamber to the crankcase.
- The oil control rings are employed to prevent the invasion of lubricating oil from crankcase to the combustion chamber and distribute the correct amount of oil to lubricate the upper cylinder.

Compression rings and oil control rings transfer most of the heat from the piston to the cylinder. Compression rings are fixed at the upper grooves of the piston and oil control rings, at the lower grooves. Current ring pack designs generally use three piston rings: two compression rings and an oil control ring (c.f., Figure 2.15). Piston ring materials include cast iron, ductile (nodular) iron, and stainless steel [105].

The seal effect of compression rings comes from two parts: the radial ring tension and the gas pressure. The latter mainly contributes to the seal effect. The side and back clearances allow the pressure in the piston groove to follow the cylinder pressure, so as the cylinder pressure increases. The increasing groove pressure presses the compression ring firmly against the cylinder wall. Figure 2.16 shows the distribution of gas pressure on the working surface of piston rings [106].

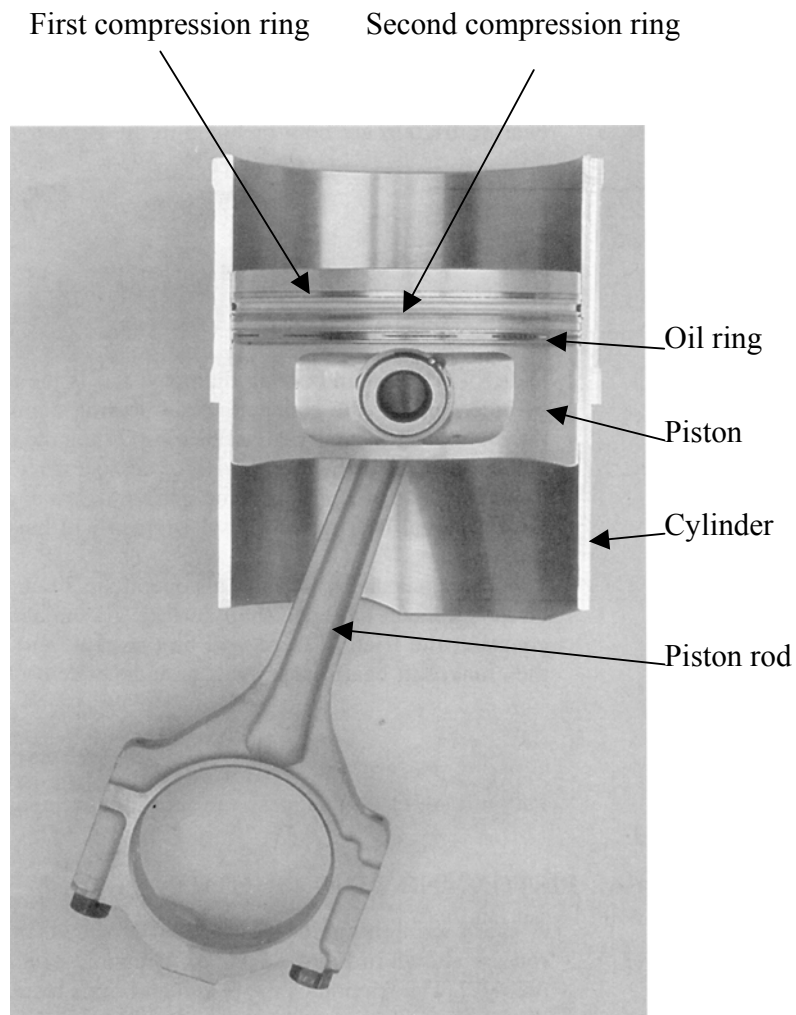


Figure 2.15. Piston rings and related details [105]

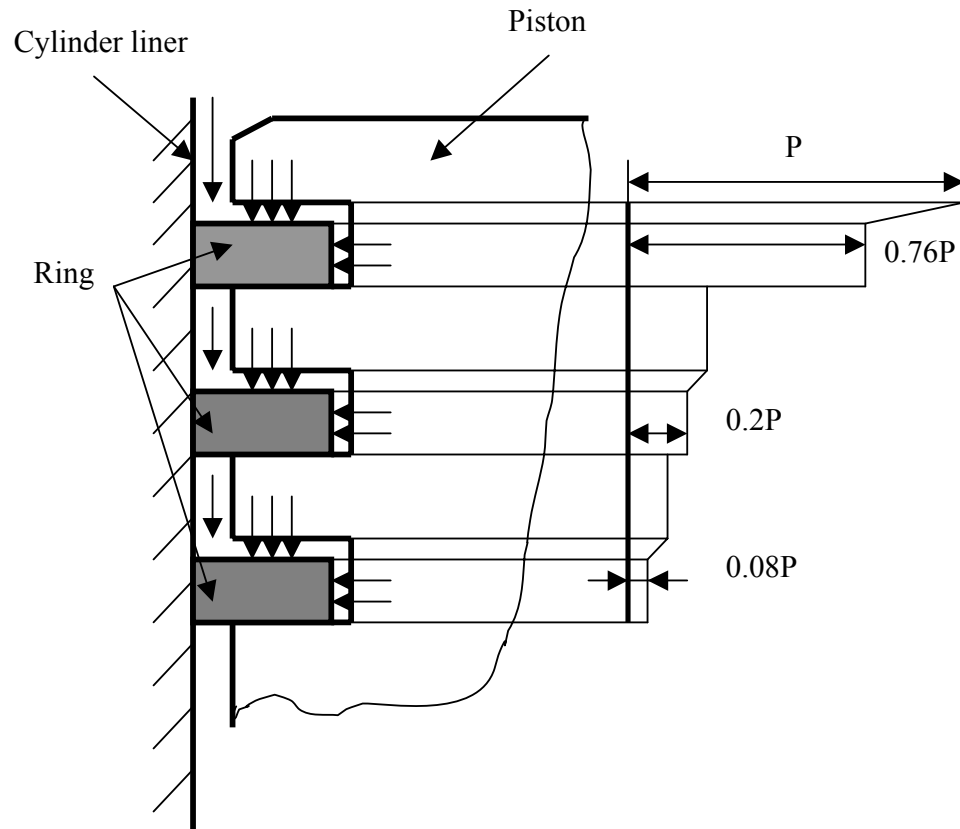


Figure 2.16. Distribution of gas pressure on the working surface of piston rings [106]

Piston rings, especially the first compression ring work in extreme conditions with corrosive environments (products of combustion) and periodically mechanical and thermal loads. The working temperature of the first compression ring may reach 200 - 300 °C [105]. The working temperature of other rings is much lower than that of the first ring.

## 2.4.2. Friction and wear of piston rings

### 2.4.2.1. Lubrication of piston rings

There are three modes of lubrication for a tribo-system known as: boundary, mixed and hydrodynamic. In the hydrodynamic lubrication, the oil film has sufficient pressure to

separate the friction surfaces. In the mixed lubrication, the thickness of the lubricant film is insufficient to avoid inter-asperity contact. The applied load is supported by a combination of hydrodynamic effects and the asperities in contacts. In the boundary lubrication, there is almost no free lubricant film separating the two surfaces. The oil film thickness is just a few molecular diameters. However, just with the presence of the lubricant, which is chemically bonded into the friction surfaces, the coefficient of friction is much lower in comparison with dry contacts.

These three friction regimes can be shown on a Stribeck diagram. The Stribeck diagram plots the coefficient of friction as a function of a dimensionless Stribeck variable (known as the Sommerfeld number):

$$S = \frac{\mu U}{W} \quad (2.6)$$

where:

$\mu$  - the lubricant dynamic viscosity

$U$  - the relative speed between the two surfaces.

$W$  - the normal load

In the Stribeck diagram, three areas corresponding to the three friction regimes are observed as seen from Figure 2.17 [107].

- Area (I) corresponds to the boundary friction regime. The coefficient of friction is almost constant.



- Area (II) corresponds to the mixed friction regime. The coefficient of friction is inversely proportional to the Sommerfeld number.
- Area (III) corresponds to the hydrodynamic friction regime. The coefficient of friction is proportional to the Sommerfeld number.

The probable lubrication regimes of some typical friction couples in internal combustion engines are also added in the diagram [108].

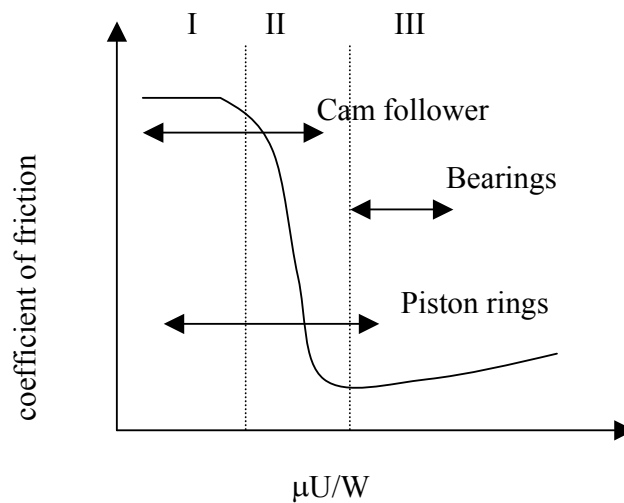


Figure 2.17. Stribeck diagram and probable lubrication regimes of typical friction couples in internal combustion engine

As seen from the figure, the friction modes of piston rings and the cylinder can be hydrodynamic, mixed, or boundary modes depending on the position of the ring in the operating stroke. It is easy to see that, during operation, the existence of a hydrodynamic lubricant film is due to pressure generated in the oil. This can be attributed to the wedge, squeeze, and stretch effect. At the top dead center (TDC) and bottom dead center (BDC)

vicinities, with the decrease of piston speed and the change in direction of piston travel, the oil film thickness is dramatically decreased because the oil pressure is not sufficient to maintain the oil film thickness. More over, at the TDC vicinities, in the expansion stroke, the gas pressure and the temperature are very high resulting in the “disappearance” of the oil film. Consequently, “surface to surface” contacts occur (boundary lubrication regime) [108-111].

#### **2.4.2.2. Friction of piston rings**

##### **2.4.2.2.1. Friction losses**

In contrast to the exhaust and the cooling losses, which are proportional to the fuel consumption rate, the friction losses are practically constant [112]. It is clear that at light load regimes (which are mostly met in automotive and motorbike engines) a great part of the total fuel energy will be lost due to friction. Furuhami [113] estimated that a reduction of friction losses by 10 % results in 4 % fuel saving at 50 % load.

The friction losses at the piston system are about 22 % to 33 % for gasoline engine and about 20 % to 30 % for diesel engines [4]. Measurement of friction in a piston system by Furuhami [114] showed that the ring package contributes as much as 60 % to 70 % to losses. Therefore, reduction of friction of piston ring package brings great benefit in reduction of fuel consumption.

##### **2.4.2.2.2. Reduction of friction losses of piston rings – cylinder system**

Figure 2.18 introduces a diagram representing the system approach to tribology [115]. It can be seen that friction of piston rings is influenced by many factors. It is possible to

obtain improvements in friction by changing one of those. However, with piston rings, researchers pointed out the three most effective solutions [116]:

- Tension reduction: if the ring tension is reduced, the engine friction decreases. The tension of compression rings cannot be reduced since it affects on the seal function of these rings. Most suitable rings that need to reduce the tension are oil rings. However, this always causes an increase in oil consumption.
- Two-ring package: this solution may cause the higher rate of gas blow-by.
- Surface treatment of the sliding surface: this is the most effective solution since there is no associated negative effect. As mentioned, at the TDC and BDC, especially just after TDC in the expansion stroke, metal-metal contact occurs, therefore with appropriate surface treatments, the friction losses considerably decrease.

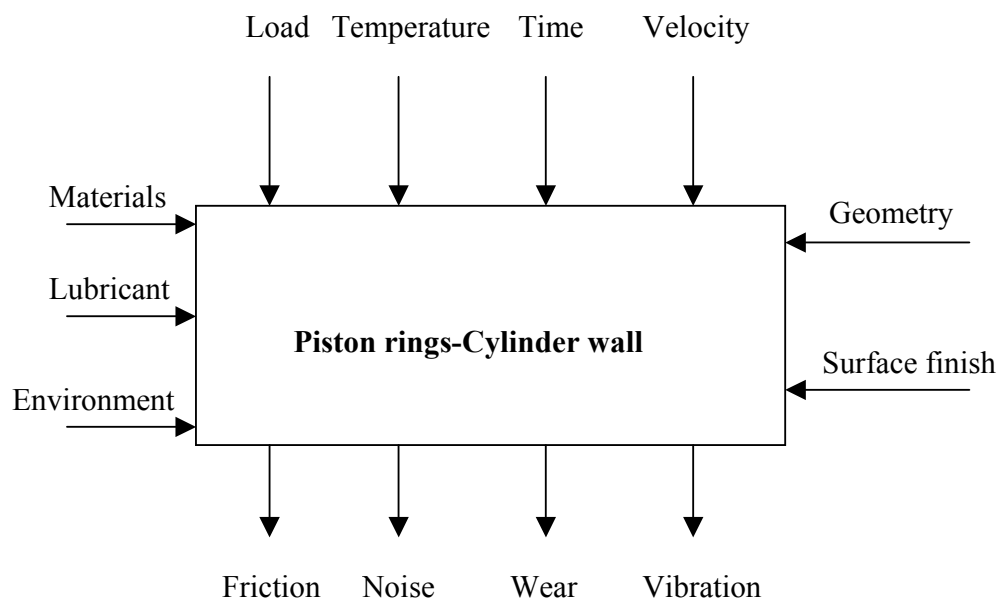


Figure 2.18. Representation of piston ring-cylinder wall system approach to tribology

#### 2.4.2.3. Wear of piston rings

Since the working environment of piston rings and cylinder liner is extreme, almost all types of wear are usually present, including:

**Adhesive wear:** that is due to the contact between the asperities of rings and the cylinder wall surface. The real asperity contacts are very small. A normal load can lead to high pressure at those points, forcing the asperities to deform and adhere strongly to each other. As a result, asperity junctions are formed (c.f., Figure 2.19). The tangential motion causes the piston ring material to be removed, resulting in material transfer from one surface to the other. Like any form of pressure welding, adhesive wear is more likely to occur if the surfaces are clean and non-oxidizing condition exists. This wear mode results in the formation of loose wear particles, which contributes to abrasive wear. The nature of material in contact, lubricating conditions and the surface finish affect the adhesive wear of piston rings.

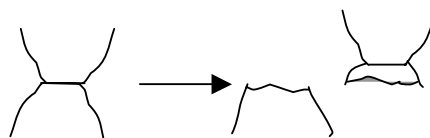


Figure 2.19. Adhesive wear

**Abrasive wear:** the abrasive wear occurs in contact between the piston rings and cylinder is due to the difference of the hardness of the ring and cylinder wall materials and due to the hard particles, which are introduced into the contact (c.f., Figure 2.20). The harder

surface asperities are pressed into the softer surface, which results in plastic flow of the softer material around the hard one (two-body situation). When the harder surface moves tangentially, ploughing and removal of softer material takes place with groove or scratches in the surface as a result. The same phenomenon occurs if there are hard particles in the contact area. In this case, the hard particles play the role as the hard material asperities. In the contacts of piston rings and cylinder wall, hard particles can be generated through external and internal means. Externally, they can arise from metal swarf (left from the manufacturing process), dust (from the air intake required for combustion), fuel, lubricating oil, and leakage from the cooling system. Internally, the hard particles can be the products of wear or abrasive ash formed during combustion of heavy fuel (in Diesel engines).

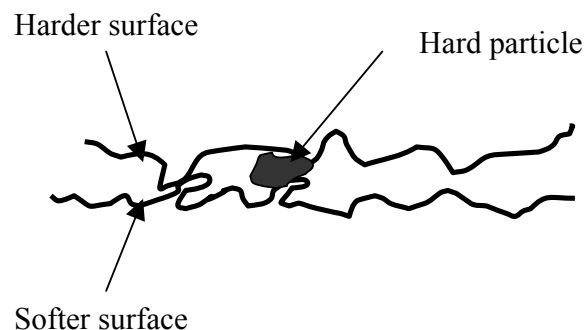


Figure 2.20. Abrasive wear

**Fatigue wear:** fatigue crack growth is now a well-documented phenomenon, which results from the surface bearing mechanical loads periodically. The periodical reverse reciprocation of piston rings in a cylinder enhances fatigue wear [117]. With piston rings,

the fatigue wear can be in the form of delamination wear. That is a kind of fatigue wear but occurs on a more microscopic scale in contact. During repeated sliding of the surface asperities on the piston rings and cylinder wall, small cracks nucleate below the surface. Further loading or deformation causes the crack to extend, propagate and join with the neighboring cracks resulting in the delamination of long thin wear sheets.

**Scuffing:** scuffing of piston rings can be understood as a gross surface damage by the formation of local welds between sliding surfaces. On non-coated piston rings, associated with scuffing is the production of a white brittle layer with a hardness of about 10 GPa [118]. The fracture and peeling off of this layer contributes hard particles to the contacts and produces a rough topography, which causes a loss of sealing ability. Scuffing occurs if the oil film thickness is insufficient to separate the contact surfaces and the temperature at the contact area is high enough. Therefore, it is probable that the process starts at around TDC in the expansion stroke where the lubricant film is thinnest and the temperatures are highest. Scuff resistance of the coatings is strongly influenced by the surface roughness. Low surface roughness helps to increase scuff resistance [119].

**Corrosive wear:** the corrosive wear is inevitable since piston rings work in an environment with chemically active substances (oxygen, organic and inorganic acids) coupled with high temperature. The mechanism of corrosive wear of piston rings can be explained by (1) Rapid formation of the protective layer, which is the product of chemical reactions. The layer can consist of oxides, organic salts, sulfides, sulfates, etc. (2) Removal of the protective layer by wear and re-exposure of the surface then takes place and corrosive attack can continue.

### **2.4.3. Coatings for piston rings**

Surface treatment is the most effective solution for reduction of friction and wear of piston rings, especially the first compression ring. Wide varieties of piston ring coatings are in use, or have been tested during the evolution of piston rings. Ring coatings may be placed into two major categories:

- Corrosion resistant and break-in coatings whose purpose is to improve shelf life and running-in capabilities and
- Wear resistant coatings to increase the total operating life of the piston rings.

#### **2.4.3.1. Running-in coatings**

Running-in coatings can be categorized as [115]:

- Iron oxide ( $\text{Fe}_3\text{O}_4$ ): piston ring is exposed in a steam atmosphere at approximately 500°C. An iron oxide coating is formed and then is sealed with oil to prevent corrosion during storage. The coating aids running-in by the mild abrasive action of the oxide.
- “Wellcoat C”: this is an iron oxide coating, incorporating sulfur compounds produced by treatment in a hot alkali/nitrite bath. The coating possesses corrosion resistance during storage and also aids running-in by the presence of sulfur compounds, which gives resistance to scuffing.
- Phosphating: the coating is formed by immersion in baths of phosphoric acid and phosphates of iron, zinc, and manganese at 40 °C-100 °C. The phosphate coatings are soft, porous and crystalline, which gives a rougher surface to absorb and retain lubricating oil.
- “Sulfinuz”: this treatment is carried out at 540 °C - 600 °C in a specially compounded salt bath for periods between 5 minutes to 3 hours. The treatment diffuses sulfur, nitrogen and carbon into the surface. The sulfur content accelerates the nitriding action in the bath.

The “Sulfinuz” treatment has been shown to be beneficial in increasing scuff resistance and reducing coefficient of friction.

- “Tufftriding”: This is a similar process to Sulfinuz, except that a stream of compressed air is used to accelerate the nitriding action and sulfur is absent in this kind of treatment. Tufftriding produces a less porous and harder surface than “Sulfinuz”.
- Soft metal electroplating: Electroplated layers of soft metals such as cadmium, tin or copper can be applied to give storage protection and aid running-in.

#### **2.4.3.2. Wear resistance coatings**

Wear resistance coatings for piston rings have been the research subject for tribologists and engineers for several decades. A good protective coating is one that not only possesses good wear resistance but also exhibits low friction during operation.

##### **2.4.3.2.1. Chromium and molybdenum**

Chromium [120, 121] is one of the most popular protective coatings used for piston rings in internal combustion engines. Chromium coatings can be produced by electroplating, plasma spraying or by sputtering. Recently, because of environmental concerns, electroplated chromium coatings have been replaced by plasma sprayed or sputtered coatings [122]. The coatings that are produced by plasma spraying have better scuff resistance and improved wear life compared to those produced by electroplating. The thickness of chromium coatings varies from 0.1mm to 0.5 mm, depending on the size and type of engines. The hardness of the chromium coating is about 10 GPa. Since the hardness is not high and there is evidence that under high temperature conditions, at the rubbing surface, the chromium tends to soften and become prone to scuffing. This



observation led to the development of molybdenum and chromium/molybdenum alloy coatings.

Molybdenum coatings can be produced by thermal or plasma spray [118]. In the former method, molybdenum wires and oxygen/acetylene flame are used as the heat source. Plasma sprayed molybdenum coatings tend to be denser and contain less oxide and it is suggested that they are less scuff resistant compared to the coatings produced by thermal spraying. Flame sprayed coatings are superior since they have high hardness and capacity for oil entrapment. The coating thickness may reach up to 0.25 mm. Molybdenum coatings can work with both cast iron and chromium plated cylinder liners and have been reported to give much better wear resistance than chromium coatings. A major drawback of molybdenum coatings is the high friction generated.

#### **2.4.3.2.2. Nitride coatings**

**Chromium nitride:** Chromium nitride can be produced by gas nitriding, ion plating or by magnetron sputtering [118, 123]. The gas nitrided layer is mainly composed of CrN, Cr(C,N) and  $\alpha$ -Fe. The prerequisite condition to applying this method is the ring material must contain sufficient chromium and carbon. The coating hardness was reported to be about 11-12 GPa and generally the wear rate is reduced by about 50% compared to chromium plate. Chromium nitride coatings produced by ion plating have a higher hardness (about 16 GPa) and higher scuff resistance. The coating properties can be changed by controlling the quantities of reaction gas, consequently, changing the component ratio of Cr, Cr<sub>2</sub>N, and CrN.

RF magnetron sputtering has been employed to produce chromium nitride coatings for piston rings. Coating stoichiometry was varied by changing the nitrogen flow. The coating hardness was reported to be about 12 GPa to 15 GPa with compressive stress varying from 2 GPa to 3.5 GPa. Wear tests showed a very effective wear reduction of about 94 % compared to chromium electroplated coatings [122, 123].

**Titanium nitride:** Titanium nitride was first coated commercially on cutting tools by the CVD method [9]. Recently, titanium nitride coatings have been produced by plasma assisted PVD [124] for piston rings. Titanium nitride coatings have good wear resistance since they have high hardness (20 - 22 GPa) [125]. However, a big drawback of titanium nitride produced by PVD is its poor adhesion to the piston ring surface. To overcome that problem, multi-layer Ti/TiN was employed [124]. The coating hardness, critical load of scratch test and wear resistance of multi-layer coatings rise with increasing layer number. Nine-layer Ti/TiN coatings show much less wear loss on both ring and cylinder liners compared to that of electroplated chromium coatings.

#### **2.4.3.2.3. Composite**

Composite coatings have been developed with hard particles such as carbides or oxides in a metal or alloy matrix. This kind of coating is known as a cermet. The promising coatings can be listed as: 88% tungsten carbide/cobalt, 75 % chromium carbide/ nickel- chromium, 75 % chromium/molybdenum [126, 127] and silicon nitride/nickel-cobalt phosphor [118]. Composite coatings have shown excellent oxidation resistance and wear resistance. However, an increase of bore wear rates has been reported. Rastegar [127] pointed out that the application of chromium carbide/ nickel-chromium composite coatings helped to

reduce the wear of piston rings to six times lower than conventional chromium coatings but caused an increase of the cylinder wear by three times.

#### **2.4.3.2.4. K-ramic**

K-ramic is an effective surface treatment for heat insulated engines [119,128, 129]. It is a ceramic coating with chromium oxide (chromia) as the base. Chromia has excellent scuff resistance in sliding at high temperature. The hardness of K-ramic coatings varies from 12 GPa to 18 GPa.

#### **2.4.3.3. Evaluation of recent protective coatings for piston rings**

To compare the friction of various piston ring materials, Yoshida et al. [119] carried out experiments with pearlitic gray cast iron liners. Ion plated (Cr, Cr<sub>2</sub>N, CrN) coatings exhibited 60, 180 and 500 % lower friction compared to K-ramic, gas nitrided (CrN, Cr(C,N),  $\alpha$ -Fe) and electroplated chromium, respectively. The wear measurement showed that ion plating coating had the smallest wear rate, followed next by K-ramic. Electroplated chromium exhibited double the wear rate compared to ion plated coating. Wear of the cylinder was reported highest with the K-ramic ring coating and lowest with the ion plated coating. Compared to others, the chromium nitride ion plating showed considerable advantages in both friction and wear behavior.

Inoue et al. [130] investigated the wear behavior of Ni-P-Si<sub>3</sub>N<sub>4</sub> composite plating, TiN deposited by PVD, nitriding and chromium plating in firing operation of a gasoline engine. The TiN coating exhibited the best wear resistance, followed by the composite coating. The chromium electroplated coating was the worst for wear resistance. The

scuffing resistance of TiN and the composite was excellent compared to the rest. The wear of the cylinder with TiN and chromium electroplated coatings was almost the same and that with nitrided and composite coatings was higher. To evaluate the corrosion resistance, sulfuric acid 2.5 % was employed and each coating was immersed for 25 minutes. The results showed that the weight loss of Mo sprayed, composite, and PVD TiN coating was nearly zero whereas that of electroplated chromium and nitrided coatings were  $70 \text{ mg/cm}^2$  and  $58 \text{ mg/cm}^2$ , respectively.

It is clear that, as protective coatings for piston rings, hard nitrides (such as chromium nitride or titanium nitride) deposited by PVD exhibit much better performance compared to conventional materials such as electroplated chromium or sprayed molybdenum.

#### **2.4.4. Summary**

Review of piston rings and their protective coatings can be summarized as follows:

- The energy loss due to friction of the piston rings - cylinder system contributes a considerable part to the total energy loss due to friction in the engine.
- Surface treatment including coating is the most effective way to reduce the wear (thus increasing the working life) and the energy loss of the piston rings - cylinder system thus reducing the fuel consumption.
- So far, nitride coatings such as TiN or CrN are considered the best protective coatings for piston rings from both wear and friction aspects. However, TiN coatings still have drawbacks such as poor adhesion to the ring and high coefficients of friction. Under dry conditions, the coefficient of friction of TiN was reported higher than 0.4 [9, 42, 44] whereas that of hydrogen-free DLC was less than 0.2 (see section 2.2.2). Therefore, for a

further increase in the working life and reliability and reduction in friction losses, a new type of DLC-based protective coatings should be developed.

## CHAPTER THREE

### EXPERIMENTAL METHODS

#### 3.1. Coating deposition

Deposition of DLC and DLC nanocomposite coatings was carried out using an E303A magnetron sputtering system (Penta Vacuum, Singapore, c.f., Figure 3.1(a)). The system is equipped with RF (1200 W) and DC (1000 W) power sources. As illustrated in Figure 3.1(b), there are four planar magnetrons. Co-sputtering can be carried out with 3 magnetrons simultaneously. Vacuum of the chamber is maintained by incorporation of an 800 l/s cryogenic UHV pump and 12 m<sup>3</sup>/h two-stage rotary backing pump. The main chamber is roughly pumped through a separate and direct path from the cryogenic pump. High vacuum pumping via the cryogenic pump is automatic once a suitable starting pressure has been obtained via the roughing pump. The vacuum system enables the pressure in the main chamber to reach  $1.33 \times 10^{-5}$  Pa ( $10^{-7}$  Torr). The process pressure is monitored via a high-accuracy capacitance manometer pressure gauge. The process pressure is kept constant by a butterfly valve.

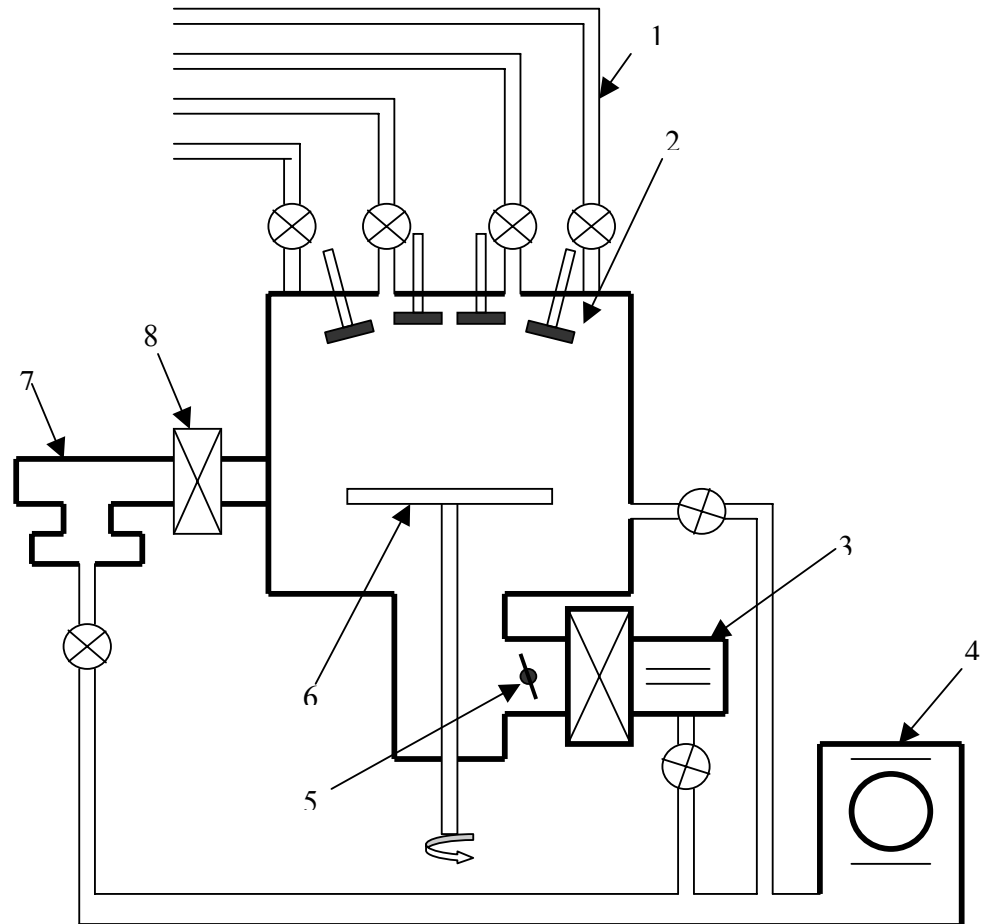
The substrate holder can rotate and can be grounded or floating or biased with DC or RF. The heater that is installed under substrate holder allows the substrate to be heated up to 600 °C.

The load lock is fitted with an automatic substrate transfer arm. Automatic operation of the system is achieved by incorporating a pre-programmed PLC of industrial standard.

To deposit DLC coatings, a pure graphite (99.999 %) target was employed. Co-sputtering of graphite and pure metallic targets (99.995 %) was carried out to deposit DLC nanocomposite coatings. The targets (100 mm diameter and 5.5 mm thickness) were located 100 mm above the substrate holder. Before deposition, the chamber is evacuated to a base pressure of  $1.33 \times 10^{-5}$  Pa. Argon was fed into the chamber as the plasma gas. The argon flow during sputtering was maintained constant at 50 sccm (standard cubic centimeter per minute).



(a)



(b)

Figure 3.1. The picture (a) and the schematic diagram (b) of E303A magnetron sputtering system

- |                 |                   |                    |
|-----------------|-------------------|--------------------|
| 1-Gas feed line | 2-Magnetrons      | 3-Cryogenic pump   |
| 4-Rotary pump   | 5-Butterfly valve | 6-Substrate holder |
| 7-Load lock     | 8-Gate valve      |                    |



Substrates used in this study were [100] Si wafers (100 mm diameter, 450  $\mu\text{m}$  thickness, 2 nm  $R_a$ ) and 440C steel pieces (55 mm diameter, 5.5 mm thickness, polished to 60 nm  $R_a$ ). Before sputtering, the substrates were ultrasonically cleaned for 30 minutes in acetone followed by 15 minutes ultrasonic cleaning in ethanol. After loading, the substrates were heated to and maintained at 150  $^{\circ}\text{C}$  for 30 minutes for outgasing.

### **3.2. Characterization**

#### **3.2.1. Image characterization**

Image characterization was carried out using an optical microscope (Zeiss), scanning electron microscope (SEM, JEOL - JSM 5600 LV), high-resolution transmission electron microscope (HRTEM, JEOL 4000 EX/II, operated at 400 kV) and atomic force microscope (AFM, Shimadzu-9500 J2).

For TEM samples, thin films were deposited on potassium bromide (KBr) pellets (8mm diameter, 1.2 mm thickness), which were produced by pressing KBr powder. Film thickness was estimated to be about 50 nm for all samples. After deposition, the pellets were dissolved in de-ionized water to float off the films for TEM study. AFM was utilized to study the surface morphology of the coatings. The measurement was conducted in ambient atmosphere in contact mode with a  $\text{Si}_3\text{N}_4$  tip. The scan size was 2  $\mu\text{m}$  x 2  $\mu\text{m}$  with set point of 2.00 V and scan rate of 1.00 Hz. The AFM is equipped with image analyzing software, which allows a 3-D image at any view with surface parameters to be obtained. The measuring pixel number of 256 x 256 was chosen from the software.

### 3.2.2. Structure of coatings

The structure of coatings was investigated using Raman spectroscopy and X-ray diffraction (XRD).

The Raman spectroscopy (Renishaw) operates at the 633 nm line excited with a He-Ne laser. In order to decrease the noise, 3 scanning accumulations were used. The curve fitting was performed using a Gaussian function. The  $I_D/I_G$  ratio estimates the  $sp^3$  fraction in the DLC. The phase study was carried out using a Philips PW1710 parallel beam horizontal diffractometer attached to a  $CuK\alpha$  40 kV/30 mA ( $\lambda = 0.15406$  nm) X-ray source. The average crystalline size was estimated using the Debye-Scherrer formula [131]:

$$D = \frac{K\lambda}{\beta \cos(\theta)} \quad [nm] \quad (3.1)$$

where D is the mean crystalline dimension normal to diffracting planes, K is a constant ( $K=0.91$ ),  $\lambda$  is the X-ray wavelength ( $\lambda = 0.15406$  nm),  $\beta$  in radian is the peak width at half-maximum peak height and  $\theta$  is the Bragg's angle.

### 3.2.3. Coating chemistry

Coating chemistry was studied by X-ray photoelectron spectroscopy (XPS) using a Kratos-Axis spectrometer with monochromatic Al  $K\alpha$  (1486.71 eV) X-ray radiation (15 kV/10 mA) and hemispherical electron energy analyzer. The base vacuum of the chamber

was  $2 \times 10^{-9}$  Torr ( $2.66 \times 10^{-7}$  Pa). The survey spectra in the range of 0-1100 eV were recorded in 1 eV step for each sample, followed by high-resolution spectra over different element peaks in 0.1 eV steps, from which the detailed composition was calculated. Curve fitting was performed after a Shirley background subtraction by non-linear least square fitting using a mixed Gauss/Lorentz function. To remove the surface contamination layer, Ar ion bombardment (ion etching) was carried out using a differential pumping ion gun (Kratos MacroBeam) with an accelerating voltage of 4 KeV and a gas pressure of  $10^{-7}$  Torr ( $1.33 \times 10^{-5}$  Pa). The bombardment was performed at an angle of incidence of  $45^\circ$  with respect to the surface normal.

### 3.2.4. Mechanical and tribological evaluation of the coatings

#### 3.2.4.1. Residual stress

Residual stress of the coatings was obtained from the change in the radius of curvature of the [100] Si substrate measured before and after deposition of the coating using a Tencor laser scanner. The stress values were calculated using the following equation [132]:

$$\sigma = \frac{E_s}{6(1-\nu_s)} \frac{t_s^2}{t_c} \left( \frac{1}{R_2} - \frac{1}{R_1} \right) \quad [\text{GPa}] \quad (3.2)$$

where  $E_s/(1-\nu_s)$  is the substrate biaxial modulus (180.5 GPa for [100] Si wafers [133]),  $t_s$  and  $t_c$  are wafer and coating thickness,  $R_1$  and  $R_2$  are the radius of curvature of Si wafer before and after deposition of coatings, respectively.

#### 3.2.4.2. Hardness and Young's modulus

Hardness and Young's modulus of coating were measured using nanoindentation (XP) with a Berkovich diamond indenter (c.f., Figure 3.2). The hardness and Young's modulus were determined by the continuous stiffness measurement technique [134]. The indentation depths were set not to exceed 10 % of the coating thickness to avoid interference from the substrate. On each sample, 10 indentations were made at random locations and the obtained value of hardness and Young's modulus was the average. From the indentation load and unload curves, the plasticity of coating was estimated by dividing the displacement after complete unloading by the maximum displacement [135] (c.f., Figure 3.3).

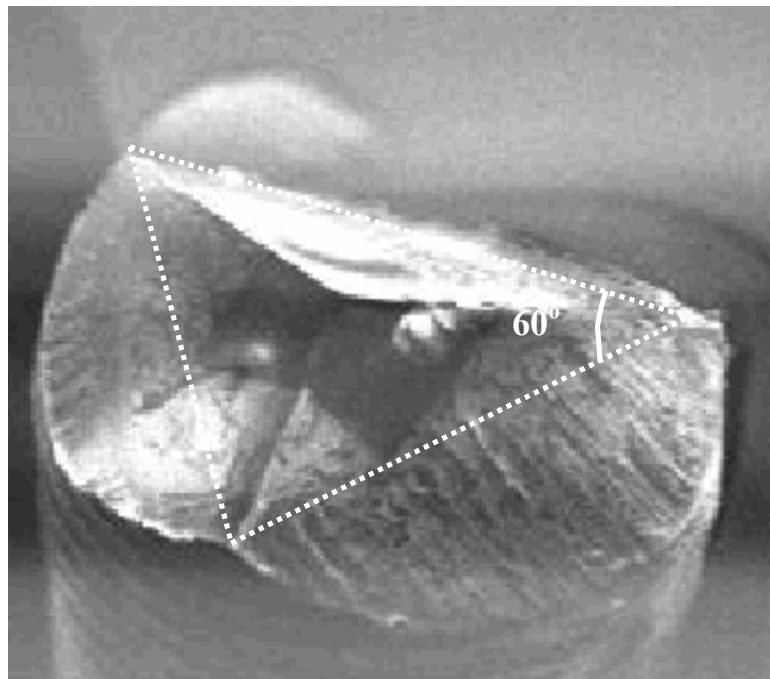


Figure 3.2. Berkovich indenter of XP nanoindentation hardness tester

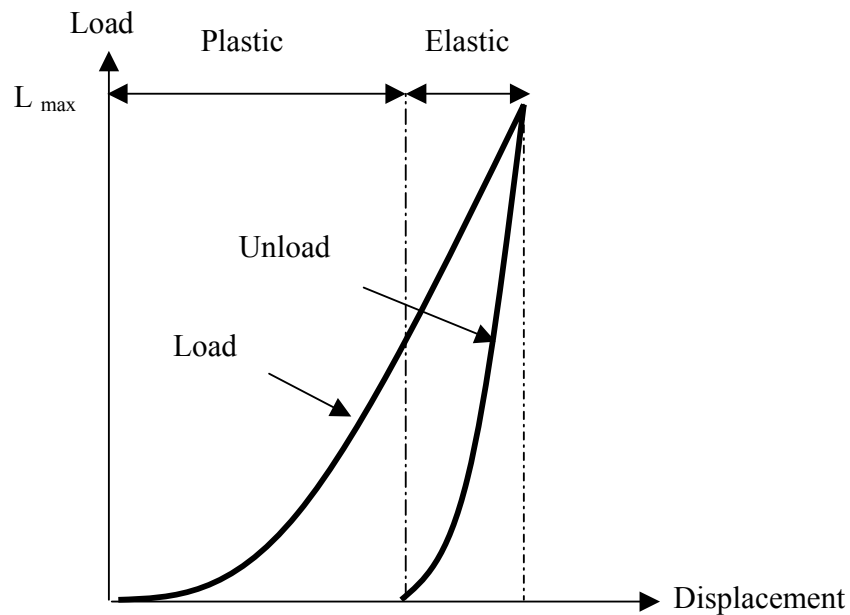


Figure 3.3. Load and unload curve obtained from nanoindentation hardness tester. The plasticity of coating is estimated by dividing the displacement after complete unloading by the maximum displacement

#### 3.2.4.3. Adhesion strength

Adhesion strength was studied in ambient atmosphere using the scanning micro scratch tester (Shimadzu SST-101) where a diamond tip stylus of  $15\text{ }\mu\text{m}$  radius was dragged on the coating with a gradually increased load. The scanning amplitude was set at  $50\text{ }\mu\text{m}$  at a speed of  $10\text{ }\mu\text{m/s}$  (c.f., Figure 3.4). As increasing the load applied to the test sample, the coefficient of friction (here in terms of output voltage rate) increased. Upon peeling (fracture) of the coating starting to occur, fractured pieces of the coatings cause the fluctuation of the cartridge output signal.

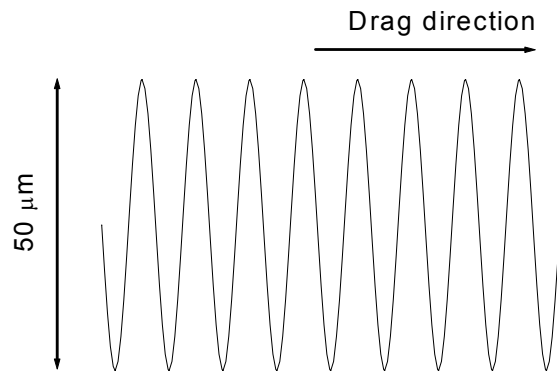


Figure 3.4. Schematic diagram of scratch test

#### 3.2.4.4. Tribotests

Tribotests were carried out using a CSEM tribometer with ball-on-disc configuration (c.f., Figure 3.5).

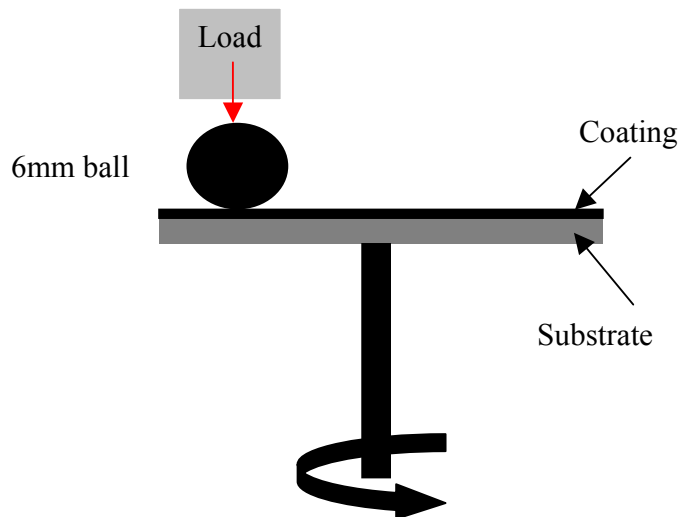


Figure 3.5. Schematic diagram of tribotest

The coefficient of friction was continuously recorded during each test. The materials of the counterparts (balls with diameter of 6 mm) used in this study were alumina ( $R_a=0.015\text{ }\mu\text{m}$ ;  $H=20\text{ GPa}$ ) and AISI 52100 (100Cr6) steel ( $R_a=0.03\text{ }\mu\text{m}$ ;  $H=8\text{ GPa}$ ). The dry (non-lubricated) tests were carried out in ambient condition ( $22\text{ }^\circ\text{C}$ , 75 % humidity) with a sliding speed of 20 cm/s. In the oil-lubricated tests, a lower sliding speed of 5 cm/s was chosen to avoid the hydrodynamic effect of the oil [41]. The oil was fed into the contact area with a flow rate of 0.05 ml/min. Shell Helix Plus 15W-50 engine oil was used as lubricant in oil-lubricated tribotests. The specification of this oil is tabulated in table 3.1.

Table 3.1. Specification of Shell Helix Plus 15W-50 engine oil

| Kinematic viscosity [cSt] |                     | Viscosity index | Density ( $15^\circ\text{C}$ )<br>[Kg/m <sup>3</sup> ] | Flash point*<br>[ $^\circ\text{C}$ ] | Pour point**<br>[ $^\circ\text{C}$ ] |
|---------------------------|---------------------|-----------------|--|--------------------------------------|--------------------------------------|
| $40^\circ\text{C}$        | $100^\circ\text{C}$ |                 |  |                                      |                                      |
| 141                       | 19.3                | 156             | 886  | 209                                  | -27                                  |

*\*Flash point: The lowest temperature at which the oil gives off enough flammable vapor to ignite and produce a flame when an ignition source is present*

*\*\*Pour point: The lowest temperature at which the oil is observed to flow*  
*The oil is added with 1.2 %Zn, 2.8 % Mg, 1.4 %Ca, 1.25 %P and 0.7 %S.*

## **CHAPTER FOUR**

### **MAGNETRON SPUTTERED HYDROGEN-FREE DLC (a-C)**

### **COATINGS**

As a basis for further development, this chapter studies pure DLC coatings deposited via magnetron sputtering and reports key parametric effects such as power density, negative bias voltage, and process pressure on the deposition rate and properties of the coatings.

#### **4.1. Effect of plasma cleaning on the adhesion of DLC coatings to the substrate**

Plasma cleaning, which helps to remove oxides or other contaminants from the surface of the substrate, is a simple method employed to enhance the adhesion of a-C to the substrates.

Figure 4.1 shows the change in surface roughness,  $R_a$  as a 440C steel substrate was plasma cleaned at chamber pressure of 0.6 Pa with various RF applied voltages for 30 minutes. Low bias voltage did not cause much increase in surface roughness of the substrate. When applied voltage was lower than 200 V, the increase in surface roughness (in terms of  $R_a$ ) was within 10 nm. As higher voltage was applied, the surface roughness increased considerably. At 500 V, the roughness increased almost 2.5 times (up to 135 nm). Pits were visually observed when the substrate was plasma cleaned at 500 V as seen from Figure 4.2. Understandably, high RF voltage causes more severe ion bombardment therefore more atoms from the substrate are sputtered off leading to a rougher surface.



Severe ion bombardment also results in greater residual stress on the surface of the substrate [62].

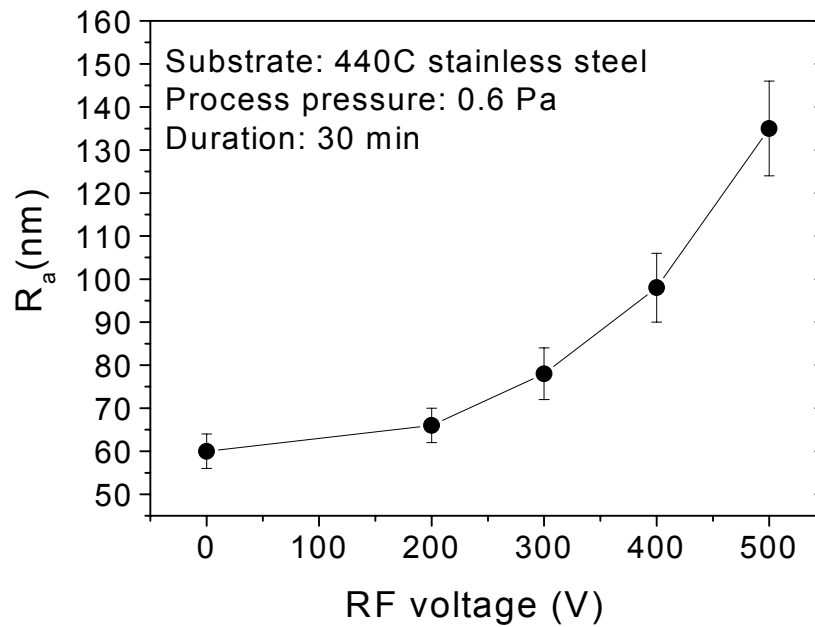
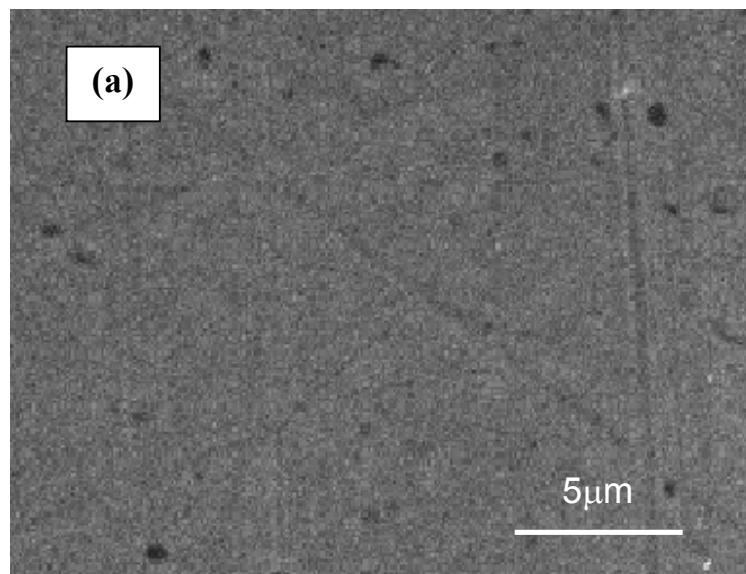


Figure 4.1. The relationship between RF bias voltage and surface roughness of the steel substrate after plasma cleaning. The surface roughness considerably increases at bias voltages higher than 200 V



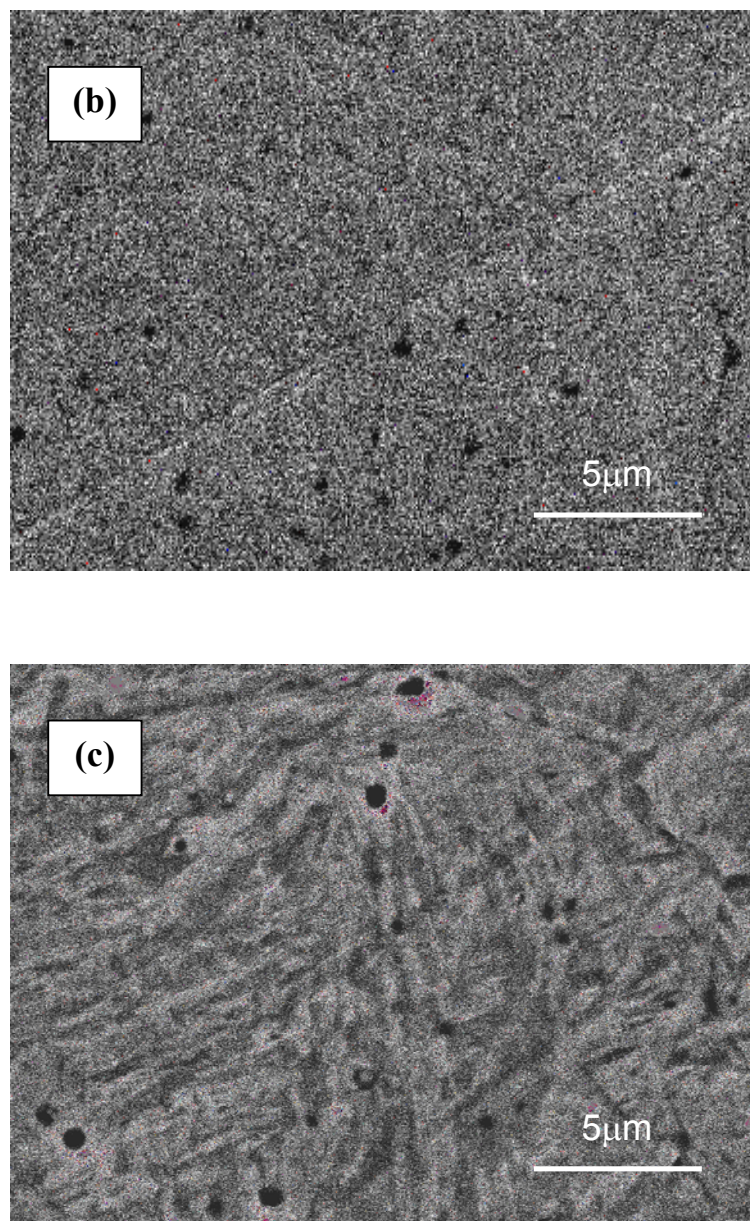


Figure 4.2. Effect of plasma-cleaning on the surface of steel substrate (a) The surface without plasma cleaning (b) Plasma cleaned at RF voltage of 200 V (c) Plasma cleaned at RF voltage of 500 V

To evaluate the effect of plasma cleaning, scratch tests were carried out with DLC coatings deposited at a power density of  $10.5 \text{ W/cm}^2$  and bias voltage during deposition of -60 V and -140 V. The coating thickness was  $1.2 \text{ }\mu\text{m}$  for both coatings. The critical load, in this case, was the load at which the coating totally peeled off (adhesive failure). Figure 4.3 shows the critical load of two DLC coatings with different plasma cleaning regimes. The coating deposited under low bias voltage exhibited better adhesion. It is caused by the microstructure, which will be discussed in section 4.5.4. However, the trend of critical load of the two coatings was almost the same. It can be seen that both coatings adhered to the substrate after deposition even without plasma cleaning. However, the adhesion strength in this case was very low (32 mN for the coating deposited under -140 V bias and 70 mN for that deposited under -60 V bias). The contaminants and oxides on non-cleaned substrates resulted in the low adhesion observed. As plasma cleaning was applied, the adhesion strength drastically increased. Maximum critical load was achieved with a 300 V of plasma cleaning. A “clean” surface combines with increased roughness, which results in more interlock and larger coating-substrate contact area, strongly enhancing the adhesion between the coating and the substrate. However, further increase in plasma cleaning voltage resulted in a decrease in critical load. High residual stress on the surface of the substrate due to severe ion bombardment is probably the main reason causing the decrease of adhesion strength at applied voltages of higher than 300 V. However, an effective method, which allows us to measure the stress generated from ion bombardment on steel substrates, is not yet available. Also, with coatings deposited under low bias voltage, plasma cleaning at voltages higher than 300 V did not cause much decrease in adhesion strength whereas a considerable decrease in adhesion strength for coatings deposited under high bias voltage was seen.

It can be seen that plasma cleaning for 30 minutes at 300 V optimized the adhesion strength of DLC to steel substrates regardless of the bias voltage applied during deposition process. Therefore, this plasma cleaning regime was chosen for all samples studied in this project.

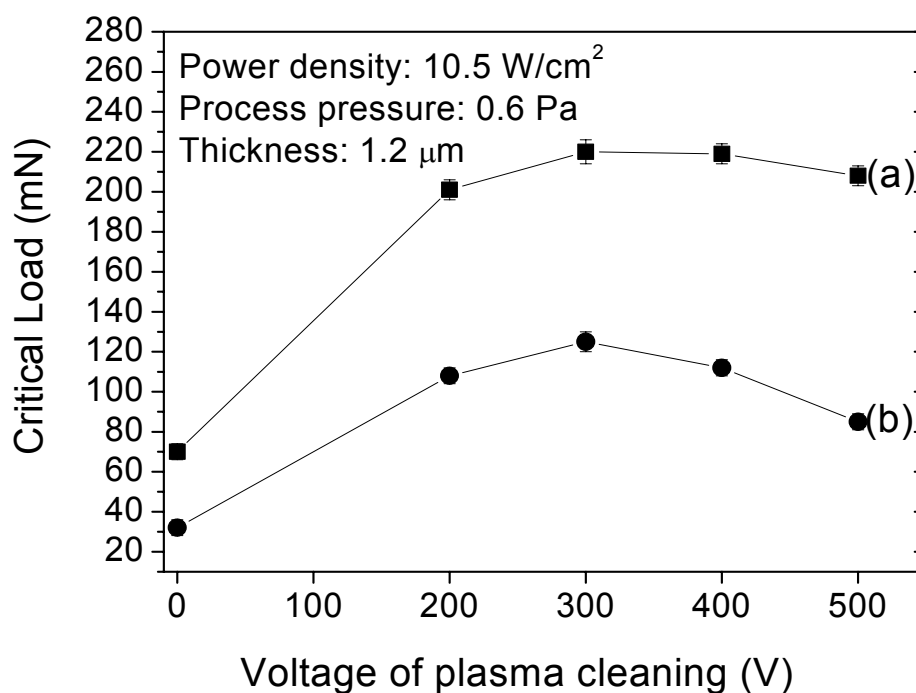


Figure 4.3. Influence of plasma cleaning voltage on the adhesion strength of DLC coatings deposited under (a) - 60 V and (b) -140 V bias. Plasma cleaning at 300 V for 30 min gives the best adhesion strength for both coatings

#### 4.2. Process pressure

The process pressure strongly influences the deposition rate and the properties of DLC coatings. From the Child-Langmuir equation [136], at a certain value of applied DC

voltage ( $V_{dc}$ ), the ion current density collected by the target is determined from the following equation:

$$J_i = \frac{4}{9} \epsilon_0 \left( \frac{2e}{M_i} \right)^{\frac{1}{2}} \frac{V_{dc}^{3/2}}{s^2} \quad [\text{mA/cm}^2] \quad (4.1)$$

where  $\epsilon_0$  is the permittivity of free space ( $8.854 \times 10^{-12}$  F/m),  $e$  is the charge of electron, and  $M_i$  is the mass of argon ion.

The sputtering rate of the target is proportional to the current density as described by the following equation [137]:

$$R_{sput} = \gamma_{sput} \frac{J_i}{e} \frac{1}{n} \quad [\text{cm/s}] \quad (4.2)$$

where  $\gamma_{sput}$  is the sputtering yield of the target,  $n$  is the atomic density of the target ( $\text{atom/cm}^3$ ), and  $e$  is the electron charge.

It has been demonstrated that an increase in the process pressure results in a decrease in the thickness of the cathode sheath [138] leading to an increase in ion current density (equation 4.1), therefore, leading to an increase in the the sputtering rate (equation 4.2). Theoretically, an increase in sputtering rate results in an increase in deposition rate. However, in practice, at high values of process pressure, the deposition rate tends to decrease. Figure 4.4 shows the deposition rate of DLC coatings deposited at a power

density of  $10.5 \text{ W/cm}^2$  and bias voltage of  $-20 \text{ V}$  at various process pressures from 0.2 to 2 Pa (the distance from target to substrate was 5 and 10 cm). The deposition rate was determined from the ratio of the coating thickness and the deposition time.

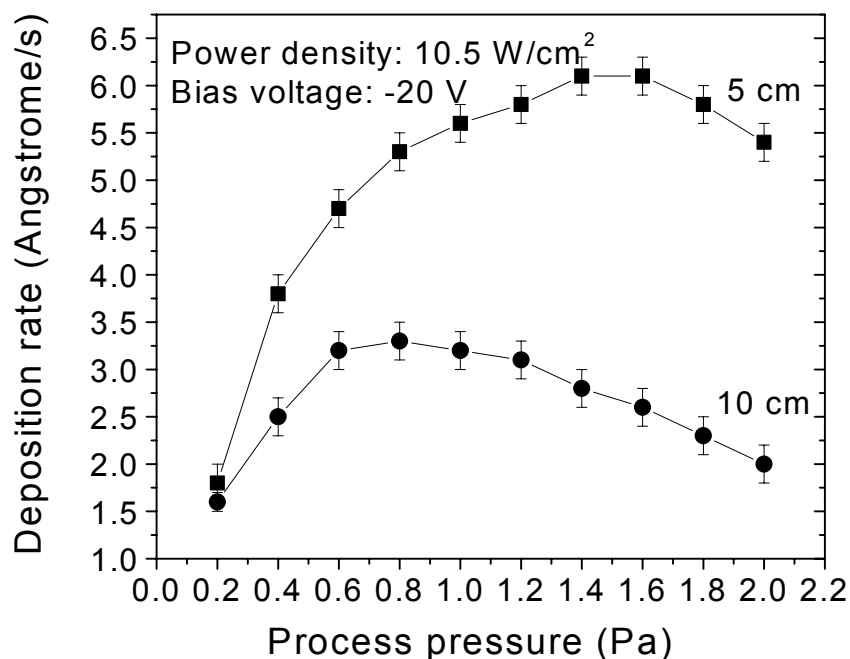


Figure 4.4. The influence of process pressure on the deposition rate of DLC coatings. At the same process pressure, the deposition rate is considerably higher as the substrate is located nearer to the target

At the same process pressure, the deposition rate was much higher when the substrate-target distance was 5 cm compared to the case of 10 cm. When the substrate was located 5 cm from the target, the deposition rate increased drastically from 1.8 to  $5.3 \text{ Å/s}$  when the process pressure increased from 0.2 to 0.8 Pa. More increase in process pressure resulted in a slight increase in the deposition rate and it reached a maximum value of about  $6.1 \text{ Å/s}$  at process pressures of 1.4 - 1.6 Pa. As the process pressure exceeded 1.6 Pa, the

deposition rate gradually decreased. When the substrate was located 10 cm from the target, the same trend was observed as the process pressure increased. A considerable increase in deposition rate followed by a period of slight increase and after reaching a maximum value, the deposition rate started decreasing. However, in this case, the pressure at which the deposition rate reached maximum value, was much lower (0.6 - 0.8 Pa).

It is well known that the mean free path (the maximum distance of an atom or an ion travel through the plasma without collision with other atoms) of atoms (or ions) sputtered from the target towards the substrate is inversely proportional to the pressure. The mean free path of a carbon atom travelling through a mixture of carbon and argon atoms can be derived from the kinetic gas theory and determined from the following equation [139]:

$$\lambda = \frac{2.2}{P} \quad [\text{cm}] \quad (4.3)$$

where P is the process pressure in Pa

Values of mean free path calculated from equation 4.3 with process pressures from 0.2 to 2 Pa are tabulated in table 4.1.

Table 4.1. The mean free paths for carbon ions at different process pressures

| Pressure (Pa)  | 0.2 | 0.4 | 0.6 | 0.8 | 1.0 | 1.2 | 1.4 | 1.6 | 1.8 | 2.0 |
|----------------|-----|-----|-----|-----|-----|-----|-----|-----|-----|-----|
| $\lambda$ (cm) | 11  | 5.5 | 3.7 | 2.8 | 2.2 | 1.8 | 1.6 | 1.4 | 1.2 | 1.1 |



At a process pressure of 0.2 Pa, the mean free path was 11 cm (larger than the substrate-target distance). Therefore the carbon atoms traveled from the target to the substrate without collision with argon atoms. This resulted in almost the same deposition rate for the substrate-target distance of 10 and 5 cm at a process pressure of 0.2 Pa. At a substrate-target distance of 5 cm, no collisions occurred when the process pressure was lower than 0.4 Pa since the mean free path was still higher than 5 cm. Therefore a sharp increase in deposition rate with increasing pressure, due to the increase in sputtering rate, was observed. As process pressure increased further, the mean free path became smaller than the substrate-target distance and collisions between sputtered carbon atoms and argon atoms occurred. More collisions caused more back-scattering of the carbon atoms. When the back-scattering rate was still low, the increase in process pressure still resulted in a considerable increase in the deposition rate (pressure in the range of 0.4 to 0.8 Pa) due to the increase of the sputtering rate. At higher pressures, the deposition rate slightly increased. As process pressure exceeded 1.6 Pa, the amount of back-scattered atoms was very high (higher than the increase in the amount of sputtered atoms due to increasing pressure) causing the decrease in the deposition rate. At the substrate-target distance of 10 cm, the amount of back-scattered atoms was high enough to cause the decrease in deposition rate as process pressure exceeded 0.8 Pa. It is clear that, back-scattering causes the decrease of deposition rate at high pressures and the higher the substrate-target distance the more the influence of back-scattering on deposition rate.

#### **4.3. Power density**

The power density of a magnetron is determined by the ratio of plasma power to target area:



$$P = \frac{W}{A} \quad [\text{W/cm}^2] \quad (4.4)$$

The power is calculated from  $W = V_{\text{dc}} I_{\text{dc}}$ ,

where  $V_{\text{dc}}$  and  $I_{\text{dc}}$  are the DC voltage and current respectively.

The power density influences the properties and deposition rate of DLC coatings. At a constant process pressure, a higher power density results in a higher energy and number of incoming carbon atoms (or ions). Figure 4.5 shows the deposition rate as a function of power density at a process pressure of 0.6 Pa, bias voltage of -20 V and substrate-target distance of 10 cm. The deposition rate increased from 0.9 to 3.2 Å/s as the power density increased from 2.5 to 10.5 W/cm<sup>2</sup>. Low power densities thus low deposition rate, apparently, are not suitable for industrial scale since usually several μm in thickness is required. For example, if the power density of 2.5 W/cm<sup>2</sup> was applied, as shown from Figure 4.5, the deposition rate was only 0.9 Å/s. Therefore, the deposition duration would be as long as 3 hours for a 1 μm DLC coating. If the power density of 10.5 W/cm<sup>2</sup> was chosen, the deposition rate increased to 3.2 Å/s and a 1 μm coating could be deposited within 0.85 hours. At such high power density, if the substrate-target distance was decreased to 5 cm then the deposition rate was 4.7 Å/s (c.f., Figure 4.4) and a 1 μm coating could be deposited within 0.6 hours.

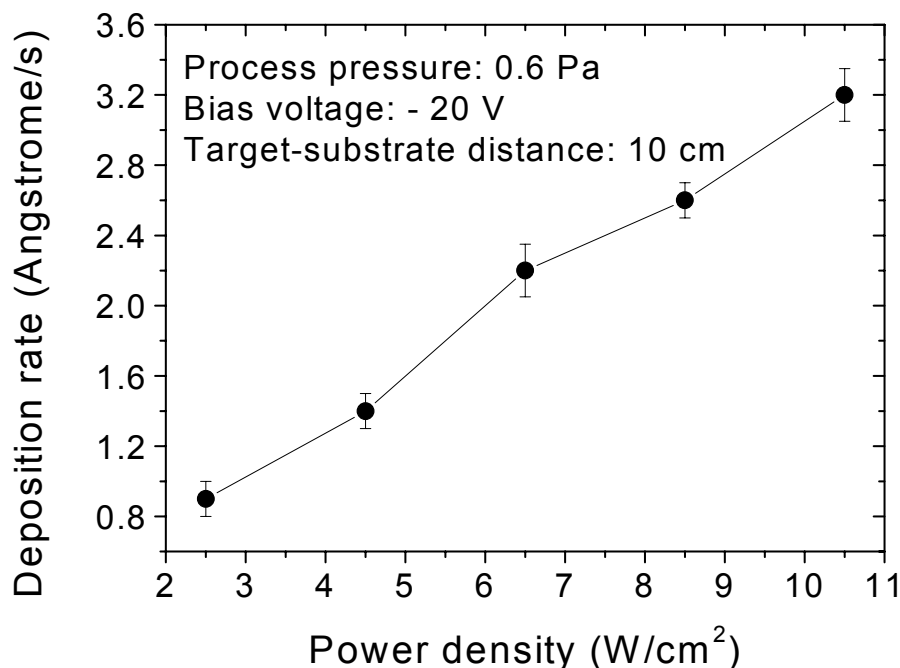


Figure 4.5. The deposition rate as a function of power density, it increases as increasing the power density

#### 4.4. Substrate bias

Different from conventional magnetron sputtering where the ratio between carbon ion and atom flux ( $\Phi_i/\Phi_c$ ) is less than 0.2 (most carbon species coming to the substrate are neutral), unbalanced magnetron sputtering (which was used in this study) produces a very high  $\Phi_i/\Phi_c$  ratio of 2 to 3 [58] (a large amount of carbon species coming to the substrate are ions). With this consideration, the substrate bias voltage is an important parameter affecting the characteristics of DLC coating since it influences the sputtered ion energy as described in the following relationship [16]:

$$E_i \propto \frac{V_b}{P^{1/2}} \quad (4.5)$$

where:

$V_b$  - substrate bias voltage

$P$  - the chamber pressure

Furthermore, with silicon wafer substrates, if RF bias was not applied then the substrate and the coating would be positively charged during deposition due to the bombardment of positive ions. The same phenomenon may occur with DLC and DLC nanocomposite coatings deposited on steel substrates since the coatings are not electrically conductive. If a coating is positively charged during the deposition process, it cannot reach a dense structure and achieve good adhesion to the substrate and peeling off will happen. DC bias cannot be a solution, even for coatings deposited on steel substrate because after the coating grows thicker than 1  $\mu\text{m}$ , a considerable drop in effective bias voltage through the coating thickness is observed [140]. Figure 4.6 shows a peeled off and fractured DLC coating, which was deposited on a silicon wafer at low power density (4.5  $\text{W}/\text{cm}^2$ ) and -20 V DC bias. The coating showed no adhesion to the substrate and completely peeled off from the substrate upon bringing to atmosphere. The pattern of peeling off is different from that caused by high residual stress (will be investigated in section 4.5.3.2). Under the same condition, if RF bias was applied, the coating had good adhesion and no peeling off was observed.

Therefore, RF bias was chosen to overcome the problem of substrate charging. The bias voltage should not be too high since re-sputtering would occur leading to a decrease of the deposition rate. The influence of bias voltage on the deposition rate is illustrated in Figure 4.7. The deposition rate decreased from 3.2 to 2.3 Å /s as the negative bias voltage increased from -20 to -140 V. At bias voltages lower than -60 V, the change in the deposition rate was negligible. The decrease was more pronounced for bias voltages higher than -100 V.

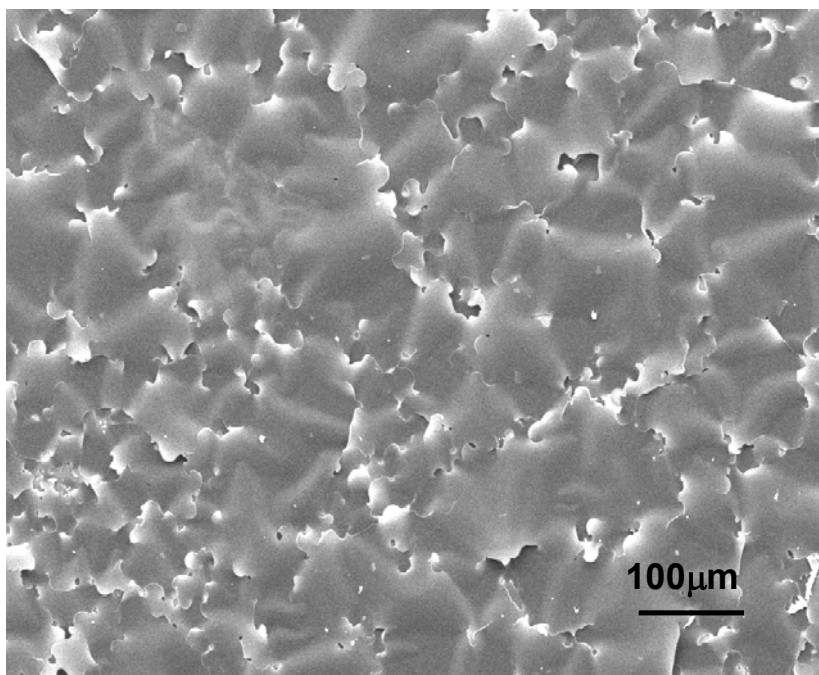


Figure 4.6. DLC coating deposited at power density of 4.5 W/cm<sup>2</sup> and DC bias voltage of -20 V

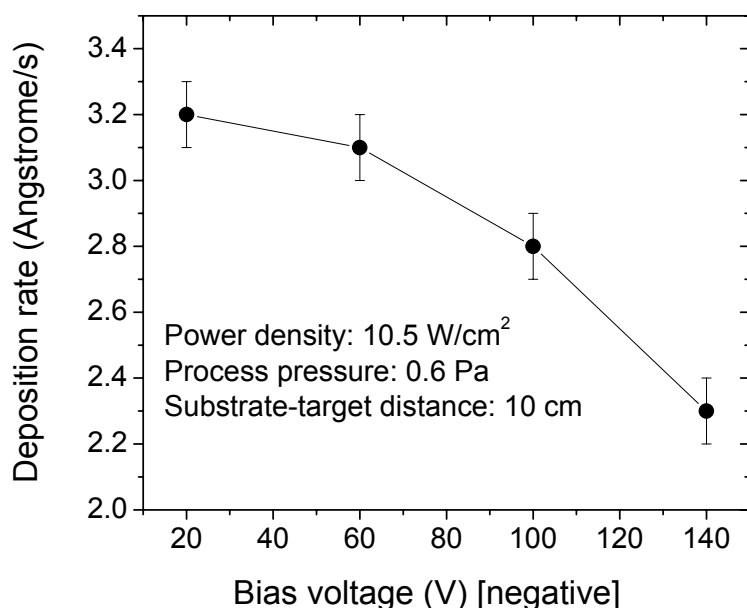


Figure 4.7. Deposition rate as a function of negative bias voltage

## 4.5. Characterization of magnetron sputtered DLC coatings

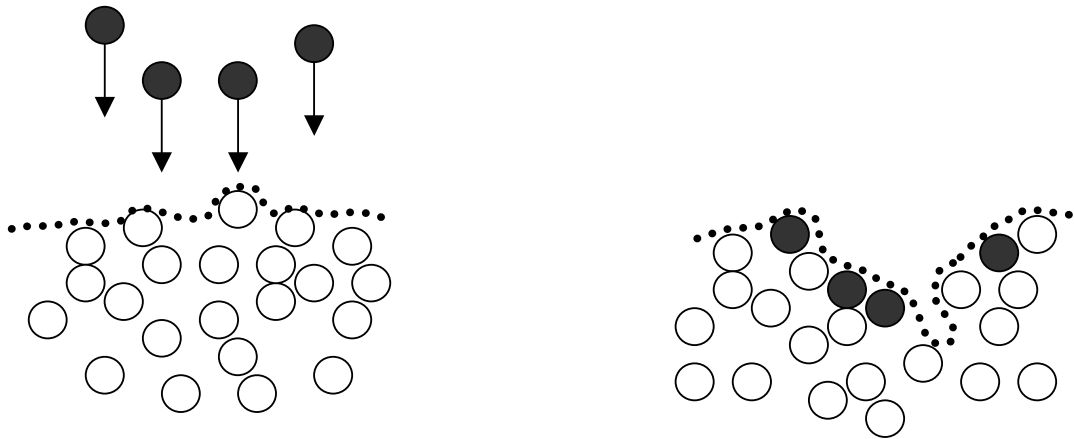
### 4.5.1. Surface morphology

Surface morphology is strongly influenced by the energy of incoming ions, which in turn, depends on the process pressure and bias voltage (equation 4.5). With higher ion energies, the surface becomes smoother due to the higher energy of ion impingement. This phenomenon is explained by the surface diffusion and ion implantation mechanisms [141]. Surface diffusion is easier to take place than bulk diffusion, since the activation energy is lower. Diffusion in the surface layers of DLC tends to generate ordered clusters with high  $sp^2$  content, i.e. with structures closer to the thermodynamically stable graphite phase than a typical DLC arrangement. Such clusters therefore form preferentially on the surface leading to substantial roughening. Surface diffusion is promoted by the energy associated with arrival of impinging ions, which remain within the surface layers (c.f., Figure 4.8

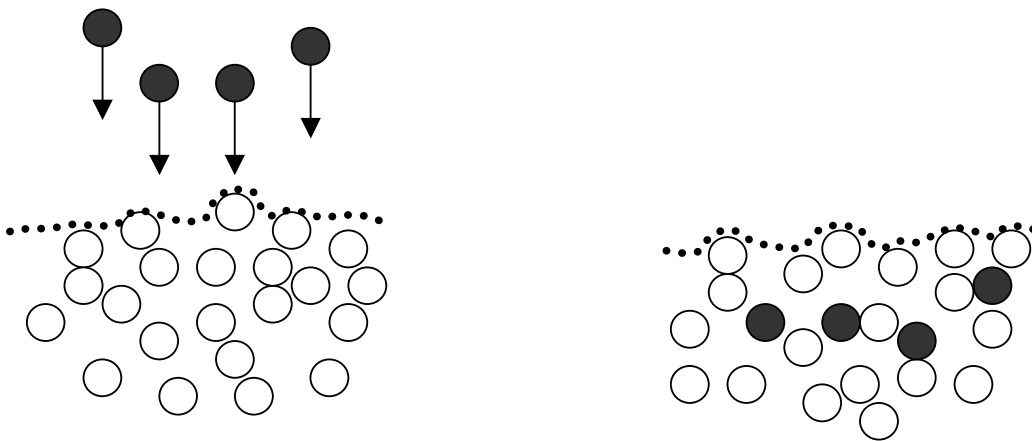
(a)). When the ion energy is high enough (with high bias voltage or low process pressure), the ion will penetrate into the interior of the structure. Under these circumstances, surface diffusion is not promoted and the ion energy tends to be dissipated into a relatively large volume in the interior. The surface is thus not affected by the ion penetration leading to a denser and more diamond-like structure (c.f., Figure 4.8 (b)). However, it should be noted that, in practice, the ion energy is not fixed in the process since RF bias voltage, various gas phase collisions, reactions, etc. give rise to a broad spectrum of energies. Aside from surface diffusion and ion implantation, re-sputtering also influences the surface morphology of the coatings. The bombarding ions or atoms can remove the pre-deposited atoms from the surface layers. Carbon ions impinging on the coating may act, not only as the carbon source, but also as the sputtering agent. In addition, the Ar ions or back-scattered Ar atoms can efficiently remove the deposited DLC coating. The re-sputtering is more pronounced when high bias voltage is applied because of the higher energy of incoming carbon and Ar ions. This causes a decrease in deposition rate as seen from Figure 4.7. The re-sputtering leads to smoother surface morphologies since protrusions are usually sputtered preferentially [142].

Figure 4.9 shows the AFM images of DLC coatings (about 1.2  $\mu\text{m}$  thickness) deposited on [100] Si wafers under a power density of 10.5  $\text{W}/\text{cm}^2$ , process pressure of 0.6 Pa with various substrate bias voltages from -20 to -140 V. As seen from the figure, DLC coatings deposited at low bias voltage show a rough surface with very large graphite clusters and many voids (Figure 4.9 (a) and (b)), which indicate a low density. In contrast, coatings deposited under high bias voltage (Figure 4.9 (c) and (d)) show a dense and smooth

surface with very small clusters. The calculated surface roughness ( $R_a$ ) of the coatings is shown in Figure 4.10.



(a)



(b)

Figure 4.8. Effect of ion energy on the surface roughness. Higher ion energy results in smoother surface

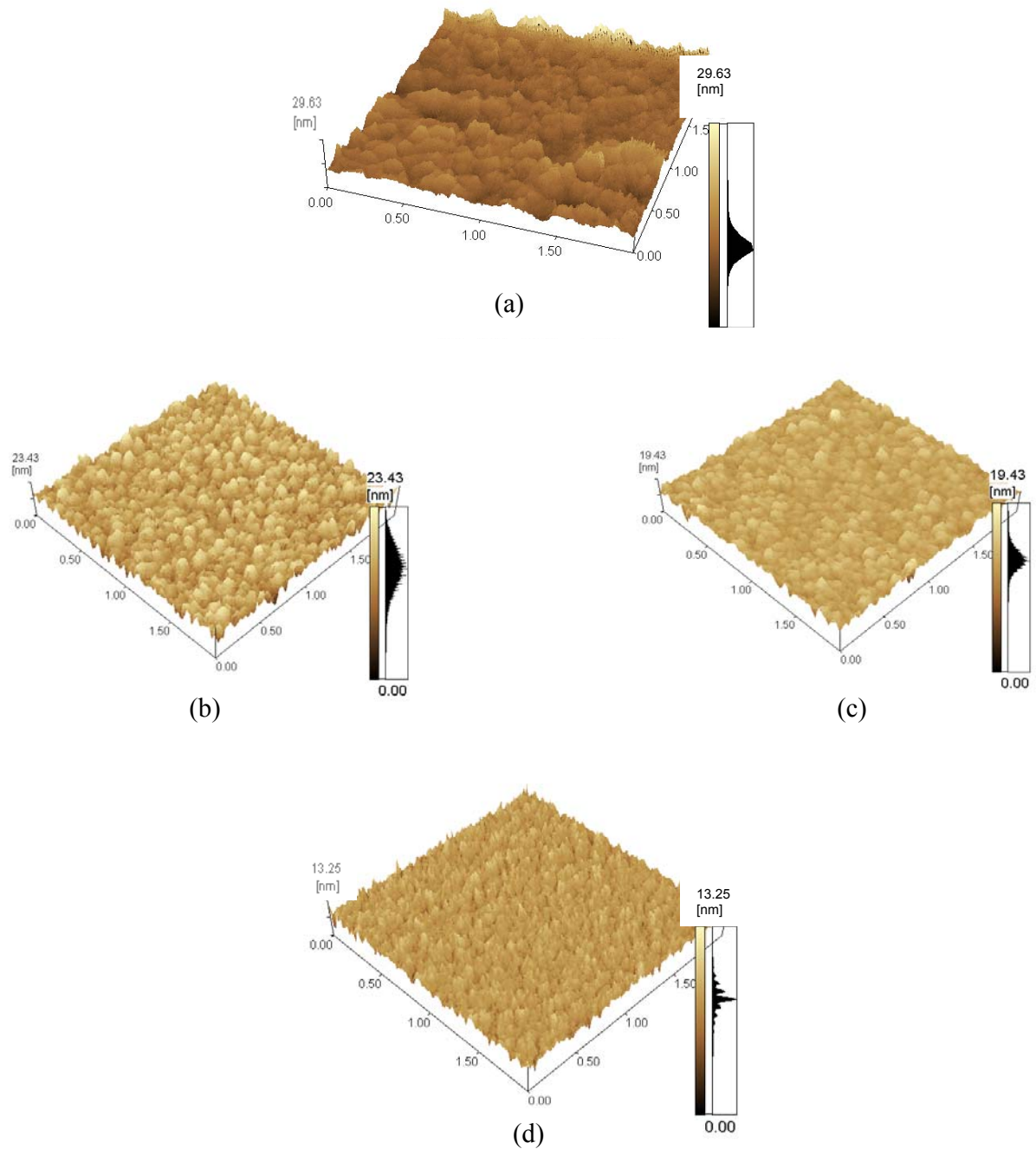


Figure 4.9. AFM images of DLC coatings (about 1.2  $\mu\text{m}$  thickness) deposited on [100] Si wafers (2nm  $R_a$ ) under different bias voltages: (a) -20 V, (b) -60 V, (c) -100 V, and (d) -

140 V



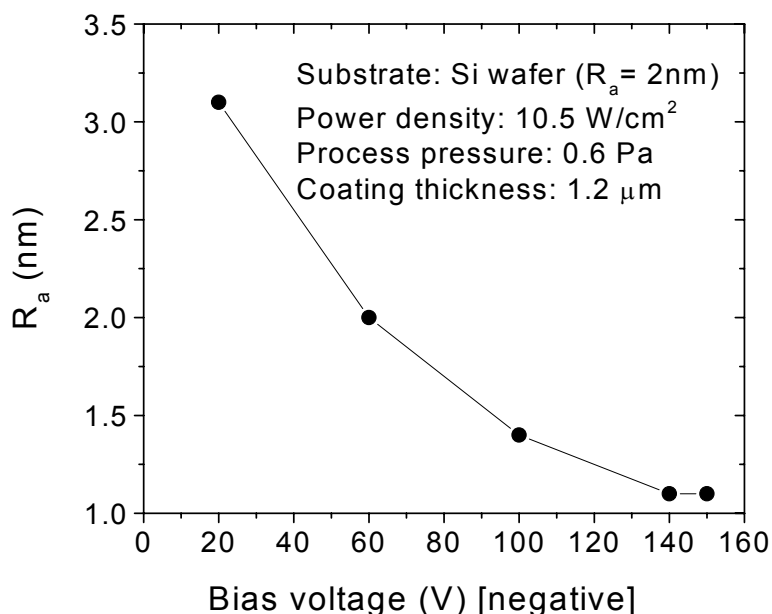
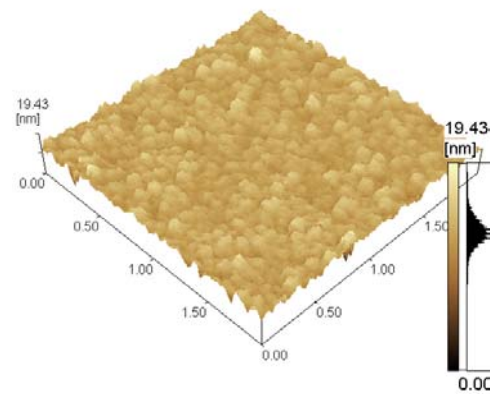


Figure 4.10. The influence of bias voltage on the surface roughness of DLC coating:  
 coating deposited under higher bias voltage has smoother surface (lower  $R_a$ )

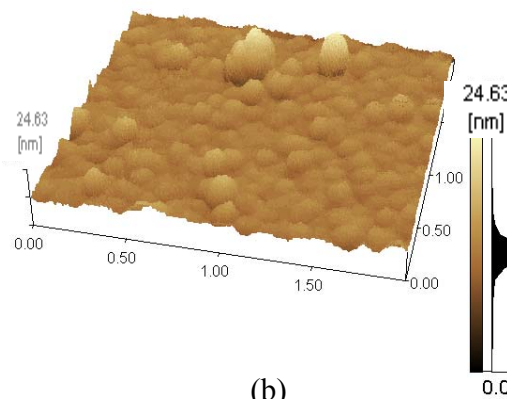
The  $R_a$  was as high as 3.1 nm for the coating deposited under -20 V bias. As bias voltage was increased to -100 V, the surface roughness decreased drastically to 1.4 nm. On further increasing bias voltage, the surface roughness slightly decreased and reached the value of 1.1 nm at a bias voltage of -140 V. After that, the surface roughness remained almost unchanged as bias voltage was further increased. The surface morphology of coatings deposited under -140 V and -150 V bias was almost similar. This observation indicates that when the energy of carbon ions reaches a critical level, the coating has the smoothest surface (minimum size of graphite clusters) and further increase in the energy (in terms of bias voltage) does not result in a smoother morphology.

The influence of process pressure on the surface morphology of DLC coatings can be seen from Figure 4.11, where AFM images of DLC coatings deposited at the same power

density ( $10.5 \text{ W/cm}^2$ ) and bias voltage ( $-100 \text{ V}$ ) at process pressures of  $0.6$  and  $1.2 \text{ Pa}$  are shown. As mentioned above, higher process pressure results in lower ion energy because more collision occurs between C and Ar ions. The morphology, therefore, becomes rougher with larger cluster sizes.



(a)



(b)

Figure 4.11. Surface morphology of DLC coating deposited at power density of  $10.5 \text{ W/cm}^2$ , bias voltage of  $-100 \text{ V}$  and different process pressures: (a)  $0.6 \text{ Pa}$  and (b)  $1.2 \text{ Pa}$ .

Rougher surface with larger graphite clusters was seen with coating deposited under higher process pressures

#### 4.5.2. Structure of DLC coatings

The TEM image of a DLC coating deposited at a power density of  $10.5 \text{ W/cm}^2$  and  $-150 \text{ V}$  bias is shown in Figure 4.12. The coating was amorphous with a broad halo in the diffraction pattern.

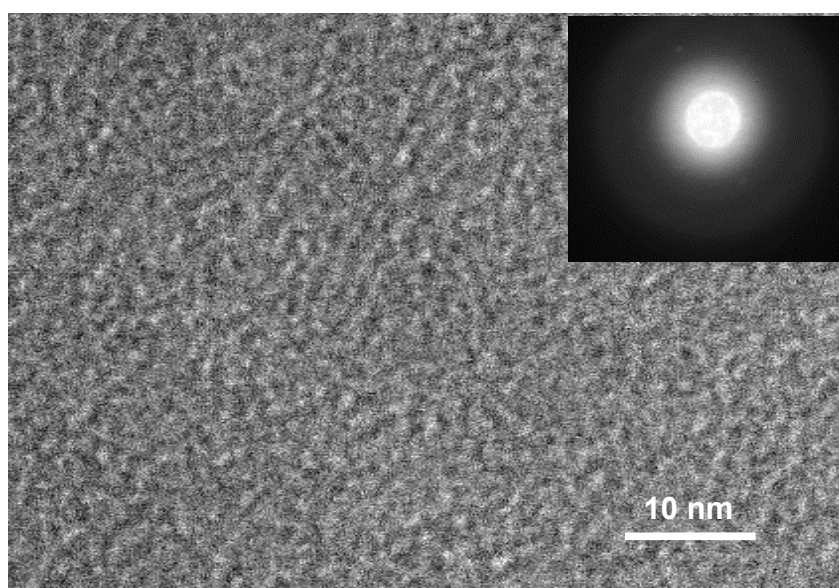
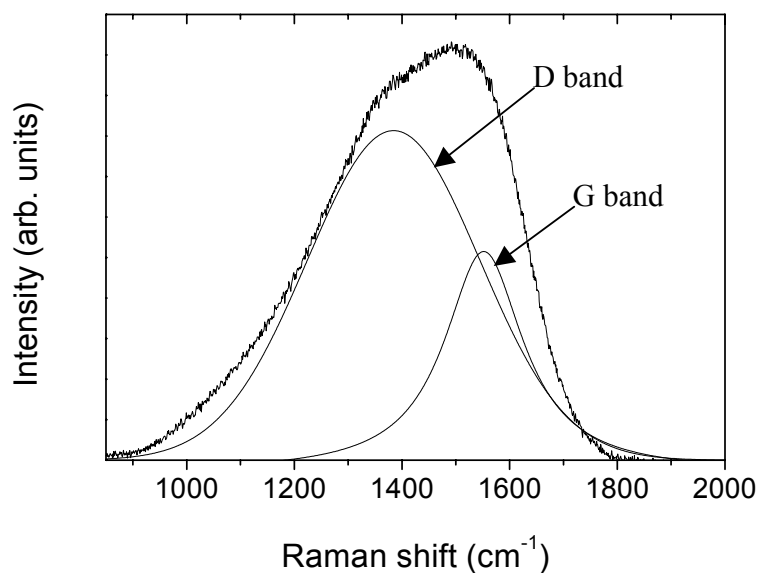


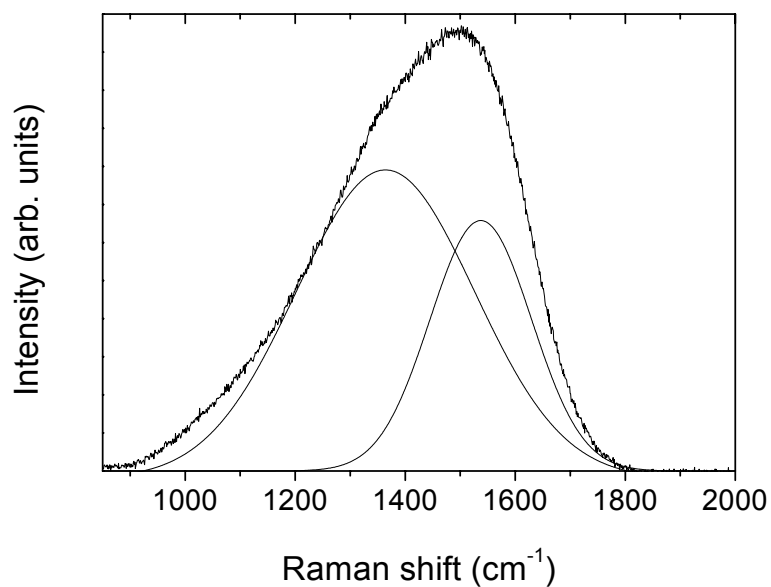
Figure 4.12. TEM image of DLC coating showing the amorphous nature with a broad halo observed from diffraction pattern

Figure 4.13 shows the Raman spectra of DLC deposited at  $-150 \text{ V}$  bias (a) and  $-60 \text{ V}$  bias (b). The range covered was from  $850$  to  $2000 \text{ cm}^{-1}$ . The same shape was seen for spectra of coatings deposited under other bias voltages: a broad peak at about  $1530 \text{ cm}^{-1}$  with a shoulder at about  $1350 \text{ cm}^{-1}$ . This broad peak was deconvoluted into two Gaussian bands at  $1530 \text{ cm}^{-1}$  (G peak) and  $1350 \text{ cm}^{-1}$  (D peak). The  $\text{sp}^3$  fraction in DLC coatings was qualitatively estimated by the ratio between the intensities of the D band and the G bands

$(I_D/I_G)$  taken from the Raman spectra: a higher  $I_D/I_G$  ratio means a lower  $sp^3$  fraction. The calculated  $I_D/I_G$  ratios are shown in Figure 4.14.



(a)



(b)

Figure 4.13. Raman spectrum with deconvoluted peaks of DLC coating deposited at power density of  $10.5 \text{ W/cm}^2$  and bias voltage of (a) - 60 V and (b) -150 V

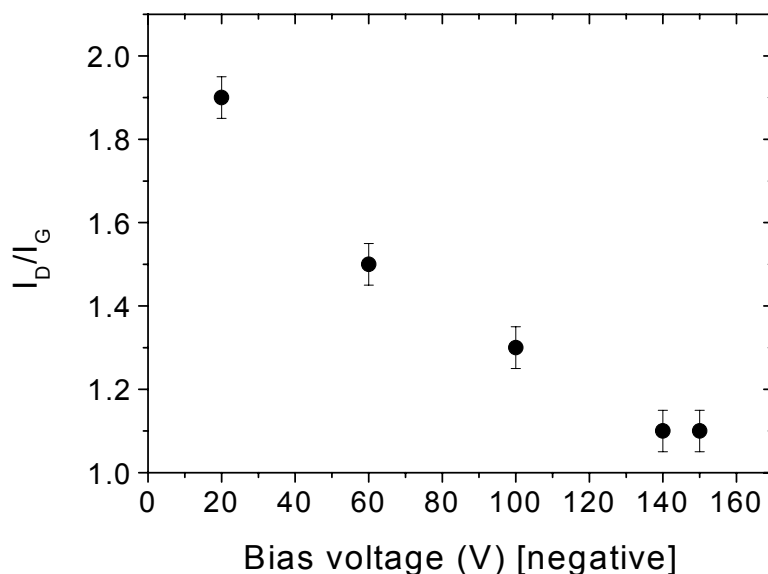


Figure 4.14.  $I_D/I_G$  ratios obtained from Raman spectra as a function of negative bias voltage: higher bias voltage results in lower  $I_D/I_G$  ratio

At bias voltage of -20 V, the  $I_D/I_G$  ratio was 1.9 and it decreased with increasing bias voltage. At -140 V bias, the  $I_D/I_G$  ratio reached 1.1 and it did not decrease with further increase of bias voltage. This indicates an increase of  $sp^3$  fraction in the DLC coating with increasing ion energy (here, in terms of negative bias voltage). The mechanism, which leads to the high  $sp^3$  fraction of highly biased coatings, is ion impingement (as discussed in section 4.5.1) and re-sputtering of carbon atoms from the graphite clusters. At high RF bias voltage, re-sputtering is significant (which causes a considerable decrease in deposition rate). As mentioned in chapter 2, the bonds of carbon atoms in the graphite structure are weak. Therefore, the carbon atoms in graphite clusters are easily dislodged. Consequently, the formation of graphite clusters in the coating is hindered. However, a

maximum  $sp^3$  fraction can only be obtained on a certain range of energy thus a certain range of bias voltage. Excess energy (in this case, when bias voltage of higher than -140 V is applied) does not result in a higher  $sp^3$  fraction in the coating. Understandably, excessive energy produces much heat in the coating. High temperature promotes graphitization, which results in a decrease of the  $sp^3$  fraction in the coating. This observation is consistent with previous work, which indicated that there is an “energy window” for carbon ions, which results in a maximum  $sp^3$  fraction in the DLC coating. When the energy exceeds this window, the  $sp^3$  fraction decreases. However, it should be noted that this window is not narrow, with optimum energies reported from 30 to 300 eV as seen from Figure 4.15. The discrepancies are due to the measurement technique and the deposition system (which influences the energy distribution of the carbon species, the incident angle of carbon ions, and the deposition rate of the DLC coating).

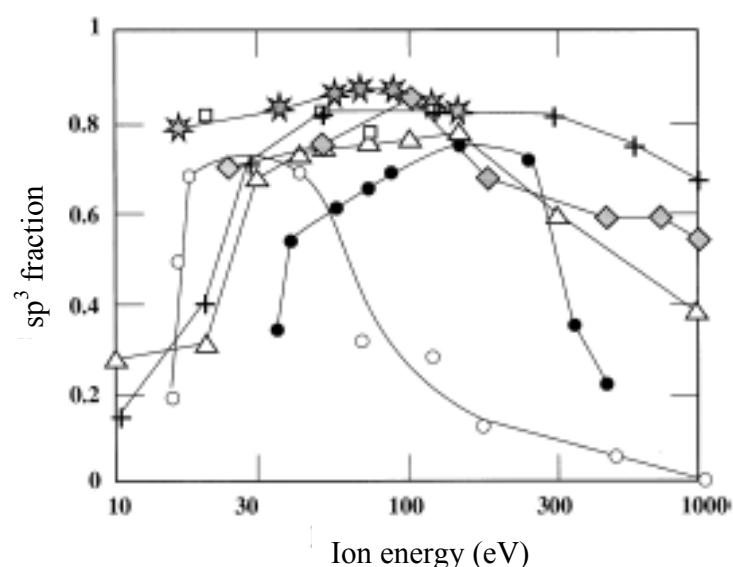


Figure 4.15.  $sp^3$  fraction as a function of energy of carbon deposited at room temperature as reported by several authors (The data was collected and drawn by Lifshitz [13])

### 4.5.3. Hardness and residual stress of DLC coatings

#### 4.5.3.1. Hardness

For hardness tests, coatings were deposited on Si [100] wafers to reach a thickness of 1.2  $\mu\text{m}$ . In order to reduce substrate effects, the indentation depth was set below 120 nm (10 % of the coating thickness). A high hardness is obtained with DLC coatings containing high  $\text{sp}^3$  fractions. The hardness and Young's modulus of DLC coatings deposited at a power density of  $10.5 \text{ W/cm}^2$  under different bias voltage from -20 V to -150 V is plotted in Figure 4.16.

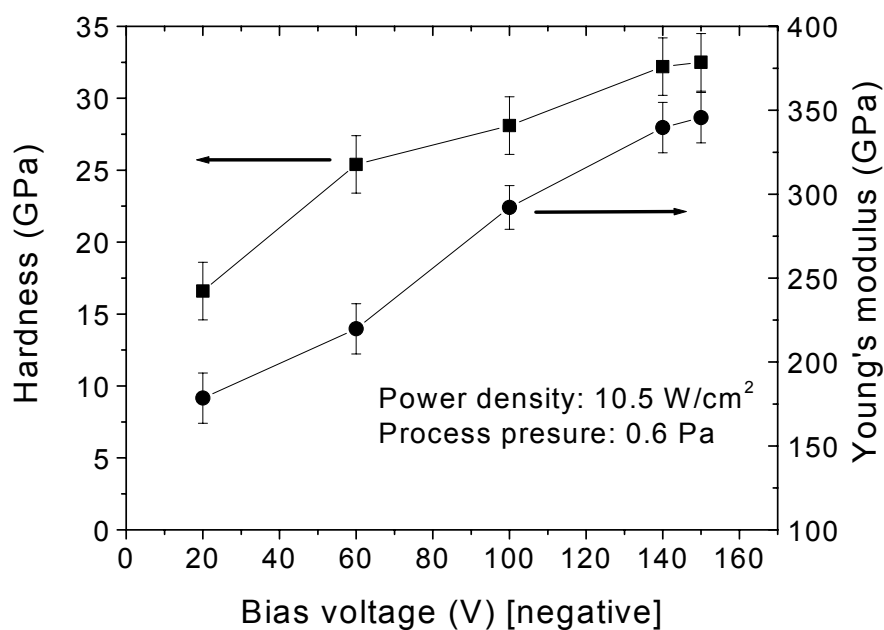


Figure 4.16. Hardness and Young's modulus of DLC coating as a function of negative bias voltage. As bias voltage increases, hardness and Young's modulus increase as a result of increase in  $\text{sp}^3$  fraction

The hardness and Young's modulus increased from 16.6 to 32.2 GPa and 178.5 to 345.6 GPa, respectively, as the bias voltage increased from -20 to -140 V. After that, further increase of bias voltage did not result in any significant increase in the hardness and Young's modulus. This is consistent with the observation of the  $sp^3$  fraction from the Raman results (c.f., Figure 4.14).

The hardness is also dependent on the process pressure. It directly relates to the ion energy as mentioned in equation 4.5. Higher process pressure leads to lower energy for the incoming carbon ions or atoms due to the decrease of the mean free path  $\lambda$ , which results in more collisions between the carbon and argon ions. This leads to a rougher surface morphology (c.f., Figure 4.11) and lower  $sp^3$  fraction and thus lower hardness. Another reason causing the decrease of hardness as increasing process pressure is the increase in the amount of absorbed gas at the boundaries of clusters leading to imperfect interconnection. Note that at low process pressure, the energy, not only of the argon ions but also of the carbon atoms and ions is high and it is sufficient to remove the gas impurities, which bond weakly to the growing coating. The Ar composition, which was measured from the XPS spectrum of DLC coatings deposited under a power density of  $10.5 \text{ W/cm}^2$ , -20 V bias voltage with different process pressures, is shown in Figure 4. 17. The results agree with the above explanation. At process pressure of 0.2 Pa, a very small amount of Ar (0.3 at.%) is included in the DLC coating. The amount of Ar in the coating increased with increasing process pressure and as process pressure was increased to 1.8 Pa, the coating contained 3.2 at. % Ar.



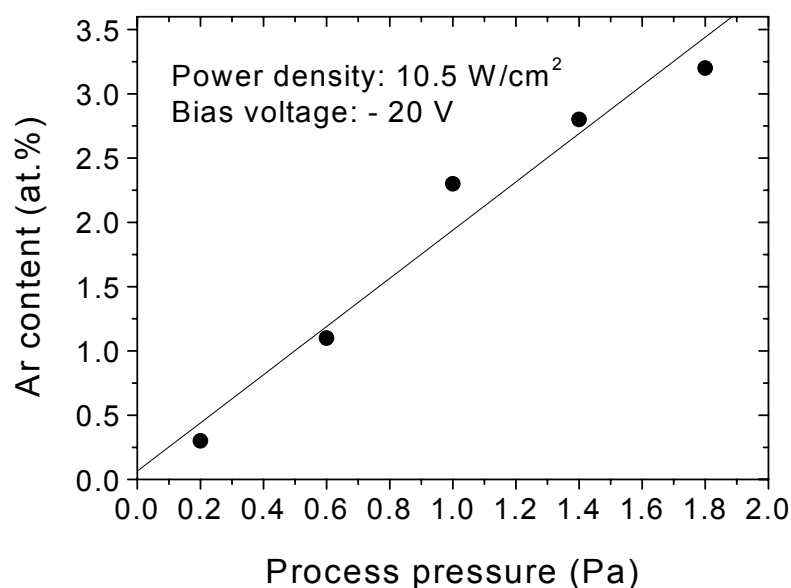


Figure 4.17. Ar content in the DLC coating as a function of process pressure. The Ar content increases linearly as process pressure increases

It should be noted that Ar contamination was not a problem with other PVD methods used to deposit DLC such as pulse laser deposition or cathodic vacuum arc since no Ar is used in these techniques. However, in magnetron sputtering, this aspect should be taken into account. A low  $sp^3$  fraction combined with a high amount of Ar contaminant resulted in low hardness DLC coatings deposited at high process pressures as seen from Figure 4.18, where the hardness and Young's modulus of DLC coatings deposited under -20 V bias at different process pressures is shown. As process pressure increased from 0.6 to 1.8 Pa, the hardness (and Young's modulus) of the DLC coatings decreased from 16.6 to 10.5 GPa (and from 178.5 to 120.2 GPa). The low hardness and Young's modulus of coatings

deposited under high process pressures do not allow such DLC coatings to be employed as protective material for engineering applications.

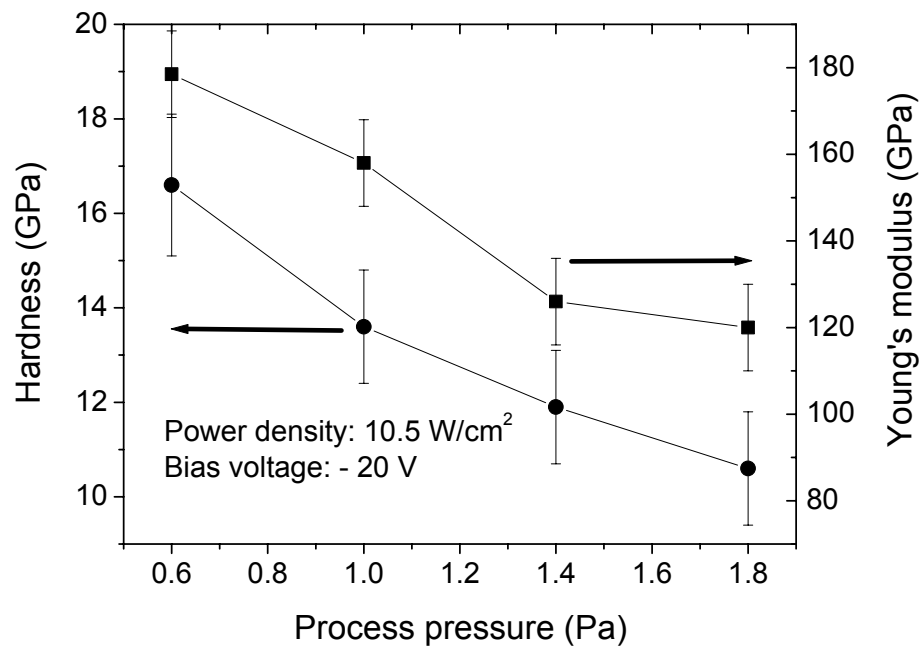
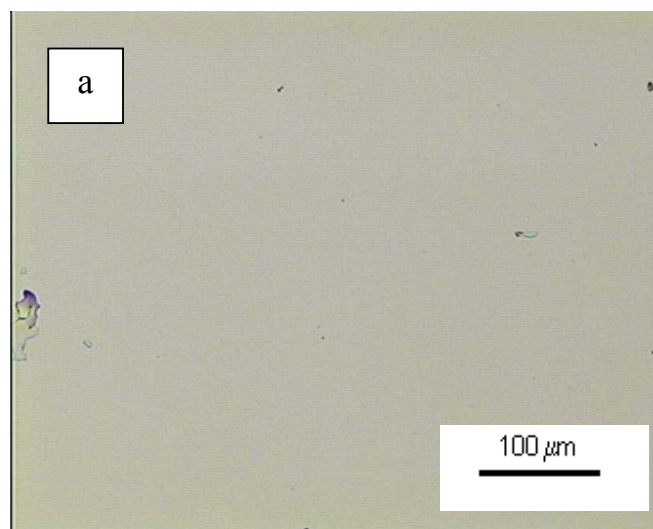


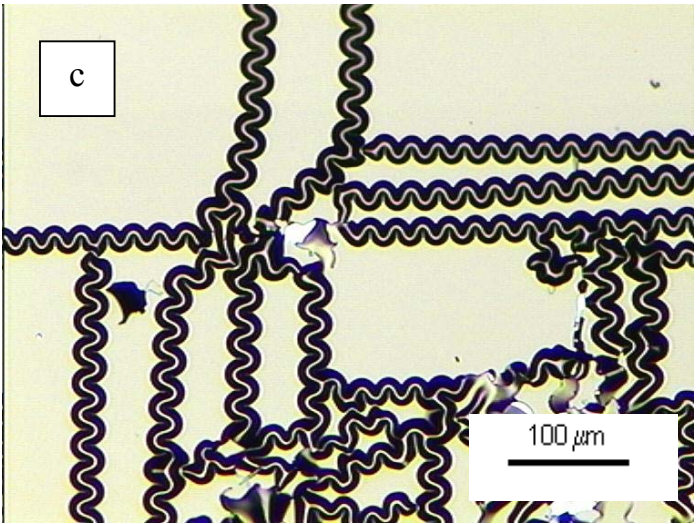
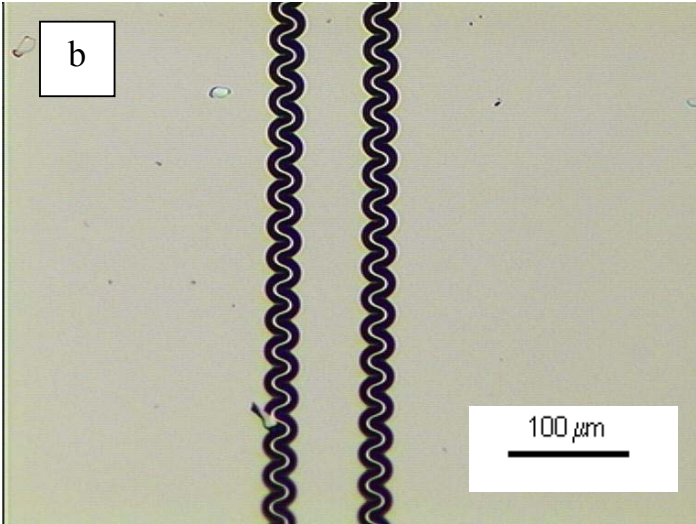
Figure 4.18. Hardness and Young's modulus of DLC coatings as a function of process pressure. The hardness and Young's modulus decreases as process pressure increases

#### 4.5.3.2. Residual stress

DLC coatings were deposited on non-heated substrates. The increase in substrate temperature is due to ion bombardment. For all DLC samples, the substrate temperature after deposition did not exceed 150 °C, therefore the thermal stress can be neglected. Also, the DLC coating is dense and chemically inert. Therefore, the post-deposition stress is negligible. With these considerations, the growth-induced stress (or intrinsic stress) is the main part contributing to the total residual stress in the coating. The energetic particle

bombardment of the surface of the growing coating is the major factor affecting the compressive growth-induced stress. Condensing and bombarding particles introduce energy into the growing DLC coating. The energy accumulates in a volume of the coating and its amount increases with increasing coating thickness. Therefore, for a given residual stress and coating-substrate bonding, there is a maximum coating thickness that can ensure the adhesion of coating and substrate. Exceeding this thickness, the residual stress in the coating will be relieved resulting in coating peeling off. Figure 4.19 (a) shows the optical micrograph (14 days after deposition) of 1.2  $\mu\text{m}$  DLC coating deposited on a Si wafer under a power density of  $10.5 \text{ W/cm}^2$  and -150 V bias. No indication of peeling was visually observed. However, a 1.5  $\mu\text{m}$  thick DLC deposited under the same deposition conditions self-destroyed due to high residual stress as seen from Figure 4.19 (b, c, d, e) (laboratory condition:  $22^\circ\text{C}$ , 70 % humidity)





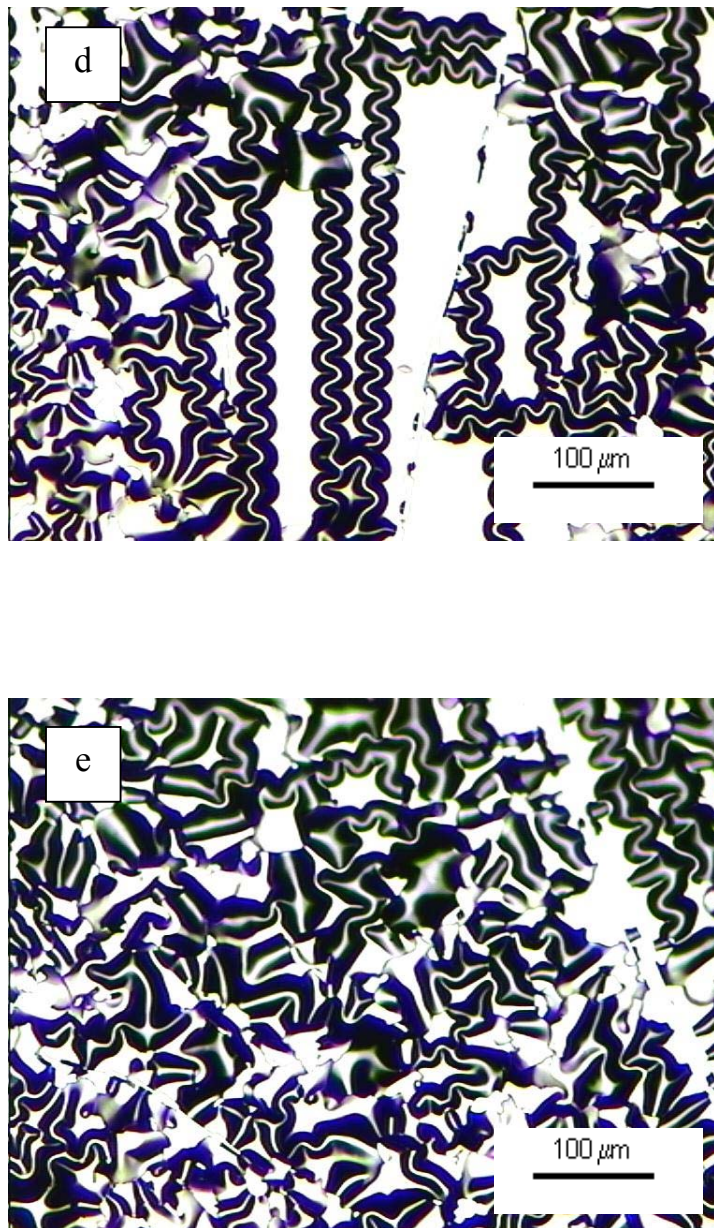


Figure 4.19. Surface of 1.2  $\mu\text{m}$  DLC coating (14 days after deposition), no sign of damage was observed (a). The self-destruction of a 1.5  $\mu\text{m}$  DLC coating deposited on a Si wafer due to high residual stress: (b) just after unloading from the chamber (c) after 15 minutes (d) after 30 minutes and (e) after 120 minutes

Stress relief began after exposure of the coating to ambient air with the formation of buckling lines of sinusoidal shape. These waves spread quickly from the outer edge of the coating to the interior. They may cut or join each other causing catastrophic destruction of the whole coating within 120 minutes. The humidity strongly accelerated the wave spreading (stress relaxation) of the coating since the moisture broke into the buckling channels and facilitated coating-substrate debonding. At a humidity of 10 % (in the desiccator), the coating was totally damaged after 8 hours.

The sinusoidal shape of the buckling lines can be explained by the theory of buckling of shells [143]. In brief, the coating is treated as a thin plate attached to the substrate by adhesive forces. The equation of buckling is determined as following:

$$I \left( \frac{\partial^4 w}{\partial x^4} + 2 \frac{\partial^4 w}{\partial x^2 \partial y^2} + \frac{\partial^4 w}{\partial y^4} \right) + \sigma_x t \frac{\partial^2 w}{\partial x^2} + \sigma_y t \frac{\partial^2 w}{\partial y^2} + 2 \tau_{xy} t \frac{\partial^2 w}{\partial x \partial y} + f = 0 \quad (4.6)$$

where

I- moment of inertia of the coating

t- coating thickness

x, y, z- coordinates relative to the substrate

u, v, w- coating coordinates as defined in the elastic theory

$\sigma_x$ ,  $\sigma_y$ - compressive stresses

$\tau_{xy}$ - shear stress

f- external force



The solution of equation 4.6 has a physical meaning as the deflection of the coating from the substrate in the normal direction. It is described as:

$$w = 1 + \cos(kx + qy) \quad (4.7)$$

The solution implies that the maximum displacement of the ridge formed by the coating buckling is along a straight line given by:

$$kx + qy = 2n\pi, n = 0, \pm 1, \pm 2, \dots \quad (4.8)$$

The solution consists of two families of parallel ridges crossing each other as described by equation 4.8. Once the buckling process begins, it proceeds in a certain direction, when it reaches a point where ridges cross each other, it will turn in the direction as shown in Figure 4.20.

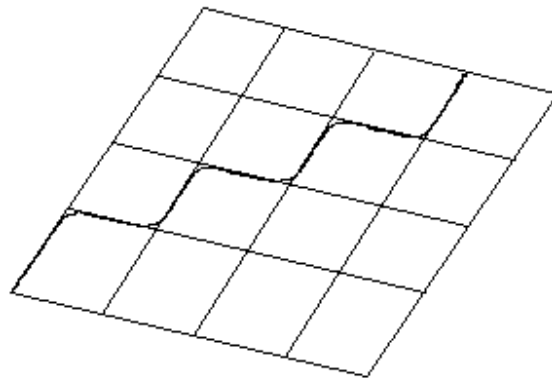


Figure 4.20. Illustration of stress relaxation style

The growth-induced stress is strongly dependent on the energy of the ions or atoms bombarding the substrate. Windischmann [144] proposed a model used to calculate the growth-induced stress based on three assumptions: (1) The bombardment of atoms and ions on the coating surface causes displacement of atoms in the coating from their equilibrium positions through a series of primary and recoil collisions, which produces volumetric distortion. (2) The mass transport and defect mobility is sufficiently low to freeze the volumetric distortion in place. (3) The relative volumetric distortion, which corresponds to the strain, is proportional to the fractional number of atoms displaced from equilibrium positions. The growth-induced stress,  $\sigma_i$ , is calculated from the following formula:

$$\sigma_i = \left[ \frac{E_c M_c}{(1 - \nu_c) D_c} \right] 4.79 \left( \frac{K \Phi_p}{N_A} \right) \delta \sqrt{E_p} = k Q \Phi_p \sqrt{E_p} \quad (4.9)$$

where

$\Phi_p$  and  $E_p$  - the flux (particles/cm<sup>2</sup>) and kinetic energy (eV) of energetic particles, respectively

$E_c$  - Young's modulus of the coating

$N_A$  - Avogadro's number,  $N_A = 6.022 \times 10^{23}$  atoms/mol

$M_c$  - Mass of coating atoms

$D_c$  - Density of coating

$K$  - Proportionality factor



$\delta$  - The factor depends on the cohesive energy of atoms in the coating ( $U_0$ ),  $M_c$ , and atomic number ( $Z_c$ )

The constant  $k = 4.79K \frac{\delta}{N_A}$ , and  $Q = \left( \frac{E_c}{1 - \nu_c} \right) \frac{M_c}{D_c}$

From equation 4.9, it can be seen that the growth-induced stress is proportional to the square root of the energy of particles bombarding the growing coating. Therefore the stress is proportional to the square root of the negative bias voltage applied to the substrate (c.f., equations 4.5 and 4.9). Figure 4.21 plots the measured stresses as a function of negative bias voltage (the dotted line is the fitted curve).

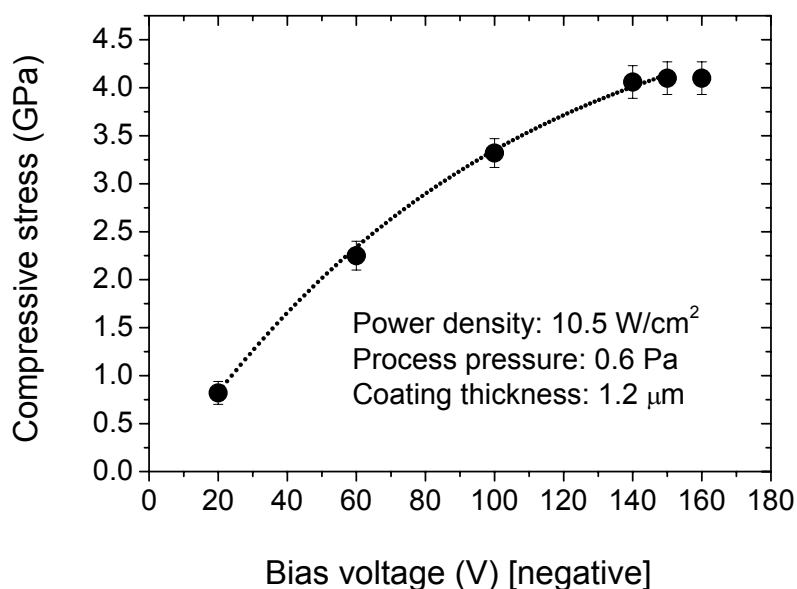


Figure 4.21. Compressive residual stress in DLC coatings as a function of negative bias voltage

As seen from the figure, the higher the bias voltage applied, the higher the residual stress. At -20 V bias, the residual stress was about 0.82 GPa. It increased to 4.1 GPa as bias voltage was increased to -140 V. The fitted curve indicates a square root relationship between bias voltage and residual stress in the coating (in the range of bias voltages from -20 to -140 V). As bias voltage exceeded -140 V, the residual stress did not change significantly. It is clear that the experimental data agrees well with the model proposed by Windischmann. However, this model is valid with bias voltages lower than -140 V only. Understandably, a high applied bias voltage results in a high energy of bombarding particles. However, when the energy is very high, formation of thermal spikes [145] reduces the stress by causing relaxation of the implanted atoms. The formation of graphite clusters therefore is enhanced. This agrees with the observation of the relationship between the  $I_D/I_G$  ratio and negative bias voltage (c.f., Figure 4.14) which indicates that at bias voltages higher than -140 V the  $I_D/I_G$  ratio does not increase any more.

#### 4.5.4. Adhesion strength

The adhesion strength of DLC is always a weak point of this coating. Low adhesion strength arises from two sources: (1) high residual stress and (2) low toughness. The influence of a high residual stress on the adhesion of DLC coatings to the substrate has been discussed in section 4.5.3.2. The stress relaxation weakens the adhesion and supports the peeling off. The low toughness (lack of plasticity) results in a brittle fracture of the coatings due to crack propagation even at low applied loads. In this section, the adhesion strength of DLC coatings deposited on steel substrates is investigated. The coatings were deposited at a power density of  $10.5 \text{ W/cm}^2$  and process pressure of 0.6 Pa. The thickness of the coatings was about  $1.2 \text{ }\mu\text{m}$ . The low critical load obtained from the

tests is plotted in Figure 4.22. For easier reference, the residual stress is also plotted on this figure. The adhesion strength (in terms of critical load) decreased with increasing bias voltage. It can be seen that the residual stress plays an important role in the adhesion strength. The coating deposited under -20 V bias had the residual stress of 0.82 GPa and the critical load was 320 mN. When the bias voltage was increased to -140 V, the residual stress increased to high value of 4.1 GPa and critical load decreased to a very low value of 118 mN.

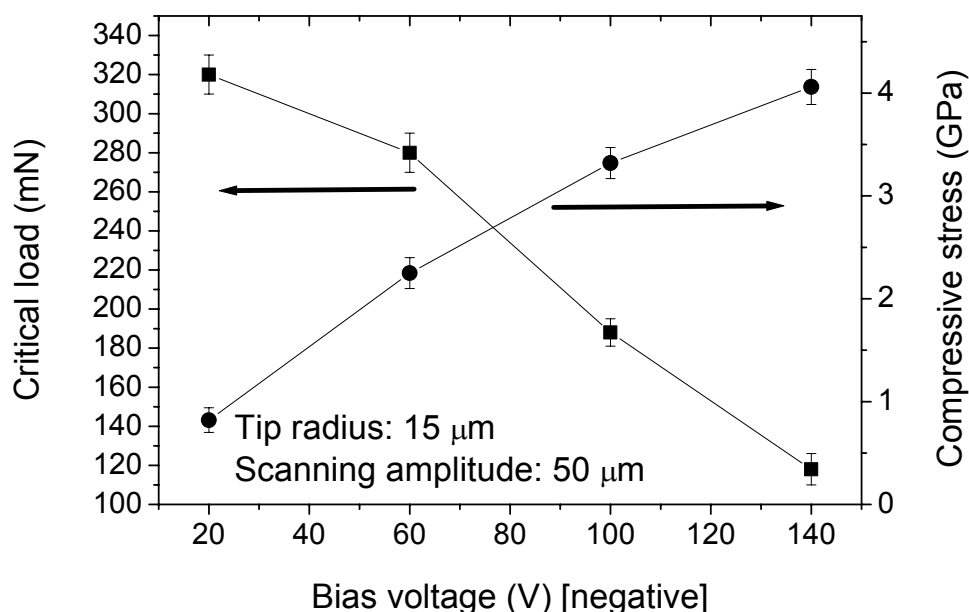
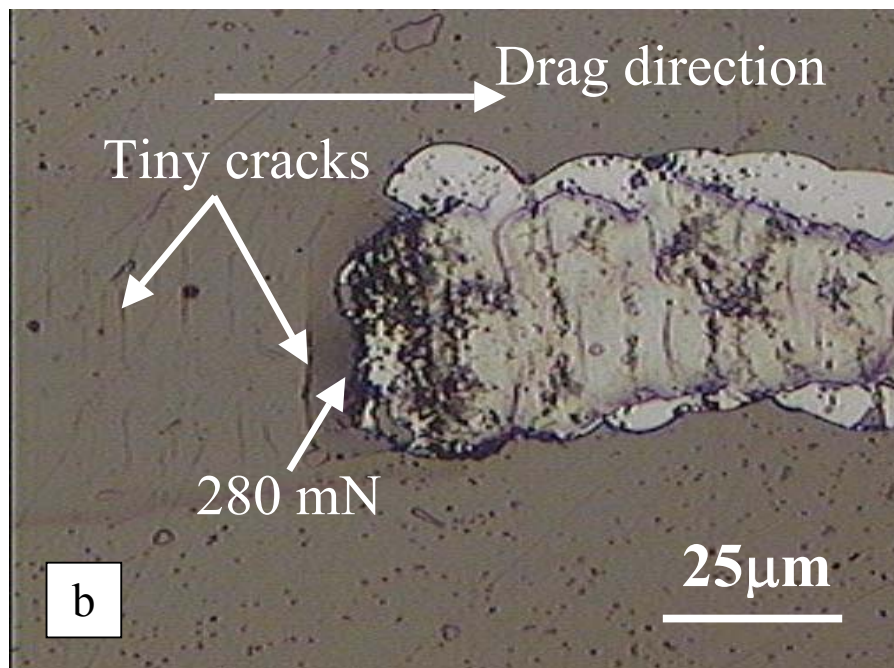
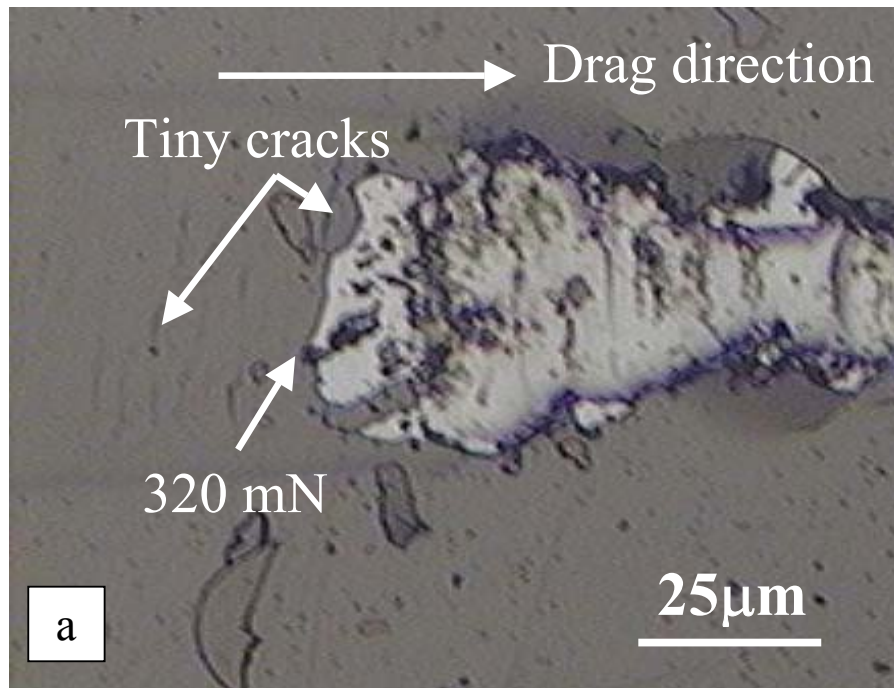


Figure 4.22. Influence of negative bias voltage on the critical load from scratch tests. The critical load decreases and the stress increases as bias voltage increases

The optical images of the scratches on the coatings after the tests are shown in Figure 4.23.



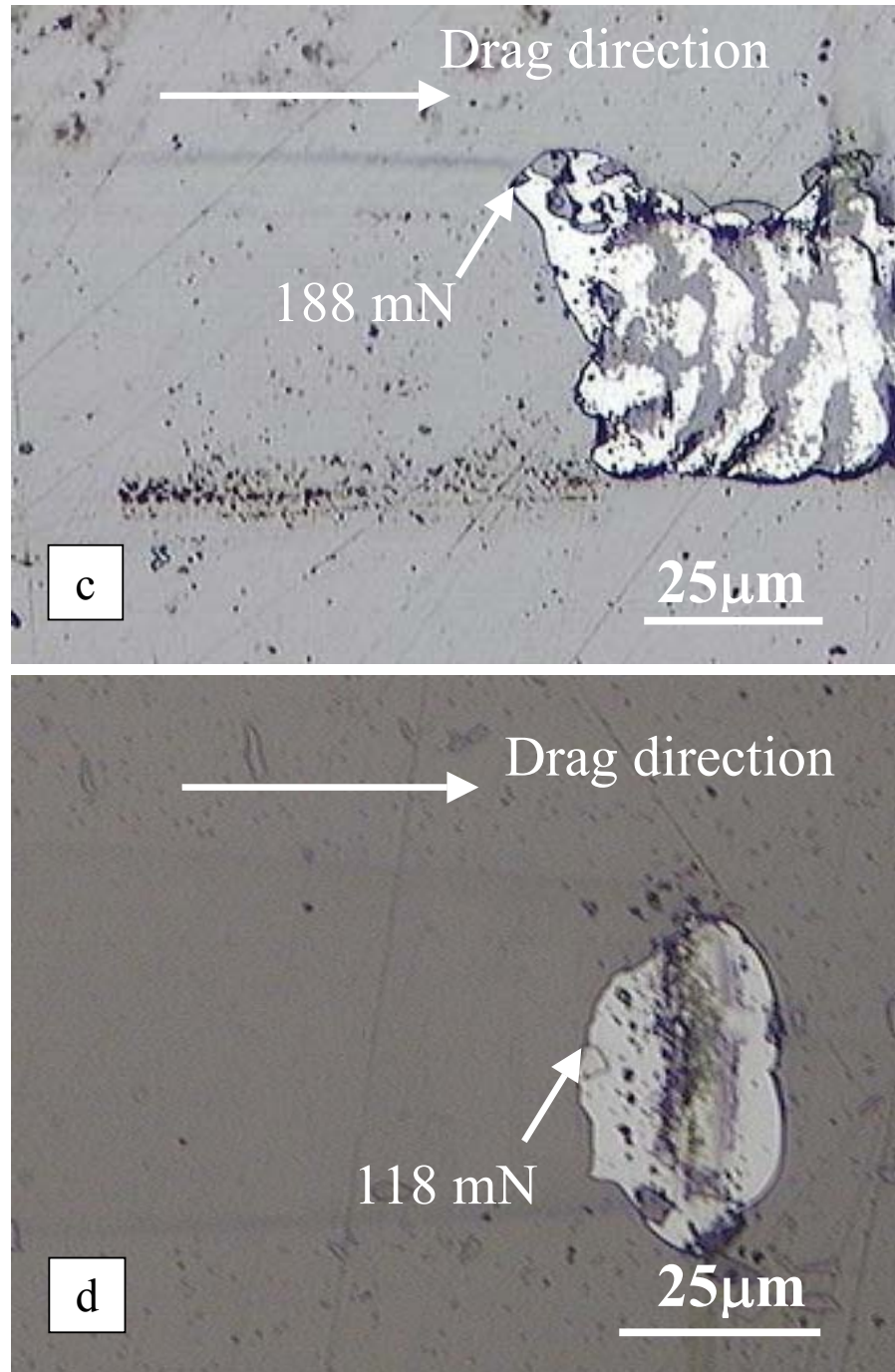


Figure 4.23. Scratches on 1.2  $\mu\text{m}$  DLC coatings deposited at a power density of 10.5  $\text{W}/\text{cm}^2$ , process pressure of 0.4 Pa under different bias voltages: (a) -20 V, (b) -60 V, (c) -100 V, and (d) -140 V. The tiny cracks are seen before the damage on coatings deposited under low bias voltages (-20 V and -60 V)

For all coatings, the low critical load (the load at which the damage starts to occur) and high critical load (the load at which the coating is totally damaged) were not distinguishable. As the load reached a certain value, the coating was totally damaged. However, before total damage, some tiny cracks were observed on the DLC coatings deposited under -20 and -60 V bias. With coatings deposited under -100 and -140 V bias, no cracks were seen along the scratch track, then all of a sudden, complete failure of the coating occurred. DLC coatings deposited under high bias voltages showed a typical type of brittle fracture: as the cracks are formed under a certain applied load, they will quickly propagate with the energy supported from stress relaxation causing catastrophic damage of the coating.

#### **4.6. Tribological properties of magnetron sputtered DLC coatings**

Figure 4.24 shows the coefficient of friction of DLC coatings deposited at a power density of  $10.5 \text{ W/cm}^2$ , process pressure of 0.6 Pa with various bias voltages (from -20 to -140 V) when sliding against an alumina counterpart. The tests were carried out in ambient air (22 °C, 75 % humidity). The applied load was 5 N and rotation radius was 16 mm. A sliding distance of 1 Km (corresponding to 9952 laps) was set. At the beginning of the tests (several tens of meters of sliding), the coefficient of friction of all coating reduced. This is due to a thin graphite-rich layer, which always exists on the surface of DLC coatings. In humid air, this layer absorbs the moisture and becomes a good lubricant. With time, more moisture was absorbed leading to a decrease in the coefficient of friction. However, after a short time this layer was removed and the coefficient of friction started to increase due to the surface-surface contact and the formation of wear particles, which came from both the DLC coating and the alumina counterpart. Coatings deposited under higher bias voltage



exhibited lower coefficients of friction due to a smoother surface. However, as the sliding distance became higher, coatings deposited under lower bias voltage exhibited lower coefficient of friction. Since the  $sp^2$  content in the coatings deposited under low bias voltage was higher, more graphite existed at the contact area. This combined with the graphite produced from the graphitization resulted in more lubricant at the contact area. The formation of more solid lubricant (as compared to that of coatings deposited under higher bias voltage) compensated for the effects of surface roughness and a net low coefficient of friction was obtained. It should be noted that the graphite-rich layer is formed only after a certain sliding distance depending on the structure of the DLC coating (when other conditions are all the same). This conclusion is supported from the observation of the trend of these friction curves. The coefficient of friction of coatings prepared at lower bias voltages (-20 V and -60 V) became stable (0.09 for coating deposited under -20 V bias and 0.1 for that under -60 V bias) after about 0.6 Km of sliding. However, the coefficient of friction of the coatings deposited under -100 and -140 V still increased even after 1 Km sliding. To see how much it can go, further sliding was undertaken for the -140 V coating by increasing the sliding distance to 2.5 Km (corresponding to 24880 laps). In this case, the coefficient of friction reached a maximum of about 0.14 at about 1.1 Km of sliding distance and then decreased and leveled off at a value of 0.12 after 1.7 Km sliding as seen from Figure 4.25.

It can be seen that, graphitization, which leads to the formation of a graphite-rich layer between the two surfaces, governs the tribological behavior of DLC coatings in dry tribotests. The graphite-rich layer not only gives the friction couple more lubricant but also reduces the generation of hard particles. Therefore, after a certain sliding distance, the

formation of the graphite-rich layer stops the increase in the coefficient of friction. The graphitization is the consequence of repeatedly applying compression (before the ball contact) and tension (after the ball contact) to the subsurface areas in the wear track. Therefore the graphitization rate increases with rotation laps.

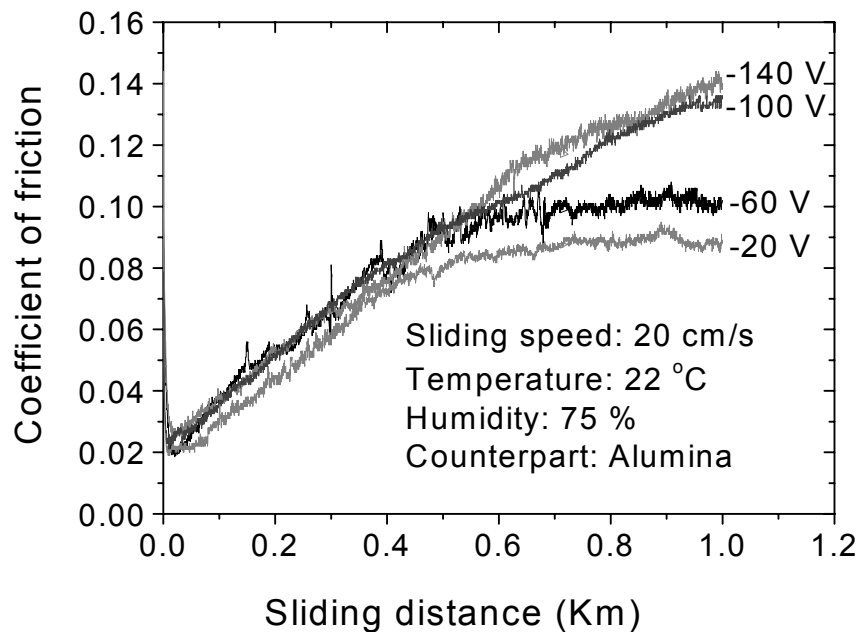


Figure 4.24. Coefficient of friction as a function of sliding distance with DLC coatings deposited under different bias voltages (counterpart is alumina)

In order to see the influence of rotation laps on the graphitization, the rotation radius was decreased to 8 mm and the same sliding distance was set (2.5 Km, corresponding to 49760 laps) (c.f., Figure 4.25). When the sliding distance was lower than 0.6 Km, the coefficient of friction was higher for the case of a lower rotation radius. Understandably, more contact frequency results in more wear particles at the contact leading to a higher



coefficient of friction. When the graphite-rich lubrication layer was formed, the surface-surface contact between the coating and the wearing counterpart was limited, less particles were produced and surface adhesion was reduced, which all led to a decrease in the coefficient of friction to a low and stable value. After about 0.6 Km sliding (corresponding to 11942 laps at 8 mm of rotation radius and 5971 laps at 16 mm of rotation radius), the coefficient of friction in the test with a lower rotation radius did not increase anymore and leveled off at about 0.11. With the higher rotation radius, less contact frequency between coating and counterpart resulted in a later formation of the graphite-rich layer. Therefore, the coefficient of friction still increased, reached a maximum value of 0.14 at about 1.1 Km and then decreased and became stable at a value of 0.12 after about 1.7 Km sliding.

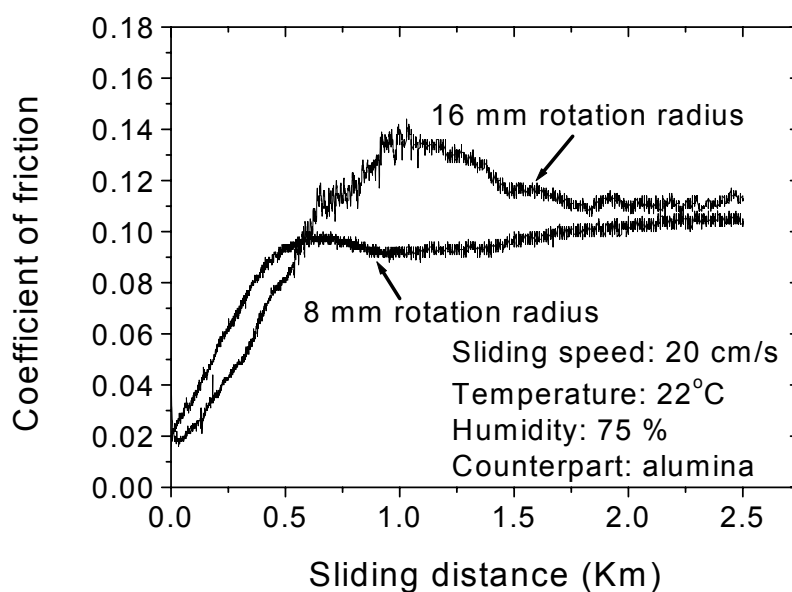


Figure 4.25. Coefficient of friction as a function of sliding distance of DLC coating deposited under -140 V bias (with rotation radius of 16 mm and 8 mm)

The influence of applied load on graphitization thus on the coefficient of friction is shown in Figure 4.26 where the coating deposited under -140 V bias was tested under applied loads of 5 and 10 N. The rotation radius was set at 8 mm. At an applied load of 10 N, the coefficient of friction was a little bit higher for the first 200 m of sliding owing to a larger number of hard particles being generated. After that, it became lower compared to that found for a load of 5 N. After 1 Km sliding, it leveled off at about 0.1, which was lower than that of the 5 N case (0.11). The higher rate of graphitization at high applied loads resulted in the lower coefficient of friction observed in the test with a load of 10 N.

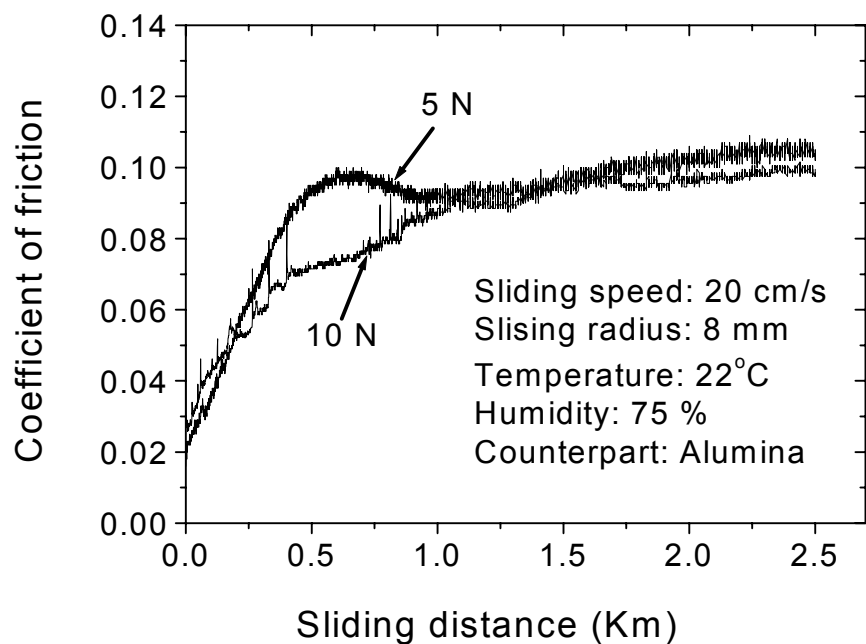


Figure 4.26. Coefficient of friction as a function of sliding distance of DLC coating deposited under -140 V bias (with applied loads of 5 and 10 N)

After tribotests, the debris was always observed on the wear scar on the ball. Figure 4.27 shows the wear track on the coating and wear scar with debris accumulated on the alumina ball after 2.5 Km sliding against a DLC coating deposited under -140 V.

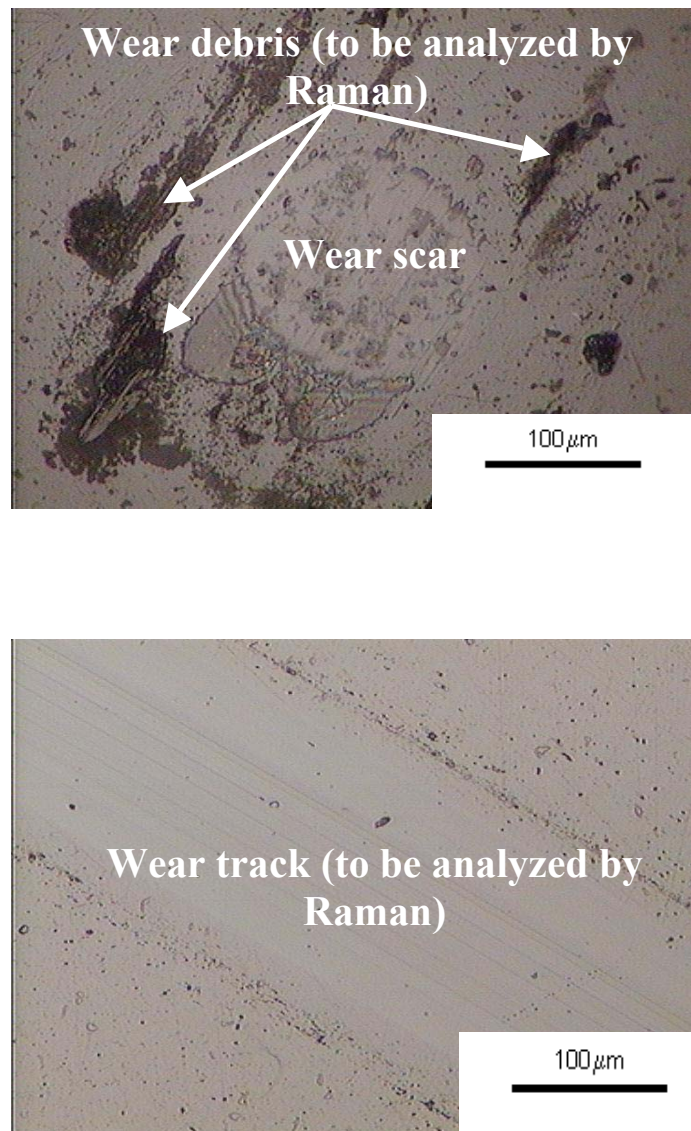


Figure 4.27. Wear scar with debris accumulated on the alumina ball and wear track on the DLC coating after a 2.5 Km tribotest

From the figure, a noticeable scar was seen on the ball with wear debris surrounding it. Raman spectra taken from the wear track on the DLC coating and wear debris in comparison with that of the DLC coating are shown in Figure 4.28.

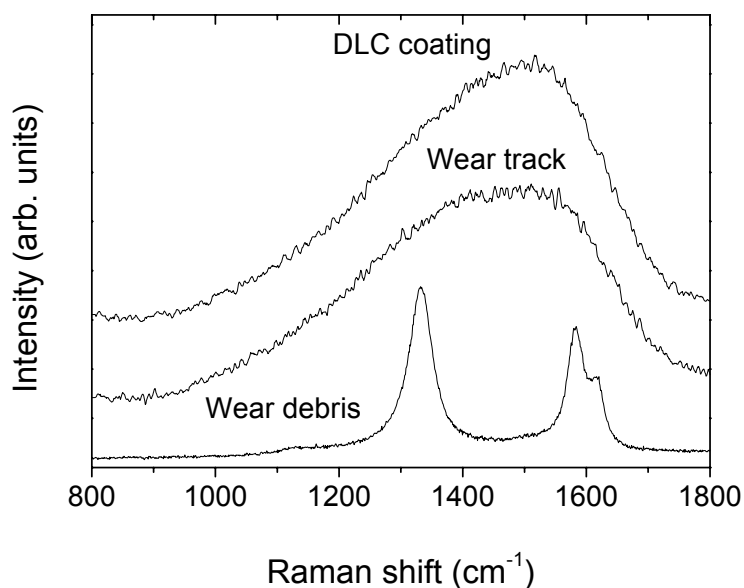


Figure 4.28. Comparison of Raman spectra of as deposited DLC coating, wear track, and wear debris

The transformation of the coating structure from amorphous DLC to polycrystalline graphite in the wear debris can be observed by following the increase in the band width and the intensity of the Raman scattering near  $1580\text{ cm}^{-1}$ . A notable increase in the G (graphite) band of the Raman taken inside the wear track indicated the  $\text{sp}^3$  to  $\text{sp}^2$  phase transition occurring at the friction contacts on the DLC coating surface. From the visual observation and the Raman analysis of the wear track and wear scar, it was clear that

graphite-like ( $sp^2$ ) was formed in the contact area between the DLC coating and the counterpart. This phase had low shear strength and was easily removed from the surface of DLC coating under stresses developed during the friction contact. The volume of the  $sp^2$  phase removed was small and some adhered to the surface of the ball forming a lubricious transfer layer. Larger volumes of the  $sp^2$  phase, which was produced as wear debris, were pushed to the side of the track and the scar. The structure of this debris was similar to that of polycrystalline graphite. Figure 4.29 presents a schematic of how this process may take place.

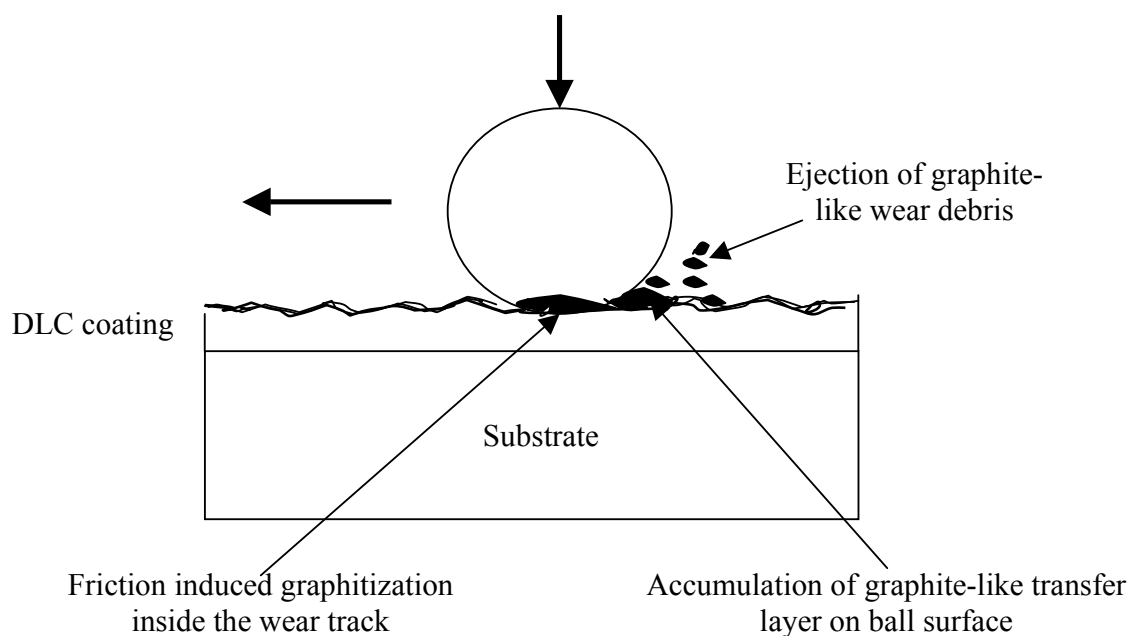


Figure 4.29. Schematic explanation of the formation of the graphite-like structure and the transfer layer accumulation observed after the wear test

Tribotests with 100Cr6 steel counterparts were also carried out in ambient air (22 °C and 75 % humidity). The rotation radius and sliding distance was set at 16 mm and 1 Km, respectively. The coefficient of frictions of DLC coatings when sliding against steel ball are shown in Figure 4.30. The same trend was seen when compared to the tribotests with the alumina counterparts (c.f., Figure 4.24): at the beginning of the tests (several tens of meters of sliding distance) the coefficient of friction decreases then starts increasing and after a certain sliding distance, it becomes stable. The stable value of coefficient of friction was lower with the coating deposited under lower bias voltage. Under the same test condition, the coefficient of friction (both starting value and stable value) was higher when steel was used as the counterpart.

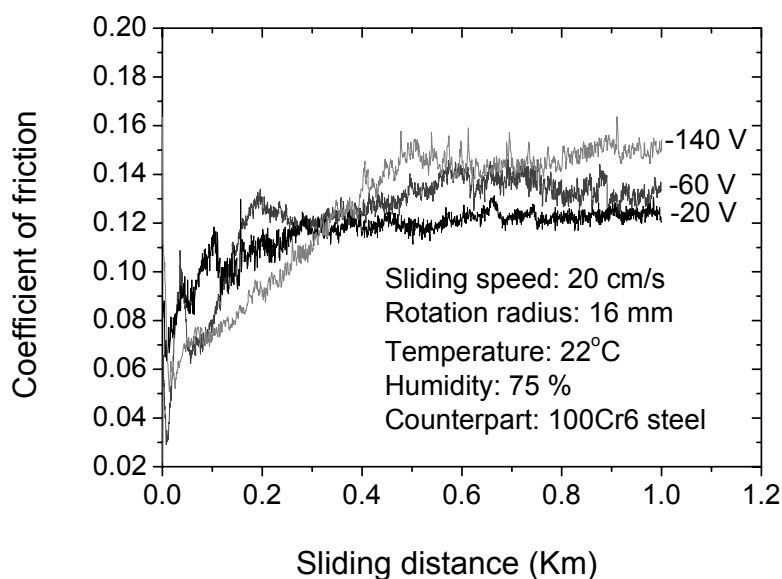
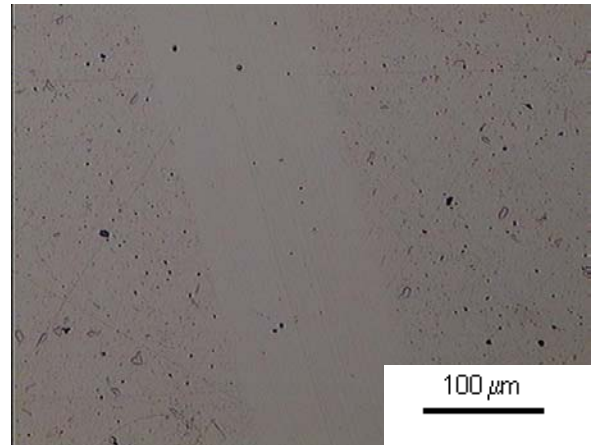
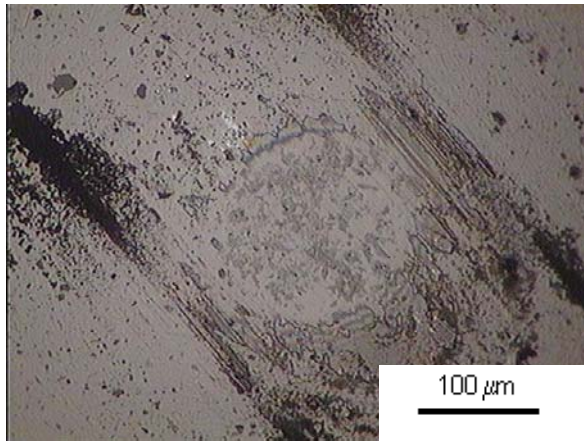


Figure 4.30. Coefficient of friction as a function of sliding distance of DLC coatings deposited under different bias voltages (counterpart is 100Cr6 steel)

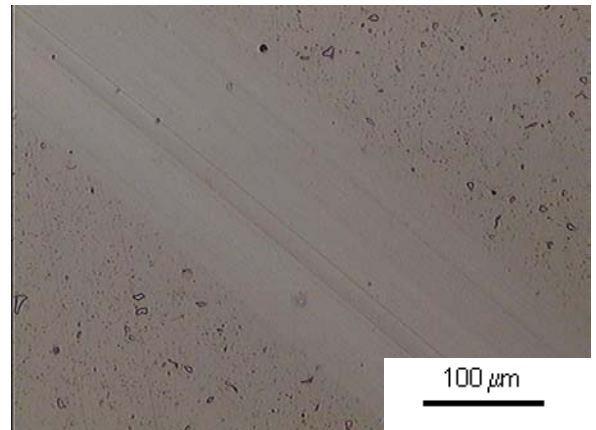
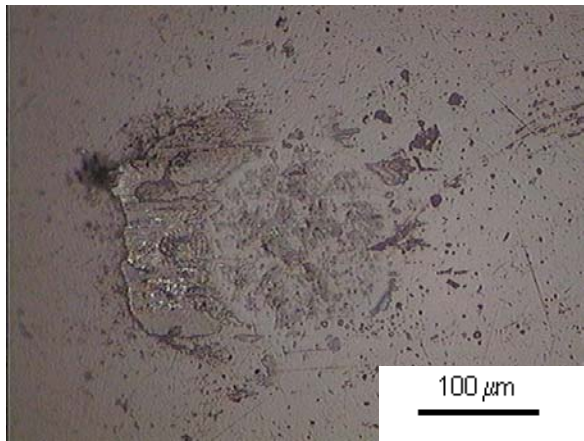
From Figures 4.24 and 4.30, the stable value of the coefficient of friction for coatings deposited at -20 V to -140 V varied from 0.09 to 0.14 with the alumina counterpart and it varied from 0.12 to 0.15 with the steel counterpart. This is related to the higher contact pressures present during sliding against the alumina. As discussed, higher contact pressure results in lower coefficient of friction for DLC coatings. The contact area is smaller for the alumina ball since the wear of alumina is less than that of steel (when comparing the wear scars from Figures 4.31 and 4.32). A smaller contact area at the same normal applied force results in a higher contact pressure, which leads to a lower friction. Another reason is the formation of an aluminum hydroxide layer during sliding against alumina ball [50] whereas iron oxide is formed during sliding against steel ball [146]. The aluminum hydroxide has lower shear strength compared to that of iron oxide. Also the amount of iron oxide is very high (high wear of the steel ball contributes more iron oxide to the contact area). These all resulted in the lower coefficient of friction observed when alumina was used as the counterpart.

After the tribotests with alumina and steel counterparts, no peeling off or spallation of any DLC coating was visually observed. Wear of the coating and counterpart was estimated from the wear scar and wear track after the tests. The scar (on the ball) and track (on the coating) after 1 Km sliding tribotests at a sliding speed of 20 cm/s are shown in Figure 4.31 (for alumina ball) and 4.32 (for steel ball).

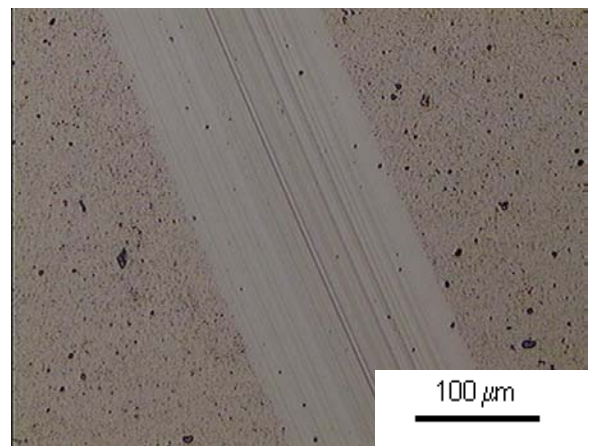
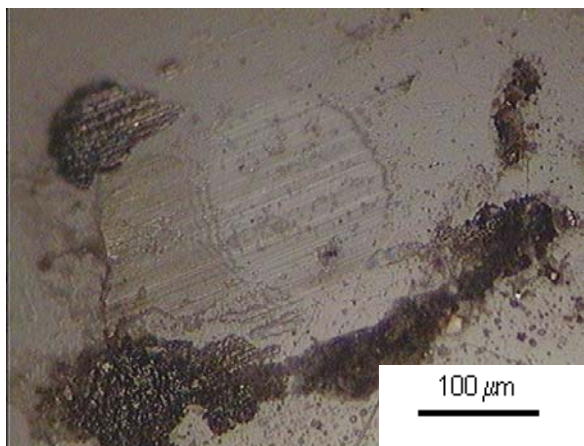




(a)

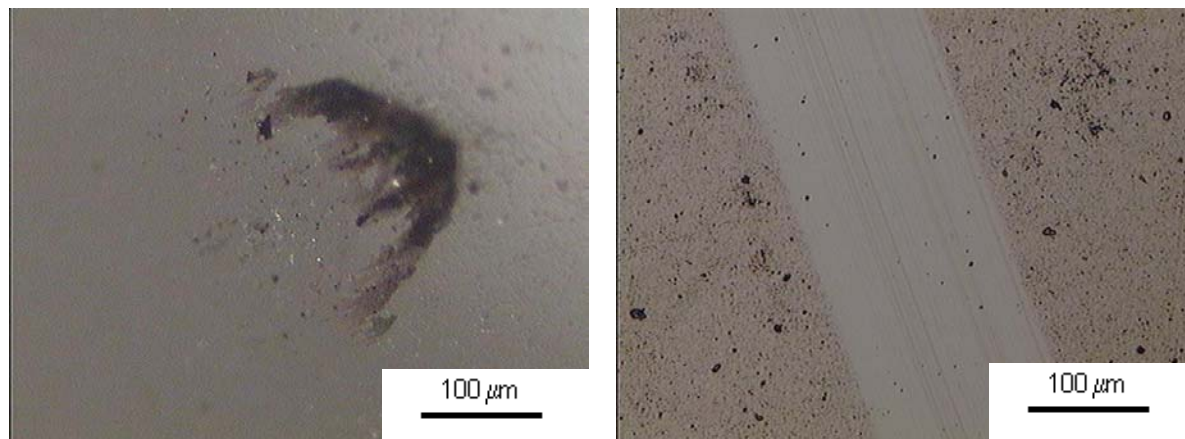


(b)



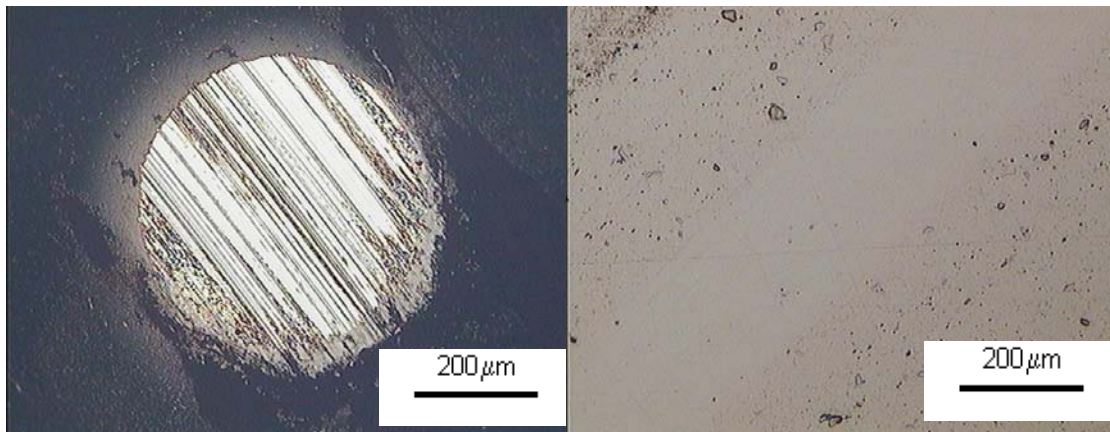
(c)



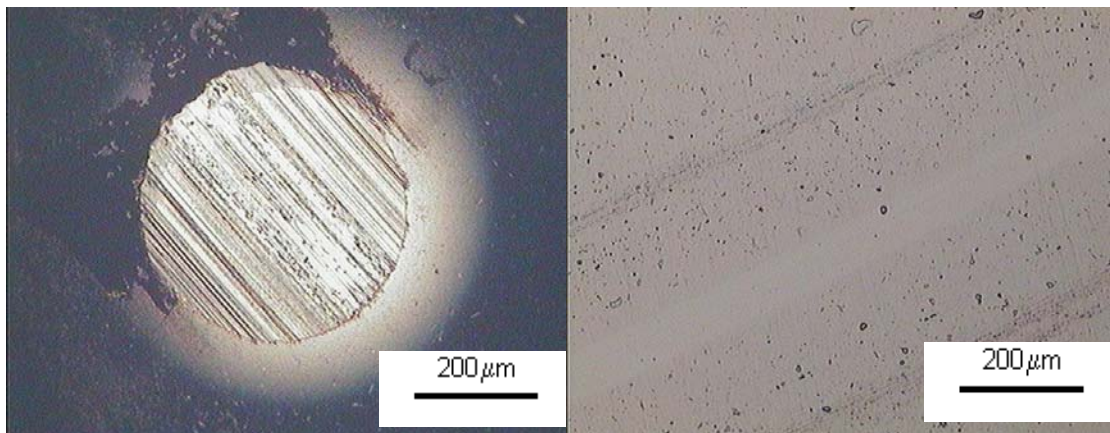


(d)

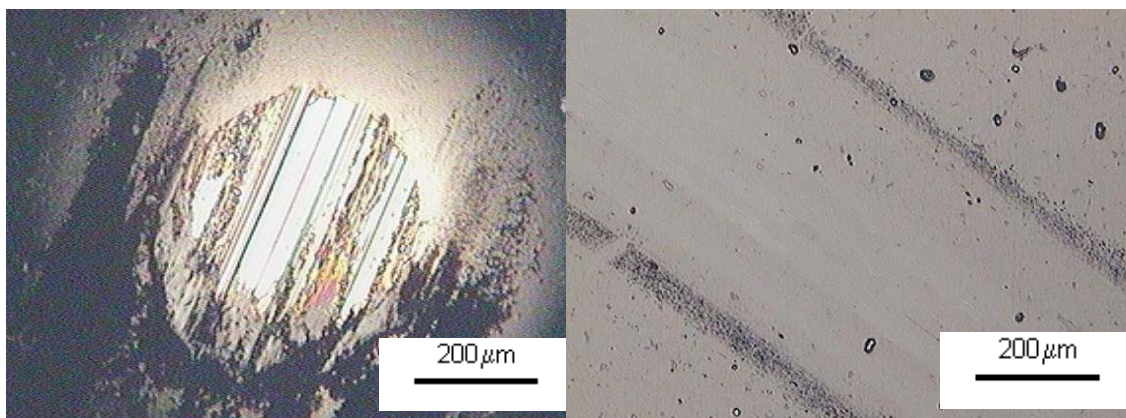
Figure 4.31. The wear scar (on the alumina ball) and wear track (on the coating) after tribotests (1 Km sliding, 16 mm rotation radius, sliding speed of 20 cm/s) for DLC coatings deposited at (a) -140 V (b) -100 V (c) - 60 V and (d) -20 V bias



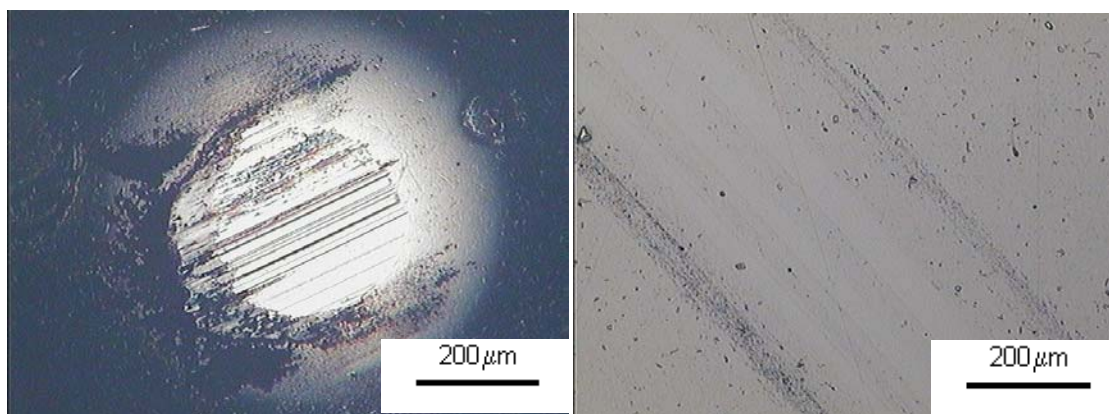
(a)



(b)



(c)



(d)

Figure 4.32. The wear scar (on the steel ball) and wear track (on the coating) after tribotests (1 Km sliding, 16 mm rotation radius, sliding speed of 20 cm/s) for DLC coatings deposited under (a) -140 V (b) -100 V (c) -60 V and (d) -20 V bias

It can be recognized that the wear scar on the ball is bigger when sliding against the DLC coating deposited under higher bias voltage. This is true with both the alumina and steel counterparts. The wear track on the coating, therefore, is wider in the case of coatings deposited at higher bias voltage. This indicates a higher wear rate of the counterpart when higher bias voltage is applied during deposition. With note that the magnification is higher in Figure 4.31, it can be easily recognized that the wear of the steel counterpart is much higher than that of the alumina after sliding against the same DLC coating with the same testing conditions and parameters. The quantitative evaluation of the wear rate (calculated using equation 2.3) of the balls is plotted in Figure 4.33. It can be seen that the wear rate of the steel counterpart is 40 - 50 times higher than that of the alumina. That is due to (1) the worse abrasive resistance (due to low hardness) of steel and (2) in the ambient air, the

corrosive wear of steel is much higher than that of alumina. Also, almost no scratches were seen on the wear track of the coatings after sliding against the steel counterpart whereas a lot of scratches were observed on the wear scar. These scratches indicated that the asperities of the DLC surface and the particles coming out from the coating ploughed into the soft surface of the steel and removed the material of the counterpart.

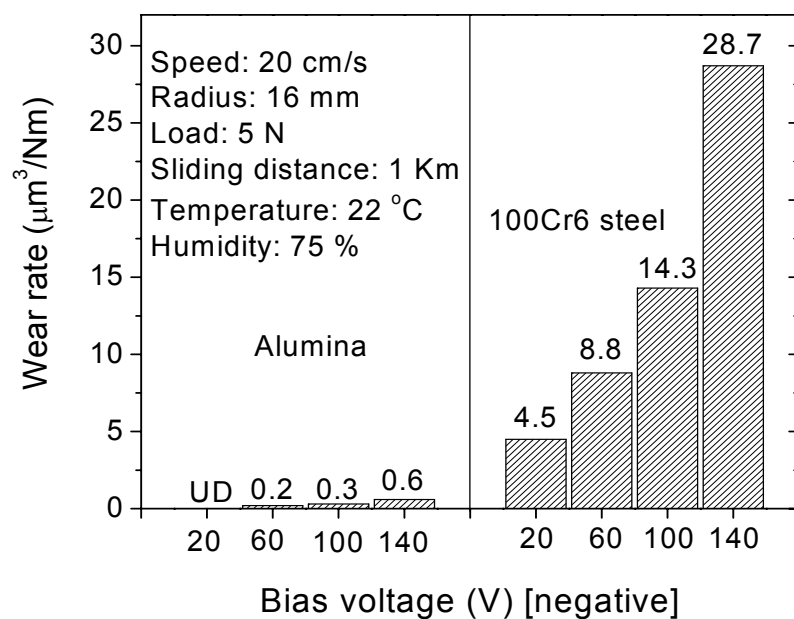


Figure 4.33. Wear rate of the alumina and 100Cr6 steel counterparts when sliding against DLC coatings deposited under different bias voltage (note: UD means undetectable)

The wear track profiles of DLC coatings sliding against an alumina counterpart are shown in Figure 4.34. Coatings deposited under higher bias voltage exhibited less wear. With coatings deposited at -140 V bias, very little wear was seen. The wear, in this case, can be considered as a smoothening of the surface roughness. This indicates very good wear



resistance of the coating, which mainly comes from the high hardness of about 32 GPa. In contrast, the coating deposited under low bias voltage (-20 V) was seriously worn leading to a deep track. This coating was softer than alumina (16.6 GPa compared to 20 GPa) therefore it was seriously abraded.

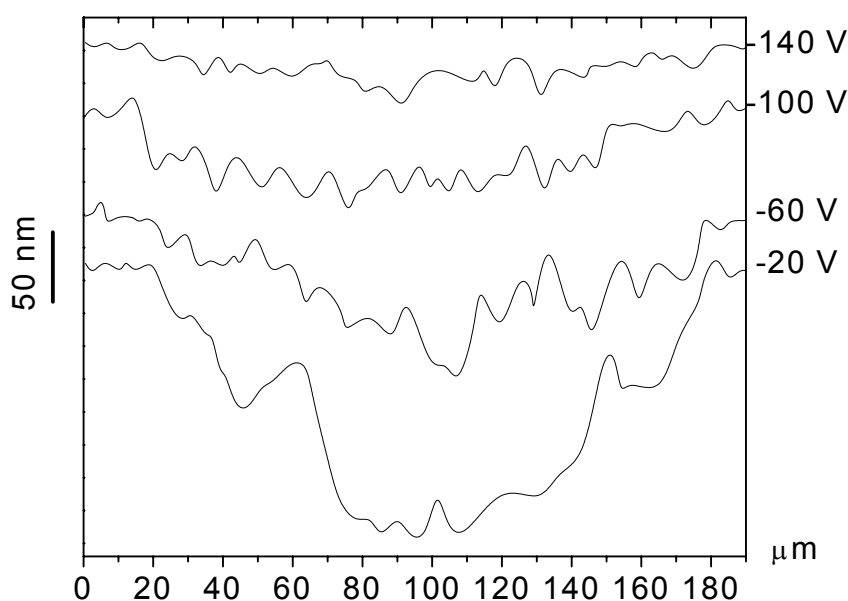


Figure 4.34. Wear track profile of DLC coatings deposited under different bias voltage after 1 Km sliding against an alumina counterpart in ambient air (22 °C, 75 % humidity) with applied load of 5 N. Coatings deposited under higher bias voltage exhibit better wear resistance (low wear)

Wear of the DLC coatings was much lower when sliding against a steel counterpart since all DLC coatings had much higher hardness compared to that of the 100Cr6 steel. After 1 Km sliding against a steel ball, the wear track of DLC coatings deposited at -140 V and -100 V could not be detected using the profilometer. The coatings seem to be polished but

not worn at all. A little wear can be seen for coatings deposited at -20 V and -60 V bias. Figure 4.35 shows the wear track profile of DLC coatings (deposited under -20 and -60 V bias) after 1 Km sliding against steel balls.

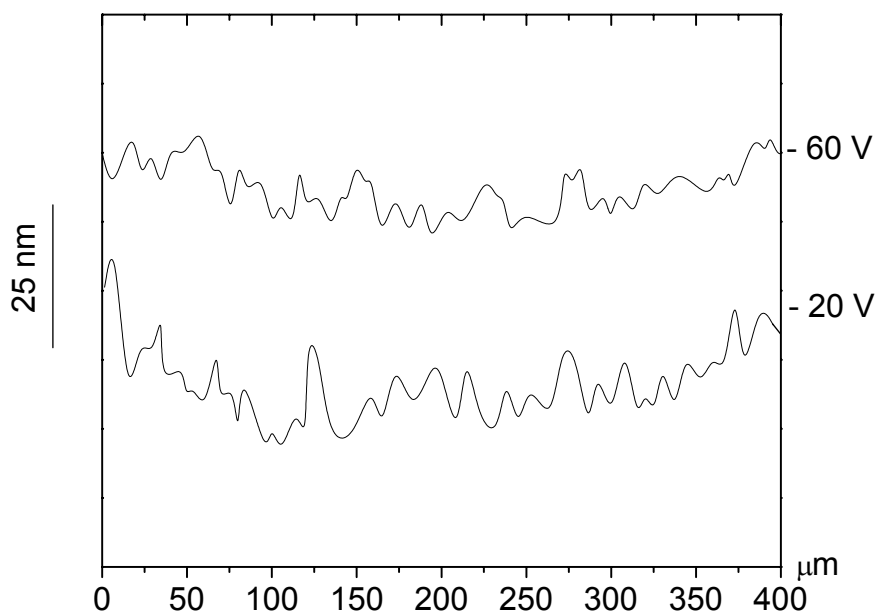


Figure 4.35. Wear track on the DLC coatings deposited under -20 V and -60 V bias after 1 Km sliding against a steel counterpart in ambient air (22 °C, 75 % humidity) with applied load of 5 N

The observations from the wear track profiles of DLC coatings after tribotests indicated that in ambient air, coatings deposited under high bias voltage exhibited much better wear resistance when sliding against steel or alumina counterparts.

#### 4.7. Enhancement of performance of magnetron sputtered DLC coatings

From previous sections, the properties of magnetron sputtered hydrogen-free DLC have been investigated. Depending on the deposition parameters, DLC exhibited different behavior. It can be seen that, the most important parameter is the energy of the carbon ions bombarding the substrate during deposition. This energy determines the coating density,  $sp^3$  fraction and residual stress and directly relates to the process pressure and negative bias voltage applied to the substrate (equation 4.5). An increase in process pressure causes the same effect as a decrease in bias voltage. However, the change in coating structure is more significant when bias voltage is changed since the ion energy is proportional to bias voltage while inversely proportional to the square root of process pressure. DLC coatings deposited under high bias voltages exhibit high hardness and good wear resistance. However, they have high residual stress and low toughness, which results in poor adhesion of the coating to the substrate. To enhance the adhesion strength of the coating while the desirable properties (hardness and wear resistance) are maintained, bias-graded deposition is a promising method. The principle of this method is described as: at a constant target power density and process pressure, the bias voltage is gradually increased from a minimum to a maximum value as the deposition is progressing and the coating thickness is increasing. This results in a DLC coating with a “graded”  $sp^3$  fraction: lower at the coating-substrate interface, higher while into the coating, and highest at the coating surface. The hardness, therefore, is also “graded” with the highest value at the coating surface and lowest value at the coating-substrate interface. DLC coatings deposited under bias-graded voltage have low intrinsic stress at the coating - substrate interface while the surface is hard leading to high adhesion strength combined with good

wear resistance. The schematic diagram of bias-graded deposition of DLC coatings is described in Figure 4.36.

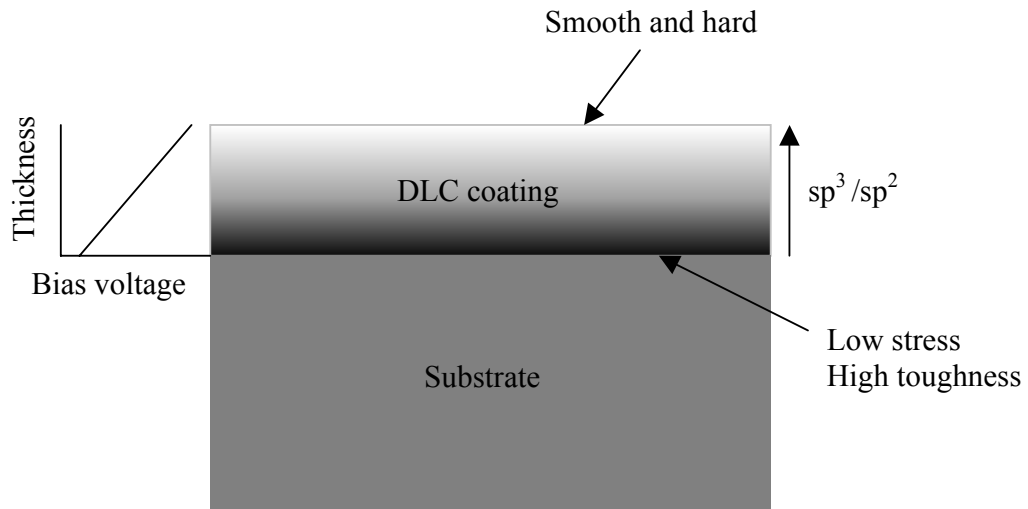


Figure 4.36. Schematic diagram of bias-graded deposition of DLC coatings: the bias voltage is gradually increased from a minimum to a maximum value as the deposition is progressing and coating thickness is increasing

Within a certain range of bias voltage (minimum and maximum value), different coating thickness can be obtained by changing the rate of increasing bias voltage (it directly relates to deposition time). Figure 4.37 plots the coating thickness measured after deposition under the bias-graded mode (the range of bias voltage was from -20 to -150 V) at a power density of  $10.5 \text{ W/cm}^2$  and process pressure of 0.6 Pa. It can be seen that at different increasing rates of bias voltage, the coating thickness was different. At a rate of 1 V/min, the coating thickness was  $2.3 \text{ }\mu\text{m}$  and it decreased to only  $0.5 \text{ }\mu\text{m}$  as the rate was



increased to 4 V/min. It should be noted that all DLC coatings deposited under bias-graded mode adhered well to the substrate.

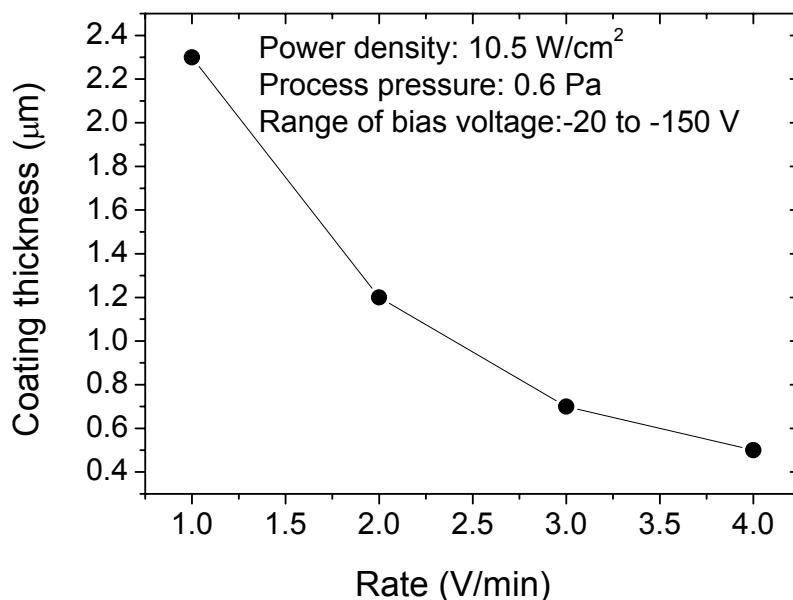


Figure 4.37. Relationship between the coating thickness and the rate of increasing bias voltage in bias-graded deposition

The hardness of the DLC deposited under the bias-graded mode varies with the coating thickness. An essentially hard surface guarantees good wear resistance of the coating in tribological applications. The surface roughness ( $R_a$ ) of bias-graded DLC coating (deposited at a rate of 2 V/min, the coating thickness was about 1.2 μm) on a Si wafer measured from the AFM was 1.4 nm, higher than that of the coating deposited under -140 V bias (1.1 nm  $R_a$ ). At a rate of 2 V/min, the residual stress of a bias-graded DLC coating (measured from the change in the radius of curvature of the Si substrate) was 1.5 GPa.

This value was much lower than that of the coating deposited under -140 V bias, where the residual stress was as high as 4 GPa. Furthermore, 1.5 GPa was just an average value. The residual stress in the vicinity to the substrate-coating interface was expected to be lower since the bias-graded DLC coating contains more  $sp^2$  in that area. From Figure 4.38, at an indentation depth of 110 nm, DLC deposited under the bias-graded mode (rate: 2 V/min) shows a high hardness of 26.1 GPa with a Young's modulus of 271 GPa.

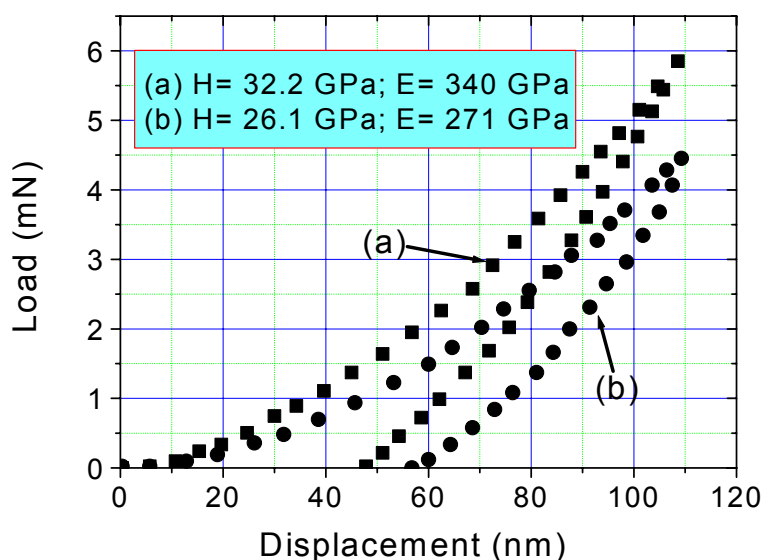


Figure 4.38. Load and unload curve from nanoindentation of coatings deposited at (a) constant bias of -140 V and (b) bias-grading over the range of -20 to -150 V with a rate of 2 V/min

The calculated plastic deformation was 43 % for the DLC coating deposited under -140 V and 50 % for the bias-graded DLC coating. This indicates the lower toughness of the DLC coatings deposited under high bias voltage compared to the ones deposited under the bias-

graded mode since the plastic behavior at highly applied load helps to prevent brittle fracture occurring in hard coatings [147]. Such plastic compliance is high for a hard coating compared to a 10 % plastic deformation for 60 GPa superhard DLC coatings deposited by pulsed laser [32], or the absence of plasticity in the superhard nanocomposites TiN/SiN<sub>x</sub> proposed by Veprek et al. [89, 90].

Good toughness combined with low residual stress and a smooth surface gives bias-graded DLC coatings a better load-bearing capability compared to those deposited under constant bias voltage as seen from the optical micrograph of the scratch after scratch test in Figure 4.39.

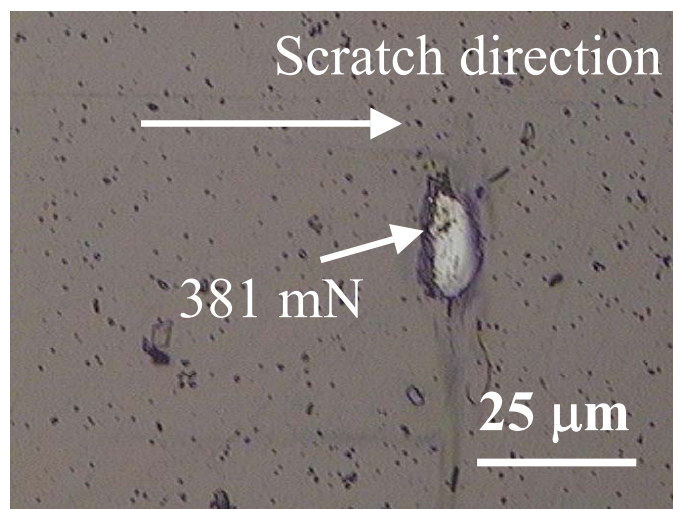


Figure 4.39. Optical image of scratch on bias-graded DLC coating after scratch test

In contrast to the DLC coatings deposited under constant bias voltage (c.f., Figure 4.23), the lower and higher critical loads of bias-graded DLC were distinguishable. As the

applied load reached the lower critical value, the coatings were partly damaged. More increase in load caused total damage to the coating. This indicated the tough behavior of the bias-graded coating: the propagation of cracks is hindered and therefore brittle fracture was prevented. The critical load of a bias-graded coating was 3 times higher than that of coating deposited at -140 V and 1.2 times higher than that of coating deposited at -20 V (c.f., Figures 4.22 and 4. 39).

#### **4.8. Thermal stability and oxidation resistance of magnetron sputtered DLC**

The thermal stability and oxidation resistance tests were carried out on coatings deposited at -150 V bias. They have highest  $sp^3$  fraction and hardness. The samples (Si wafers coated with DLC) were heated in a furnace in air to a certain temperature. After unloading from the furnace, the samples were cooled down in the ambient air to the room temperature then the Raman analysis was carried out. Figure 4.40 shows the Raman spectra of a DLC coating after thermal exposure for 60 minutes at different temperatures. As seen from the figure, the spectrum did not change much as the temperature increased up to 300 °C. The increase in G peak frequency (ranging from 3 to 15  $cm^{-1}$ , c.f., Figure 4.41) indicated some change in the structure of the DLC coating, possibly related to a slight decrease in the  $sp^3/sp^2$  fraction in the coating. Above 300 °C, structural changes in the DLC coating became apparent. The appearance, at 400 °C, of the Raman band near 1350  $cm^{-1}$  coincided with a further shift of the G band to higher frequencies and a considerable increase in the  $I_D/I_G$  ratio from 1.2 (at 300 °C) to 1.9 (at 400 °C)(c.f., Figure 4.41). This indicated a high rate of graphitization occurred in the coating, which led to a decrease in hardness from 28.6 (at 300 °C) to 16.6 GPa (at 400 °C) as seen from Figure 4.42.

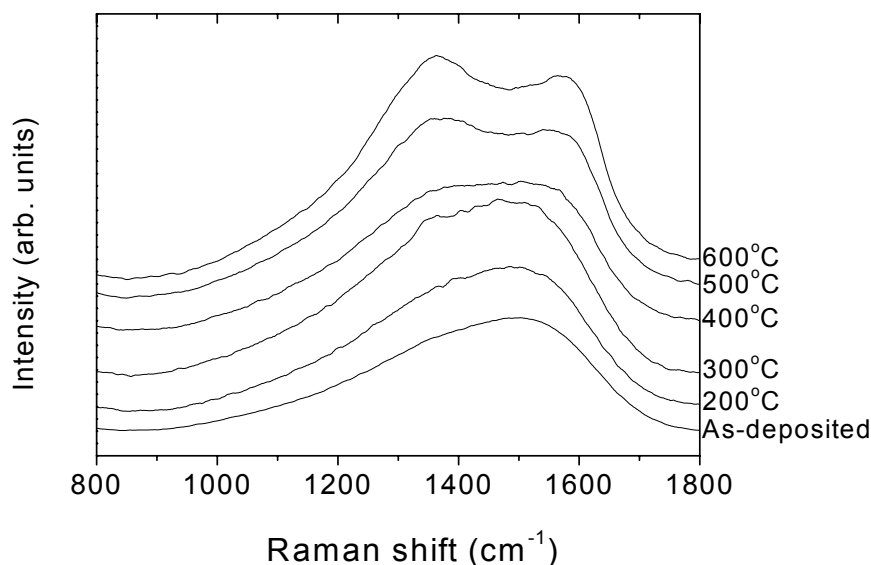


Figure 4.40. Raman spectra of DLC coatings annealed at different temperature for 60 minutes

As annealing temperature increased to 500 °C, the hardness of the coating decreased to a very low value of 8.1 GPa, corresponding to a high  $I_D/I_G$  ratio of 3.6. Since the thickness of the coating after 60 minutes annealing at 600 °C reduced to about 350 nm, the hardness measurement was not carried out for this sample. Figure 4.43 plots the coating thickness measured from a step jump by profilometer (masking was used to make the step). It can be seen that the coating thickness did not change after 60 minutes annealing up to 300 °C. A slight reduction in thickness was seen at a temperature of 400 °C (about 15 %). At temperatures higher than 400 °C, the loss of thickness drastically increased (about 35 % at 500 °C and 62 % at 600 °C). The loss of coating thickness was attributed to the oxidation of carbon following the reaction:  $C + O_2 \rightarrow CO_2 \uparrow$ . The carbon dioxide moves out of the coating causing the loss of thickness.

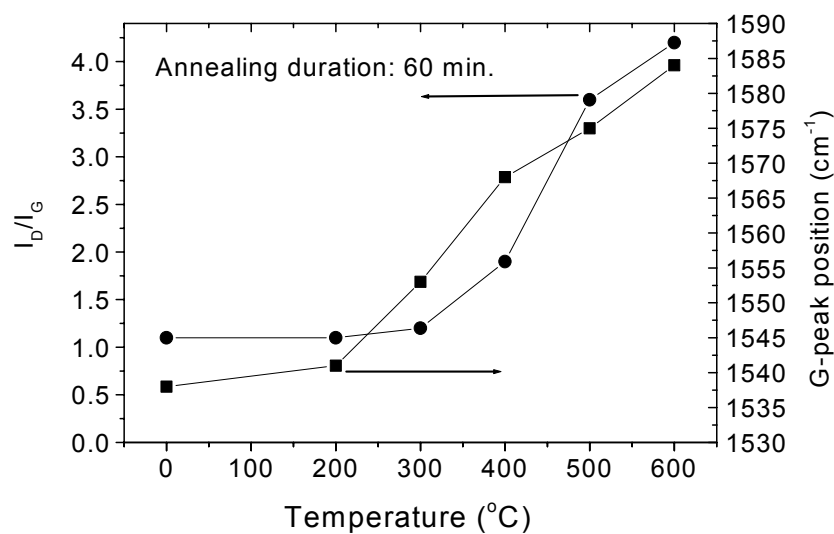


Figure 4.41. The relationship between annealing temperature,  $I_D/I_G$  ratio and G-peak position

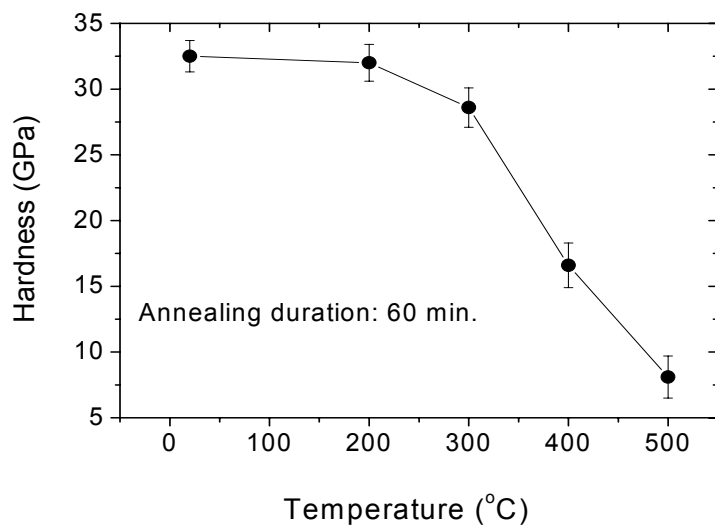


Figure 4.42. Correlation between hardness and annealing temperature of DLC coating

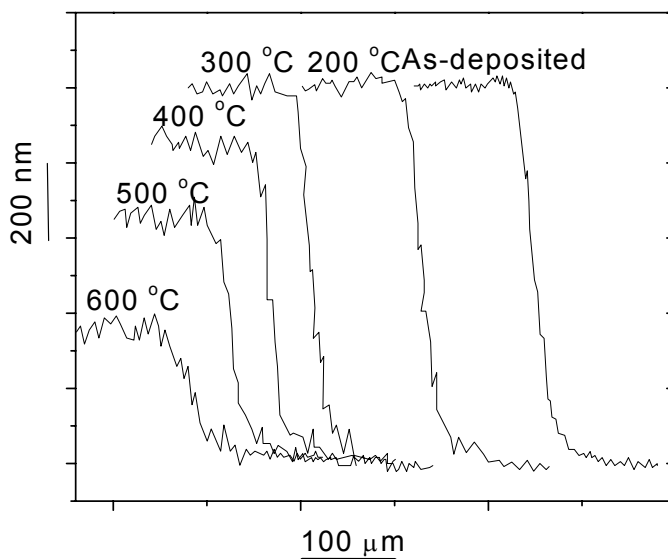


Figure 4.43. The change of the coating thickness after 60 minutes annealing in air at different temperatures

#### 4.9. Summary

From studies in this chapter, some key points can be drawn:

- At high power densities (e.g. 10.5 W/cm<sup>2</sup>), the deposition rate of hard DLC is suitable for industrial scale use: a 1μm coating can be deposited within 30-60 minutes depending on the bias voltage, process pressure and the substrate-target distance.
- To prevent coatings being positively charged, which results in poor adhesion, RF bias should be applied to the substrate instead of DC.
- Deposition parameters strongly influence the coating properties. An increase in bias voltage (or decrease in process pressure) causes an increase in the energy of ions bombarding the substrate. Under highly energetic ion bombardment, surface diffusion is not promoted and the incoming ions tend to penetrate into the interior of the structure

leading to high density, smooth morphology and high  $sp^3$  fraction with associated high hardness and residual stress. The hardness of magnetron sputtered DLC varies from 15 to 33 GPa. A high stress of about 4 GPa limits the coating thickness to less than 1.5  $\mu\text{m}$  on a Si wafer. The stress relaxation (with sinusoidal waves) damages the coating as its thickness exceeds a critical value. There is a square root relationship between residual stress and bias voltage.

- DLC coatings have low toughness and they show brittle fracture at high applied loads in scratch tests, especially for coatings deposited under high bias voltages. A higher applied bias voltage results in a lower critical load, mainly, due to high residual stress. The lower and higher critical loads are not distinguishable: as applied load reaches a certain value, the coating is totally damaged.

- Magnetron sputtered DLC coatings exhibit a low coefficient of friction in ambient air (0.08 to 0.14 when sliding against alumina and 0.12 to 0.15 when sliding against stainless steel). Coatings deposited under lower bias voltage, exhibit lower friction. However, the coatings deposited under high bias voltage exhibit better wear resistance. This is true for both counterparts (alumina and steel). The formation of a graphite-rich layer, which acts as a solid lubricant in humid air is the main factor contributing to the low coefficients of friction observed.

- Bias-graded deposition is an effective method for enhancement of the adhesion strength and the toughness of DLC coatings. At 110 nm indentation depth, a 1.2  $\mu\text{m}$  thick bias-graded DLC coating exhibits higher plasticity during indentation deformation (50 %) compared to that of DLC deposited under constant bias voltage (43 %). Meanwhile the hardness of bias-graded DLC is as high as 26 GPa. The average value of residual stress is only 1.5 GPa (that of the DLC deposited at -150 V is 4.1 GPa). The critical load of bias-



graded coating determined from scratch tests is 3 times higher than that of coatings deposited under -140 V bias.

- The structure of magnetron sputtered DLC is stable up to 300 °C. Higher than that, graphitization occurs leading to a drastic decrease in coating hardness. From 400 °C, oxidation takes place leading to a loss of coating thickness.

- For real applications, the properties of DLC coating should be modified. The problems to be overcome are:

- + Residual stress: the stress should be decreased to a range of a few hundreds MPa in order to deposit thick coatings for an acceptable working life. Also, good adhesion between the coating and substrate is needed.

- +Toughness: the toughness should be at an acceptable level so that no brittle fracture occurs at a high applied load. The expected value of plasticity for a good toughness is higher than 50 %.

- +Thermal stability: the coating should have good thermal stability and oxidation resistance for applications at high temperatures.

- Bias-grading is a good method for deposition of DLC coatings with such desirable properties. However, it is not an optimum method since the stress in the coating is still at a high level and the problem of thermal stability and oxidation resistance could not be totally solved.

## **CHAPTER FIVE**

### **MAGNETRON SPUTTERED DLC NANOCOMPOSITE COATINGS**

From chapters 2 and 4, it can be seen that a nanocomposite is possibly the best solution to overcome the drawbacks associated with DLC while maintaining other desirable properties. Magnetron sputtering is one of the most suitable techniques for deposition of this kind of coating. In this study, DLC nanocomposite coatings were deposited via co-sputtering of graphite and metallic targets (Al and Ti). The combination of a soft metal such as Al into DLC to enhance the coating toughness, in fact, is a kind of “miniaturization” of the same methodology of making cermets (composites made of ceramics and metals) [148]. The oxidation resistance of the composite coating is expected to be much better than that of DLC since Al on the surface will react with oxygen to form an oxide layer, which plays the role of a barrier to prevent the diffusion of oxygen into the interior of the coating. Ti plays the major role of maintaining the coating hardness through formation of nanograins of TiC crystallites. Since TiC is a strong phase and the nanograins are almost free of dislocations or if there are, the dislocations cannot operate as the grains are at nanosize (see chapter 2, section 2.3.1), a high volume fraction of this nanocrystalline phase strongly enhances the coating hardness. In addition the TiC nanograins enhance the coating toughness since the cracks will deflect and terminate at the boundary between the amorphous matrix and the nanograins. Also, at highly applied loads, the grains will slide in the amorphous matrix to relax the stress, therefore the energy, which is required for crack propagation no longer exists leading to a further

enhancement of coating toughness. In order to prevent the thermal stress, the composite coatings were deposited at low temperature (150 °C) on negatively biased substrates. The power density on the graphite target was kept constant at 10.5 W/cm<sup>2</sup> and that of the metallic targets was varied for different compositions. The targets were located at a distance of 10 cm above the substrate. The process pressure was kept constant at 0.6 Pa (at an Ar flow rate of 50 sccm).

## **5.1. Effect of Al-incorporation on the properties of DLC**

### **5.1.1. Composition and coating structure**

Generally, at the same power density, the sputtering yield of Al is 6-7 times higher than that of C [102] therefore the power density of the Al target in this study was selected at a much lower level (from 0 to 1.8 W/cm<sup>2</sup>) than that of the graphite target (10.5 W/cm<sup>2</sup>). The composition of the C and Al in the coating was determined from XPS spectra by calculating the area under the peaks of C 1s at 284.6 eV, Al 2p at 72.6 eV, and O 1s at 532.4 eV [147, 149]. Since the process pressure was low enough (0.6 Pa), the Ar included in the coating was negligible and was not taken into account. Figure 5.1 shows a typical XPS spectrum of Al-“doped” DLC (without ion etching). Apart from the difference in the intensity and width of the peaks, the XPS profile is almost the same for all the different power densities applied to Al target. It is easy to recognize a large amount of oxygen contaminating the coating. Al 2p XPS spectra (with fitting curves) of the Al-“doped” DLC coatings deposited under -150 V bias with different power densities of Al target are shown in Figure 5.2.

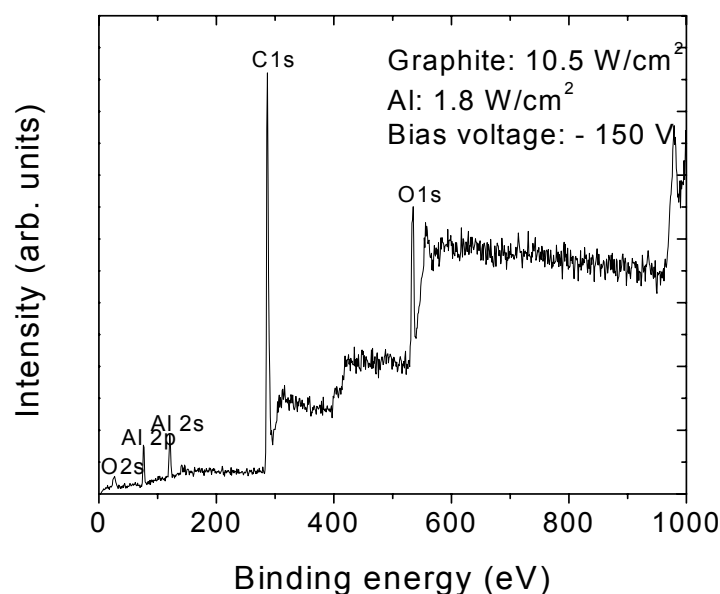


Figure 5.1. XPS spectrum of Al-“doped” DLC coating

The symmetrical single peaks at 74.2 eV indicate that almost all the Al on the surface was bonded with oxygen to form aluminum oxide [150]. Al is extremely reactive with oxygen. Therefore just after unloading from the deposition chamber, Al on the coating surface was oxidized. Figure 5.3 shows the XPS spectra of Al 2p before and after 15 minutes ion etching. After etching, the peak was shifted to 72.6 eV with a higher intensity. It indicates that Al exists in the coating as elemental aluminum. The higher intensity of the Al 2p peak after etching as compared to that before etching is due to the removal of carbon and oxygen contaminated on the coating surface. Also, a small amount of Al-O bonds was detected from the deconvoluted peak at 74.2 eV. The oxygen is believed to contaminate the coating during the deposition process. Although the chamber was pumped to a base pressure of  $1.33 \times 10^{-5}$  Pa, there was always a small amount of oxygen in the chamber

available to contaminate the coating. No bond between Al and C at 73.6 eV [149] was seen in the coating even for the coating deposited with a  $1.8 \text{ W/cm}^2$  power density on the Al target. Figure 5.4 shows the XPS spectrum (after etching) of the C 1s where the peak of the C-C bonds at 284.6 eV and C-O bonds at 286.3 eV were seen. It again confirms that no chemical bonding exists between C and Al since no peak at 281.5 eV was observed. The composition of coatings as calculated from XPS spectra (after etching for 15 minutes) is tabulated in table 5.1. The Al content in the coating increased from 5.1 to 19.6 at.% as the power density on the Al target increased from 0.6 to  $1.8 \text{ W/cm}^2$ . The oxygen content in the coating was 2-4 at.%, a small amount.

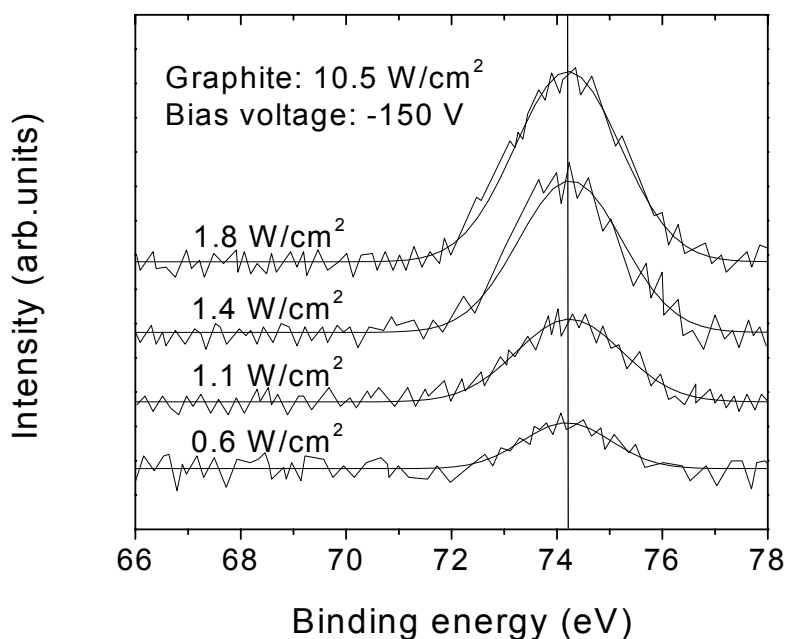


Figure 5.2. XPS spectra of the Al 2p for Al-“doped” DLC deposited under -150 V bias at different power densities on the Al target (power density of graphite:  $10.5 \text{ W/cm}^2$ )

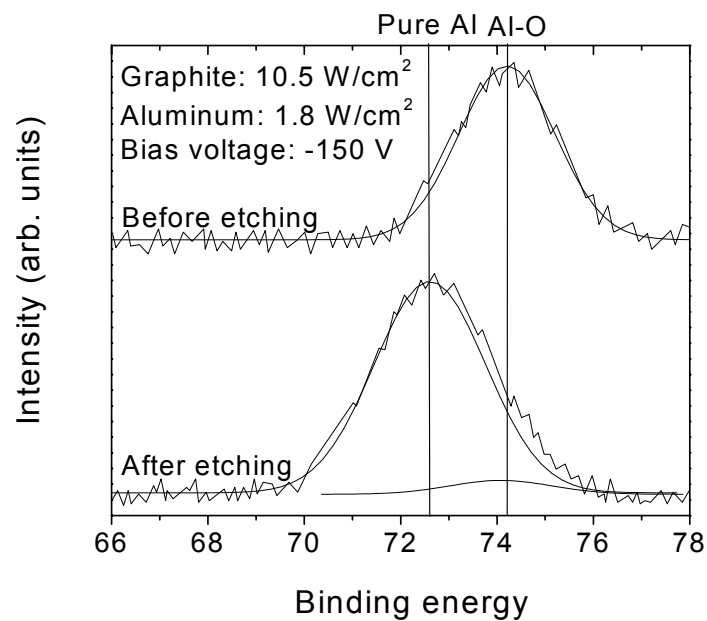


Figure 5.3. XPS spectra of Al 2p for Al-“doped” DLC before and after etching for 15 minutes

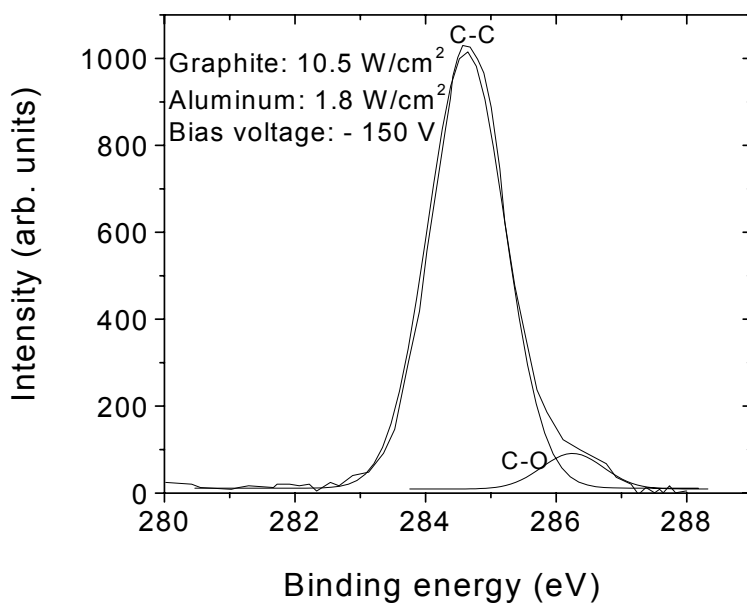


Figure 5.4. XPS spectrum of C 1s for Al-“doped” DLC after etching for 15 minutes

Table 5.1. Composition of the Al-“doped” DLC coating deposited under -150 V bias and power density on the graphite target of 10.5 W/cm<sup>2</sup>.

| Power density of Al target (W/cm <sup>2</sup> ) | C (at. %) | Al (at. %) | O (at. %) |
|---|-----------|------------|-----------|
| 0.6   | 93        | 5          | 2         |
| 1.1   | 87        | 9          | 4         |
| 1.4   | 83        | 14         | 3         |
| 1.8   | 77        | 19         | 4         |

At the same target power density, the change of Al concentration at different bias voltages (in the range from -20 to -150 V) was not significant as seen from Figure 5.5 where the Al concentration in the Al-“doped” DLC is plotted as a function of bias voltage. Therefore, the parameter that can be used to effectively control the composition of metal in the coating is the power density on the metallic target.

Al-“doped” DLC coatings are amorphous. Figure 5.6 shows the XRD spectra of an Al-“doped” DLC coating (19 at.%Al) and [100] Si wafer. The XRD profile of the Al-“doped” DLC did not have any noticeable peak except the peak from the Si substrate at around 69° 2 $\theta$ . This indicates that the Al in the coating is not crystalline. This conclusion is supported by the TEM image (c.f., Figure 5.7) combined with diffraction pattern (a broad halo was seen).

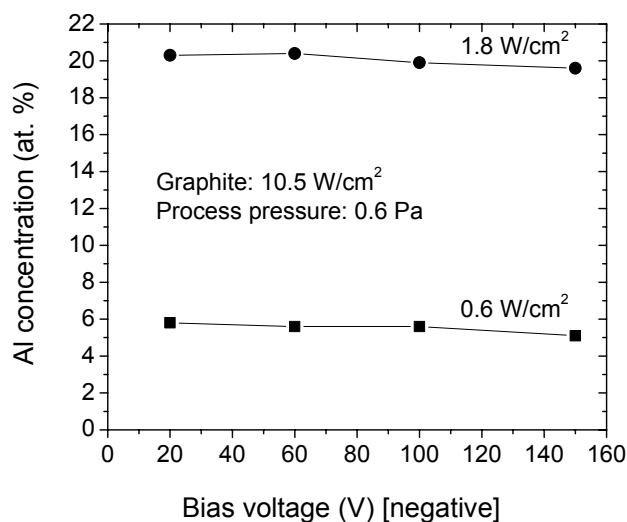


Figure 5.5. Relationship between bias voltage and Al concentration in Al-“doped” DLC coatings deposited under different power densities on the Al target. The Al concentration does not considerably change as applied bias voltage is varied

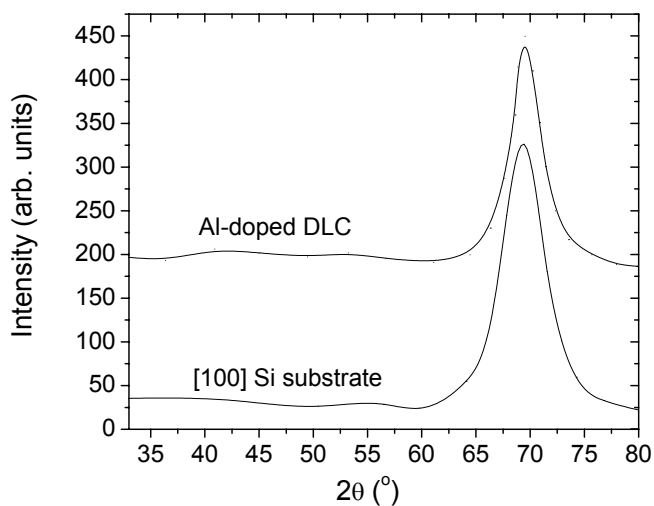


Figure 5.6. XRD spectra of Al-“doped” DLC coating (19 at.% Al) and a [100] Si substrate. No noticeable peak is seen except the one of [100] Si wafer at 69° 2θ



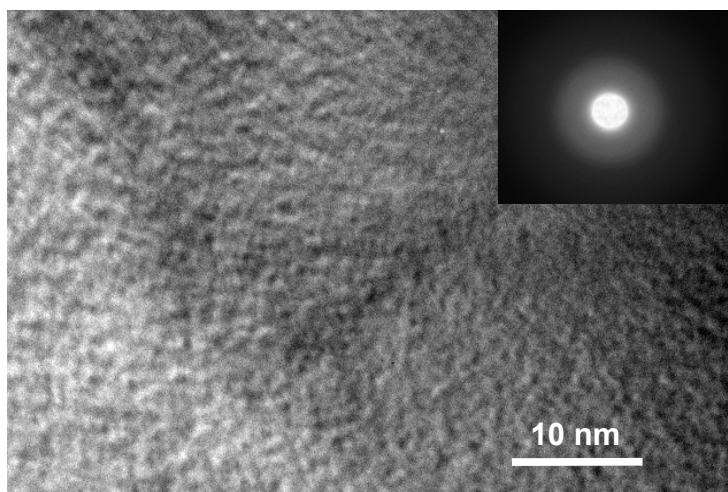


Figure 5.7. TEM micrograph with diffraction pattern of Al-“doped” DLC coating (19 at.% Al). The coating is amorphous: a broad halo is seen from the diffraction pattern

Figure 5.8 shows Raman spectra of Al-“doped” DLC for different Al compositions. The range covered was from 850 to 1900  $\text{cm}^{-1}$ . Outside this range, no feature was observed. The  $I_D/I_G$  ratios, which were calculated from the intensity of the G and D peaks, were also put onto the diagram. The  $I_D/I_G$  ratio increased with increasing power density on the Al target. The Al content in the coating also increased. Without Al, the  $I_D/I_G$  ratio was 1.1 and it increased to 2.7 as the Al content increased to 19 at.%. This indicates that incorporation of Al hinders the formation of  $\text{sp}^3$  sites leading to an increase in  $\text{sp}^2$  fraction in the a-C of the Al-“doped” DLC coating. Also, a high  $I_D/I_G$  ratio of 2.7 when the power density on the Al target was 1.8  $\text{W}/\text{cm}^2$  (corresponding to 19 at.%Al) indicates that the  $\text{sp}^2$  sites started organizing into small graphitic clusters [141, 151].

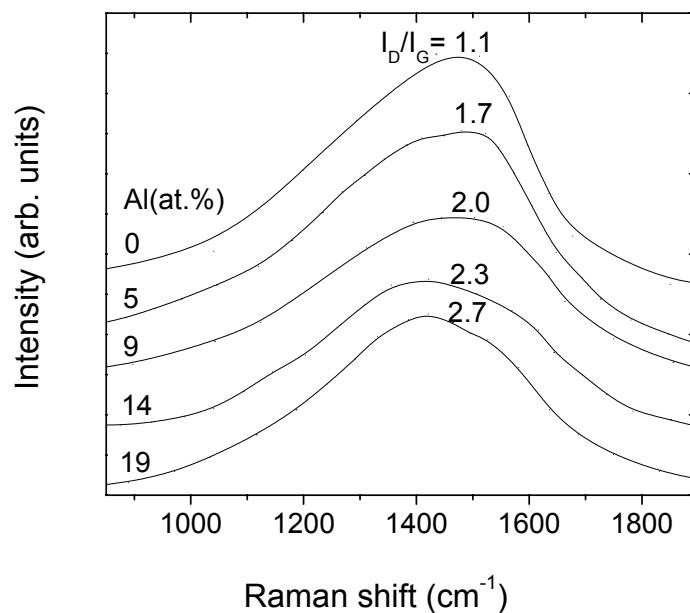


Figure 5.8. Raman spectra of Al-“doped” DLC coatings with different Al concentrations

### 5.1.2. Hardness, residual stress and adhesion strength of Al-“doped” DLC coatings

The hardness and Young’s modulus of Al-“doped” DLC coatings decreased with increasing Al concentration in the coating. Without addition of Al, the hardness of a pure DLC coating was 32.5 GPa and it decreased to a low level of 7.8 GPa when the coating was “doped” with 19 at.%Al as seen from Figure 5.9. This is the consequence of the increase in the  $sp^2$  fraction when more Al is added to the coating. In addition, Al is a soft material. Therefore the hardness of the coating is further decreased. However, the increase of the  $sp^2$  fraction in the coating due to the addition of Al is the most important factor contributing to the relaxation of the residual stress. It has been proved by Sullivan et al. [152] that while the atomic volume of a  $sp^2$  site exceeds that of a  $sp^3$  site, its in-plane

size is less due to its shorter bond length. Thus the formation of  $sp^2$  sites with their  $\sigma$  plane aligned in the plane of compression greatly relieves biaxial compressive stress.

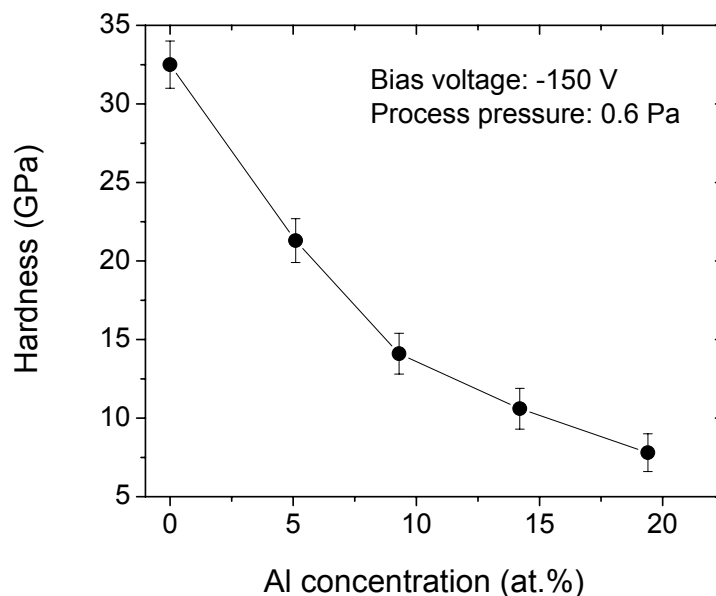


Figure 5.9. The hardness of DLC coating as a function of Al concentration

Figure 5.10 plots the relationship between residual stress of Al-“doped” DLC coatings (thickness of about 1.2  $\mu\text{m}$ ) and Al content. Without Al, the residual stress was as high as 4.1 GPa. When 5 at.% Al was added, the stress dropped to 0.9 GPa (4.5 times reduction) and the  $I_D/I_G$  ratio increased from 1.1 to 1.7 (1.5 times increase). It has been proved that for DLC coatings with high  $sp^3$  fraction, the stress considerably decreases with very little variation of strain in the coating [68]. If more Al was added such a big drop in residual stress was not observed but rather a gradual decrease took place. With 19 at.% Al added, the measured residual stress was only 0.2 GPa.

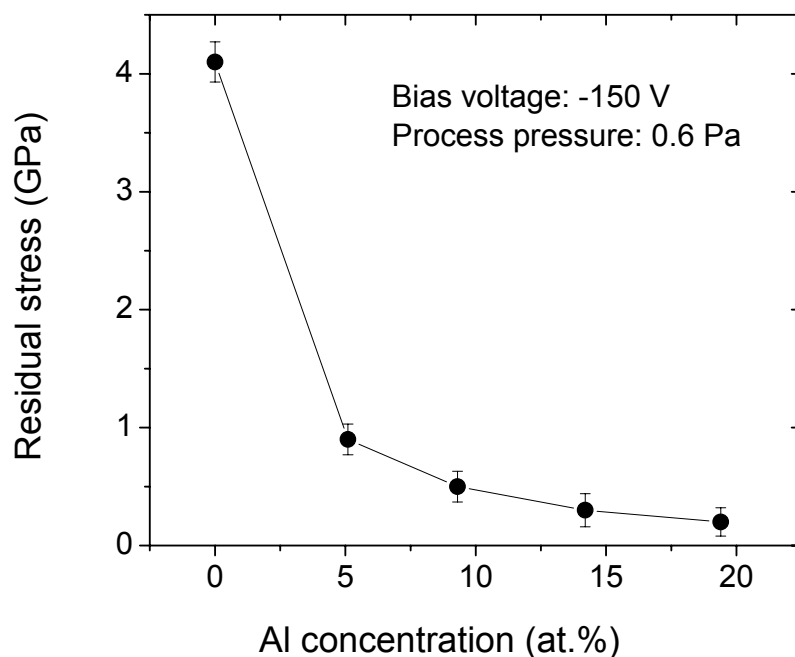


Figure 5.10. Residual stress as a function of Al content in Al-“doped” DLC coatings

Addition of Al results in a considerable increase in adhesion strength of the coating to the substrate. This is due to two reasons: (1) the low residual stresses in the coating and (2) the high toughness achieved because Al is a tough material and the coating contains more graphite-like structure. Both effects can be seen from the results of scratch tests: high critical load combined with plastic behavior but not brittle like pure DLC.

Figure 5.11 shows the optical micrographs of scratches after scratch tests on DLC “doped” with 5 and 19 at.% Al. Coatings with different Al contents exhibited different behavior in the scratch tests.

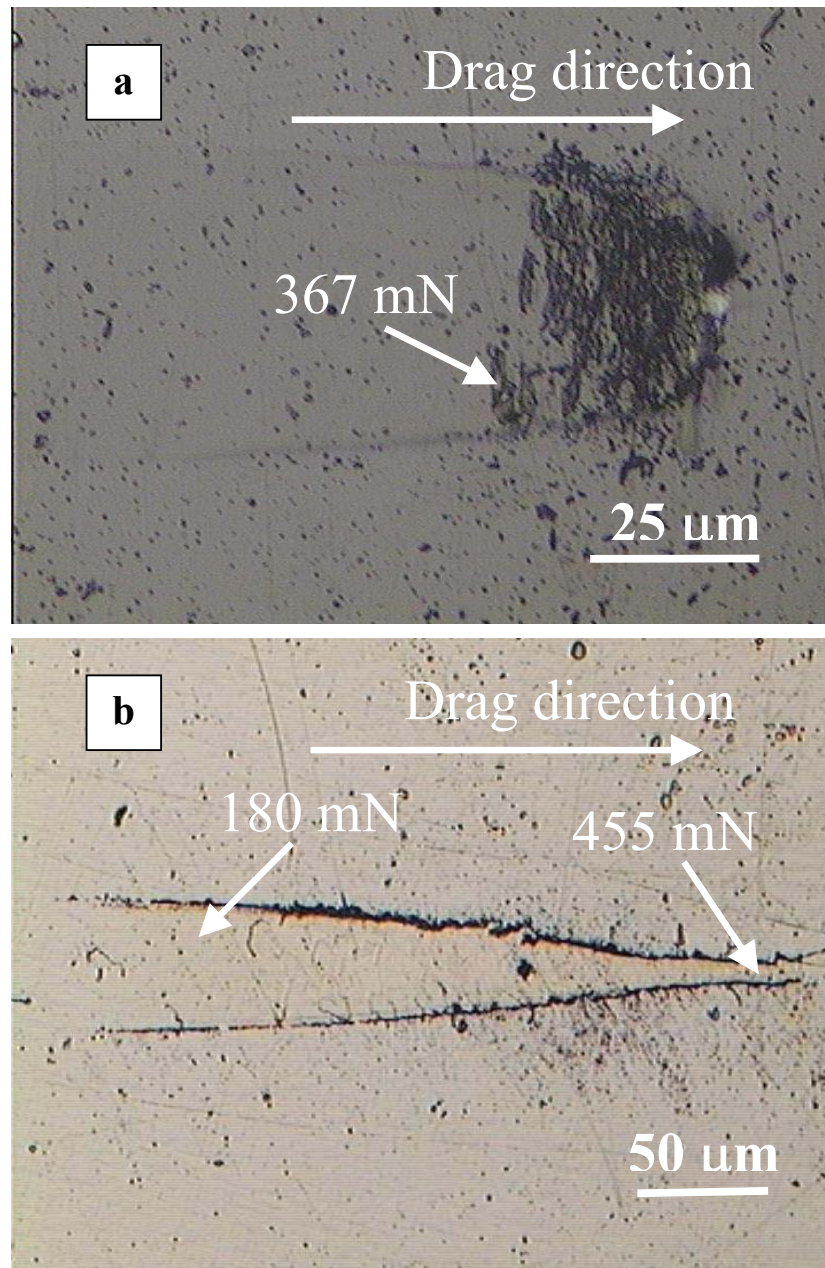


Figure 5.11. Optical micrographs of scratches on the coatings after scratch tests of Al-  
“doped” DLC coatings: (a) 5 at.% Al and (b) 19 at.% Al

The damage of coatings “doped” with 5 at.%Al occurred at an applied load of about 367 mN. However, at such a high load, the coating exhibited only partial damage. This is

different from the results obtained from pure DLC coatings (c.f., Figure 4.23 in chapter 4) where at low applied loads (less than 240 mN), the coatings were totally damaged. As 19 at.%Al was added, no fracture was seen. Since this coating had low hardness (7.8 GPa), as the load reached about 180 mN, the diamond tip had already ploughed deeply into the coating causing a gradual decrease in the scanning amplitude. Up until the end of the test, when the load reached 455 mN, no fracture or interfacial failure were observed indicating the high toughness and adhesion strength of this coating. It is clear that the more the Al was added into DLC the more the adhesion strength was improved. However, DLCs “doped” with high Al content have low hardness therefore the application of these coatings is limited.

## **5.2. Effect of Ti-incorporation on the properties of DLC**

### **5.2.1. Composition and coating structure**

Ti is added into DLC by the co-sputtering of graphite and Ti targets. The power density on the graphite target was 10.5 W/cm<sup>2</sup> whereas that on the Ti target was changed for different compositions. The process pressure was maintained at 0.6 Pa and the substrate temperature was kept constant at 150 °C during deposition.

After unloading from the deposition chamber, the coatings were contaminated with a large amount of oxygen and carbon coming from the atmosphere. Therefore ion etching was carried out for 15 minutes before XPS analysis of each sample. The oxygen which was incorporated into the coatings during deposition (less than 5 at.%) was excluded from the calculations. Fitting the C 1s and the Ti 2p<sub>3/2</sub> peaks allows us to discriminate between the three occurring phases in the coating: a-C, TiC and metallic Ti. The C 1s positions of the

C-C in a-C and C-Ti in TiC are 284.6 and 281.8 eV, respectively [147]. The Ti 2p<sub>3/2</sub> peak of Ti in TiC is at 454.9 eV and that of metallic Ti is at 453.8 eV [153]. The Ti 2p also has another peak (Ti 2p<sub>1/2</sub>) at 461 eV for Ti in TiC and 459.9 for metallic Ti. The composition of coatings deposited at different power densities on the Ti target and under -150 V bias is tabulated in table 5.2. Those values were calculated from the C 1s and Ti 2p XPS spectra, which are shown in Figures 5.12 and 5.13. At the same power density on the Ti target, the Ti content in the coating remained almost unchanged when different bias voltages (in the range from -20 to -150 V) were applied. This is similar to the case of adding Al to a-C (c.f., Figure 5.5).

Table 5.2. Composition of Ti-“doped” DLC coatings deposited at different power densities of Ti target (power density of graphite target was 10.5 W/cm<sup>2</sup>) under -150 V bias

| Power density of Ti target (W/cm <sup>2</sup> ) | Ti (at.%) | C (at.%) | Coating structure |
|---|-----------|----------|-------------------|
| 0   | 0         | 100      | a-C               |
| 0.8   | 3         | 97       | a-C(Ti)           |
| 1.4   | 8         | 92       | nc-TiC/a-C        |
| 1.8   | 16        | 84       | nc-TiC/a-C        |
| 2.1   | 25        | 75       | nc-TiC/a-C        |
| 2.4   | 30        | 70       | nc-TiC/a-C        |
| 2.7   | 36        | 64       | nc-TiC/a-C        |
| 3.0   | 45        | 55       | nc-TiC/a-C        |
| 3.3   | 48        | 52       | TiC               |
| 4.0   | 53        | 47       | TiC               |

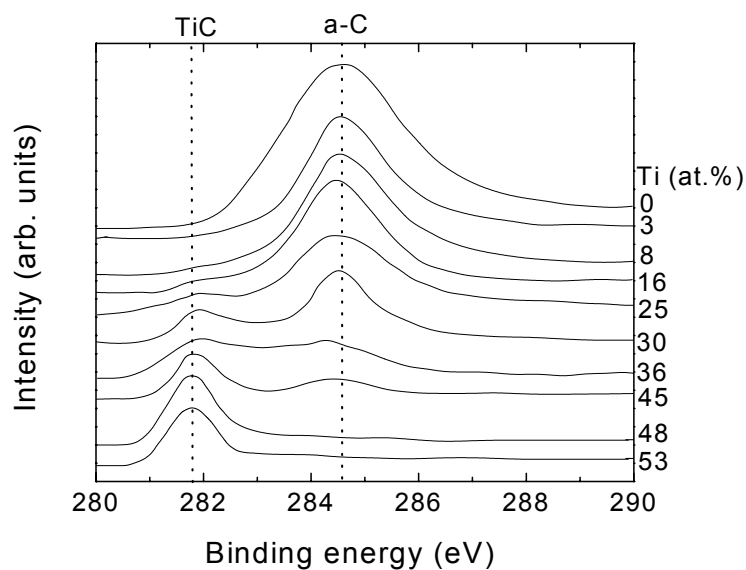


Figure 5.12. XPS spectra of C 1s of Ti-“doped” DLC coatings deposited under -150 V bias with different Ti contents

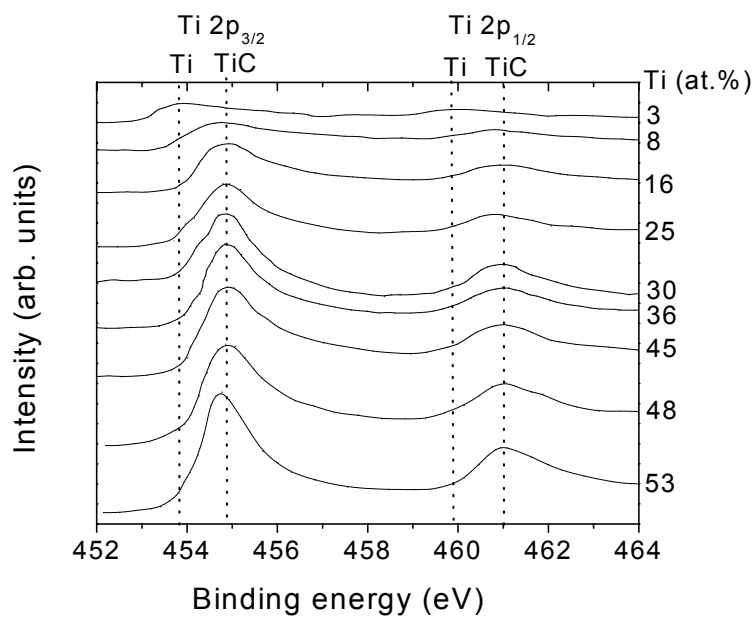


Figure 5.13. XPS spectra of Ti 2p in Ti-“doped” DLC coatings deposited under -150 V bias with different Ti contents



From Figure 5.12, at 0 at.%Ti (i.e., 100 % a-C) only the C-C bond was observed at 284.6 eV. As the Ti content in coatings increased, the carbide (TiC) peak at 281.8 eV appeared and grew while the a-C peak decreased. At 3 at.%Ti, almost no TiC was seen and Ti existed in the coating as elemental Ti, which gave a peak at 453.8 eV of Ti 2p in Figure 5.13. The limitation of the formation of TiC at low Ti content can be attributed to the low power density applied to the Ti target (e.g. 0.8 W/cm<sup>2</sup> for 3 at.% Ti). At low power densities, the energy of the sputtered Ti ions may not high enough to support the formation of Ti-C bonds. The formation of TiC was seen as 8 at.%Ti was added (the power density on the Ti target was 1.4 W/cm<sup>2</sup>) and from the Ti 2p spectrum it can be seen that only a part of Ti bonded with C to form TiC. At 16 at.%Ti and more, most Ti in the coating bonded with C to form TiC (as seen from the Ti 2p<sub>3/2</sub> XPS spectra in Figure 5.13, a single peak, which can be attributed to TiC, was seen at 454.9 eV). As the Ti content exceeded 48 at.%, the peak associated with a-C was almost undetectable from the XPS spectra of the C 1s (c.f., Figure 5.12) indicating that there was virtually no a-C in these coatings (all the carbon bonded with Ti to form TiC). Also, from Figure 5.13, a considerable amount of metallic Ti was seen in the coating “doped” with 53 at.%Ti (the Ti 2p<sub>3/2</sub> peak was considerably shifted towards 453.8 eV). Figure 5.14 presents the composition of a-C, TiC, and Ti (calculated from XPS) in the coatings at different atomic concentrations of Ti. The amount of metallic Ti was calculated by subtracting the carbide contribution to the Ti 2p obtained by peak fitting from the total Ti content. From the figure, the concentration of a-C and TiC was in the range 50-50 at.% at about 27 at.%Ti incorporation. Therefore, at Ti contents less than 27 at.%, the a-C is dominant and TiC becomes dominant if Ti content exceeds 27 at.%.

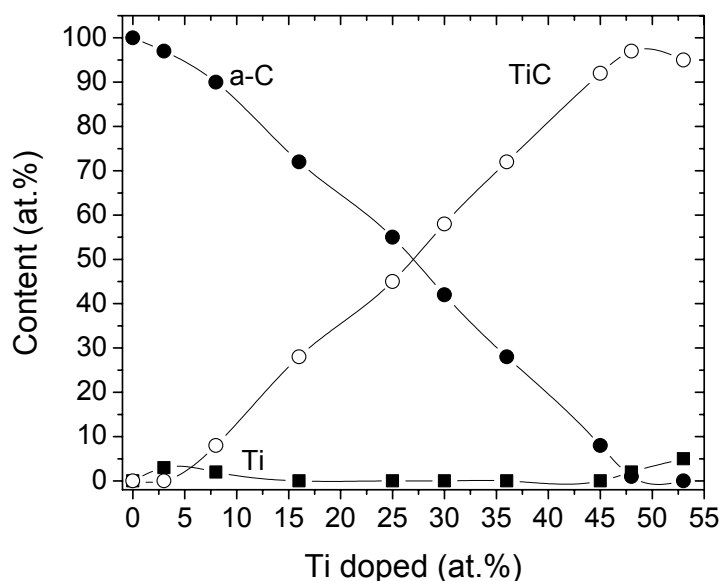


Figure 5.14. The content of a-C, TiC and metallic Ti as a function of Ti addition  
(calculated from the XPS data presented in Figures 5.12 and 5.13)

Figure 5.15 shows the XRD spectra of the coatings at different Ti contents. At 3 at.% Ti, the coating is amorphous. Also, as mentioned above, Ti exists in this coating as elemental Ti. Therefore this coating was denoted as a-C(Ti) (Ti containing a-C) in table 5.2. Above 8 at.%Ti incorporation, the formation of the TiC crystalline phase was observed. Peaks at  $35.9$ ,  $41.7$ , and  $60.4^\circ 2\theta$  were attributed to the [111], [200], and [220] diffraction modes of TiC. The intensity of those peaks increased with increasing Ti content. No dominant texturing was observed. From 8 to 45 at.%Ti, as seen from XPS and XRD results (c.f., Figure 5.14 and 5.15), the crystalline TiC and a-C co-existed. Therefore the coatings were denoted as nc-TiC/a-C (the prefix nc- stands for nanocrystal since the size of the TiC grains is in the range of nanometers as will be shown later) in table 5.2. At higher contents of Ti, there was almost no a-C in the coating but only crystalline TiC and a small

amount of metallic Ti. The coatings, in this case, were denoted as nc-TiC in table 5.2. It can be seen that, at -150 V bias, the nanocomposite can be obtained if the Ti content is from 8 to about 45 at.%. Outside this range, the resultant coating may be Ti containing a-C or crystalline TiC. At Ti concentration of 25 at.% onwards, a small shift of the TiC peaks to the smaller Bragg's angle was seen. That was believed to come from the compressive stress generated in the coating during the deposition process. It was mainly intrinsic stress because the coatings were deposited under low deposition temperature. Thus the thermal stress was negligible. At lower Ti contents, the residual stress was low and no shift of the peaks was seen.

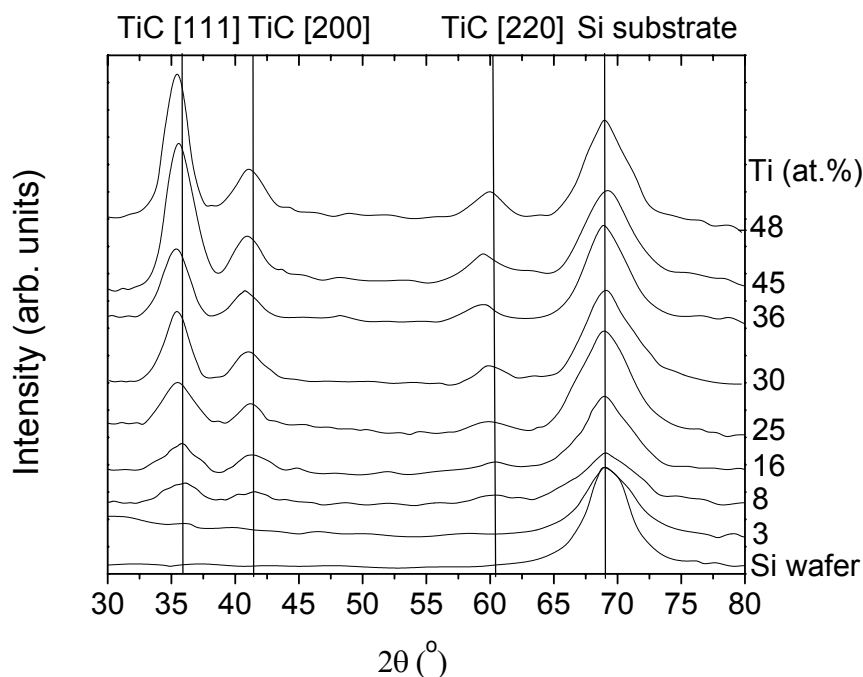


Figure 5.15. XRD spectra of Ti-"doped" DLC coatings deposited under -150 V bias with different Ti concentrations

Ignoring the effect of microstrains due to the compressive stress, the grain size of TiC can be estimated using the Debye-Scherrer formula (equation 3.1). The calculated grain size is plotted in Figure 5.16.

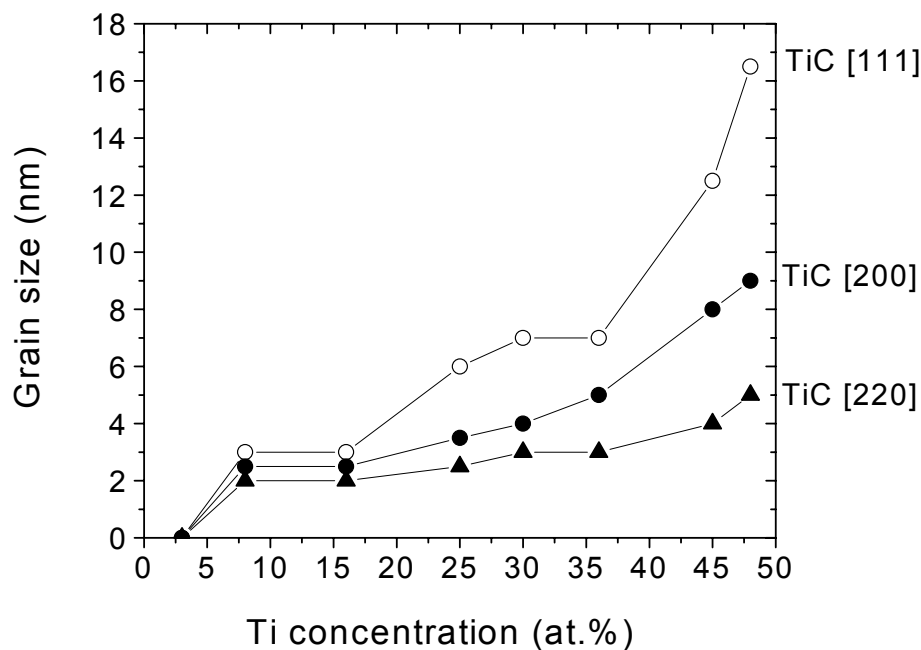
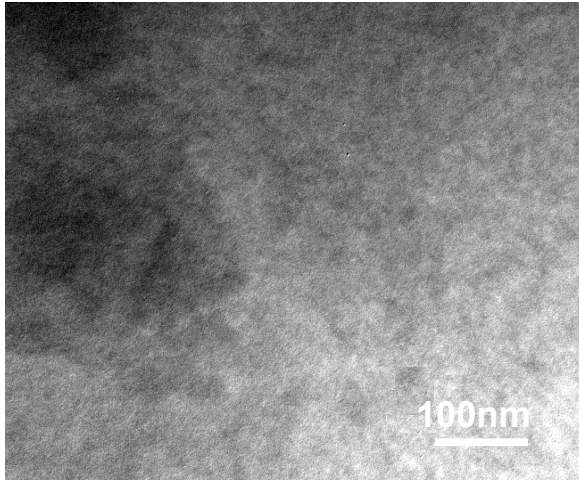


Figure 5.16. Grain size of TiC as a function of Ti concentration (calculated from XRD results in Figure 5.15)

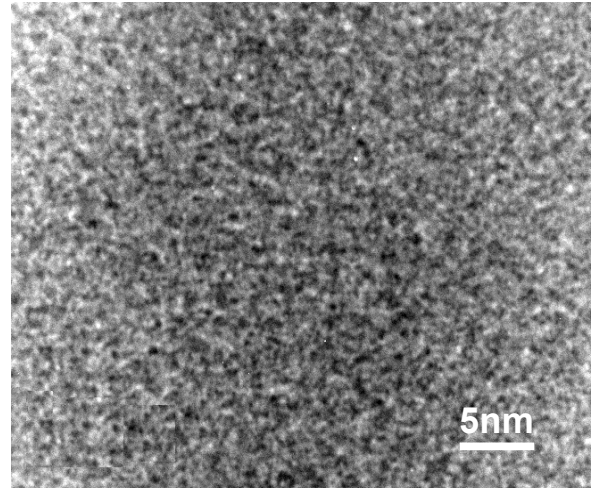
The grain size increased with increasing Ti concentration. On average, TiC [111] crystallites were largest followed by that of TiC [200] and the TiC [220] crystallites were smallest. For TiC [111], the grain size increased from 3 to 17 nm as the Ti incorporated increased from 8 to 48 at.%. With increasing Ti, there are more  $\text{Ti}^{4+}$  ions readily available for the growth of TiC crystallites. At the same time, as Ti increases, the relative amount of a-C is reduced (c.f., Figure 5.14), thus the constraints exert on the growth of the

crystallites are alleviated. All these combine to result in an increase in the grain size of TiC with increasing Ti incorporation.

Figure 5.17 shows the TEM micrographs of coatings with different Ti contents. At 3 at.%Ti, no TiC grains were seen. The coating was amorphous. At 8 at.% Ti, the TiC grains in the a-C matrix were observable: a few grains scattered within an a-C matrix. The density of grains increased with increasing Ti content in the coating. At 45 at.%Ti, very little a-C was seen. The coating contains almost only large TiC grains. Also, it is difficult to recognize the grains in the matrix. Therefore, a bright field image is included for easier recognition of the grains and estimation of their size. Above 8 at.%Ti incorporation, the diffraction patterns of coatings were almost similar: sharp rings with almost uniform intensity for the [111], [200] and [220] directions (c.f. Figure 5.18). This indicates a random orientation ([111], [200] or [220]) of the TiC grains in the a-C matrix. The observation from TEM agrees well with results obtained from XRD. The intensity of the TiC [311] and TiC [222] is very weak indicating that very few TiC crystallites are oriented these directions. Therefore, the Bragg's peaks of TiC [311] and TiC [222] (at  $72.3$  and  $76.2^\circ 2\theta$ , respectively) were not observable in the XRD spectra. The grain size observed from the TEM micrographs as compared to that calculated from XRD spectra is plotted in Figure 5.19. The trend of grain size observed from TEM and XRD was the same: the grain size increased as increasing Ti content in the coating. However, the grain size calculated from XRD spectra was smaller than that observed from TEM. In the calculation of grain size (using the Debye-Scherrer formula) the effect of microstrains (due to the residual stress) in broadening the Bragg's peak was ignored. This assumption results in smaller values of grain size obtained from calculation compared to the real one.

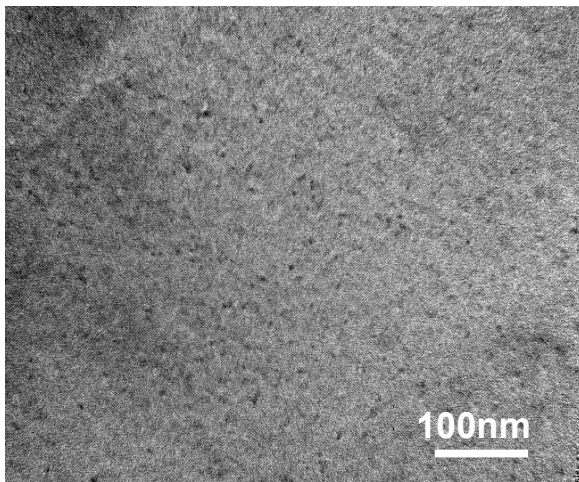


(Amorphous)

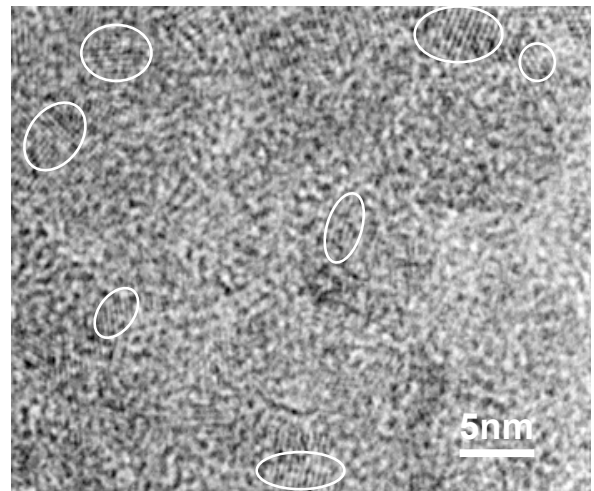


(Amorphous)

3 at.%Ti

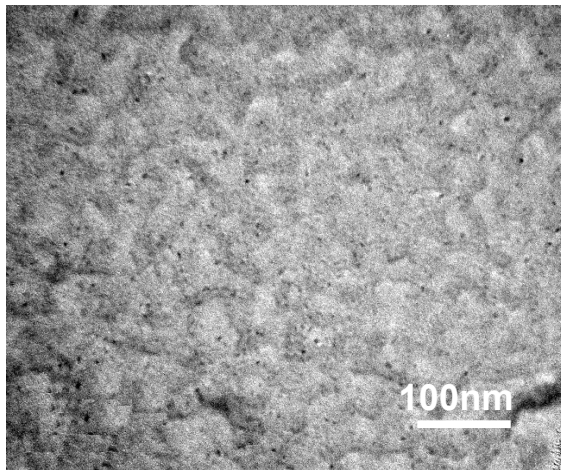


(Dark spots are nanograins)

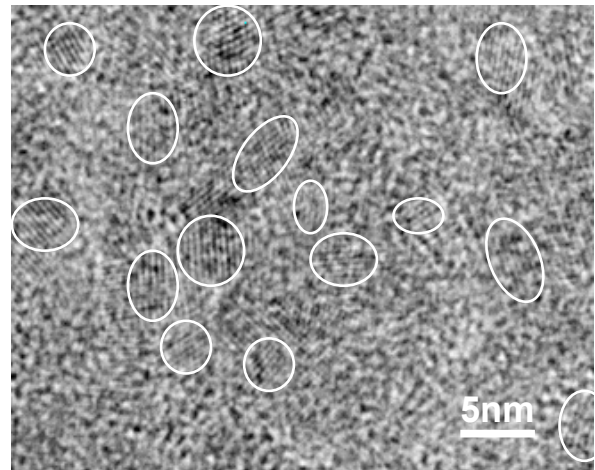


8 at.%Ti

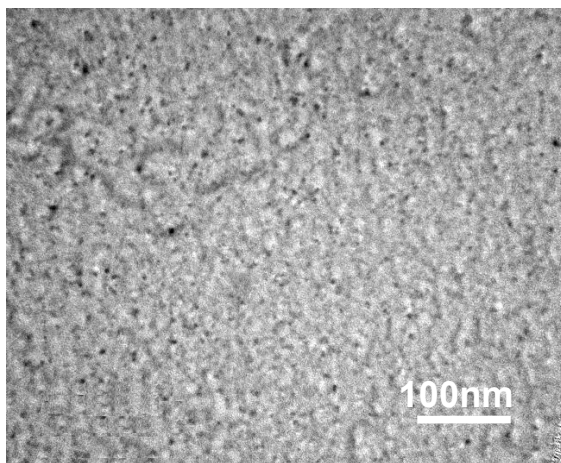




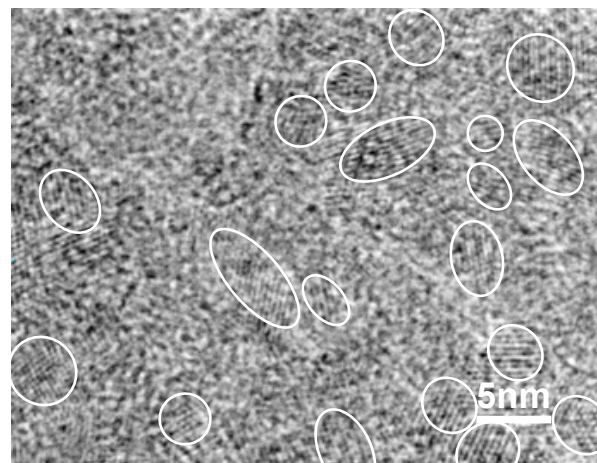
(Dark spots are nanograins)



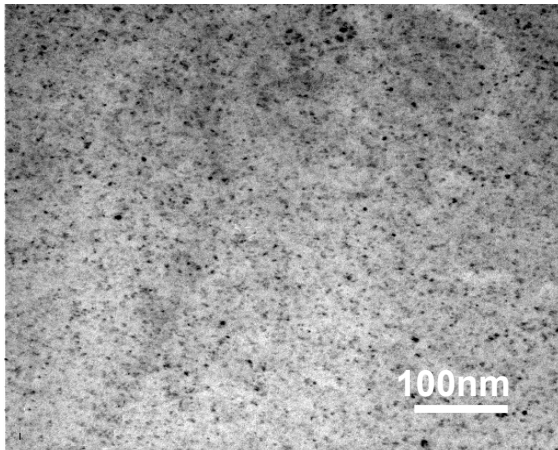
16 at.%Ti



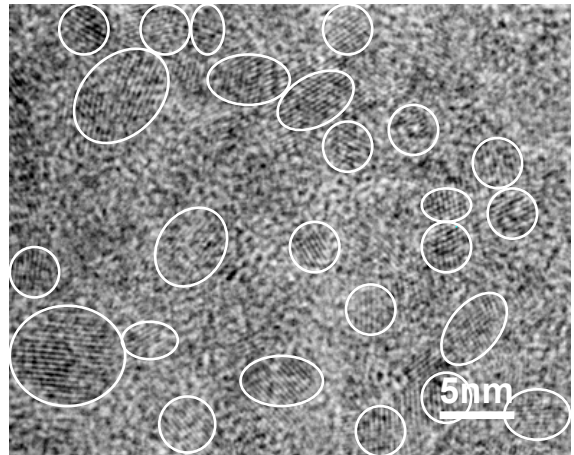
(Dark spots are nanograins)



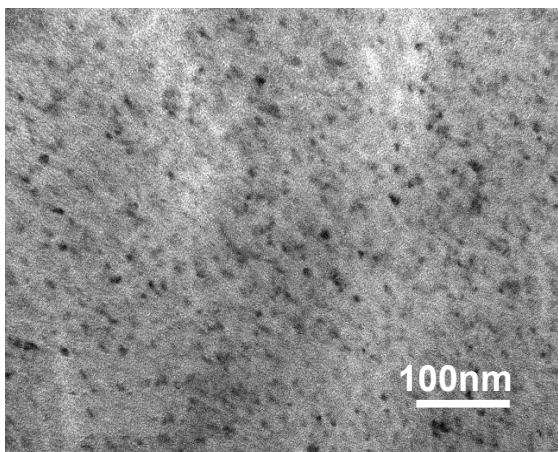
25 at.%Ti



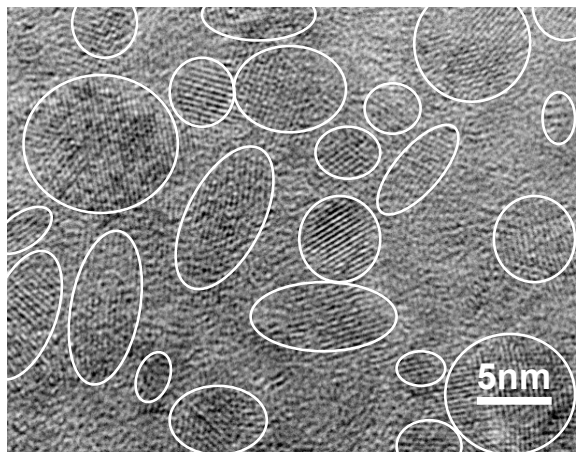
(Dark spots are nanograins)



30 at.%Ti

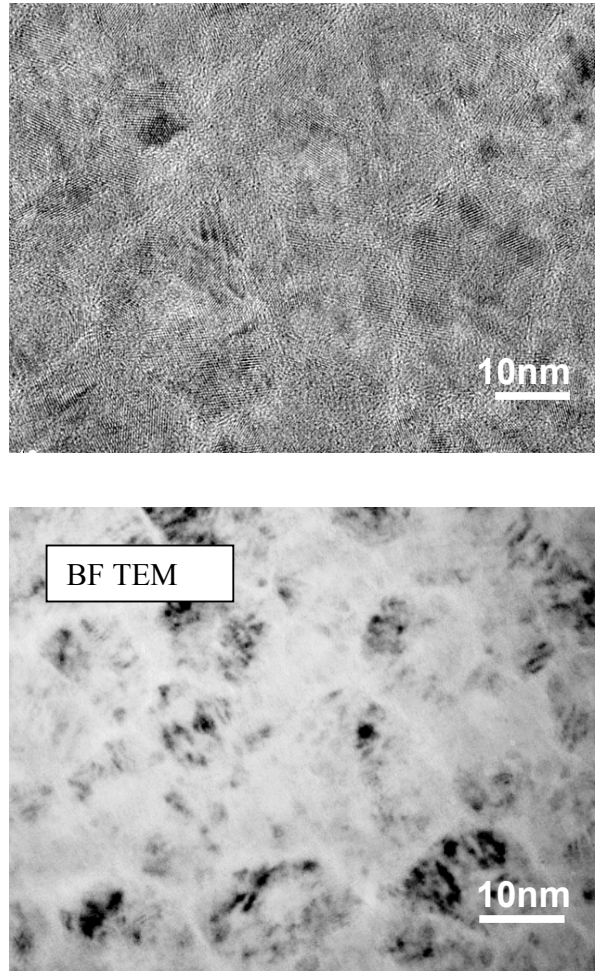


(Dark spots are nanograins)



36 at.%Ti





45 at.%Ti

Figure 5.17. TEM micrographs of coatings with different Ti contents. At 3at.%Ti, the coating is amorphous. The TiC nanograins are observed from 8 at.%Ti onwards. The size and fraction of crystallites increase with increasing Ti content. At 45 at.%Ti, the coating contains almost TiC grains (bright field (BF TEM) is added for an easier recognition of grains )

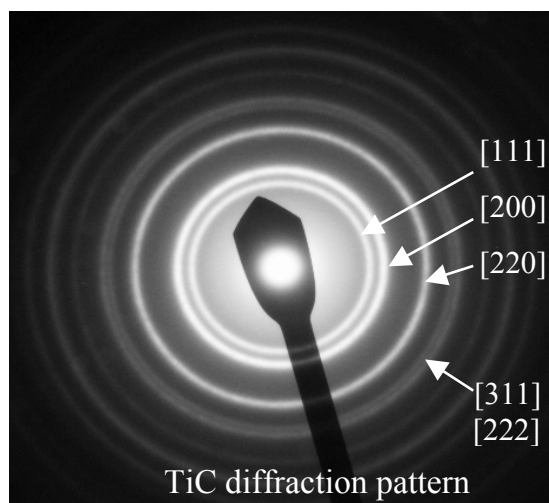


Figure 5.18. Diffraction pattern of nc-TiC/a-C coatings indicating the random orientation of the TiC crystallites

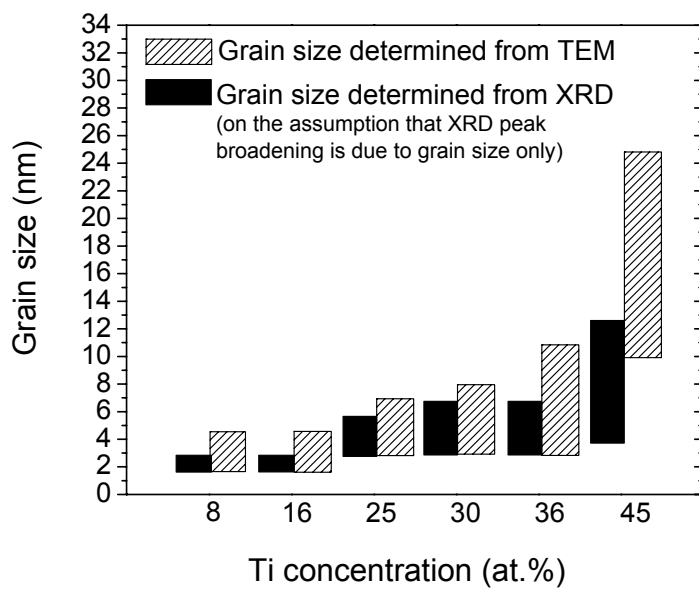


Figure 5.19. Grain size of TiC determined from TEM and XRD. The grain size increases as Ti content increases

Table 5.3. Summary of the structure of nc-TiC/a-C deposited under -150 V bias with different compositions of Ti (from XPS, XRD and TEM results).

| Ti content (at.%) | Composite Description  | TiC grain size (nm) | TiC phase volume (%) | a-C interface thickness (nm) |
|-------------------|--|---------------------|----------------------|------------------------------|
| 0                 | Amorphous  | 0                   | 0                    | N/A                          |
| 3                 | Amorphous  | 0                   | 0                    | N/A                          |
| 8                 | { Random inclusion of TiC grains encapsulated into a-C matrix      | 2-5                 | 5                    | >10                          |
| 16                |  | 2-5                 | 18                   | <10                          |
| 25                | { Considerable amount of TiC grains encapsulated in the a-C matrix | 3-7                 | 28                   | <10                          |
| 30                |  | 3-8                 | 39                   | <8                           |
| 36                |  | 3-11                | 69                   | <5                           |
| 45                | Almost TiC grains with a minor amount of a-C phase                 | 10-25               | 93                   | <2                           |

Raman spectra and the  $I_D/I_G$  ratio for nc-TiC/a-C coatings are shown in Figure 5.20. From the figure, the intensity of the carbon peak decreased as more Ti was added into the coating and no peak was seen for the coating “doped” with 45 at.% Ti. This is due to the decrease of a-C when more Ti was added (Ti bonds with C to form TiC). As seen from Figure 5.14, when 45 at.% Ti was added, the coating contained only 10 at.%C. Such a small amount was not enough to produce a peak in the Raman spectrum.

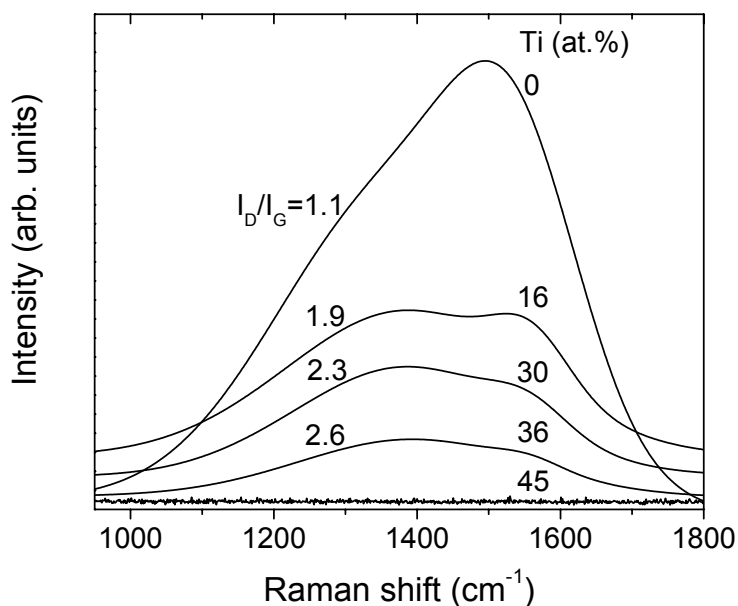


Figure 5.20. Raman spectra of nc-TiC/a-C nanocomposite coatings for compositions of Ti of 0, 16, 30, 36, and 45 at. %

The increase of the  $I_D/I_G$  ratio indicates that the  $sp^3$  fraction decreases when Ti is added. That is the same as the case of addition of Al. However, addition of Al resulted in a greater decrease in  $sp^3$  fraction (increase in  $I_D/I_G$  ratio). From Figures 5.8 and 5.20, addition of 16 at.%Ti resulted in an  $I_D/I_G$  ratio of 1.9 whereas the addition of only 9 at.%Al resulted in an  $I_D/I_G$  ratio of 2. The Al added goes into the a-C matrix and disturbs the carbon structure in comparison to the addition of Ti where the Ti forms nanograin TiC with C.

### 5.2.2. Hardness and residual stress

The trend of hardness and Young's modulus when "doping" Ti was different from the case of "doping" Al. Al exists in the coating as elemental Al and this leads to a decrease

of hardness as more Al is added due to the decrease of the  $sp^3$  fraction in a-C and Al itself is a soft metal. When Ti was added above a certain level, nanograins of strong phase TiC were formed. In this case, the hardness of the coatings was not only dependent on the  $sp^3$  fraction of a-C but also on the nanocrystalline phase of TiC (the size of grains, their volume fraction and distribution in the a-C matrix). Figure 5.21 plots the coating hardness and Young's modulus as a function of Ti concentration.

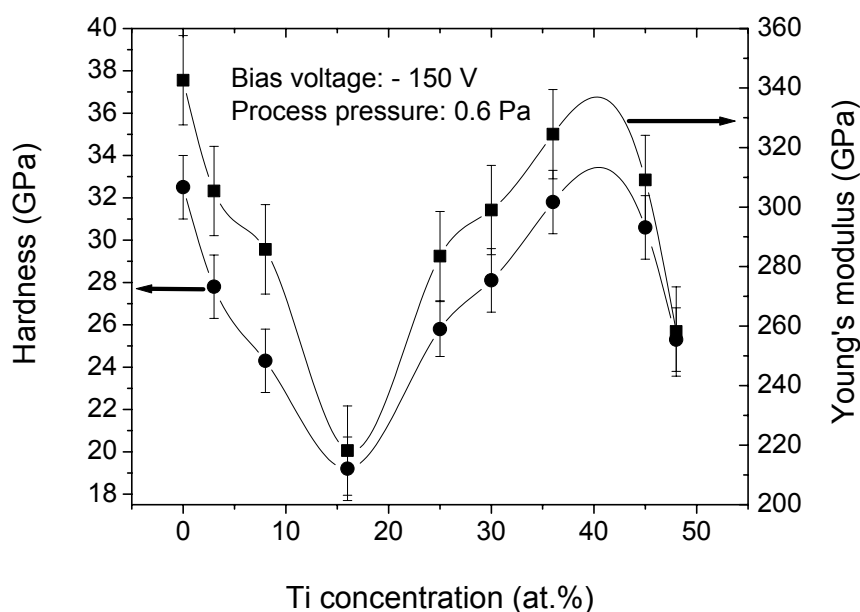


Figure 5.21. Coating hardness and Young's modulus of nc-TiC/a-C as a function of Ti concentration

Pure a-C coating had highest hardness and Young's modulus of 32.5 and 342.6 GPa, respectively. On increasing Ti content, the coating hardness decreased and then increased owing to different mechanisms: as discussed before, at low Ti content (less than 16 at.%),

the addition of Ti in the coating only serves as “doping” (virtually no TiC formation or very few TiC crystallites were found scattered in the a-C matrix, c.f., Figure 5.17 and table 5.3 ). Addition of Ti decreased the  $sp^3$  fraction in the a-C matrix (c.f., Figure 5.20) which resulted in a decrease in the hardness. Starting from 16 at.%Ti, a considerable amount of TiC nanograins were formed and these increased with increasing addition of Ti (c.f., table 5.3) resulting in a recovery of hardness to 32 GPa at 36 at.%Ti after off-setting the effect of the high  $sp^2$  fraction in the matrix. With further increase of Ti, the coating hardness decreased as a result of grain coarsening. A fitting curve connects the experimental data in Figure 5.21 indicates that a maximum hardness of about 32-33 GPa, which is comparable to that of pure a-C, can be obtained at Ti contents of 38 - 42 at.%. In this range of Ti content, the grain sizes of the TiC are about 3 - 25 nm, the a-C interface thickness is less than 5 nm and the volume fraction of TiC nanograins is about 70 - 90 % (c.f., table 5.3). It is clear that, superhardness (higher than 40 GPa) is not achievable in this case because the two simultaneous conditions required for superhardness are not satisfied. Firstly, the grain size of TiC is not small enough ( $< 10$  nm) to totally suppress the operation of dislocations, and secondly, the a-C interface is not thin enough ( $< 1$  nm) to support the coherence strain-induced enhancement of hardness [89].

The relationship between residual stress and Ti concentration is shown in Figure 5.22. When Ti was co-sputtered, the residual stress in the coating decreased from 4.1 GPa (a-C) to 0.9 GPa (16 at.%Ti) then increased gradually to 2.1 GPa at 45 at.%Ti. At higher Ti contents, it slightly decreased. The decrease of residual stress as Ti was added is understandable from the increase in  $sp^2$  fraction, which helps to relax the compressive stress accumulated in the coating during the deposition process. Also, it should be noted

that, the energy of the sputtered species coming to the substrate during co-sputtering of two targets (graphite and Ti) is considerably lower owing to more probability of collisions between species in the plasma compared to case when only the graphite target is sputtered. When a considerable amount of TiC is formed (from 16 at.%Ti) with association of less a-C inclusion, the hard phase of TiC hinders the relaxation of stress. The more TiC nanograins formed the less stress was relaxed leading to an increase in residual stress as more Ti was added. However, the highest residual stress observed in nc-TiC/a-C was about 2 GPa, which is much lower than that of pure a-C (about 4 GPa).

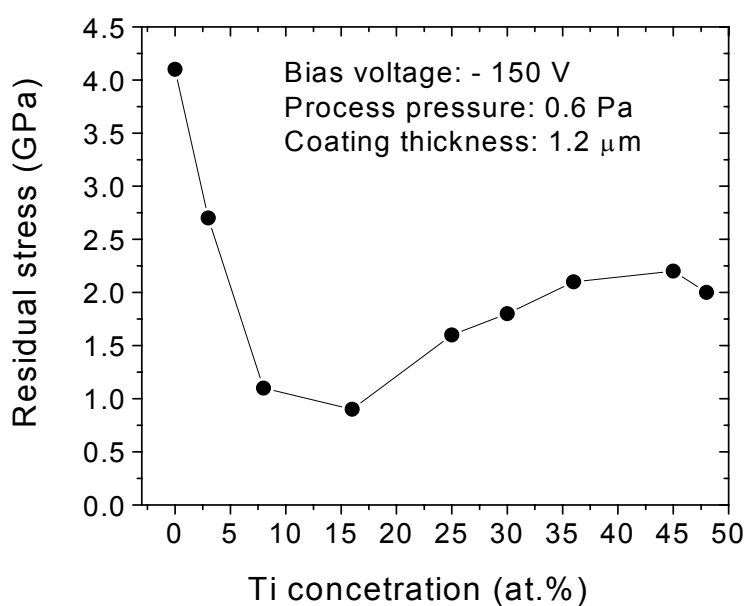


Figure 5.22. Residual stress of nc-TiC/a-C coatings as a function of Ti concentration

A high hardness (about 32 GPa) with a residual stress of only half of that of a pure a-C coating was obtained in nanocomposite nc-TiC/a-C. Therefore, co-sputtering Ti and carbon to form nanocomposites is an effective method to maintain the hardness at a high

level while keeping low residual stress. From Figures 5.10 and 5.22, it is clear that Al is better than Ti in reduction of residual stress.

### 5.2.3. Surface roughness and coefficient of friction in dry conditions

Figure 5.23 plots the surface roughness (with AFM images to illustrate the surface morphology of coatings) of nc-TiC/a-C coatings (1.2  $\mu\text{m}$  thickness, deposited on a Si wafer) as a function of Ti content. With increasing Ti content, surface roughness of the coatings increased. From the figure, at 3 at. % Ti, the surface roughness of the coating was 1.9 nm  $R_a$ , a little bit higher than that of pure a-C (1.1 nm  $R_a$ ). After that,  $R_a$  considerably increased to about 5 nm as 8 at.%Ti was added. From 8 to 36 at.%Ti,  $R_a$  gradually increased from 5 to about 8 nm. At higher Ti contents,  $R_a$  increased dramatically and reached a high value of 18.3 nm at 48 at.%Ti. From XPS, XRD, TEM and Raman results, it was clear that more Ti incorporation resulted in a large fraction of crystalline phase (thus less amorphous carbon) with larger grain size, which led to rougher morphologies.

Figure 5.24 shows the coefficient of friction of coatings sliding against a 100Cr6 steel ball in ambient air (22 °C, 75 % humidity). From the figure, the coefficient of friction increased from 0.17 to 0.24 as the Ti content increased from 3 to 36 at.%. The a-C matrix influences significantly the friction of nc-TiC/a-C coatings through the formation of a graphite-rich layer. As mentioned earlier, this layer acts as solid lubricant in humid air. When more Ti was added, more TiC crystallites formed thus less a-C matrix was in direct contact with the wearing ball. This resulted in less solid lubricant between the two sliding surfaces and higher coefficients of friction were seen. Another reason causing the increase



in friction was the increase of surface roughness as more Ti was added as mentioned above. The development of the coefficient of friction exhibited an abrupt change at about 45 at.% Ti. At that at.%Ti, the concentration of a-C was approximately 10 at.% (c.f., Figure 5.14). Such low amount of a-C can no longer transform into graphitic lubricant leading to a dramatic increase in coefficient of friction. The coatings, in this case, exhibited the same friction behavior as TiC.

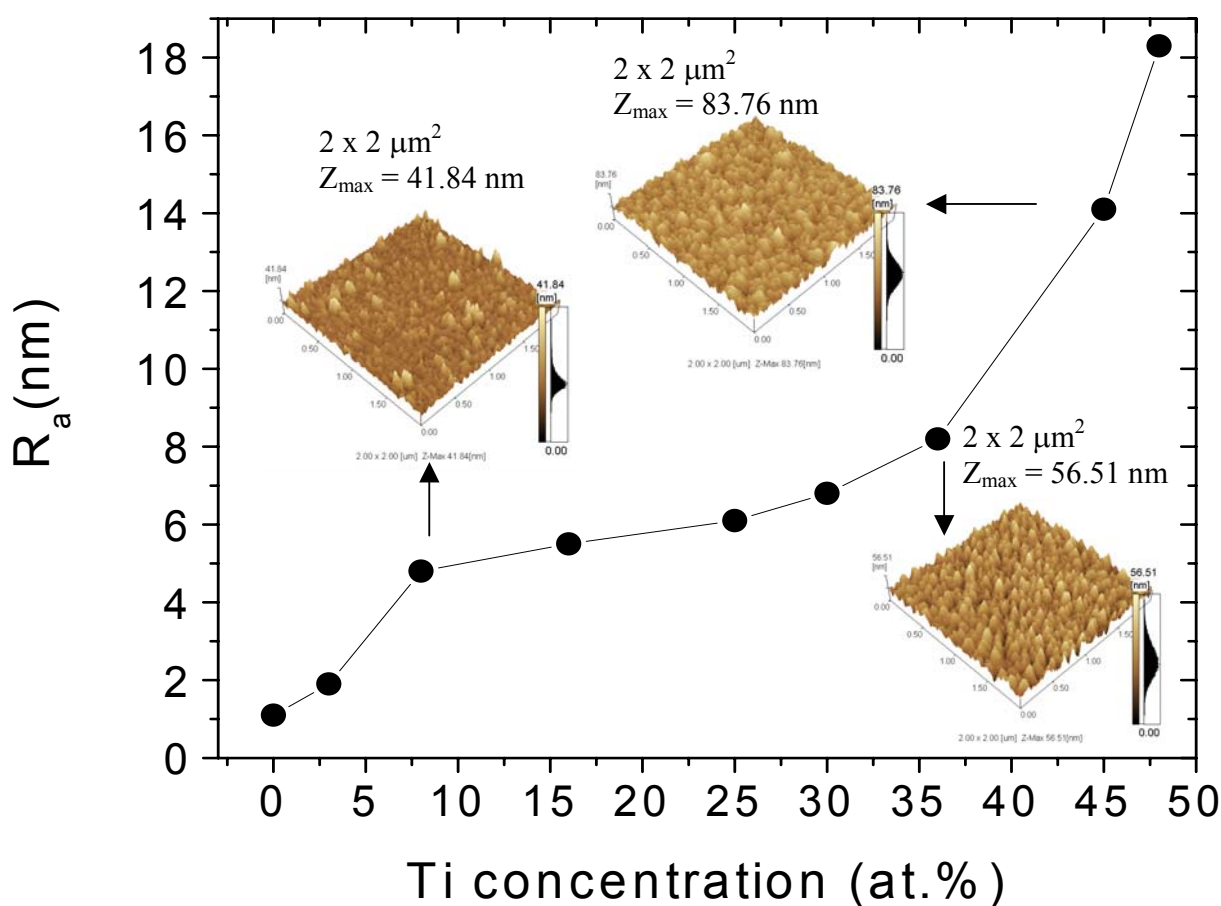


Figure 5.23. Surface roughness ( $R_a$ ) as a function of Ti concentration

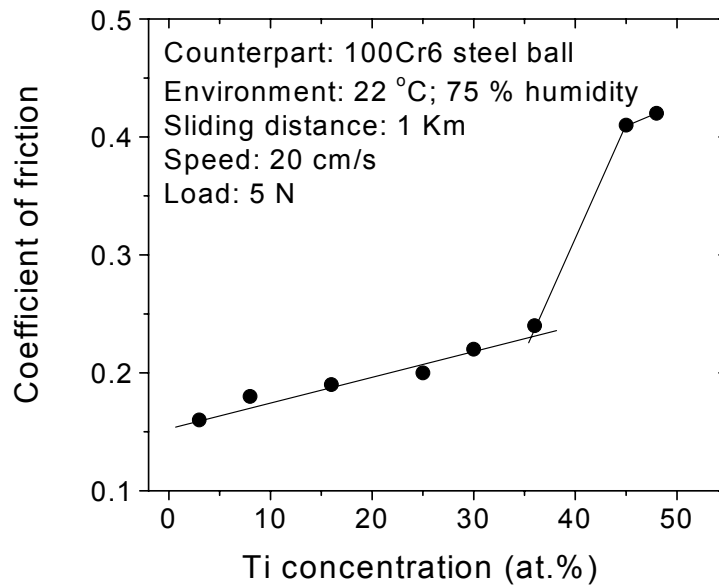


Figure 5.24. Coefficient of friction of nc-TiC/a-C coatings with different Ti contents (the values in the diagram were steady after 1 Km sliding). The coefficient of friction increases as more Ti is added to the a-C

### 5.3. nc-TiC/a-C(Al) nanocomposite coatings

This novel nanocomposite is designed to have high toughness, low residual stress, adequate hardness thus wear resistance, good thermal stability and oxidation resistance and low friction in dry and lubricated conditions. To satisfy these expectations, a spectrum of conditions must be met. The key design considerations are summarized as follows:

- A combination of hard crystalline TiC and a tough, relatively hard amorphous matrix of Al-“doped” DLC by co-sputtering of graphite, Ti and Al targets.
- To prevent the generation of thermal stress in the coating, a low temperature (<150 °C) should be used during the deposition process.

- The size of the TiC grains should be maintained at about 10 nm or less to minimize the operation of dislocations and restrict the crack size.
- To restrict the path of straight cracks the thickness of the amorphous interface should be as low as possible (< 10 nm is preferred).
- To facilitate grain boundary sliding, the nanograins should be randomly oriented.
- To enable self-lubrication, a sufficient amount of a-C should exist in the matrix. To ensure that the coefficient of friction does not exceed 0.25 in dry conditions, the content of a-C in the coating should be higher than 20 at.%.

#### **5.3.1. Deposition and structure of nc-TiC/a-C(Al) coatings**

As mentioned in the previous sections, the negative bias voltage did not significantly influence the composition when Ti or Al was co-sputtered with carbon. Therefore, the composition of nanocomposite coatings was controlled through changing the power density on the targets. The power density on graphite target was  $10.5 \text{ W/cm}^2$  for all samples. From section 5.2, it can be seen that with a power density on the Ti target of  $2.7 \text{ W/cm}^2$ , the amount of TiC crystalline phase is high enough to maintain a high hardness while the a-C content is adequate for self-lubrication to take place. Therefore, the power density on the Ti target was chosen to be  $2.7 \text{ W/cm}^2$ . The power density on the Al target was varied from  $0.6$  to  $1.8 \text{ W/cm}^2$  for different compositions. The substrates were biased at  $-150 \text{ V}$  and the process pressure was kept constant at  $0.6 \text{ Pa}$  during deposition for all samples. The composition of the coatings deposited with different power densities on the Al target were calculated from the areas under the C 1s, Ti 2p and Al 2p peaks in the XPS spectra. The results are tabulated in table 5.4 (the coatings were etched using an Ar ion

beam for 15 minutes before analysis; less than 4 at.% of oxygen contaminated was ignored in the calculations).

Table 5.4. Composition of nc-TiC/a-C(Al) coatings deposited

| Power density of Al target (W/cm <sup>2</sup> ) | Composition |    |    | Notation  |
|---|-------------|----|----|---|
|   | C           | Ti | Al |   |
| 0.6   | 62          | 35 | 3  | C <sub>62</sub> Ti <sub>35</sub> Al <sub>3</sub>  |
| 1.1   | 60          | 34 | 6  | C <sub>60</sub> Ti <sub>34</sub> Al <sub>6</sub>  |
| 1.4   | 57          | 32 | 11 | C <sub>57</sub> Ti <sub>32</sub> Al <sub>11</sub> |
| 1.8   | 56          | 31 | 13 | C <sub>56</sub> Ti <sub>31</sub> Al <sub>13</sub> |

Figure 5.25 shows the C 1s, Ti 2p and Al 2p XPS profiles of C<sub>56</sub>Ti<sub>31</sub>Al<sub>13</sub> coating. It should be noted that except for the intensity of the peaks, there was no difference between the XPS spectra of all four coatings. The results revealed from XPS spectra of the four coatings meet the expectations of the coating design:

- The Al existed in the coating as elemental Al. A symmetrical single peak at 72.6 eV was seen in the Al 2p spectra.
- Except for the bonds of the oxides, Ti - C was the only chemical bond found in the coating. The peaks at 281.8 eV in the C 1s profile and at 454.9 eV (461 eV for Ti 2p<sub>1/2</sub>) in the Ti 2p profile are attributed to TiC. This indicates that under the deposition conditions, other carbides such as aluminum carbide or aluminum-titanium carbide did not form.
- All Ti bonded with C to form TiC. No shift of the Ti 2p peaks to lower binding energies was seen from the spectra. Therefore there was no elemental Ti in the coatings.

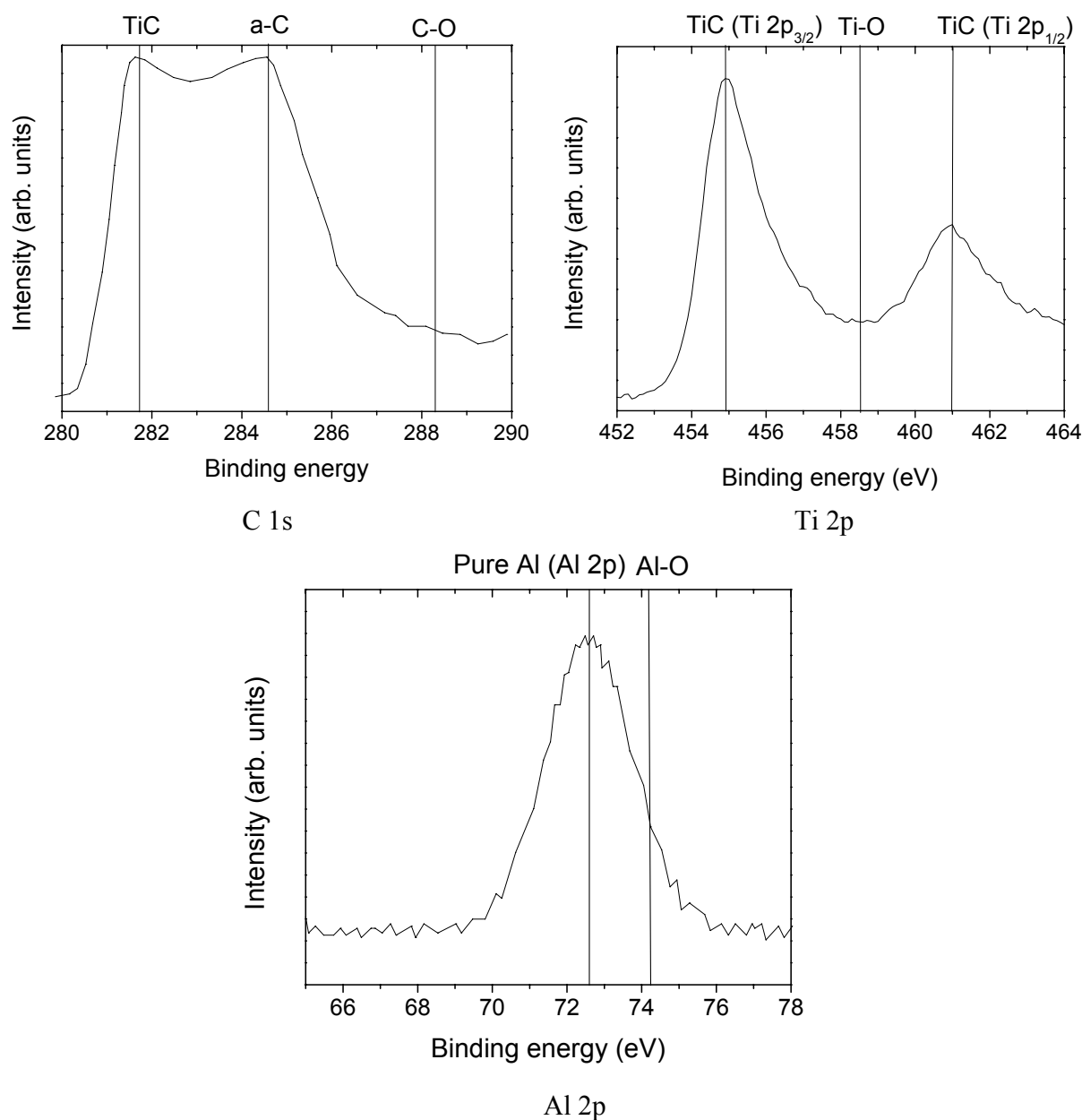


Figure 5.25. C 1s, Ti 2p and Al 2p XPS spectra of  $C_{56}Ti_{31}Al_{13}$  coating (power density of graphite:  $10.5 \text{ W/cm}^2$ , Ti:  $2.7 \text{ W/cm}^2$  and Al:  $1.8 \text{ W/cm}^2$ ) (15 minutes etching was applied before analysis)

XRD spectra of nc-TiC/a-C(Al) coatings are shown in Figure 5.26. It can be seen that TiC was the only crystalline phase in these coatings and the TiC nanograins were randomly

oriented with [111], [200], and [220] directions. The more Al added the lower the intensity of the peaks was since the amount of TiC was lower as more Al was added into the coating. However, as more Al was added, the peak intensities and the widths in all directions became more consistent, indicating uniform grain size and random orientation. As more Al was added, no shift of the peaks was seen, which indicated that the coating had low residual stress. According to XPS and XRD results, the structure of the four coatings is a nanocomposite with nanocrystallites of TiC embedded in the matrix of Al-“doped” DLC (nc-TiC/a-C(Al)). The grain size of all nc-TiC/a-C(Al) coatings was 2 - 5 nm as calculated from the XRD spectra using Debye-Scherrer formula (equation 3.1). The calculated values should be very near the real ones since nc-TiC/a-C(Al) had low residual stress (not much shift of TiC peaks was seen compared to the case of nc-TiC/a-C). Therefore the effect of residual stress on broadening the Bragg’s peaks was negligible.

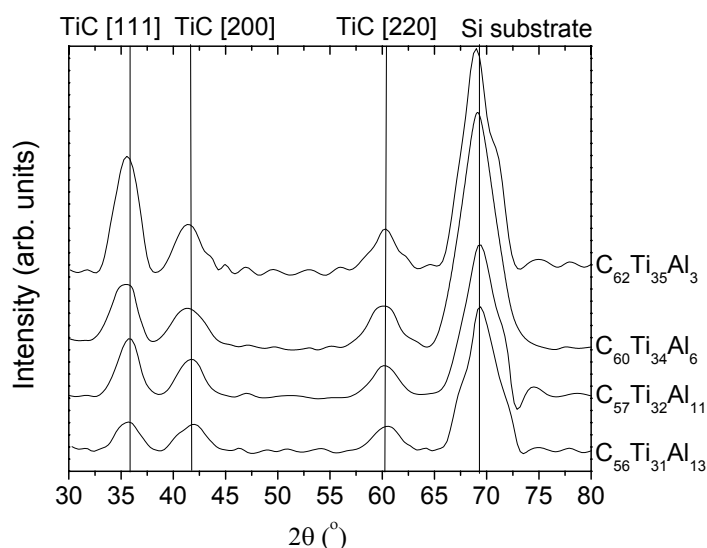


Figure 5.26. XRD spectra of nc-TiC/a-C(Al) coatings

Figure 5.27 shows the bright field (BF) with diffraction patterns (a) and HR TEM micrographs (b) of a nc-TiC/a-C(Al) ( $C_{56}Ti_{31}Al_{13}$ ) coating. The diffraction pattern confirmed the existence of randomly oriented TiC nanograins. Also the BF TEM shows a high volume fraction of TiC nanograins in the matrix of Al-“doped” DLC. The grain size was determined to be from 2-6 nm, which is very consistent with the results calculated from XRD (2-5 nm). From table 5.2 and 5.3, co-sputtering of graphite (10.5 W/cm<sup>2</sup>) and Ti (2.7 W/cm<sup>2</sup>) resulted in a nanocomposite nc-TiC/a-C coating (36 at.%Ti) with grain size from 3 to 11 nm. When Al was incorporated by co-sputtering of graphite (10.5 W/cm<sup>2</sup>), Ti (2.7 W/cm<sup>2</sup>) and Al (0.6-1.8 W/cm<sup>2</sup>), the grain size of TiC was less than 6 nm. It is clear that incorporation of Al reduces the grain size of TiC. The interface thickness of the amorphous phase was determined to be less than 5 nm, comparable to that of the nc-TiC/a-C coating.

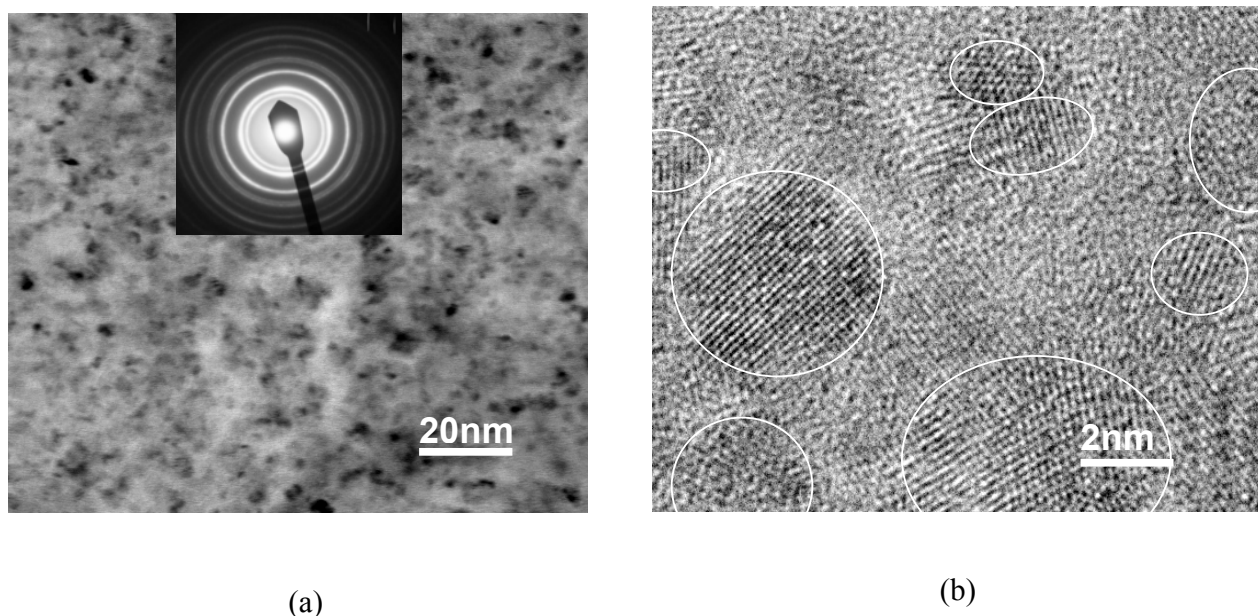
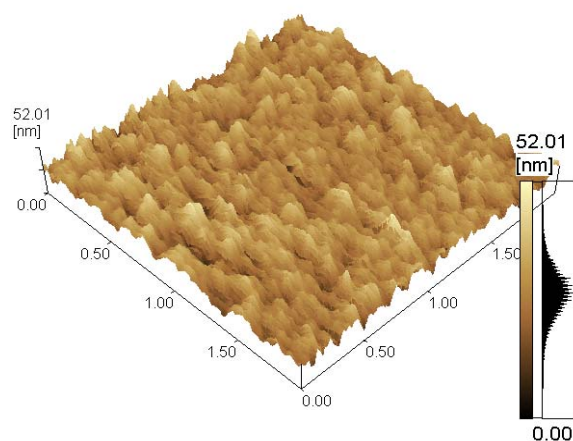
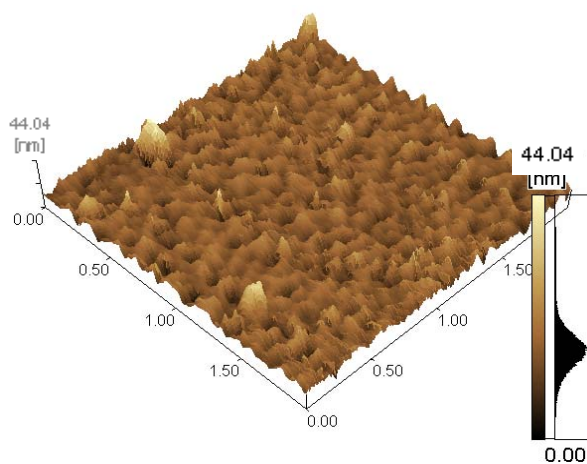


Figure 5.27. BF TEM (with diffraction pattern) and HR TEM of a nc-TiC/a-C(Al) ( $C_{56}Ti_{31}Al_{13}$ ) nanocomposite coating. In BF TEM, the dark spots are TiC nanograins

Figure 5.28 shows the surface morphology of nc-TiC/a-C(Al) ( $C_{62}Ti_{35}Al_3$  and  $C_{56}Ti_{31}Al_{13}$ ) coatings. The surface roughness of  $C_{62}Ti_{35}Al_3$  and  $C_{56}Ti_{31}Al_{13}$  was 6.9 and 5.4 nm  $R_a$ , respectively. nc-TiC/a-C(Al) has a smoother morphology than nc-TiC/a-C and more Al added resulted in an even smoother surface.



(a)



(b)

Figure 5.28. AFM images of  $C_{62}Ti_{35}Al_3$  and  $C_{56}Ti_{31}Al_{13}$  nanocomposite coatings



### 5.3.2. Mechanical properties of nc-TiC/a-C(Al) coatings

Mechanical properties of DLC, nc-TiC/a-C and nc-TiC/a-C(Al) coatings investigated in this study are tabulated in table 5.5.

Table 5.5. Mechanical properties of DLC, nc-TiC/a-C and nc-TiC/a-C(Al) coatings

| Coatings       | Deposition<br>[power density (W/cm <sup>2</sup> )] |     |     |         | Stoichio-<br>metry                                | Hardness<br>(GPa) | Young's<br>modulus<br>(GPa) | Stress<br>(GPa) |
|----------------|--|-----|-----|---------|---|-------------------|-----------------------------|-----------------|
|                | C  | Ti  | Al  | Bias(V) |   |                   |                             |                 |
| DLC            | 10.5   | 0   | 0   | -150    | C   | 32.5              | 342.6                       | 4.1             |
| nc-TiC/a-C     | 10.5   | 2.7 | 0   | -150    | C <sub>64</sub> Ti <sub>36</sub>                  | 31.8              | 324.5                       | 2.1             |
| nc-TiC/a-C(Al) | 10.5   | 2.7 | 0.6 | -150    | C <sub>62</sub> Ti <sub>35</sub> Al <sub>3</sub>  | 27.3              | 297.5                       | 1.3             |
| nc-TiC/a-C(Al) | 10.5   | 2.7 | 1.8 | -150    | C <sub>56</sub> Ti <sub>31</sub> Al <sub>13</sub> | 19.5              | 220.4                       | 0.5             |

The hardness and Young's modulus of nc-TiC/a-C(Al) was less than that of DLC and nc-TiC/a-C. However the big benefit here was the low residual stress of the nc-TiC/a-C(Al) coatings. As investigated in sections 5.1 and 5.2, addition of Al or Ti into DLC considerably reduced the residual stress of the coating. When Al and Ti were added into DLC at the same time a low residual stress was obtained. It is interesting that C<sub>56</sub>Ti<sub>31</sub>Al<sub>13</sub> had very low residual stress of 0.5 GPa while its hardness was at the relatively high level of about 20 GPa. Such hardness is suitable for wear resistant applications in the engineering. More importantly, the low residual stress allows thick adherent coatings to be deposited leading to a long working life for the coating.

Figure 5.29 plots the load and unload curve of a nc-TiC/a-C(Al) ( $C_{56}Ti_{31}Al_{13}$ ) coating. The plasticity during indentation deformation was estimated to be 58 %. Such a very high plasticity indicates a high toughness for the coating (which can be visually seen from scratch tests). From Figure 4.38, it can be seen that the plasticity of DLC and bias-graded DLC was considerably lower than that of nc-TiC/a-C(Al) (43 and 50 %, respectively).

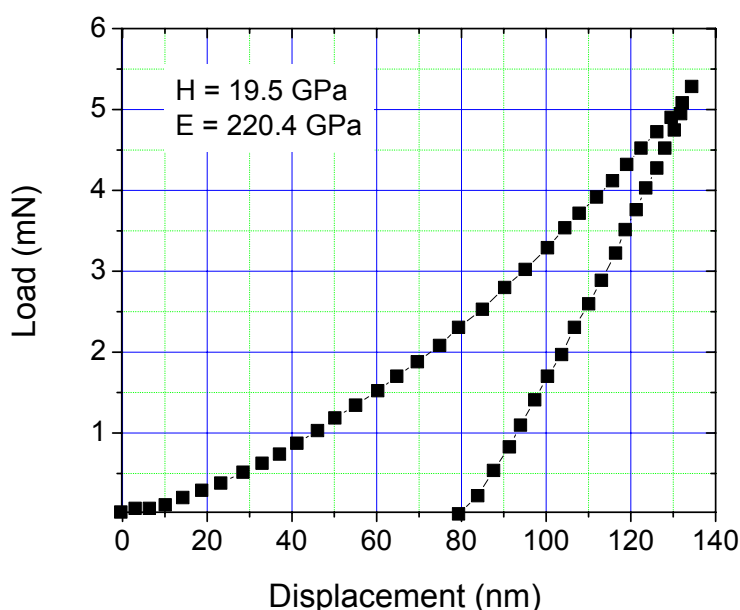


Figure 5.29. Load and unload curves from the nanoindentation of a nc-TiC/a-C(Al) coating. The plasticity of the coating was 58 %

Figure 5.30 plots the adhesion strength (in terms of the lower critical load from scratch tests) of DLC (deposited at a constant bias of -140 V), bias-graded DLC (deposited at a bias rate of 2 V/min), nc-TiC/a-C ( $C_{64}Ti_{36}$ ) and nc-TiC/a-C(Al) ( $C_{56}Ti_{31}Al_{13}$ ) coatings deposited on 440C steel substrates. As can be seen from the plot, DLC deposited under a high bias voltage of -140 V exhibited the lowest adhesion strength (118 mN). For bias-

graded DLC, the adhesion strength was 3 times higher (381 mN). Since the surface roughness was low for both DLC deposited under a constant bias of -140 V and bias-graded DLC (1.1 and 1.4 nm  $R_a$  on the Si wafer), the considerable increase in adhesion was attributed to the combination of low residual stress and high toughness of the bias-graded DLC especially at the interface between the coating and substrate. The adhesion strength of the nc-TiC/a-C coating was 253 mN, more than twice that of DLC deposited under -140 V bias owing to a much lower residual stress and the toughness enhancement of the nanocomposite configuration (the size of the cracks was limited and their propagation was hindered). However, this critical load was still lower than that of the bias-graded DLC coating (381 mN) because of two reasons. Firstly, the residual stress of nc-TiC/a-C was higher than that of bias-graded DLC (2.1 GPa compared to 1.5 GPa). Furthermore, it should be noted that the residual stress was obtained from the change in curvature of a whole [100] Si wafer, i.e., an average of the whole coating regardless of possible variation due to structural grading in case of bias-graded deposition. In bias-graded DLC coatings, the  $sp^3$  fraction increases from the substrate-coating interface towards the outer surface of the coating. The local residual stress at the interface should be a lot lower than that close to the surface (where  $sp^3$  is the highest). Secondly, the roughness of nc-TiC/a-C was 8.2 nm  $R_a$  (on a Si wafer), which was much higher than that of the bias-graded DLC coatings (1.4 nm  $R_a$  on Si). This resulted in higher friction and thus higher shear stress at the contact area. These two reasons gave rise to a higher critical load for the bias-graded DLC compared to that of nc-TiC/a-C. In the case of the nc-TiC/a-C(Al), a very high critical load of 697 mN was obtained. The extremely low residual stress of 0.5 GPa played an important role in this. Another important contribution can be attributed to the extremely high toughness as a consequence of adding Al to form an a-

C(Al) matrix in which nanosized TiC grains were imbedded. In this case, the propagation of the micro-cracks, which are generated in the scratch process, was hindered at the boundaries between the matrix and the grains. Meanwhile, the crack propagation energy was relaxed in the tough matrix. The smoothness of the surface (5.4 nm  $R_a$  on Si) also contributed towards the high critical load.

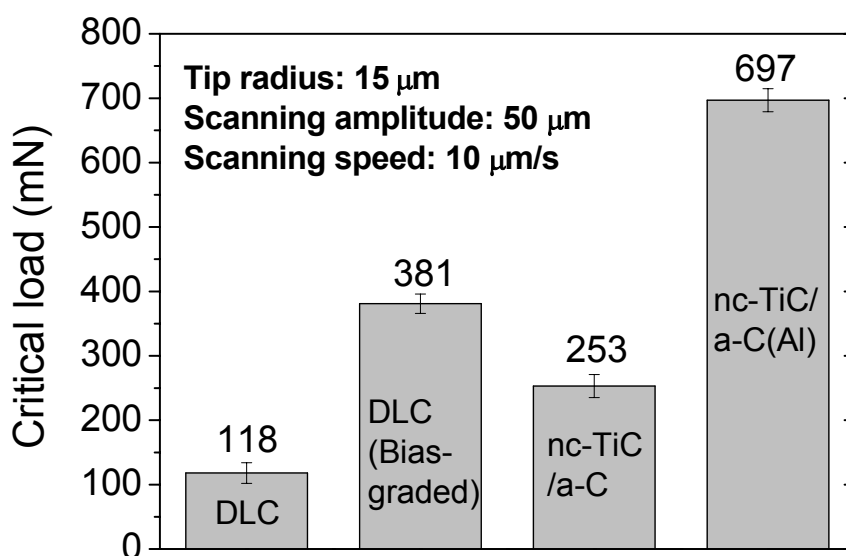
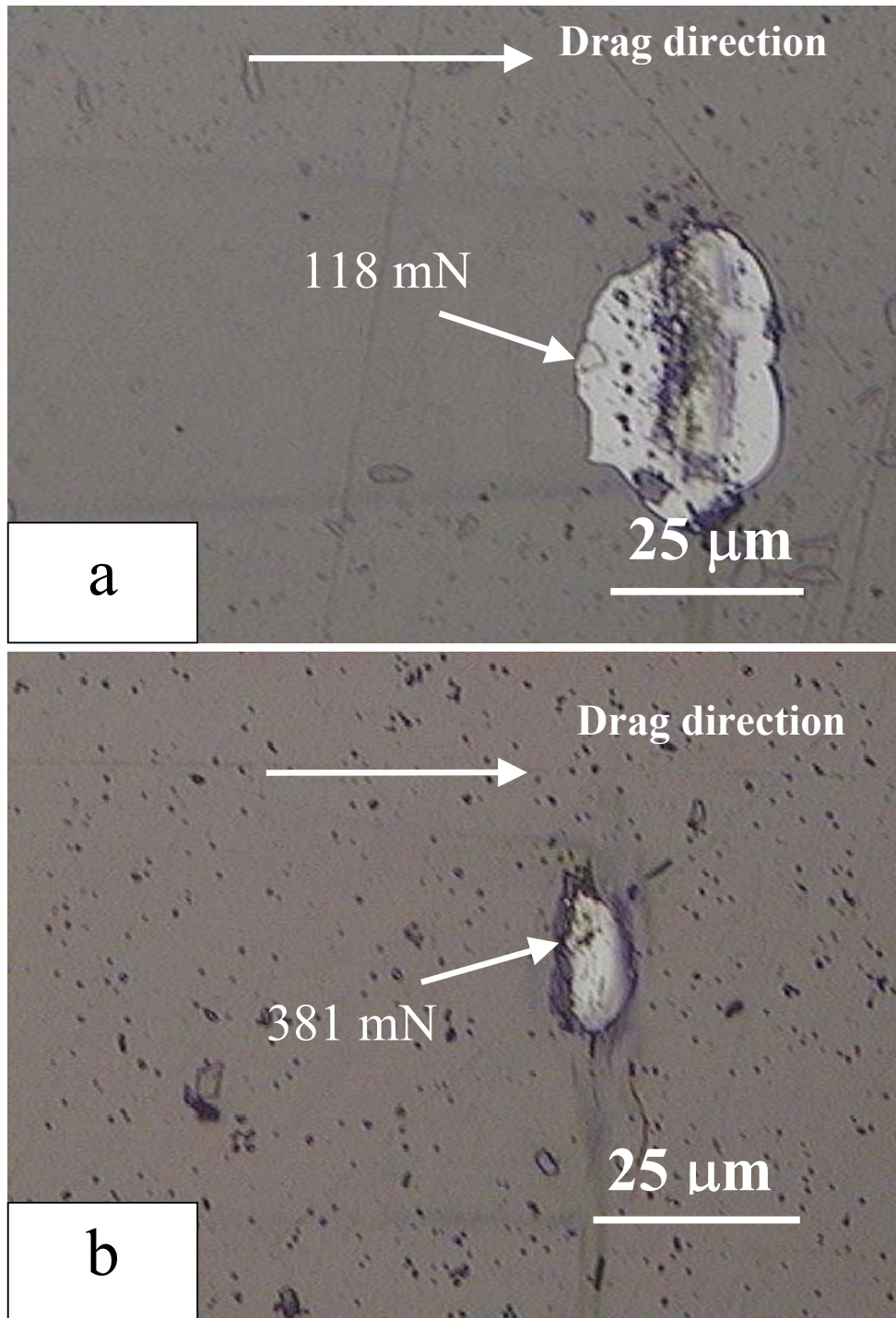


Figure 5.30. Lower critical load obtained from scratch tests of DLC (-140 V bias), DLC (bias-graded), nc-TiC/a-C, and nc-TiC/a-C(Al) coatings

As can be clearly seen from the optical micrographs of the scratch tracks in Figure 5.31, DLC coating deposited under -140 V bias delaminated in a brittle manner as the load reached 118 mN, and the lower critical load and the higher critical load were not distinguishable. For bias-graded DLC and nanocomposite coatings, however, damage inflicted on the coating was not continuous (sporadic) as load continued to increase (c.f., Figure 5.31 (b), (c) and (d)). The fractured surface of the nc-TiC/a-C(Al) coating appeared

very “plastic” (Figure 5.31 (d)): the cracks formed but did not produce spallation - instead, the tip was seen to plough into the coating. As the tip ploughed deeper, the scanning amplitude decreased because the force exerted on the tip to vibrate in the transverse direction was not enough to overcome the resistance created by the material piled up.





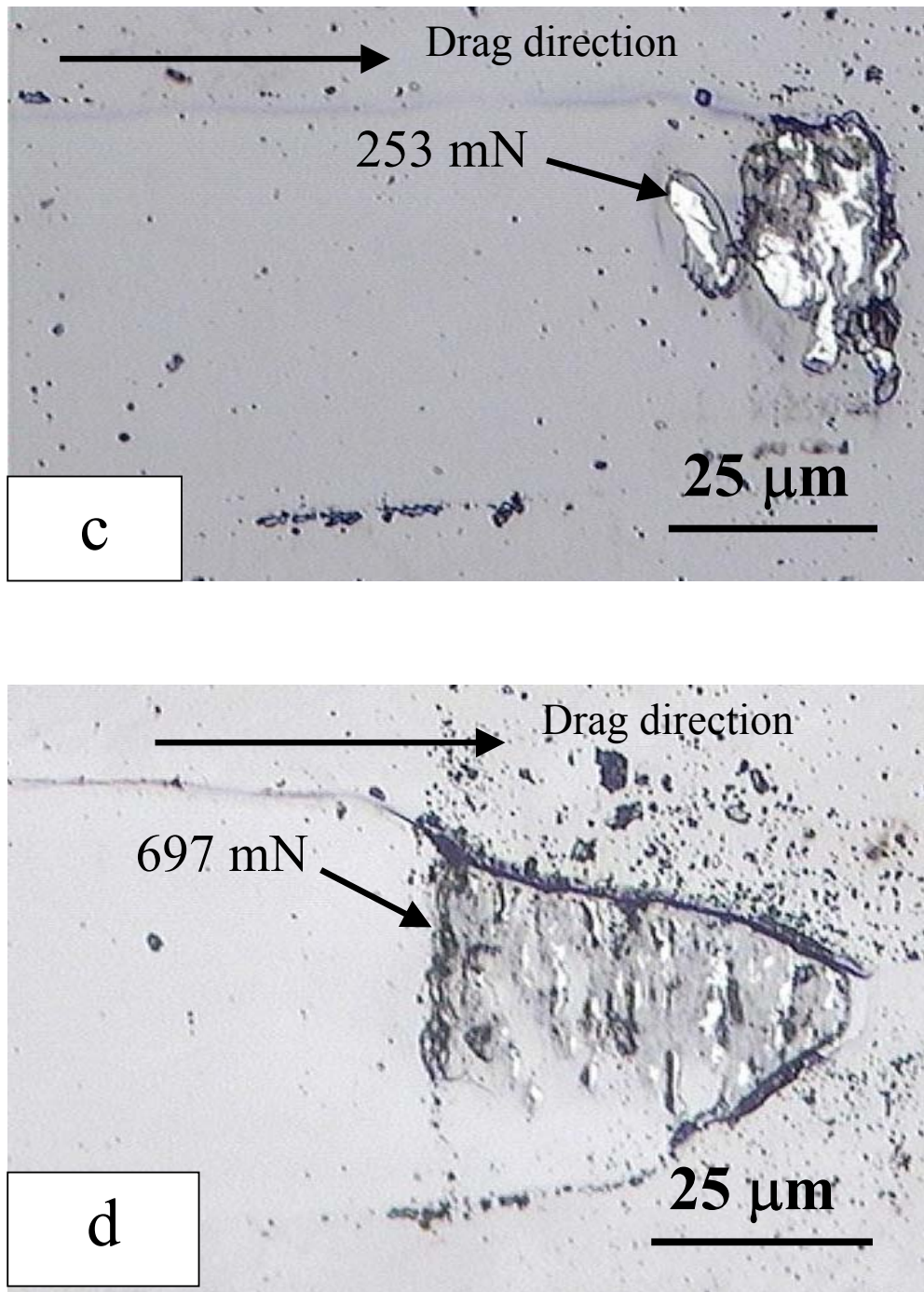


Figure 5.31. Optical micrographs of scratch tracks on the coating of (a) DLC deposited under constant bias of -140 V, (b) bias-graded DLC, (c) nc-TiC/a-C and (d) nc-TiC/a-C(Al)

#### 5.4. Thermal stability of nc-TiC/a-C(Al) coatings

$C_{56}Ti_{31}Al_{13}$  (19.5 GPa hardness) was used as the object of this study. Figure 5.32 shows the Raman spectra of the coating after 60 minutes annealing in an Ar environment at different temperatures. The  $I_D/I_G$  ratio of a-C in the matrix increased with increasing temperature. This behavior is the same for pure DLC where a more graphite-like structure was formed at high temperature. The change of the a-C structure happened as temperature exceeded 300 °C. At high temperatures (>500 °C) carbon in the matrix was almost graphite-like with a large cluster size. Further increase in temperature did not cause much increase in  $I_D/I_G$  ratio ( $I_D/I_G$  ratio increased from 4.5 to 4.6 as the temperature increased from 500 to 600 °C). Although the amount of graphite-like structure increased with temperature the coating hardness did not change much and remained as high as the original value of about 19 GPa up to 400 °C (c.f., Figure 5.33). Even after annealing at a high temperature of 600 °C for 60 minutes, the hardness was still as high as 17 GPa. This indicates good thermal stability for the coating. It should be noted that after annealing for 60 minutes at 400 °C, the hardness of pure DLC (32.5 GPa hardness) coating was only half of the original value (c.f., Figure 4.42), and at 500 °C, the hardness was only about 8 GPa. For pure DLC, the major contribution to the coating hardness is the  $sp^3$  fraction, which is sensitive to temperature. The hardness of nanocomposite coatings mainly comes from the hard nanocrystalline phase of TiC, which is not influenced as the temperature increases up to 600 °C. As can be seen from Figure 5.34, the XRD spectrum of nc-TiC/a-C(Al) before and after annealing in Ar was not noticeably different. Therefore, the hardness of the nanocomposite coating was less sensitive to temperature than pure DLC.

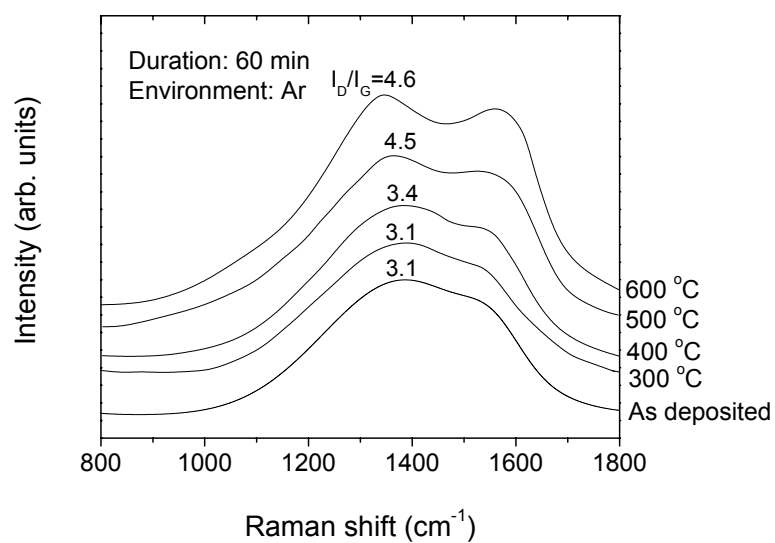


Figure 5.32. Raman spectra of nc-TiC/a-C(Al) nanocomposite annealed at different temperatures for 60 minutes in an Ar environment

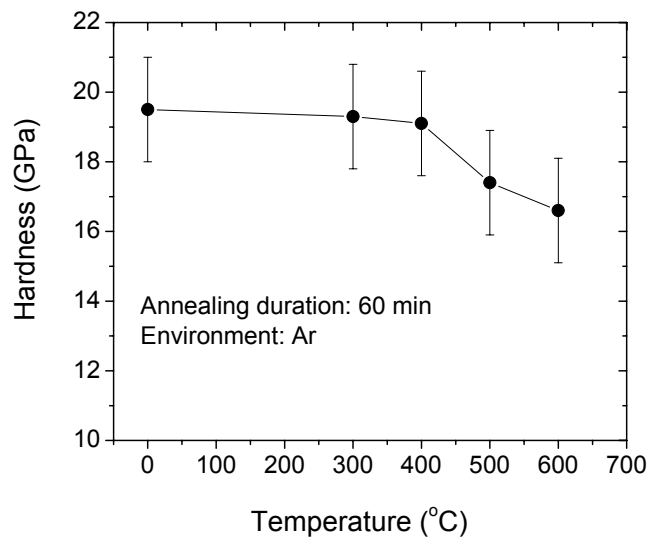


Figure 5.33. Hardness of nc-TiC/a-C(Al) nanocomposite as a function of annealing temperature



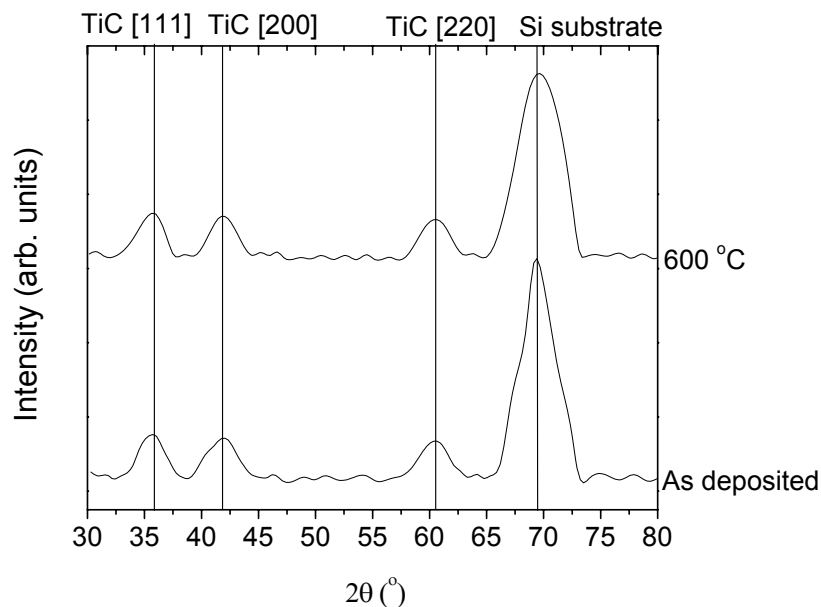


Figure 5.34. XRD spectrum of nc-TiC/a-C(Al) coating before and after 60 minutes annealing in an Ar environment at 600 °C

Figure 5.35 shows XPS spectra (Al 2p) of the nanocomposite coating after annealing at different temperatures in air. From the spectra, after unloading from the chamber, in atmosphere, all Al on the surface bonded with oxygen to form aluminum oxide (the peak at 74.2 eV). As the annealing temperature was increased to 600 °C, Al-O was the only chemical bond of Al detected. The Ti 2p spectra are shown in Figure 5.36. The peaks at 454.9 and 461 eV were attributed to TiC ( $2p_{3/2}$  and  $2p_{1/2}$ , respectively), at 458.6 and 464.3 eV to  $TiO_2$ , and at 456.2 and 462 eV to  $TiC_xO_y$ . As investigated in section 5.3.1, Ti in the coating mostly bonded with C in the TiC nanocrystalline phase. From the spectra, when the temperature was lower than 300 °C, the oxidation of TiC was very limited. The oxygen existed in  $TiC_xO_y$ . The formation of  $TiO_2$  was seen at an annealing temperature of

400 °C. From the results, it can be seen that TiC was considerably oxidized at about 400 °C. The oxidation, which leads to the formation of TiO<sub>2</sub> is expressed by the following reaction:



At 500 °C, a large amount of TiO<sub>2</sub> was formed (51 at.% Ti bonded with oxygen) and when the annealing temperature was increased to 600 °C, almost all the TiC was oxidized to form TiO<sub>2</sub>.

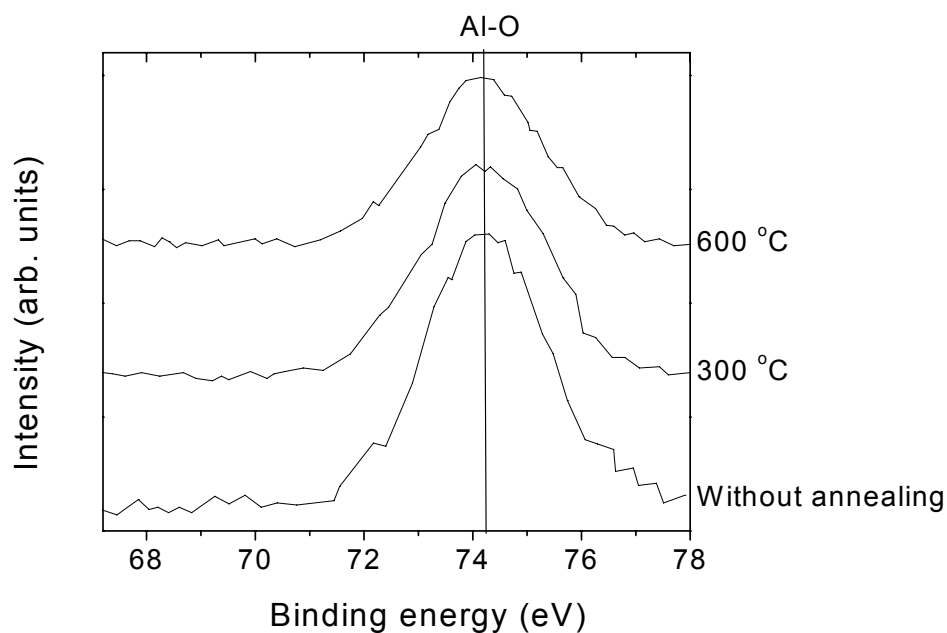


Figure 5.35. XPS spectra (Al 2p) of nc-TiC/a-C(Al) nanocomposite coating at different annealing temperatures in air for 60 minutes

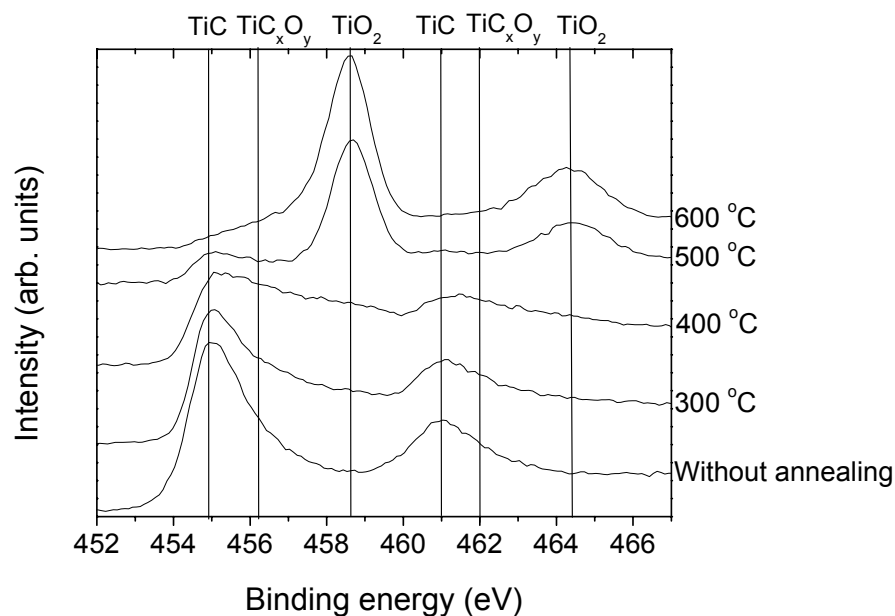


Figure 5.36. XPS spectra (Ti 2p) of nc-TiC/a-C(Al) nanocomposite coating at different annealing temperatures in air for 60 minutes

As mentioned in section 4.8 (chapter 4), the reaction between carbon and oxygen at high temperature (400 °C) resulted in the loss of coating thickness:



This also occurred on the surface of the nanocomposite coating where the carbon dioxide was formed from the reactions between TiC and oxygen (equation 5.1) and between C (in the matrix) and oxygen (equation 5.2). Aside carbon dioxide, aluminum oxide (formed at room temperature) and titanium oxide (formed at high temperature) are also products of the oxidation. These oxides remain on the coating and act as a barrier layer (especially aluminum oxide [154]) to prevent the diffusion of oxygen into the coating. Therefore, the

loss of coating thickness was not seen when annealing the nc-TiC/a-C(Al) nanocomposite in ambient air, even at 600 °C for 60 minutes (c.f., Figure 5.37). Also, it can be easily recognized that the formation of the oxide layer resulted in a very rough morphology.

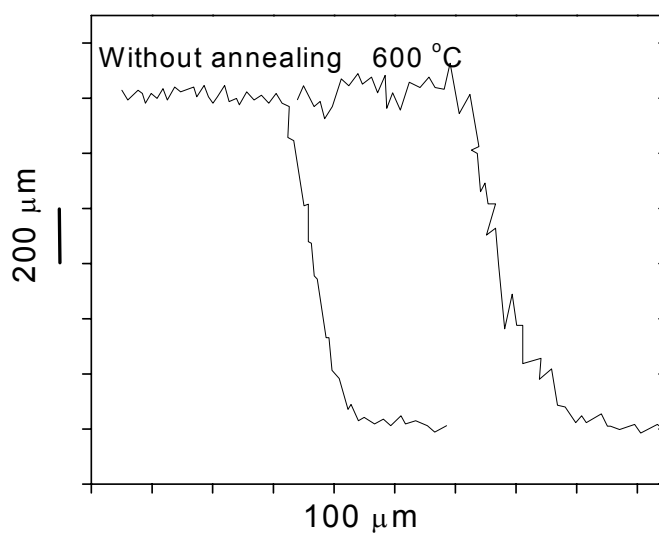


Figure 5.37. The coating thickness of nc-TiC/a-(Al) nanocomposite coating before and after annealing in air at 600 °C obtained from profilometer

The thickness of the oxide layer was determined from an XPS depth profile based on the oxygen percentage detected. It is determined as the etching depth at which the oxygen content was less than 4 at.% (this oxygen contaminated the coating during the deposition process) and does not change when more etching is continued. Figure 5.38 shows the XPS depth profiles of the coating without annealing, after 60 minutes annealing in air at 300 °C, and after 60 minutes annealing in air at 600 °C.

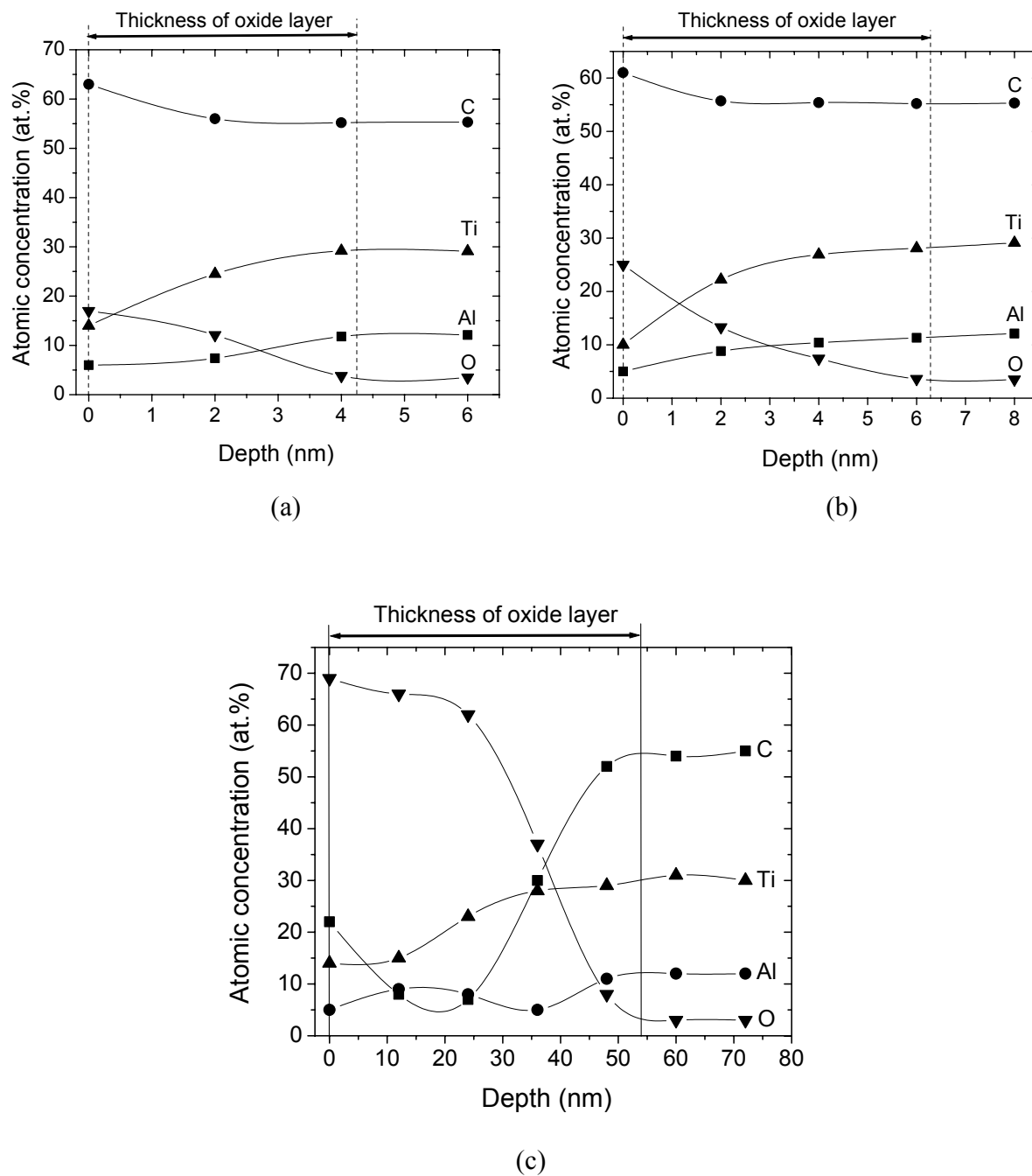


Figure 5.38. XPS depth profile of nc-TiC/a-C(Al) nanocomposite coating (a) without annealing (b) after annealing at 300 °C for 60 min and (c) after annealing at 600 °C for 60 minutes in air

As seen from the figure, without annealing, the thickness of oxide layer was about 4.2 nm. At 300 °C, the increase in thickness of the oxide layer was not significant (the thickness of oxide layer was about 6.3 nm). It should be noted that without annealing the thickness of oxide layer on the nanocomposite (Ti,Cr)CN/DLC was already about 20 nm [155]. At high temperature of 600 °C, the thickness of the oxide layer dramatically increased to about 55 nm. Under the same annealing condition, the oxide layer on the TiN coating was reported to be 200 nm and that on TiAlN was 35-180 nm depending on the Al content in the coating [154, 156]. These data illustrate the importance of Al in the oxidation resistance of the nanocomposite coating. The addition of Al, even at low amounts considerably enhances the oxidation resistance. As mentioned before, aluminum oxide is a good barrier to prevent oxygen diffusing into and oxidizing the coating. From the experimental results, nc-TiC/a-C(Al) exhibited much better oxidation resistance compared to that of pure DLC, DLC-based nanocomposites which do not contain Al such as (Ti,Cr)CN/DLC, and TiN. The oxidation resistance of nc-TiC/a-C(Al) was comparable to that of TiAlN under testing temperatures up to 600 °C.

## 5.5. Tribology of nc-TiC/a-C(Al) coatings

Tribological properties of a  $C_{56}Ti_{31}Al_{13}$  nanocomposite were investigated in comparison with that of pure DLC (deposited under -140 V bias) and nc-TiC/a-C ( $C_{64}Ti_{36}$ ).

### 5.5.1. Dry condition

Figure 5.39 plots the coefficient of friction of nc-TiC/a-C(Al) ( $C_{56}Ti_{31}Al_{13}$ ) and nc-TiC/a-C ( $C_{64}Ti_{36}$ ) when sliding against a 100Cr6 steel counterpart in ambient air as a function of

sliding distance. It should be noted that the amount of a-C in these nanocomposites was 23 and 30 at.% for nc-TiC/a-C(Al) and nc-TiC/a-C, respectively. For these two nanocomposite coatings, the a-C in the matrix was mostly graphite-like with a high  $I_D/I_G$  ratio (3.1 for nc-TiC/a-C(Al) and 2.6 for nc-TiC/a-C, respectively). Therefore, the graphite-rich phase was available for lubrication. This is different from pure DLC, where the graphite-rich lubricant layer can only form after graphitization taking place.

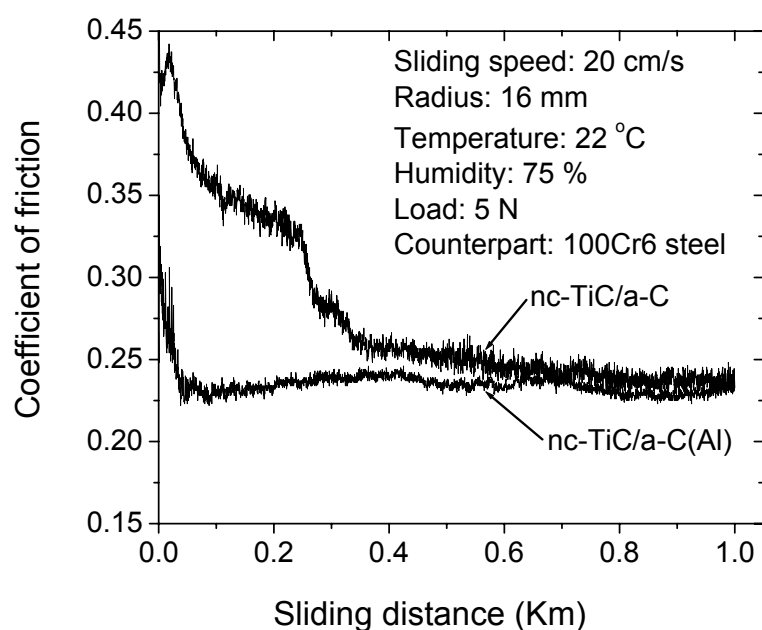


Figure 5.39. Coefficient of friction vs. sliding distance of nc-TiC/a-C(Al) ( $C_{56}Ti_{31}Al_{13}$ ) and nc-TiC/a-C ( $C_{64}Ti_{36}$ )

As seen from the figure, the running-in stage of nc-TiC/a-C(Al) was shorter (about 0.1 Km) with much lower coefficient of friction compared to that of nc-TiC/a-C. A 32 GPa hard nc-TiC/a-C has a rougher morphology (8.2 nm  $R_a$  on a Si wafer, c.f., Figure 5.23)

than that of a 19.5 GPa hard nc-TiC/a-C(Al) coating (5.4 nm  $R_a$  on a Si wafer, c.f., Figure 5.28). Such a rough surface with hard and large asperities (the size of TiC grains in nc-TiC/a-C is 5-11 nm compared to less than 6 nm in nc-TiC/a-C(Al)) in the nc-TiC/a-C resulted in higher friction with more vibration observed. It required considerably longer duration to reach a steady state. At steady state, the coefficient of friction of nc-TiC/a-C(Al) was about 0.23, a bit lower than that of nc-TiC/a-C (0.24) even though the amount of a-C was lower (23 at.% compared to 30 at.%). The main reason was the high hardness and roughness of the nc-TiC/a-C caused more wear of the steel counterpart as seen from the optical micrographs of the wear scars after the test (c.f., Figure 5. 40). The higher wear rate of the counterpart contributed more iron oxide into the tribolayer formed between the two sliding surfaces. The wear of the steel counterpart was lower when sliding against nc-TiC/a-C(Al) and the wearing coating contributed not only a-C but also Al (in the form of aluminum hydroxide since the tribotest was carried out in a high humidity condition) into the contact. As mentioned in section 4.6, aluminum hydroxide has lower shear strength compared to that of iron oxide giving rise to a slightly lower friction observed in nc-TiC/a-C(Al). From Figure 4.30 (chapter 4), at steady state, the coefficient of friction of pure DLC when sliding against a steel counterpart was 0.11-0.15 depending on the deposition conditions (bias voltage). Compared with these values, the friction of nanocomposite coatings was higher. This is due to the smoother surface of the pure DLC and much more graphite in the tribolayer (pure DLC contains 100 % C). However, the coefficients of friction of DLC nanocomposite coatings were much lower than that of popular ceramic coatings, which are currently used in industry such as TiN, TiC, CrN, etc. The coefficients of friction of these generally are from 0.4 to 0.9 [9, 42-44].



The wear track profiles on the coatings and wear scars on the balls after the tribotests for nc-TiC/a-C(Al) and nc-TiC/a-C are shown in Figure 5.40. For comparison, those of the DLC coating deposited under -140 V bias (32.5 GPa hardness) are also added. From the wear track profiles, it can be seen that the wear of nc-TiC/a-C and DLC coatings was very low and the wear track was not detectable. These coatings have much higher hardness (about 32 GPa) compared to that of 8 GPa of the steel counterpart. Wear of the counterparts, therefore, was very high with big wear scars observed. However, the wear scar on the ball sliding against DLC was smaller than that on the ball sliding against nc-TiC/a-C (the wear scar diameter was 498 and 575  $\mu\text{m}$ , respectively). Understandably, pure DLC has a much smoother morphology compared to that of nc-TiC/a-C and it contains 100 % a-C, which produces a larger amount of graphite-like lubricant in the contact area leading to a lower wear of the counterpart and lower coefficient of friction. Softer than nc-TiC/a-C and DLC, nc-TiC/a-C(Al) exhibited a lower wear resistance. The wear track on nc-TiC/a-C(Al) was observable. However, the wear of the counterpart, with the wear scar diameter of 387  $\mu\text{m}$ , was much lower than that formed by sliding against nc-TiC/a-C and DLC (where the wear scar diameter was 498 and 575  $\mu\text{m}$ , respectively).

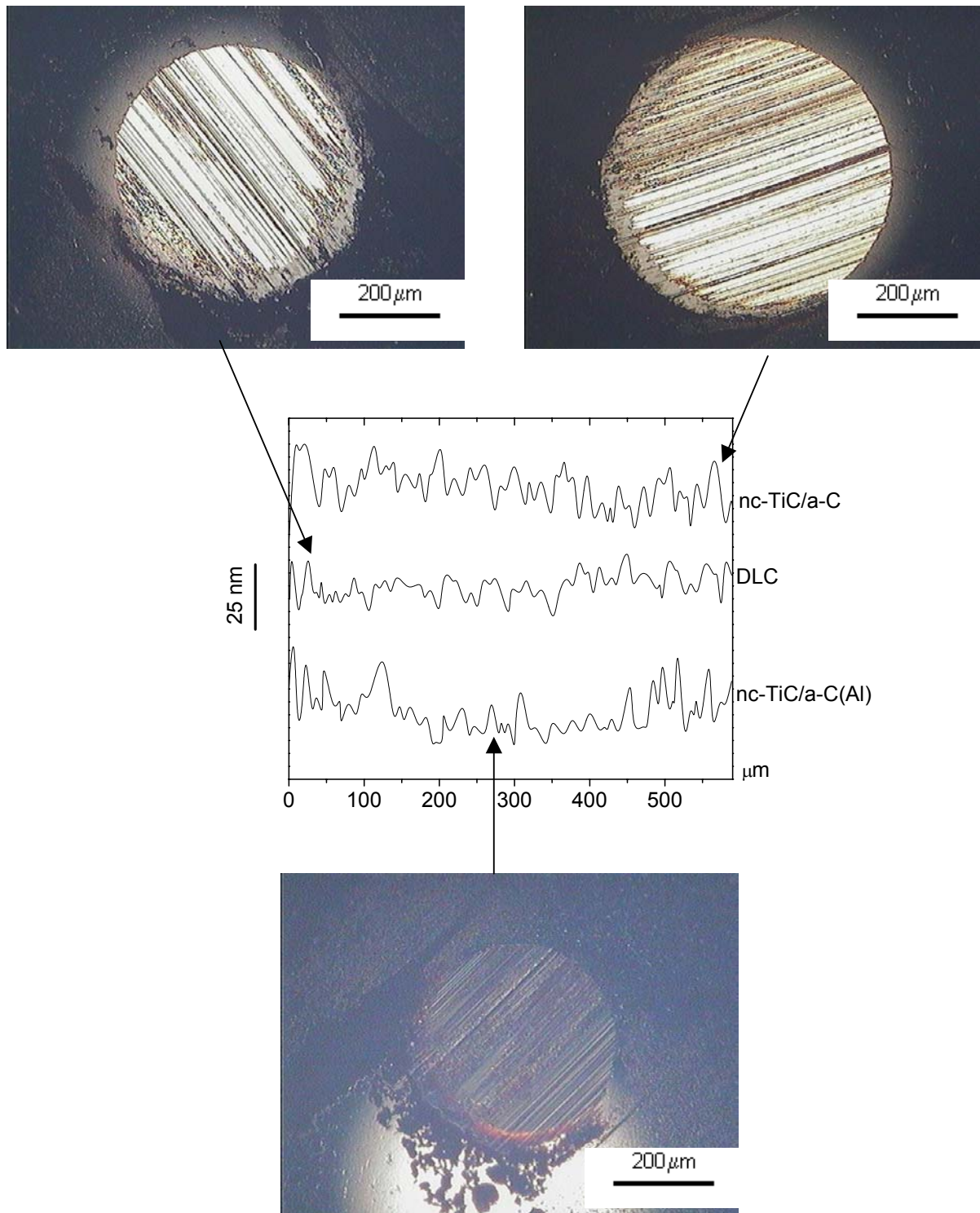


Figure 5.40. Wear track profiles on the coatings and wear scars on steel balls after 1 Km ball-on-disc tribotests in ambient air (22 °C, 75 % humidity)

### 5.5.2. Oil-lubricated condition

Under oil-lubricated conditions, the lubrication mechanism is totally different from that under dry conditions. With oil lubrication, the oil prevents the formation of the tribologically beneficial layer, changes the friction mechanism at the contact and governs the friction behavior of the oil-lubricated contact. Therefore, the thickness and stability of the oil film between the coating and counterpart surface plays an important role in friction and wear of coatings and counterparts. In oil-lubricated tribotests, because the oil is not pressurized into the contact, the oil film between the two surfaces is not thick enough to separate the coating surface and the counterpart. The lubrication regime, therefore, was boundary but not hydrodynamic and contacts between the asperities of the two surfaces occurred. Under such lubrication conditions, the interaction between the coating surface, counterpart surface with lubricating oil and the additive is vital in order to maintain the oil film (even very thin) for lubrication. Generally, the mechanism of boundary lubrication includes [157]:

- Formation of a layer of molecules adsorbed by Van der Waals forces. To form such layers a molecule must have a polar end, which attaches to the metal and a non-polar end, which associates with the oil solution. Therefore, to assure good adhesion of the oil to the tribo-surfaces, the first condition is that appropriate metal(s) must be added into lubrication oil (in Shell Helix oil Ca, Mg, and Zn are added).
- Formation of high-viscosity layers by reaction of the oil component in the presence of rubbed surfaces. This film may give a hydrodynamic effect and may be linked to the surface by Van der Waals forces.

- Formation of inorganic layers due to reactions between active oil components and the tribo-surface materials. These layers (sulphides, phosphides) have low shear strength and help to prevent scuffing (for this, in Shell Helix oil S and P are added).

It is well known that the interaction between oil and tribosurfaces, which results in good boundary lubrication occurs when tribosurfaces are metallic (e.g. steels or pure metals) and active metals produce a much better effect than inert metals [158].

Figure 5.41 plots the coefficient of frictions of nc-TiC/a-C(Al), nc-TiC/a-C and DLC coatings as a function of sliding distance. For the oil-lubricated condition, very low vibration allowed the accuracy in estimation of the coefficients of friction to be up to 3 decimal digits. From the figure, after the running-in stage, all three coatings exhibited very low coefficient of frictions (0.04-0.05) compared to that under dry conditions (0.15, 0.23 and 0.24 for DLC, nc-TiC/a-C(Al) and nc-TiC/a-C, respectively). nc-TiC/a-C(Al) exhibited the lowest friction followed by nc-TiC/a-C and DLC exhibited the highest coefficient of friction. The experimental results can be explained from the nature of the three coatings. DLC is a chemically inert material. Therefore the interaction between the oil and DLC coating was very limited. The DLC surface therefore was the “passive member” in the contact and such interactions occur only with the mating surface (steel ball counterpart). In the case of nanocomposite coatings, there is not only the interaction between steel counterpart and oil but also that between the oil and the coating’s surface due to the metals in the nanocomposite coatings. This resulted in a thicker and more stable oil film leading to the observed lower coefficients of friction. It can be easily seen that the nc-TiC/a-C(Al) coating has the best interaction with oil since Al is an active metal and it

exists in the coating as elemental Al. Therefore, it is not surprising that nc-TiC/a-C(Al) exhibited the lowest friction in the oil-lubricated condition. The wear tracks on all three coatings were not detectable after the tests indicating the excellent wear resistance of DLC, nc-TiC/a-C and nc-TiC/a-C(Al) under the boundary lubrication regime with engine oil.

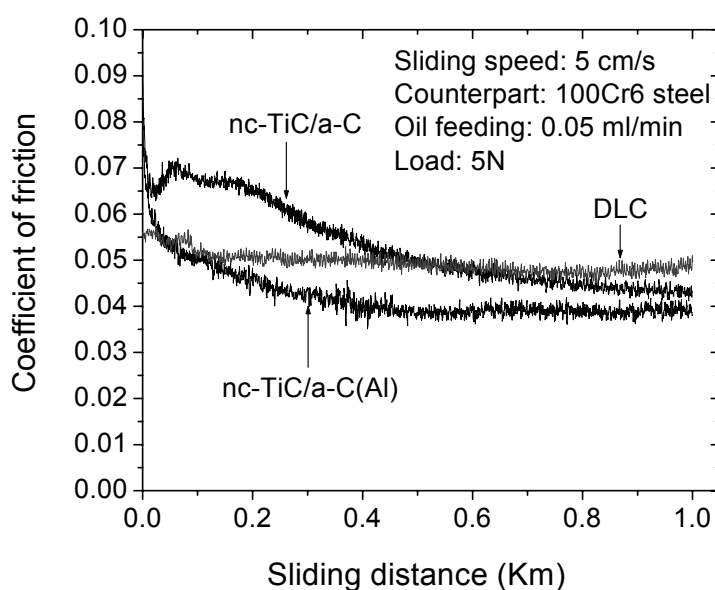


Figure 5.41. Coefficient of friction of nc-TiC/a-C(Al), DLC and nc-TiC/a-C as a function of sliding distance in the oil-lubricated condition

The wear scars on the ball after oil-lubricated tests are shown in Figure 5.42. The smallest wear scar was the one sliding against nc-TiC/a-C(Al) (with a diameter of 220  $\mu\text{m}$ ). The effective boundary lubrication, as mentioned above, resulted in the low wear of the counterpart. The wear of ball sliding against nc-TiC/a-C was highest (the diameter of wear scar was 246  $\mu\text{m}$ ) and that of the ball sliding against DLC was a little bit smaller (the

diameter of wear scar was 240  $\mu\text{m}$ ). The high wear observed on the ball when sliding against nc-TiC/a-C probably was the consequence of the rough morphology of nc-TiC/a-C coating. It is clear that nc-TiC/a-C(Al) possesses excellent tribological properties under oil-lubricated conditions with low friction (0.04) and excellent wear resistance (the wear was not detectable after 1 Km sliding against a 100Cr6 steel ball). Also, the wear of counterpart was much lower compared to that sliding against DLC or nc-TiC/a-C coatings.

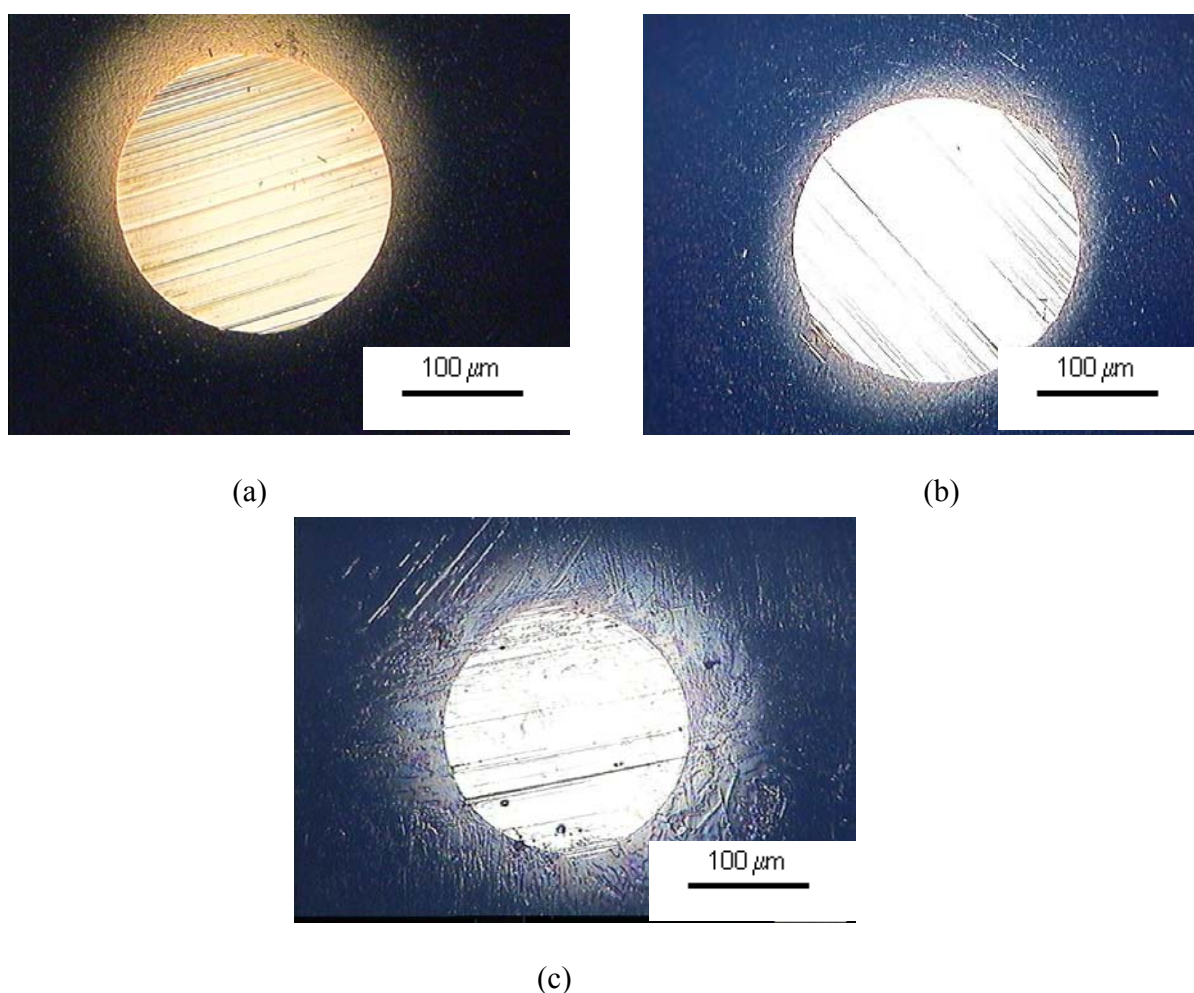


Figure 5.42. Wear scars on steel counterparts after 1 Km sliding against (a) DLC, (b) nc-TiC/a-C and (c) nc-TiC/a-C(Al) sliding under oil-lubricated condition



## 5.6. Summary

Studies in this chapter can be summarized as follows:

- At the same power density and process pressure, the negative bias voltage does not considerably influence the composition of coatings deposited via co-sputtering of graphite, Ti and Al targets. Therefore, changing the power density is an effective way to deposit nanocomposite coating with different compositions.
- Co-sputtering of Al and graphite targets results in a very low stress and tough Al-“doped” DLC (or a-C(Al)) coating at the expense of its hardness. Al exists as clusters of atoms in the coating.
- Co-sputtering of graphite and Ti forms a nanocomposite with TiC nanograins embedded in the amorphous matrix of DLC (nc-TiC/a-C). The size of the nanograins is strongly dependent on the Ti content (thus the power density of Ti target) and varies from a few to about 30 nm. Higher Ti content (higher power density on the the Ti target) results in a larger grain size and rougher surface morphology. The hardness of the nanocomposite coatings is not only dependent on the  $sp^3$  fraction of the DLC matrix but also (mainly) on the TiC nanograins (the size, the volume fraction and the DLC interface thickness). At low Ti contents (less than 8 at.%) the formation of nanograins is very limited with very few nanograins scattered in the a-C matrix. At high Ti contents (more than 45 at.%) the coatings mostly consist of nanocrystalline TiC and they exhibit TiC-like properties (rough surface and high friction). A high hardness of 32 GPa can be obtained with 36 at.% Ti added (the grain size is 3-11 nm and the DLC interface thickness is less than 5 nm) while the residual stress of this coating is only 2 GPa (half of that of pure DLC).
- Nanocomposite nc-TiC/a-C(Al) coatings where the randomly oriented nanograins of TiC (the grain size is less than 6 nm) are embedded in the matrix of Al-“doped” DLC were

deposited by co-sputtering of graphite, Ti and Al targets. A relatively high hardness of about 19.5 GPa was obtained. This coating has a very low residual stress of 0.5 GPa, smooth morphology (5 nm in Ra for a 1.2  $\mu\text{m}$ -thick coating deposited on a Si wafer) and exhibits very high adhesion strength (lower critical load of almost 700 mN). Furthermore, this nanocomposite exhibits “plastic” behavior instead of brittle as is usually observed in DLC or hard ceramic coatings. The plasticity during indentation of nc-TiC/a-C(Al) is as high as 58 %.

- Since the hardness of nc-TiC/a-C(Al) mainly comes from the TiC nanocrystallites, it is not sensitive to the temperature and remains at the original value (about 19.5 GPa) after annealing up to 400 °C for 60 minutes. At annealing temperature of 600 °C, the hardness still remains at a high value of 17 GPa.
- The oxidation resistance of nc-TiC/a-C(Al) coating is much better than that of pure DLC and TiN and is comparable to that of TiAlN.
- nc-TiC/a-C(Al) exhibits a low coefficient of friction in dry (0.23) and extremely low under oil-lubricated conditions (0.04). It exhibits good wear resistance in both dry and oil-lubricated conditions. Also, the wear of the steel ball when sliding against nc-TiC/a-C(Al) is much lower than that of the balls sliding against DLC and nc-TiC/a-C in both dry and oil-lubricated tests. nc-TiC/a-C(Al) is a good candidate for tribological applications, especially in poorly lubricated conditions.



## **CHAPTER SIX**

### **PRELIMINARY CASE STUDY: APPLICATION OF nc-TiC/a-C(Al) NANOCOMPOSITE AS PROTECTIVE COATING FOR PISTON RING IN INTERNAL COMBUSTION ENGINE**

So far, to the best knowledge of the author, there has not been any systematic investigation concentrating the application of DLC or DLC-based composites as protective coatings for piston rings in internal combustion engines. From the studies in chapter 4, pure DLC could not be used as a protective coating for piston ring since the high residual stress does not allow thick coatings to be deposited. The thickness of less than 1.5  $\mu\text{m}$  or even, a few  $\mu\text{m}$  (if bias-graded deposition is applied) could not meet the requirement of an acceptable mileage within one overhaul life of the engine. Furthermore, pure DLC coatings exhibit brittle behavior, bad thermal stability, and bad oxidation resistance. In chapter 5, the characterization of nc-TiC/a-C(Al) indicates that this material possesses excellent properties for tribological applications. The low friction in dry and boundary-lubricated conditions (much lower than that of conventional nitride and carbide coatings) will contribute much to the reduction of friction losses in the engine leading to a considerable decrease in fuel consumption. A high hardness of 20 GPa (comparable to TiN and higher than CrN) combined with good thermal stability and oxidation resistance (much better than TiN) gives the coating good wear resistance under extreme working

conditions of piston rings. Last but not least, low residual stress allows thick coatings to be deposited for a long working life.

In this study, the engine tests were carried out with a  $C_{56}Ti_{31}Al_{13}$  nanocomposite coating. The deposition conditions and mechanical properties of this coating were stated in table 5.5 (section 5.3.2, chapter 5). As a control coating, an 18 GPa hard TiN was also deposited by reactive magnetron sputtering on a piston ring at a power density on the Ti target of  $4 \text{ W/cm}^2$ , bias voltage of -80 V and process pressure of 0.6 Pa (40 sccm Ar + 10 sccm  $N_2$ ).

### 6.1. The engine

The engine used in this test is a two-stroke gasoline engine (c.f., Figure 6.1) with cylinder capacity of 41 cc, cylinder bore of 39.8 mm and stroke of 32.5 mm. The cylinder bore is plated with Cr.

A propeller with size of 18-10 (diameter: 18 inches, pitch: 10 inches) was installed to apply the load to the engine. An output of 2 HP is required for a revolution speed of 5000 RPM for this propeller. The maximum combustion pressure is 5.2 MPa. Referring to Figure 2.16, the maximum pressure on the working surface of the first piston ring (thus, on the coating) is estimated to be about 4 MPa ( $0.76 \times 5.2$ ). During the tests, the RPM of propeller was maintained at  $5000 \pm 100$  by controlling the fuel feeding. The fuel used for the engine was M92 gasoline mixed with 4 % Shell Helix Plus engine oil. The specification of Shell Helix Plus engine oil was stated in table 3.1 (section 3.2.4.4, chapter 3).



(a)



(b)

Figure 6.1. The engine (a) without propeller (b) installed with propeller for testing

## 6.2. Piston ring

The piston ring (c.f., Figure 6.2) was made from cast iron with alloying elements. The chemical composition is shown in table 6.1.

Table 6.1. Chemical composition of cast iron piston ring

| Element     | Fe   | C   | Si  | Mn  | Cr  | W    | V    | Ti   | P   | S    |
|-------------|------|-----|-----|-----|-----|------|------|------|-----|------|
| Content (%) | 92.1 | 3.9 | 2.4 | 0.6 | 0.2 | 0.15 | 0.15 | 0.05 | 0.4 | 0.05 |

The geometry of the ring:

Inside diameter: 36.32 mm

Outside diameter: 39.37 mm

Thickness: 1.65 mm

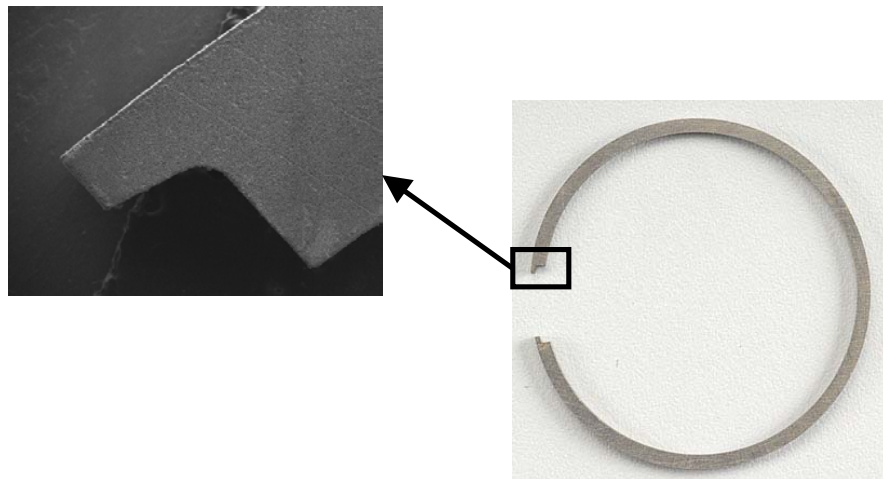


Figure 6.2. Piston ring and the ring gap area

The ring gap area (see Figure 6.2) was investigated since the wear of the ring gap area is more serious compared to other areas on the circumference of piston ring [106].

### 6.3. Testing procedure

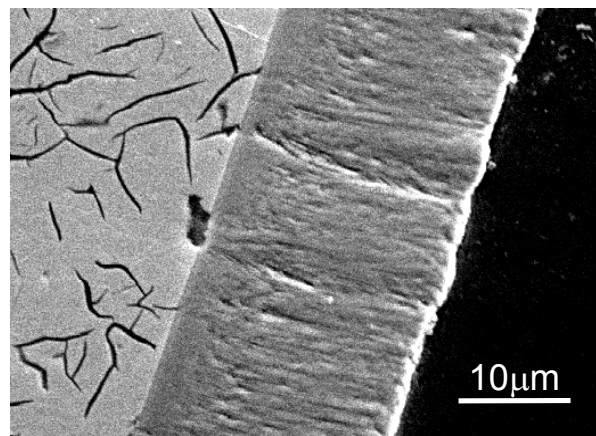
There were two types of samples. One type was the whole piston rings, which were utilized for engine tests. The other was pieces cut from the rings, after deposition, these pieces were polished to measure the coating thickness.

The engine tests were carried out for 610 hours. After the first 30 hours of running the piston rings were removed from the engine, then ultrasonically cleaned for 20 minutes to estimate the running-in wear by SEM. After that the rings were reinstalled and another 580 hours testing was carried out. Finally, the piston rings were removed then polished for SEM investigation.

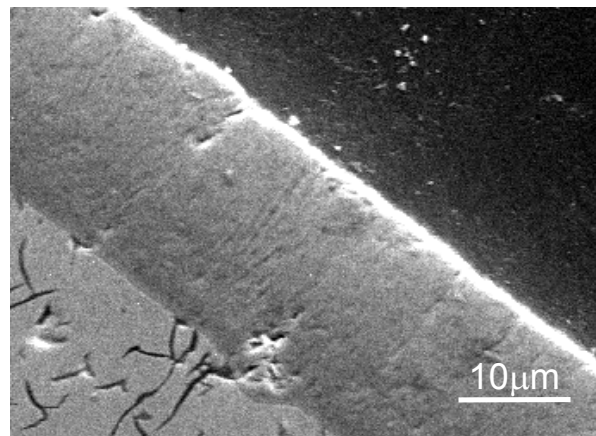
### 6.4. Results

The cross-sections of TiN and nc-TiC/a-C(Al) coatings deposited on piston rings are shown in Figure 6.3. From SEM images, 20 points were randomly chosen for measuring the coating thickness and the average was considered the coating thickness. Coating thickness of  $23.2 \pm 0.3$  and  $21.3 \pm 0.3$   $\mu\text{m}$  was estimated for TiN and nc-TiC/a-C(Al) coatings, respectively. The thickness of both coatings was consistent along the circumference of the piston ring. It can be recognized that nc-TiC/a-C(Al) exhibits a denser structure compared to TiN.

Figure 6.4 shows the fractography of TiN and nc-TiC/a-C(Al) coatings on piston rings after the first 30 hours testing. The remaining thickness was averaged from the values measured at 20 random points. The remaining thickness was estimated to be  $19.9 \pm 0.8$  and  $18.4 \pm 0.5$   $\mu\text{m}$  for TiN and nc-TiC/a-C(Al), respectively.

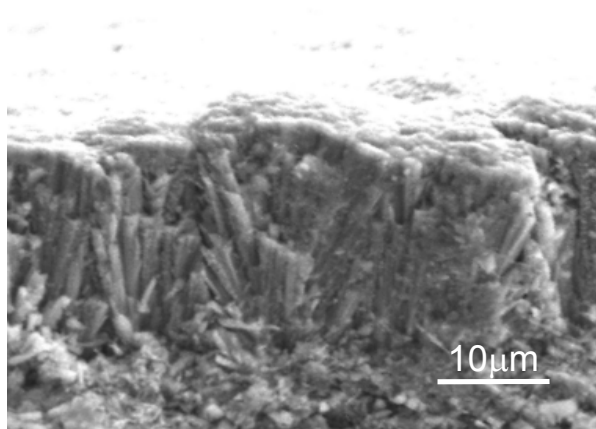


(a)

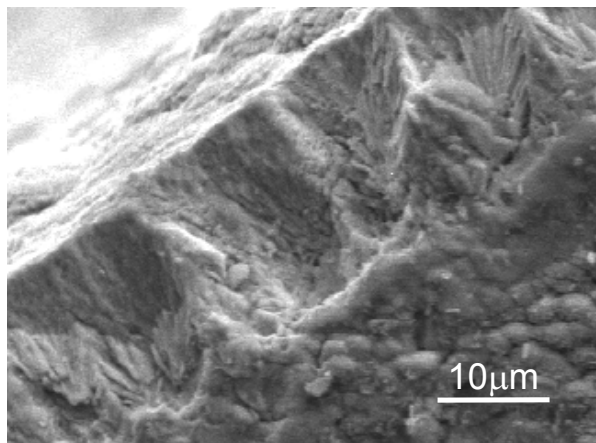


(b)

Figure 6.3. SEM cross-section images of (a) TiN and (b) nc-TiC/a-C(Al) coatings deposited on piston ring. The thickness was estimated to be  $23.2 \pm 0.3$  and  $21.3 \pm 0.3$   $\mu\text{m}$  for TiN and nc-TiC/a-C(Al), respectively



(a)

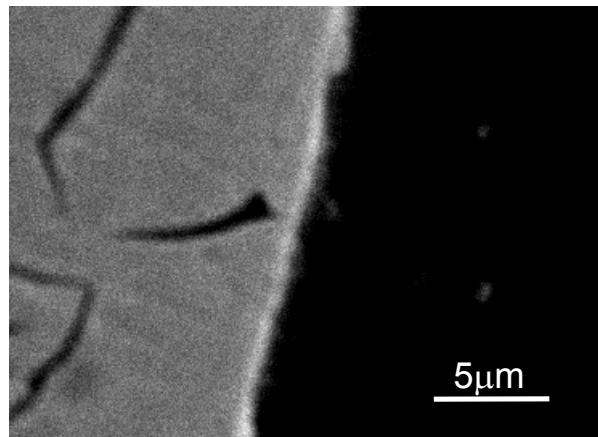


(b)

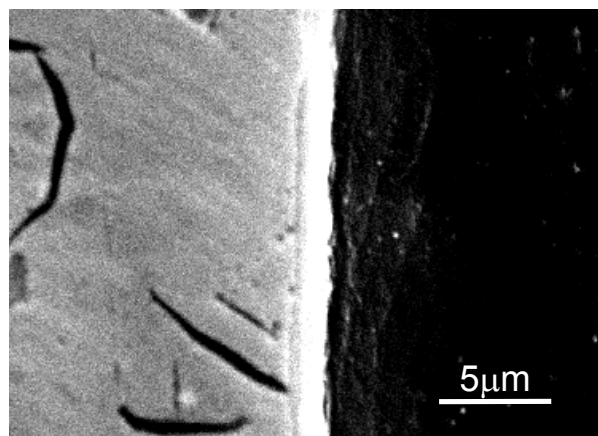
Figure 6.4. SEM images of TiN (a) and nc-TiC/a-C(Al) after 30 hours engine test. The thickness remaining was estimated to be  $19.9 \pm 0.8$  and  $18.4 \pm 0.5$   $\mu\text{m}$  for TiN and nc-TiC/a-C(Al), respectively

Figure 6.5 shows the SEM images of the remaining coatings after a total 610 hours testing. The TiN wore out whereas the nc-TiC/a-C(Al) coating remained at a thickness of

$2.1 \pm 0.2 \mu\text{m}$ . The nc-TiC/a-C(Al) coating still adhered very well to the piston ring and no sign of spallation or peeling-off was observed. The results from engine tests are summarized in table 6.2.



(a)



(b)

Figure 6.5. Remaining coating after engine test for 610 hours. The TiN wore out (a) and for the nc-TiC/a-C(Al) a  $2.1 \pm 0.2 \mu\text{m}$  thickness remained (b)



Table 6.2. Results from engine tests

| Coatings       | Thickness after ( $\mu\text{m}$ ) |      |            | Wear rate ( $\mu\text{m}/100\text{h}$ ) |            | Specific fuel consumption (g/HP.h) |            |
|----------------|-----------------------------------|------|------------|---|------------|------------------------------------|------------|
|                | 0                                 | 30 h | (30+580) h | First 30 h                              | Next 580 h | First 30 h                         | Next 580 h |
| TiN            | 23.2                              | 19.9 | 0          | 11                                      | > 3.4      | 236                                | 225        |
| nc-TiC/a-C(Al) | 21.3                              | 18.4 | 2.1        | 9.6                                     | 2.8        | 227                                | 221        |

Assuming that the TiN coating just wore out right before the test completing, the wear rate would be  $3.4 \mu\text{m}/100\text{h}$ . Therefore, the real wear rate of the TiN coating will be higher than that value. From the table, the wear of the nc-TiC/a-C(Al) was considerably lower than that of TiN (13 % in the first 30 hours running-in and more than 17 % in the next 580 hours). Better wear resistance, considerably lower fuel consumption were seen when the piston ring was coated with nc-TiC/a-C(Al) as compared to TiN. With nc-TiC/a-C(Al) coated ring about 3 % fuel was saved for the first 30 hours and about 2 % for the next 580 hours. The lower fuel consumption strongly relates to the lower friction when nc-TiC/a-C(Al) was used as a protective coating for the piston ring.

### 6.5. Summary

A novel DLC-based nanocomposite nc-TiC/a-C(Al) exhibits a much better performance compared to TiN, which is considered one of the best material for protective coating of piston rings. The experimental results indicate that when the piston ring is coated with nc-

TiC/a-C(Al), a reduction of more than 17 % in the wear rate and 2 % in fuel consumption is obtained compared to that coated with TiN.

Note that a nc-TiC/a-C(Al) coating can be easily deposited by magnetron sputtering (which is considered as a “clean” technique compared to electroplating). This novel material shows a high potential for applications in the industry.

## CHAPTER SEVEN

### CONCLUSIONS AND FUTURE WORK

#### 7.1. Conclusions

The following conclusions can be drawn from this project:

- Magnetron sputtered DLC coatings can be deposited at high deposition rate ( $6 \text{ \AA/s}$  or  $2.2 \text{ \mu m/h}$ ). The mechanical properties of DLC coatings strongly depend on the deposition parameters (target power density, substrate bias voltage and process pressure). DLC coatings have high hardness and exhibit excellent tribological properties. However, high residual stresses (can be more than  $4 \text{ GPa}$ ) limit the coating thickness to less than  $1.5 \text{ \mu m}$  and results in poor adhesion strength. At high applied load, DLC coatings exhibit brittle fracture. Poor thermal stability and oxidation resistance limits the working temperatures of DLC to less than  $400 \text{ }^{\circ}\text{C}$ .
- Bias-graded deposition, where the bias voltage is gradually increased from a minimum to a maximum value as the deposition is progressing and coating thickness is increasing, is a solution to overcome the problems of residual stress and toughness. When bias-graded deposition is applied, the DLC coating will have a gradual increase of  $\text{sp}^3$  fraction from the substrate-coating interface to the coating surface. The resultant coatings, therefore, have better adhesion strength and higher toughness (compared to the coatings deposited under constant bias voltage) meanwhile a hard surface for a good wear resistance is assured. However, the average stress of bias-graded DLC is still relatively high (more than  $1 \text{ GPa}$ ) and the problems of poor thermal stability and oxidation resistance cannot be

solved. Therefore, magnetron sputtered DLC is not suitable for protective coatings of piston rings in internal combustion engines.

- The design of novel DLC-based nanocomposites (nc-TiC/a-C(Al)) has been developed. This new generation of coating inherits the desirable properties of DLC in combination with low residual stress, high hardness, high toughness, good thermal stability and oxidation resistance. The formation of a high volume fraction of TiC nanograins helps to maintain the coating hardness at a high level of about 20 GPa. The decrease in the energy of incoming ions due to more collisions occurring when co-sputtering is carried out, the decrease in  $sp^3$  fraction and the presence of Al in the matrix result in a very low level of residual stress (0.5 GPa) in the coating. The nanocomposite configuration, which hinders crack propagation and supports grain boundary sliding at high applied loads, is combined with a tough matrix of Al-“doped” DLC to enhance the coating toughness. The plasticity during indentation deformation of nc-TiC/a-C(Al) is as high as 60 %. The nanocomposite shows a stable structure, after annealing at 600 °C for 60 minutes and not much decrease in coating hardness was observed. The oxidation resistance of nc-TiC/a-C(Al) is much better than that of pure DLC and TiN and comparable to that of TiAlN under testing temperatures up to 600 °C. The a-C in the matrix ensures self-lubrication, which results in very low friction (less than 0.25) in dry (non-lubricated) conditions. The existence of metals supports the formation of bonds between the lubricating oil and coating, which results in a stable oil film between the coating and the counterpart. Consequently, an extremely low coefficient of friction of 0.04 (even lower than that of DLC) was obtained with nc-TiC/a-C(Al) coatings when sliding against a steel counterpart under boundary lubrication conditions.

- The engine tests, which were carried out with a 41 cc gasoline engine, showed that nc-TiC/a-C(Al) is a promising material for protective coatings of piston rings in internal combustion engines. Much lower wear rate compared to that of TiN (which is presently considered one of the best materials for protective coatings of piston rings) was observed. Compared to TiN coated piston rings, nc-TiC/a-C(Al) coated piston rings result in a 2 % decrease in fuel consumption. This novel DLC-based nanocomposite shows great potential for protective coatings of piston rings in internal combustion engines.

## **7.2. Future work**

To bring nc-TiC/a-C(Al) coating to industry, further work should be done on the engine tests, including:

- Investigation and evaluation of the wear of the cylinder liner when the piston rings are coated with the nanocomposite.
- Undertaking engine tests with various engine types and sizes under different regimes of operation. Applying the theory of probability to estimate the working life of the nanocomposite coatings in comparison with TiN and CrN coatings.

That work could be future M.Eng projects.

For better control of coating properties and for development of carbon-based nanocomposite coatings with other metals added to the DLC matrix, further work can be carried out, including:

- Development of mathematical models to simulate the stress relaxation when Ti and Al are co-sputtered with carbon.

- Development of mathematical models to simulate the contact between nanocomposite coatings and steel counterparts in boundary oil-lubricated conditions. The influence of sliding speed, surface roughness and the interaction between the coating and the counterpart with lubricating oil and additives on the stability of oil film should be included.

That work could be future Ph.D projects.

## References

1. M. Ham, A. Lou, Diamond-like carbon films grown by a large scale direct current plasma chemical vapor deposition reactor: System design, film characteristics, and applications, *Journal of Vacuum Science Technology A* 8 (3) (1990)2143-2149
2. A. Matthew, S.S. Eskildsen, Engineering applications for diamond-like carbon, *Diamond and Related Materials* 3(1994)902-911
3. B.K Tay, D. Sheeja, S. P. Lau, X. Shi, B.C. Seet, Y.C Yeo, Time and temperature-dependent changes in the structural properties of tetrahedral amorphous carbon film, *Surface and Coatings Technology* 130(2000)248-251
4. E. Ciulli- “ A review of internal combustion engine losses – Part 1: specific studies on the motion of piston, valves and bearings”- *Proceedings of the Institution of Mechanical Engineers* 206(1992)223-235
5. C. Wheast, Handbook of Chemistry and Physics, 50th edition, Cleveland, Ohio, 1969
6. P. A. Thornton, V. J. Colangelo, Fundamentals of Engineering Materials, *Prentice-Hall Inc., Englewood Cliff, New Jersey, 1985*
7. M. N. Yoder, Diamond: potential and status, in “*Diamond and diamond-like films and coatings*”, p.1, *Plenum Press, New York, 1991*
8. M. Frenklach, Homogenous nucleation of Diamond Powder in the gas phase, *Journal of Applied Physics* 66(1989)395
9. K. Hormberg, A. Matthews, Coatings tribology, *Tribology series* 28(1994).
10. P.R.Chalker, Characterization of diamond and diamond-like films, in “*Diamond and diamond-like films and coatings*”, p.127, *Plenum Press, New York, 1991*
11. M.A. Tamor, W.C. Vassel, Raman ‘fingerprinting’ of amorphous carbon films, *Journal of Applied Physics* 76(1994)3823-3830
12. J. C. Angus, Diamond-like hydrocarbon and carbon films, in “*Diamond and diamond-like films and coatings*”, p.173,*Plenum Press, New York, 1991*
13. Y. Lifshitz, Diamond-like carbon- present status, *Diamond and Related Materials* 8 (1999)1659-1676
14. S. Zhang, X.T. Zeng, H. Xie, P. Hing , A phenomenological approach for the  $I_D/I_G$  ratio and  $sp^3$  fraction of magnetron sputtered a-C films, *Surface and Coatings Technology* 123 (2000)256-260
- 15 . A.C. Ferrari. J. Robertson, Interpretation of Raman spectra of disordered and amorphous carbon, *Physical Review B*, 61(20) (2000)14095-14107
16. Y. Catherine, Preparation techniques for diamond-like carbon, in “*Diamond and diamond like films and coatings*”, p.193, *Plenum Press, New York, 1991*
17. P.Holiday, Physical properties of carbon films produced using a hybrid physical vapor deposition, *Surface and Coatings Technology* 47(1991)315

18. A. D. Alaoui , Optical properties of carbon films deposited using a hybrid physical vapor deposition technique, *Surface and Coatings Technology* 47(1991)327
19. D.E Paterson , B.J Bai , C. J Chu , R. H Hauge , J.L Margrave, New Diamond Science and Technology, *Materials Research Society*, p.433, Pittsburgh, 1991
20. P. Deak, J. Giber, Theoretical thermochemistry of diamond-like carbon film growth, *Surface and Coatings Technology* 47(1991)517
21. H. Liu, D. S. Dandy, Studies on nucleation process in diamond CVD: an overview of recent development, *Diamond and Related Materials* 4 (1995) 1173-1188
22. H. Kaufman, Industrial application of plasma and ion surface engineering, *Surface and Coatings Technology* 74-75(1995)23-28
23. F.Z. Cui, D.J. Li, A review of investigation on biocompatibility of diamond-like carbon and carbon nitride films, *Surface and Coatings Technology* 131(2000)481-487
24. S. Veprek, The search for novel, superhard materials, *Journal of Vacuum Science Technology A* 17(5)(1999)2401-2420
25. R.F. Davis, Diamond Films and Coatings, p.3, *Noyes Publications*, Park Ridge, New Jersey, 1993
26. P.J. Fallon, V.S. Veerasamy, C.A. Davis, J. Robertson, G. Amaratunga, W.I. Milne, J. Koskinen, Properties of filtered-ion-beam-deposited diamond-like carbon as a function of ion energy, *Physics Review B* 48(1993)4777-4782
27. E. Liu, X. Shi, H.S. Tan, L.K. Cheah, Z. Sun, B.K. Tay, J.R. Shi, The effect of nitrogen on the mechanical properties of tetrahedral amorphous carbon films deposited with a filtered cathodic vacuum arc, *Surface and Coating Technology* 120-121(1999)601-606
28. S.D. Gorpinchenko, S.M. Klotzman, E.V. Kuzmina, S.A. Plotnikov, I.S. Trachtenberg, Wear resistance of diamond-like coatings, *Surface and Coatings Technology* 47(1991)201-208
29. N. Savvides, B. Window, Diamond-like amorphous carbon films prepared by magnetron sputtering of graphite, *Journal of Vacuum Science Technology A* 3(1985)2386-2390
30. A. H. S. Jones, D. Camino, D.G. Teer, J. Jiang, Novel high wear resistant diamond-like carbon coatings deposited by magnetron sputtering of carbon targets, *Proceedings of the Institution of Mechanical Engineers*, 212 (1998) 301-306
31. E. Mounier, P. Juliet, E. Quesnel, Y. Pauleau, Dependence of tribological properties on deposition parameters for non hydrogenated amorphous carbon films produced by magnetron sputtering, *Surface and Coatings Technology* 76-77 (1995)548-552
32. A.A. Voevodin, M.S. Donley, J.S. Zabinski, J. E. Bultman, Mechanical and tribological properties of diamond-like carbon coatings prepared by pulsed laser deposition, *Surface and Coatings Technology* 76-77(1995)534-539
33. F. Xiong, Y.Y. Wang, V. Leppert, R. P. H. Chang, Pulsed laser deposition of amorphous diamond-like carbon films with ArF (193 nm) excimer laser, *Journal of Materials Research* 8(1993)2265



34. A.A. Voevodin, S.J.P. Laube, S.D. Walek, J.S. Solomon, M.S. Donley, J.S. Zabinski, Pulsed laser deposition of diamond-like amorphous carbon films from graphite and polycarbonate targets, *Journal of Applied Physics* 78(1995)4123-4130
35. J. Krishnaswamy, A. Rengan, J. Narayan, K. Vendam, C.J. McHargue, Thin-film deposition by a new laser ablation and plasma hybrid technique, *Applied Physics Letters* 54(1989)2455-2457
36. J.J. Cuomo, J.P. Doyle, J. Bruley, J.C. Liu, Ion-beam sputtered diamond-like carbon with densities of 2.9 g/cc, *Journal of Vacuum Science Technology A* 9 (4) (1991)2210-2215
37. C. Weissmanten, K. Bewilogua, K. Breuer, D. Dietrich, U. Ebesbach, H.J. Erler, B. Rau, G. Reisse, Preparation and properties of hard i-C and i-BN coatings, *Thin Solid Films* 96(1982)31
38. T. Miyazawa, S. Misawa, S. Yoshida, S. Gonda, Preparation and structure of carbon film deposited by a mass-separated C<sup>+</sup> ion beam, *Journal of Applied Physics* 55 (1984)188-193
39. A.A. Voevodin, J.M. Schneider, C. Capera, P. Stevenson, A. Matthews, Studies of atom beams produced by a saddle field source used for depositing diamond-like carbon films on glass, *Vacuum* 46(1995)299-303
40. A. Raveh, L. Martinu, H.M. Hawthorne and M.R. Wertheimer, Mechanical and tribology properties of dual-frequency plasma-deposited diamond-like carbon, *Surface and Coatings Technology* 58 (1993)45-55
41. H. Ronkainen, S. Varijus, K. Holmberg, Friction and wear properties in dry, water, and oil lubricated DLC against alumina and DLC against steel contacts, *Wear* 222(1998)120-128
42. I.L. Singer, S.Fayeulle, P.D Ehni, Friction and wear behavior of TiN in air: the chemistry of transferred films and debris formation, *Wear* 149(1991)375-394
43. S. Myake, R. Kaneko, Micro tribological properties and potential applications of hard lubricating coatings, *Thin Solid Films* 212 (1992)256-261
44. T. Jamal, R. Nimmagada, R.F Bunshah, Friction and adhesive wear of titanium carbide and titanium nitride coatings, *Thin Solid Films* 73 (1980)254-254
45. A. Grill, Tribology of diamond-like carbon and related materials: an updated review, *Surface and Coatings Technology* 94-95(1997)507-513
46. J. Frank, K.Enke, A. Richard, Diamond-like carbon, properties and applications, *Metals and Materials Nov.* (1990) 695-700
47. K. Miyoshi, Studies of mechanochemical interactions in the tribological behavior of materials, *Surface and Coatings Technology* 43-44 (1990)799-812
48. R. Memming , H.J Tolle, P.E. Wierenga, Properties of polymeric layers of hydrogenated amorphous carbon produced by a plasma-activated chemical vapour deposition process II: Tribological and mechanical properties, *Thin Solid Films* 143 (1986)31-41

49. D.Paulmier, H. Zaidi, H. Nery, T. Le Huu, Tribological behavior of diamond-like coatings: effect of active gases in atomic and molecular states, *Surface Coatings Technology* 62 (1993) 570-576
50. A.A. Voevodin, A.W. Phelps, J.S Zabinski, M.S Donley, Friction induced phase transformation of pulsed laser deposited diamond-like carbon, *Diamond Related Materials* 5(1996)1264-1269
51. Y.Liu, A. Erdemir, E.I. Meletis, An investigation of the relation ship between graphitization and friction behavior of DLC coatings, *Surface and Coatings Technology* 86-87(1996)564-568
52. H. Ronkainen, S. Varjus, J. Koskinen, K. Holmberg, Differentiating the tribological performance of hydrogenated and hydrogen –free DLC coatings, *Wear* 249(2001)260-266
53. H. Ronkainen, S. Varjus, K. Holmberg, Tribological performance of different DLC coatings in water-lubricated conditions, *Wear* 249(2001)267-271
54. D.Drees, J.P Celis, E. Decampeneer, J. Maneve, The electrochemical and wear behavior of amorphous diamond-like carbon coatings and multilayed coatings in aqueous environments, *Surface and Coatings Technology* 86-87(1996)575-580
55. Y. Pauleau, Generation and evolution of residual stress in physical vapor-deposited thin films, *Vacuum* 61(2001)175-181
56. M.F. d' Heurle, *Metallurgical Transactions* 1(1970)725
57. S. Zhang, H. Xie, X. Zeng, P. Hing, Residual stress characterization of diamond-like carbon coatings by an X-ray diffraction method, *Surface and Coatings Technology* 122 (1999)219-224
58. E. Mounier, Y. Pauleau, Mechanisms of intrinsic stress generation in amorphous carbon thin films prepared by magnetron sputtering, *Diamond and Related Materials* 6(1997)1182-1191
59. D.R. McKenzie, Y. Yin, N.A. Marks, C.A. Davis, B.A. Pailthorpe, G.A.J. Amaratunga, A.S. Veerasamy, Hydrogen-free amorphous carbon preparation and properties, *Diamond and Related Materials* 3(1994)353-360
60. D. Sheeja, B.K Tay, S.P Lau, Xu Shi, Tribological properties and adhesive strength of DLC coatings under different substrate bias voltage, *Wear* 249(2001)433-439
61. H.K. Tonshoff, A. Mohlfeld, C. Gey, J. Winkler, Mechanical pretreatment for improved adhesion of diamond coatings, *Surface and Coatings Technology* 116-119 (1999)440-446
62. S. Zhang, H. Xie, Improving adhesion of amorphous carbon on cemented carbide through plasma cleaning, *Surface and Coatings Technology* 113(1999)120-125
63. A. Matthews, A. Leyland, K. Hormberg, H. Ronkainen, Design aspects for advanced tribological surface coatings, *Surface and Coatings Technology* 100-101(1998)1-6
64. A.A. Voevodin, R. Bantle, A. Matthews, Dynamic Impact Wear of  $\text{TiC}_x\text{N}_y$  and Ti-DLC Composite Coatings, *Wear* 185(1995)151-157

65. V.F. Dorfman, Diamond-like nanocomposite, *Thin Solid Films* 212 (1992)267-273
66. H. Dimigen, H. Hubsch, R. Memming, Tribological and electrical properties of metal containing hydrogenated carbon films, *Applied Physics letters* 50 (1987)1056-1058
67. H. Sjostrom, L. Hultman, J.E. Sundren, Microstructure of amorphous C:H and metal-containing C:H films deposited on steel substrate, *Thin solid films* 232(1993)169-179
68. A.C. Ferrari, B. Kleinsorge, N.A. Morrison, A. Hart, V. Stolojan, J. Robertson, Stress reduction and bond stability during thermal annealing of tetrahedral amorphous carbon, *Journal of Applied Physics* 85 (10) (1999)7191-7197
69. D.R. Tallan, J.E. Parmeter, M.P. Siegal, R.L. Simpson, The thermal stability of diamond-like carbon, *Diamond and Related Materials* 4(1995)191-199
70. D.Y. Wang, C.L. Chang, W.Y. Ho, Oxidation behavior of diamond-like carbon films, *Surface and Coatings Technology* 120-121(1999)138-144
71. H. Liu, A. Tanaka, K. Umeda, The tribological characteristics of diamond-like carbon films at elevated temperature, *Thin Solid film* 346(1999)162-168
72. H. S. Nalwa, Handbook of Nanostructured Materials and Nanotechnology, v1, Academic Press, 2000.
73. R.W. Siegel, *Annual Review of Materials Science* 21(1991)149
74. H.J Hofler, R.S. Averback, H. Hahn, H. Gleiter, Diffusion of bismuth and gold in nanocrystalline copper, *Journal of Applied Physics* 74 (1993)3832
75. T.Hioki, Y. Itoh, A. Itoh, S. Hibi, J. Kawamoto, Tribology of carbonaceous films formed by ion-beam- assisted deposition of organic material, *Surface and Coatings Technology* 46(1991)233-243
76. Y. Itoh, S. Hibi, T. Hioki, J. Kawamoto, Tribological properties of metals modified by ion-beam assisted deposition of silicone oil, *Journal of Material Research* 6 (1991)871
77. K. Oguri, T.Arai, Tribological properties and characterization of diamond-like carbon coatings with silicon prepared by plasma-assisted chemical vapour deposition, *Surface and Coatings Technology* 47 (1991)710-721
78. K. Oguri, T. Arai, Friction coefficient of Si-C, Ti-C and Ge-C coatings with excess carbon formed by plasma-assisted chemical vapour deposition, *Thin Solid Films* 208(1992)158-160
79. A.Grill, V. Patel, *Diamond Films and Technology* 6 (1996)13
80. L. Wan, A.F. Egerton, Preparation and characterization of carbon nitride films, *Thin Solid Films* 279(1996)34-42
81. Sam Zhang, M.J. Tan, P. Hing, H. Xie, H.L. Wong, W.L. Ng, Nitrogenated carbon layer on magnetic recording disks, *Journal of Materials Processing Technology* 89-90 (1999)556-560
82. Q.We, A.K. Sharma, J. Sankar, J. Narayan, Mechanical properties of diamond-like carbon composite thin films prepared by pulsed laser deposition, *Composite: Part B* 30(1999)675-684

83. B.K. Tay, P. Zhang, On the properties of nanocomposite amorphous carbon films prepared by off-plane double bend filtered cathodic vacuum arc, *Thin Solid Films* 420-421(2002)177-184
84. K. Bewilogua, C.V. Cooper, C. Specht, J. Schroder, R. Wittorf, M. Grischke, Effect of target material on deposition and properties of metal-containing DLC (Me-DLC) coatings, *Surface and Coatings Technology* 127(2000)224-232
85. R. Monteiro, P. Marie, Y.L. Roger, W. Rene, B. Ian, Synthesis and characterization of thin films of WC<sub>x</sub> produced by mixing W and C plasma steam, *Surface and Coatings Technology* 94-95(1997)220-225
86. M. Grischke, *Fortschrittsberichte VDI-Reihe 5, Nr.179, VDI-Verlag, Dusseldorf, 1989* (In German)
87. M. Fryda, *Fortschrittsberichte VDI-Reihe 5, Nr.303, VDI-Verlag, Dusseldorf, 1993* (In German)
88. J. Musil, Hard and superhard nanocomposite coatings, *Surface and Coatings Technology* 125(2000)322-330
89. S. Veprek, S. Reiprich, A concept for the design of novel superhard coatings, *Thin Solid Films* 268(1995)64-71
90. S. Veprek, New development in superhard coatings: the superhard nanocrystalline-amorphous composites, *Thin Solid Films* 317(1998)449-454
91. Veprek, P. Nesladek, A. Niederhofer, F. Glatz, M. Jilek, M.Sima, Recent progress in the superhard nanocrystalline composites: towards their industrialization and understanding of the origin of the superhardness, *Surface and Coatings Technology* 108-109(1998)138-147
92. S. Veprek, Electronic and mechanical properties of nanocrystalline composites when approaching molecular size, *Thin Solid Films* 297(1997)145-153
93. A.A. Voevodin, S. Prasad, J.S. Zabinski, Nanocrystalline carbide/amorphous carbon composites, *Journal of Applied Physics* 82(2)(1997)855-858
94. A.A. Voevodin, J.S.Zabinski, Supertough wear resistant coatings with “chameleon” surface adaptation, *Thin Solid Films* 370(2000)223-231
95. Dieter, Mechanical Metallurgy, in “*Materials Science and Engineering Series*”, McGraw-Hill, 1976
96. A. Niederhofer, P. Nesladek, H.-D. Mannling, K. Moto, S. Veprek, M. Jilek, Structural properties, internal stress and thermal stability of nc-TiN/a-Si<sub>3</sub>N<sub>4</sub>, nc-TiN/TiSi<sub>x</sub>, nc-(Ti<sub>1-y</sub>,Al<sub>y</sub>Si<sub>x</sub>)N superhard nanocomposite coatings reaching the hardness of diamond, *Surface and Coatings Technology* 120-121(1999)173-178
97. P. Holubar, M. Jilek, M. Sima, Present and possible future applications of nanocomposite coatings, *International Conference on Metallurgical Coatings and Thin Films, San Diego, 4-2000*

98. W.J. Meng, R.C. Tittsworth, L.E. Rehn, Mechanical properties and microstructure of TiC/amorphous hydrocarbon nanocomposite coatings, *Thin Solid Films* 377-378 (2000) 222-232
99. B. Feng, D.M. Cao, W.J. Meng, J. Xu, R.C. Tittsworth, L.E. Rehn, P.M. Baldo, G.L. Doll, Characterization of microstructure and mechanical behavior of sputter deposited Ti-containing amorphous carbon coatings, *Surface and Coatings Technology* 148(2001)153-162
100. O. Wanstrand, M. Larsson, P. Hedenqvist, Mechanical and tribological evaluation of PVD WC/C coatings, *Surface and Coatings Technology* 111(1999)247-254
101. A.A. Voevodin, J.P. O' Neill, J.S. Zabinski, Tribological performance and tribochemistry of nanocrystalline WC/amorphous diamond-like carbon composites, *Thin Solid Films* 342(1999)194-200
102. R. J. Hill, Physical Vapor Deposition, *The BOC Group Inc., CA*, 1986
103. R. D. Arnell, P.J. Kelly, Recent advances in magnetron sputtering, *Surface and Coatings Technology* 112(1999)170-176
104. J. Musil, J. Vlcek, Magnetron sputtering of alloy and alloy-based films, *Thin Solid Films* 343-344(1999)47-50
105. S.D. Haddad, N. Watson, Design and application in Diesel engine, *John Wiley & Sons*- 1984
106. X.L Bui, Friction and wear of piston rings in internal combustion engines, *M.Eng. thesis, Vietnam Maritime University*, 1997
107. L.L. Ting, Development of a reciprocating test rig for tribological studies of piston engine moving components- Part1: Rig design and piston ring friction coefficients measuring method, *SAE paper* 930685 (1993)1-8
108. M. Priest, C.M. Taylor, Automobile engine tribology – approaching the surface, *Wear* 241(2000)193-203
109. I. Sherington, E.H. Smith, Experimental methods for measuring the oil film thickness between the piston-rings and cylinder-wall of internal combustion engines, *Tribology International* 18 (1985)315-320
110. S. Furuhashi, C. Asahi, M. Hiruma-“ Measurement of piston ring oil film thickness in an operation engine”- *ASLE transactions* 26 (1983)325-332
111. K. Shin, Y. Tateishi, S. Furuhashi, Measurement oil film thickness between piston ring and cylinder, *SAE paper* 830068 (1983)1187-1201
112. Y. Tateishi, Tribological issues in reducing piston ring friction losses, *Tribology international* 27(1994)17-23
113. S. Furuhashi, For reduction of engine frictional losses, *Internal Combustion Engine* 21(1982)74-85
114. S. Furuhashi, Measurement of piston friction force in actual operating diesel engine, *SAE paper* 790855 (1979)2896-2914



115. D.L. Butler, Topographic characterization of cylinder liner wear, *Ph.D. thesis, University of Birmingham, 1999*
116. M. Nakada, Trends in engine technology and tribology, *Tribology International* 27(1994)3-7
117. N. A. Tuan, N.V. Them, Tribology and solutions to enhance working life of machines, *Science and Technology Publisher, Hanoi, 1990*
118. D. Scott, Materials and metallurgical aspects of piston ring scuffing- A literature survey, *Wear* 33 (1975)293-315
119. H. Yoshida, K. Kusama, J. Sagawa, Effects of surface treatments on piston ring friction force and wear, *SAE paper 900589(1990)1236-1245*
120. C.R. Ferguson, A.T. Kirkpatrick, Internal combustion engines, *John Wiley & Son Inc., 2001*
121. R.S. Day, J.A. Reynold, N. Tommis, *Associated Engineering Group Technical Symposium, Paper 9, 1970*
122. E. Broszeit, C. Friedrich, G. Berg, Deposition, properties and applications of PVD Cr<sub>x</sub>N coatings, *Surface and Coatings Technology* 115(1999)9-16
123. C. Friedrich, G. Berg, E. Broszeit, F. Rick, J. Holland, PVD Cr<sub>x</sub>N coatings for tribological application on piston rings, *Surface and Coatings Technology* 97(1997)661-668
124. S. Zhou, Z. Peijun, Z. Leheng, X. Xinfu, H. Aimin, Z. Weiquan, Multi-layer compound coating on cast iron piston ring by multi-arc and magnetron sputtering ion compound plating technique, *Surface and Coatings Technology* 131(2000) 422-427
125. J. Deng, M. Braun, Tribological behavior of TiN, TiC<sub>x</sub>N<sub>y</sub> and TiC coatings prepared by unbalanced magnetron sputtering technique, *Surface and Coatings Technology* 70 (1994)49-56
126. T. S. Eyre, Review of piston ring and cylinder liner materials, *Tribology International* 4(1979)79-89
127. F. Rastegar, D.E. Richardson, Alternative to chrome: HVOF cermet coatings for high horse power diesel engine, *Surface and Coatings Technology* 90(1997)156-163
128. A.V. Levy, D. Boon, E. January, A. Davis, Sliding wear behavior of protective coatings for diesel engine components, *Wear* 101(1985)127-140
129. A.V. Levy, N. Jee, Unlubricated sliding wear of ceramic materials, *Wear* 121(1988)363-380
130. T. Inoue, Development of automotive piston rings with high resistance to wear and scuffing, *Proceeding of International Conference in Tribology, p155-160, Nagoya, Japan, 1990*
131. M.V. Zdujic, O.B. Milosevic, L.C. Karanovic, *Materials Letters*, 13(1992)125-128
132. A. Brenner, S. Senderoff, A spiral contractometer for measuring stress in electrodeposits, *Journal of Research of the National Bureau of Standards* 42(1949)89

133. W.A. Brantley, Calculated elastic constants for stress problems associated with semiconductor devices, *Journal of Applied Physics* 44(1973)534-535
134. G.P. Pharr, Measurement of mechanical properties by ultra-low load indentation, *Journal of Material Science and Engineering A* 253(1998)151-159
135. A.C.Fisher-Cripps, Nanoindentation, in *Mechanical Engineering Series*, Springer, New York, 2002
136. G. Turban, in Interactions plasmas froids materiaux, Edited by C. Leijeune, p.79 Editions de Physique, Les Ulis, France, 1988 (In French)
137. M.A. Lieberman, A.J. Lichtenberg, Principles of plasma discharges and materials processing, p.470, John Wiley & son Inc., New York, 1994
138. E. Mounier, Y. Pauleau, Effect of energetic particles on the residual stress in non-hydrogenated amorphous carbon films deposited on grounded substrates by DC magnetron sputtering, *Journal of Vacuum Science Technology A* 14(4) (1996)2535-2543
139. E.W. McDaniel, Collision Phenomena in Ionized Gases, Wiley, New York, 1964
140. A.A. Voevodin, C. Rebholz, J.M. Sneider, P. Stevenson, A. Mathews, Wear resistant composite coatings deposited by electron enhanced closed field unbalanced magnetron sputtering, *Surface and Coatings Technology* 73 (1995)185-197
141. Y. Lifshitz, G.D. Lempert, E. Grossman, I. Avigal, C. Uzan-Saguy, R. Kalish, J. Kulik, D. Marton, J.W. Rabalais, Growth mechanisms of DLC films from C<sup>+</sup> ions: experimental studies, *Diamond and Related Materials* 4(1995)318-323
142. A. Rodriguez-Navarro, W. Otaro-Rivera, R. Messier, L.J. Pilione, Development of preferred orientation in polycrystalline AlN thin films deposited by rf sputtering system at low temperature, *Journal of Materials Research* 12(1997)1850-1855
143. D. Nir, Stress relief forms of diamond-like carbon thin films under internal compressive stress, *Thin Solid Films* 112(1984)41-50
144. H. Windischmann, An intrinsic stress scaling law for polycrystalline thin films prepared by ion beam sputtering, *Journal of Applied Physics* 62(1987)1800-1807
145. C.A. Davis, A simple model for the formation of compressive stress in thin films by ion bombardment, *Thin Solid Films*, 226(1993)30-34
146. C. Donnet, M. Belin, J.C. Auge, J.M. Martin, A. Grill, V. Patel, Tribochemistry of diamond-like carbon coatings in various environments, *Surface and Coating Technology* 68-69(1994)626-631
147. A.A. Voevodin, J.S. Zabinski, Load-adaptive crystalline-amorphous nanocomposites, *Journal of Materials Science* 33(1998)319-327
148. S.T. Mileiko, Metal and Ceramic Based Composites, Elsevier, New York, 1997
149. M. Maruyama, F.S. Ohuchi, L. Rabenberg, Catalytic carbide formation at aluminum - carbon interfaces, *Journal of Materials Science Letters* 9(1990)864-866
150. H. Randhawa, High-rate deposition of Al<sub>2</sub>O<sub>3</sub> films using modified cathodic arc plasma deposition processes, *Journal of Vacuum Science Technology A* 7 (3)(1989)2346

- 
151. R.O. Dillon, J. Woollam, V. Katkanant, Use of Raman scattering to investigate disorder and crystallite formation in as-deposited and annealed carbon films, *Physics Reviews B* 29 (1984)3482-3489
  152. J.P. Sullivan, T.A. Friedmann, A.G. Baca, Stress Relaxation and Thermal Evolution of Film Properties in Amorphous Carbon, *Journal of Electronic Materials* 26(1997)1021-1029
  153. T. Zehnder, J. Patscheider, Nanocomposite TiC/a-C:H hard coatings deposited by reactive PVD, *Surface and Coatings Technology* 133-134(2000)138-144
  154. P. Panjan, B. Navisek, M. Cekada, A. Zalar, Oxidation behavior of TiAlN coatings sputtered at low temperature, *Vacuum* 53(1999)127-131
  155. S. Zhang, Y. Fu, H. Du, X.T. Zeng, Y.C. Liu, Magnetron sputtering of nanocomposite (Ti,Cr)CN/DLC coatings, *Surface and Coatings Technology* 162(2002)42-48
  156. S. Inoue, H. Uchida, Y. Yoshinaga, K. Koterazawa, Oxidation behavior of  $(\text{Ti}_{1-x}\text{Al}_x)\text{N}$  films prepared by r.f. reactive sputtering, *Thin Solids Films*, 300(1997)171-176
  157. C.H. Bovington, Friction, wear and the role of additives in their control, in "Chemistry and technology of lubricants", Edited by R.M. Mortier, S.T. Orszulik, p.320, Blackie Academic and Professional, UK, 1997
  158. F. Bowden, D. Tabor, The friction and lubrication of solids, Clarendon Press, Oxford, 1986